STUDY ON ELECTRICAL CHARACTERISTICS OF XLPE INSULATION OF HIGH VOLTAGE CABLE

YANG JUANJUAN

School of Electrical & Electronic Engineering

A thesis submitted to the Nanyang Technological University
in partial fulfillment of the requirement for the degree of
Doctor of Philosophy

2009

ACKNOWLEDGMENTS

I take this opportunity to express my deepest appreciation to my supervisor, Assistant Professor Zhang Daming, for his invaluable guidance in the form of stimulating suggestions and criticisms, understanding, patience and encouragement throughout my research.

I also would like to express my deep gratitude to my former supervisor, Associate Professor Sivaswamy Birlasekaran, for his invaluable advice and guidance at the beginning of the project.

I wish to thank Professor Lalit Kumar Goel, Head of Power Engineering, Division of EEE for his continued support and encouragement.

I still cannot forget to say thanks to Professor Choi San Shing, the former Head of Power Engineering for his kind concern and support.

The research would be impossible without the financial support provided by Nanyang Technological University (NTU) in the form of a research scholarship. For this I am much appreciated.

I thank the contributions of Mr. Lim Kim Peow, Mrs. Ng-Tan Siew Hong, Jennifer, and Mr. Tsay Chi Huang of System Protection Laboratory of EEE for their kind assistance and continued technical support in the course of my research.

Many thanks also go to all my friends at NTU who made my life here so enjoyable.

Last but not least, I am deeply grateful to my husband, Wang Huili, and my parents, for their affectionate love, unfailing support, patience and encouragement over these three years of my graduate program.

LIST OF PUBLICATIONS

Publications related to this research project:

[1] J. J. Yang and D. M. Zhang, "Newton-Raphson method to determine the intrinsic permittivity of XLPE cable," *Proceedings of the 8th International Power Engineering Conference, 2007*. (IPEC 2007). pp. 405-410, 2007.

[2] J. J. Yang and D. M. Zhang, "Dimensional effects on the measurement of permittivity of semiconducting materials used in high voltage XLPE cables," *Proceedings of the 8th International Power Engineering Conference, 2007*. (IPEC 2007). pp. 241-246, 2007. Published in the special issue of *International Journal of Emerging Electric Power Systems*, Vol.9, No.1, 2008.

[3] J. J. Yang, R. F. Huang and D. M. Zhang, "A field-circuit coupled method to accurately determine intrinsic complex permittivity of XLPE insulation material," *IEEE Transactions on Dielectrics and Electrical Insulation,* Vol.15, No.2, pp. 341-349, 2007.

[4] J. J. Yang and D. M. Zhang, "Partial Discharge Phenomena Due to Electrical Treeing in XLPE," *Proceedings of the 1st IEEE Conference on Industrial Electronics and Applications* 2006. (ICIEA2006). pp. 1665-1670, 2006.

[5] J. J. Yang and S. Birlasekaran, "Characteristic Features of Electrical Treeing in XLPE and PE," *Proceedings of the 7th International Power Engineering Conference*, 2005. (IPEC 2005), pp. 1-6, 2005.

[6] J. J. Yang and S. Birlasekaran, "Diagnosis of electrical treeing phenomenon in XLPE insulation," *Proceedings of Electrical Insulation Conference and Electrical Manufacturing Expo*, 2005. pp. 20-25, 2005.

[7] S. Birlasekaran, J. J. Yang, M. A. Pe, and T. S. Han, "Study of partial discharge in XLPE and PE," *Proceedings of the 19th Nordic Insulation Symposium*, NORD-IS05, Trondheim, Norway, 2005, pp. 1-4, 2005.

Publications not related to this research project:

[8] T. M. Lim, S. B. Cheng, J. J. Yang, and X. W. Wu, "Design and parameter estimation of hybrid magnetic bearings for blood pump applications," *Journal of Mechanical Systems and Signal Processing*, 2008. (Under review)

[9] T. M. Lim, S. B. Cheng, J. J. Yang, and X. W. Wu, "Magnetic Levitation of a One DOF System Using Simultaneous Actuation and Displacement Sensing Technique," *Journal of Mechatronics*, 2008. (Minor modification)

[10] J. J. Yang, Y. Liu, X. Tian, and X. L. Cao, "Comparison of dielectric-loss property of nonlinear anti-corona materials," *Journal of Insulation Materials*, vol. 37, pp. 1-4, 2004.

[11] J. J. Yang, Y. Liu, and X. L. Cao, "Simulative calculation and test validation of the electric field stress grading bushing optimized by nonlinear dielectric," *Journal of Insulation Materials*, pp. 1-3, 2003.

[12] X. Wang, J. J. Yang, X. L. Cao, X. Man, and J. S. Lv, "The Electric Testes of Ordinate Insulation in Converter Transformer by the Method of Applying Voltage on Single-phase," Properties and Applications of Dielectric Materials, 2003. *Proceedings of the 7th International Conference on*, vol. 3, pp. 1170-1173, 2003.

[13] Y. Liu, J. J. Yang, and X. L. Cao, "Application of Nonlinear Resistance and Capacitance Configuration in Ameliorating the Electrical Field Distribution," Properties and Applications of Dielectric Materials, 2003. *Proceedings of the 7th International Conference on* vol. 2, pp. 745-748, 2003.

[14] K. Wang, J. J. Yang, Y. Xu, X. L. Cao, and L. S. Zhong, "Studies on the VHF detection of PD in HV cable and joint," *Journal of Electric Wire & Cable*, pp. 1-4, 2002.

ABSTRACT

Polyethylene polymers, especially cross-linked polyethylene (XLPE), are widely used in high voltage transmission cables. Electrical treeing is one of the most important degradation mechanisms in aged XLPE cable system. Partial discharge (PD) technique is one of the effective methods to identify this slowly developing fault. For studying the aging mechanism, space charge accumulation and local electric field are the important parameters.

Increased electrical stress is simulated by typical point-plane electrode geometry. For PD pulses distributed in 20 ms, some time-domain distributions have been analyzed, including φ-q, n-q, Δu-Δt and Weibull distributions. For single PD pulses, various analyses have been carried out to study the frequency content. The effects of stress level and aging time have been compared in three test modes. Two types of electrical trees have been identified based on PD analysis and optical recording. Observed light emission supported the theory of emission by protons due to high-energy electrons. The above analyses are supported with dielectric response measurements.

The needle-plane electrode configuration has been analyzed in respect of the influences of geometry parameters on the electric stress. The electric field distribution in three cases helps understand the initiation and growth of electrical trees. Considering the field- and thermal- dependent nonlinear conductivity of polyethylene, the transient distributions of electric field and space charge density are analyzed under different waveforms. Significant temperature rise occurs when a fast-rise waveform is applied. Going deeper to the macroscopic scale, Poisson's equation, continuity equation and transport equation are combined to form a bipolar charge transport model. COMSOL® is successfully applied to solve such multiphysics problem. By assuming unique and exponential deep trapping levels, respectively, a one-dimensional (1D) problem of field and space charge density is solved for two types of computation cells. The first type is traditionally used in charge transport analyses, while the second one is specially designed for the needle-plane electrode geometry. The two assumptions are not equivalent. However, the former model is useful to explain the long time decaying and the latter one exhibits the features of field-limited space charge.

To study the high frequency response of XLPE cable, the complex permittivity is an important parameter. For XLPE, a large measurement error takes place due to the fringing effect from traditional parallel-electrode system. Based on the field-circuit coupled theory, a correction curve can be acquired by assuming initial values. And the influence factors of this curve have been analyzed. The field-circuit coupled method is verified by a measurement. This method shows advantage in accuracy over the traditional guarded-electrode measurement and it has the theoretical practicability to eliminate the limit on sample dimension and electrode configuration. Since the high-permittivity semicon shows a dominant effect on high frequency loss, the dimensional effect has also been investigated and a mathematical model has been set up. Due to the electric field distortion, the dimensional effect makes the apparent complex permittivity deviate from the intrinsic value above hundreds of MHz. Moreover, when the intrinsic permittivities of both XLPE and semicon are unknown, the apparent values of permittivity could be different from the intrinsic values due to the fringing and dimensional effects. The field-circuit coupled method has been proven still applicable. The complex permittivities of XLPE and semicon can be iteratively derived from the measurement results by using Newton-Raphson method.

TABLE OF CONTENTS

LIST OF FIGURES

LIST OF TABLES

LIST OF ABBREVIATIONS AND SYMBOLS

1D	One Dimensional
2D	Two Dimensional
AC	Alternate Current
AE	Acoustic emission
ANN	Artificial Neutral Network
BEM	Boundary element method
CAs	Cellular Automata
CCD	Charge Coupled Device
DC	Direct Current
DR	Dielectric Response
EL	Electroluminescence
EPR	Ethylene Propylene Rubber
ERA	Electrical Research Association
ESR	Electron Spin Resonance
FDTD	Finite Difference Time Domain
FEM	Finite Element Method
FFT	Fast Fourier Transform
FIR	Finite Impulse Response filters
FT	Fourier Transform
FTIR	Fourier Transform Infra-Red spectroscopy
HFCT	High Frequency Current Transformer
HPFF	High Pressure Fluid-Filled
HPGF	High Pressure Gas-Filled
HV	High voltage
Hz	Hertz
IIR	Finite Impulse Response
LV	Low voltage
NN	Neural Network
NTU	Nanyang Technological University

PD	Partial discharge
PE	Polyethylene
PEA	Pulsed Electro-Acoustic
PIPS	Piezoelectrically Induced Pressure Step
PILC	Paper-Insulated Lead-Covered
PPP or PPLP	Laminate of Paper and Polypropylene
PRPDA	Phase Resolved Partial Discharge Analyzer
PWP	Pressure Wave Propagation
SCFF	Self-Contained Fluid-Filled
SCLF	Space Charge-Limited Field
TDR	Time-Domain Reflectometry
TLT	Transmission-Line Theory
TP	Thermal Pulse
TSC	Thermally Stimulated Currents
TSD	Thermally Stimulated Discharge
TSP	Thermal Step Pulse
UHF	Ultra High Frequency
UV	UltraViolet
XLPE	Cross-linked Polyethylene
A	Richardson constant
k_B	Boltzmann constant
h	Planck constant
e	Element charge
+ve	Positive half-cycle
α	Scale parameter of Weibull distribution
β	Shape parameter of Weibull distribution
γ	Propagation constant
ρ	Charge density
Δu (V)	Voltage difference between two consecutive peak pulses
Δt (s)	Time difference between two consecutive peak pulses
µm	Micro meter
nm	Nano meter

μs	Micro second
ns	Nano second
φ	Phase or potential
φ-q-n	Phase – magnitude-number
ε'	Real part of complex permittivity
ε''	Imaginary part of complex permittivity
$\varepsilon_r^{'}$	Real part of relative complex permittivity
$\varepsilon_r^{''}$	Imaginary part of relative complex permittivity
$\varepsilon_m^{'}$	Real part of measured complex permittivity
$\varepsilon_m^{''}$	Imaginary part of measured complex permittivity
$\varepsilon_c^{'}$	Real part of calculated complex permittivity
$\varepsilon_c^{''}$	Imaginary part of calculated complex permittivity
ω	Radial frequency
θ	Tip angle of needle
σ	Conductivity
μ	Mobility
v	Attempt to escape frequancy
κ	Thermal conductivity
w	Barrier coefficient
Δ	Trap depth or element size of FEM mesh
Γ	Boundary condition
A	Area
B	Trapping coefficient
C_{p}	Equivalent capacitance
D	Needle radius
d	Distance between needle and plane electrodes
E	Electric field
f	Frequency
G	Conductance
(i, j)	Point position in FEM grid

J	Total current density
j	Current density
N'	Pre-exponential factor
P	Power dissipation
P_d, Q_e	Real / imaginary part of complex power
q	Charge/ PD amplitude
q_{m}-φ, $H_{\max}$-φ	Maximum PD amplitude to phase
q_{ave}-φ, H_{mean}-φ	Average PD amplitude to phase
q-n, H-φ	PD amplitude to number
R_{p}	Equivalent resistance
R	Radius of space charge region
r_0	Needle tip radius
S_E, S_H	Complex power
S	Combination coefficient
T	Temperature
T_0	Shape parameter
t	Time
U or V	Applied voltage
x, y, z	Rectangular coordinate variables
r, ϕ, z	Cylindar coordinate variables

Chapter 1 Introduction

1.1 Motivation

The demand for polymeric insulating materials in power apparatus such as cables, transformers, motors, and capacitors is growing. Polymers have excellent electrical properties. In addition, good mechanical stiffness, high corrosion resistance, ease of formation, and low cost of manufacturing and maintenance often make them the best choice of insulating materials for many applications [1]. The development of polyethylene in 1941 triggered a dramatic change in the insulation of cables for the transmission and distribution of electrical energy.

Cross-linked polyethylene (XLPE) cable was first patented in 1959 for a filled compound and in 1963 for unfilled by Dr. Frank Percopio. The significantly higher initial-stage cost of such cable slowed its acceptance for utility purposes until 1980s [2]. For transmission class cables (defined as cables operating above 46 kV), as the application of synthetic polymers to cable technology matured, XLPE gradually displaced paper as the insulation material of choice for transmission voltages up to 230 kV. XLPE is the prime extruded material used for transmission cables besides distribution class cables (mostly 15 to 35 kV), although the laminate of paper and polypropylene (PPP or PPLP) has been employed for voltages above 230 kV. In Singapore, where underground high voltage (HV) XLPE cables operate most at 230 kV, after nearly 20 years of service, the degradation of HV cable is being observed at cable joints regularly and some of those cable joints had to be replaced. As the early XLPE cable population is aging, its impaired reliability is becoming the cause for serious concern.

Even with the present-day technology, it is almost impossible to completely eliminate defects that can be accidentally introduced into polymeric insulation during material processing and cable manufacturing. In cables operating in a dry environment, the degradation takes the form of a tree-like growth called electrical trees [3], while cables especially medium voltage cables operating in a humid environment develop water trees [4]. Although a water tree will ultimately convert to an electrical tree [5], especially when subjected to lightning and/or switching surges, it is not an issue, since HV power cables

usually are hermetic. Once an electrical tree starts, cable breakdown is imminent and can occur in less than a year at service voltage. Thus, for power cables operating in dry as well as in wet environments, it is the electrical tree that is usually responsible for cable breakdowns.

Monitoring the condition of the XLPE insulation of HV cables is an important research area due to the extensive use of XLPE cables. To carry out on-site (online or offline) measurements, many different testing technologies are attempted to help identify those cables that need repair, rehabilitation, or replacement. Each of these methods has some advantages as well as disadvantages. Among these methods, partial discharge (PD) measurement is one of the sensitive indicators of different localized damages, costs less than other methods, and can be on-line and non-intrusive testing. However, in order to improve the long-term reliability of XLPE power cables, it is essential to understand the mechanism of breakdown of XLPE solid insulation materials, i.e. identification of defects and degradation which has not been fully understood yet. Thus, the attention to purely research work still needs to be paid in laboratories. The analysis of the PD patterns is one of the main subjects in connection with electrical trees. It is necessary to elucidate a correlation between the electrical trees and their PD patterns considering their stage of the growth such as initiation and the propagation [6, 7]. Also, voluminous data on PD contain valuable information about mechanisms of the underlying aging process that leads to complete breakdown. Besides traditional phase distribution method, there are also other methods, such as Weibull distribution [8, 9], shape, symmetry and correlation distribution [10] using statistical parameters analysis [11] which examines around twenty statistical parameters associated with PD distribution. After extracting the main features using known PD discharges, fractal parameters [12, 13], neural network paradigms [14, 15], fuzzy classification [16] and wavelet coefficients [17, 18] are attempted to recognize the different types of PD. It is noted that the correlation between all the measured variables and the discharge processes is limited. It should also be noted that single parameter may not provide a reliable quantity to make a conclusive assessment of the state of the insulation. This is due to the random characteristics of PDs and the large mount of data acquired. Instead, multiple analyzing methods are required to identify the characteristics of electrical treeing in XLPE cable. Furthermore, besides putting much focus on the

development for PD signal processing techniques, other assistant methods may be applied, such as optical observation and dielectric response measurement.

Polyethylene as a semi-crystalline material has some unique characteristics. To better understand the phenomena in such insulation bulk, simulation techniques are an important supplement to measurements. Needle-plane electrode geometry is a typical electrode system in order to produce serious electric stress concentration. Its parameters have some influences on the electric field distribution along with the space charge distribution. The nonlinear conductivity is also an important property of polyethylene, which is dependent on electric field and even temperature. Thus it needs paid attention to in practical analysis. Since space charges have time-related features during transport, the transient problem is necessarily solved under different applied voltage waveforms. Furthermore, to research the general mechanism of charge transport phenomenon in insulation bulk, typical models should be applied in computation at the macroscopic scale. Regarding to the fact that multiphysics problem is basically a composition of several partial differential equations, the COMSOL Multiphysics® software will be applied in the solving.

Using sensitive PD detection, defects can often be detected during field testing, prior to breakdown. Capacitive, inductive, galvanic, or directional coupling methods are available for sensing PD. With the knowledge of the propagation velocity through the cable and the time delay between the signals observed to the left and to the right of a cable, an estimation of the PD location can be given. Shielded power cables can be considered as lossy transmission lines. Propagation losses occur in power cables when pulses propagate through them. The high frequency attenuation of the cable causes the peak amplitude of a PD pulse, as well as the pulse energy, to decrease as a function of distance propagated. Thus the ability to detect and locate a PD source is limited by attenuation. All the materials that make up a cable contribute to the propagation characteristics (attenuation and phase velocity) of the cable. Significant high frequency losses are caused by the propagation of radial electric displacement current (which increases with frequency) through the resistance of these layers [19]. The effect of the semiconducting layers on the PD propagation has been widely studied [19-22]. Its permittivity is verified to be frequency-dependent. This is a common property for any dielectric material when the

frequency band is sufficiently wide, as it is for XLPE material. Thus, it may not be sufficiently accurate to assume the same permittivity value of XLPE at 1 MHz as that at 1 GHz. Investigating the frequency-dependence of XLPE material is meaningful since partial discharge pulses contain a wide range of frequency components. In addition, as a manufacturing product, XLPE is made in a large scale industrial process in reactors which are never "tight". As a result, the dielectric properties of XLPE undoubtedly have some statistical variability. The case for semicon is even worse, as the high frequency properties of interest are completely unspecified and may vary by batch, extrusion conditions, cable history, etc. Shear stresses during cable operation will break up the carbon agglomerates which provide conductivity so that the properties of the semicon will evolve with time [23]. In laboratory, to test the aging status of cable segment, standard sample of cable material is usually measured. Up to present, various permittivity measurement methods have been used in experiment [24-30] for different materials. One needs to realize that it is the intrinsic values of complex permittivity and conductivity for the materials that are important, and not the measured values. According to the theory given by literature [31], the measured permittivity of a material may differ significantly from its intrinsic value if there is a dimensional effect in it or if the fringing effect becomes pronounced, such is the case with the two-parallel-electrode method. Illustration and enhanced research can be found in literature [28, 30] and [32, 33], where an air-filled capacitor is studied. Compared to the relative permittivity of semicon, the relative permittivity of XLPE insulation is very small, usually around three. Fringing effect is for sure significant when the conventional two-parallel-electrode method is used to measure permittivity. Even with a guard electrode, the energy stored in the ambient still may not be ignored. No literature reports an effective method to calculate the permittivity for an XLPE sample with a two-parallel-electrode configuration and without a guard. Additionally, dimensional effect is a subject in materials characterization research. Nobody has studied this effect on intrinsic permittivity measurement of semicon of XLPE cable. The traditional three-electrode measurement requires strictly on sample dimension and instrument, which limits the availability in applications. New effective determination method is in great need which is suitable for samples with different dimensions. In addition, the method to be developed would be better if it is suitable for many types of materials including XLPE and semicon.

1.2 Objectives

This research work intends to investigate the electrical characteristics of HV (230 kV) XLPE cable material.

To characterize the initiation and propagation of electrical trees, partial discharge measurement, dielectric response measurement and optical observation are to be combined and the difference of treeing is to be compared at different levels of applied voltage, with different rise rates of applied voltage and with aging time at constant HV. To do that, data acquisition system is to be developed.

Signal processing techniques are to be developed to analyze the PDs in electrical treeing. It is aimed to characterize the PD random occurrence in 20 ms of multiple AC cycles using the well known classical method before developing other analyzing methods. To evaluate the characteristics of pure PD in controlled laboratory environment, XLPE samples with needle-plane electrode configuration to generate electrical treeing will be designed and tested. Moreover, polythene (PE) samples due to their transparent property are also to be prepared and tested in the same procedure in order to observe the tree formation.

Besides the experimental study, theoretical analysis for space charge accumulation and electric field distribution will be investigated. The needle-plane configuration is to act as the object. The simulation tool, COMSOL Multiphysics® v3.4, will be applied to calculate the effects of needle size, space charge, and voltage. Started from the needle-plane geometry whose size parameters will be analyzed according their effects on the electric field, and then simplified model designed for the analysis of tree growth, the field and thermal dependences of polyethylene conductivity will be considered in order to analyze the field and space charge distributions with aging time under different applied voltage waveforms. And the temperature rise is also to be studied in respect of the influences of applied voltage waveform. Furthermore, at the macroscopic scale, the space charge transport phenomena will be analyzed referring to the models developed by other researchers. Combining the experiences of charge transport modeling in parallel-plane electrode system and space charge distribution computation in coaxial coordinate system, charge transport procedure will be analyzed for the needle-plane electrode geometry.

PDs will propagate along the cable. The frequency-dependent property of XLPE cable materials especially semicons have influences on the high-frequency response characteristics of cable. Due to the rather low permittivity of XLPE compared with that of semicon, fringing effect cannot be ignored in measurement and calculation. A new method will be developed to consider that factor and the measurement configuration is to be achieved as simple as possible. And since the semiconducting layer plays an important role in PD propagation along power cables, dimensional effect due to its high permittivity in measurement is to be studied. New method is to be verified by analyzing the fringing effect and dimensional effect and tracking the intrinsic permittivity. After that, a calculation method is to be developed to determine the intrinsic permittivity of XLPE and semicon simultaneously.

1.3 Major contribution of the thesis

As a result of the research work, the following original contributions have been made.

1. Ultra high frequency (UHF) PD measurement setup was developed in Nanyang Technological University (NTU) HV laboratory with combination of dielectric response measurement and optical observation equipment. The new contribution is the automatic data acquisition system to capture PD activity in the desired multi 20 ms cycles from 2 channels simultaneously at a sampling rate up to 1 GS/s for PD distribution study in 20 ms and single pulse analysis. Programma® Insulation Diagnostics System Products, IDA200™, was applied to measure the frequency spectrum of equivalent resistance/capacitance and loss angle tangent. Charge-coupled-device (CCD) camera was set up close to the sample under test to record the light emission from electrical treeing. And the tree formation was observed by a microscope with a magnification factor up to 80.

2. Samples to generate electrical trees were designed and fabricated. They were tested at the controlled laboratory conditions with different applied voltages, different rise rates of applied voltage and different aging times at constant HV. The characteristics of PDs without any propagation distortion were investigated to understand the discharge mechanism.

3. Characterization methods for PD identification were investigated. The following signal processing techniques were applied to laboratory data. The φ-q-n distribution was already reported in the literature. Δu-Δt analysis and mixed Weibull distribution were also applied. These techniques were applied to traditional 20 ms-period PD distribution known as group PDs analysis. And the study on single PD known as single PD analysis was also carried out in respect of wave shape, calculated capacitance and rise/fall time. Equivalent F-T plane technique combined the analyses of group PDs and single PD.

4. The needle-plane electrode configuration was investigated by simulation models with/without space charge effect. The influences of needle size and shape, space charge and applied voltage on the electric field distribution were analyzed. A model of electrical treeing was developed and analyzed in three abstract but representative cases.

5. Considering the conductivity of polyethylene which is dependent on the field and thermal distributions, the field-limited space charge distribution, as well as field distribution is analyzed under different conditions: DC voltage, triangular waveform, and AC voltage. Temperature rise is calculated regarding to different rise time of the applied voltage.

6. Bipolar charge transport model is applied to analyze the accumulation phenomena of space charge in polyethylene bulk. COMSOL Multiphysics® software is able to effectively solve the multiphysics problem. Two assumptions have been applied: unique and exponential deep trapping level, respectively. And for each of them, two types of 1-dimensional (1D) cells are applied for computation in rectangular and cylinder coordinate system, respectively. The electric field distortion and distributions of electrons and holes, mobile and trapped, are analyzed with stressing time.

7. A field-circuit coupled method was developed to contravene the deviation of measured value from the intrinsic one due to fringing effect, which can effectively take into account the energy stored in the ambient and thus correct the measurement error. It has no limitations on the dimensions of test samples and fixtures, and also a guard electrode will not be required. A mathematical model was established to study

the difference between the measurable and intrinsic permittivity for the XLPE insulation material. A correction curve of measurable permittivity versus intrinsic value was established for XLPE sample with given dimensions. The influence factors like the size of sample and electrode were analyzed. A measurement was carried to verify the developed method, and the intrinsic value of XLPE sample was determined utilizing the methods in references. The proposed field-circuit coupled method shows obvious advantage over normal electrode-with-guard method.

8. Based on field-circuit theory, a mathematical model for a capacitor made of semicon used in XLPE cable was set up to investigate the dimensional effect in the measurement of its permittivity. Newton-Raphson method was used to determine intrinsic value based on its measured permittivity. The method provided in this research can be used to estimate how small the sample should be in order to make the measured permittivity close to or just equal to its intrinsic value.

9. Assuming a most difficult situation and combining the results of No. 7 and No. 8 listed above, two mathematical models for a capacitor made of XLPE and semicon from a 230 kV XLPE power cable were set up to determine the intrinsic value of permittivity. From numerical calculation, the four unknown parameters (real and imaginary parts of permittivity for these two materials) can be found by iterations based on Newton-Raphson method. Due to the dimensional effect from semicon and the fringing effect from XLPE, the measured or apparent permittivity is different from the intrinsic value. Newton-Raphson method can be used to effectively determine the intrinsic value based on its measured permittivity.

1.4 Organization of the thesis

This thesis is organized into six chapters with the contents described below:

Chapter 1: Introduction

The motivation for this research, the objectives, the major contributions of this project and the layout of this thesis are presented.

Chapter 2: Literature Review of Studies on HV XLPE Cable

An overview of treeing phenomena in HV XLPE cable, treeing measurement techniques, various analysis techniques for PDs due to electrical treeing in XLPE cable insulation, and studies related to PD propagation are summarized. Based on the above, research work for the 3-year period is reported.

Chapter 3: Electrical Treeing Phenomena in XLPE Material

The details are presented, including the electrical treeing testing system with the combination of PD measurement, dielectric response measurement and optical observation, the selection of data acquiring resistance, the PD calibration, and the fabricated samples of XLPE and PE insulation materials to generate PDs due to electrical treeing. The electrical treeing phenomena are characterized considering the factors of level and rising rate of applied voltage, as well as aging time at constant HV. Various techniques for group PD analysis and single PD pulse analysis are applied to carry out signal processing.

Chapter 4: Modeling of Electric Field and Space Charge Distributions in XLPE

The modeling of space charge accumulation as well as electric field distribution is investigated. The needle-plane configuration is the object. The electric field distribution is analyzed in respect of the effects of needle size, space charge, and applied voltage. And then, three cases are studied for electrical tree growth. Furthermore, the field- and thermal-dependent conductivity of polyethylene is considered in the analyses for the field and space charge distribution according to the space charge-limited field (SCLF) theory. At last, at the macroscopic scale, the bipolar charge transport model is applied to the analysis of space charge accumulation with stressing time under DC voltage. Two assumptions for trap level, as well as two types of cells are considered in the computation, respectively.

Chapter 5: Determination of Intrinsic Permittivity of XLPE Cable Materials

A field-circuit coupled method is developed to contravene the deviation of measured value from the intrinsic one due to fringing effect, especially for XLPE material. And the dimensional effects on the permittivity measurement of semiconducting materials are investigated. Based on these two studies, Newton-Raphson method is applied to determine the intrinsic permittivity of materials of XLPE cable.

Chapter 6: Conclusions and Recommendations

This chapter summarizes the findings and presents recommendations for future research work.

Chapter 2 Literature Review of Studies on HV XLPE Cable

2.1 Introduction

With the increasing demands for electrical energy, energy transmission voltages also are increasing. Transmission of bulk power over large distances, as a consequence of increased trading of electricity between countries, will require efficient, high-voltage cable systems, including cables for use in urban areas and for underground and submarine crossings. At present, highly reliable underground transmission lines are found in three forms: high pressure fluid-filled (HPFF), high pressure gas-filled (HPGF), and self-contained fluid-filled (SCFF). Insulation for these cables usually consists of cellulose paper or polypropylene-paper laminate tapes and a dielectric fluid. Today, the operation voltage of extruded transmission power cables has increased to 500 kV [34, 35]. Polymer-insulated electrical cable on the market essentially consists of the following parts: conductors, semiconducting shields, and insulation. Although an eventual breakthrough of superconducting materials would dramatically change the structure of power transmission systems, experts predict that the practical, widespread application of this technology will probably not be within the next 10 to 20 years.

Polyethylenes, $(CH_2\text{-}CH_2)_n$, are very long macromolecules, where n is the link number. The CH_2 groups are strongly joined by bonds of the shared electron valence type. The ends of the different chains contain methyl ($\text{-}CH_3$) or vinyl ($\text{-}CH{=}CH_2$) groups. PE is a thermoplastic: the upper operational temperature is limited to 70°C approximately. By crosslinking of the macromolecules the operational temperature is increased to 90°C approximately. In XLPE the macro molecules are incorporated in a network in which the effective molecular weight has become infinite. The polymer either cross-linked or not, is semi-crystalline, which means that it is partly crystalline and partly amorphous [36]. XLPE was first taken as an insulating material for the 3-6 kV rated distribution power cable in 1960s, and now has been successfully used as the main insulation for the HV or EHV power cables, 110-500 kV rated, because of its superior electrical and mechanical properties.

The life expectancy of HV power cables is adversely affected by treeing, a pre-breakdown phenomenon and accounts for a premature failure of cables in service. Water treeing is one of the most important failure mechanisms of medium voltage power cable particularly in the case of underground or submarine cable. Water treeing results from a localized chemical reaction which changes the polymer from hydrophobic to hydrophilic [37]. However, HV cable, meaning transmission class cable, is almost always hermetic, in which case water treeing is not an issue. Further, it becomes clear that the onset points of breakdown in XLPE cables are still the small defects in XLPE insulation, although the exhaustive elimination of defects has improved performance. Therefore, the study of electrical treeing phenomena from the defects is important to improve the insulating performance of XLPE cables [35]. In field study, many techniques for on-line condition monitoring and off-line field testing have been developed. In laboratory research, there are also many types of methods to study the characteristics of material itself and electrical treeing phenomenon. Among these techniques, PD detection and analysis technique has been developed sufficiently, and it is an effective tool to characterize the fault status of cable.

Electrical treeing is a local phenomenon, where only specific sections of the cable have been subjected to degradation. In practice, replacement of only these parts would improve the cable condition and will be considerably more cost-effective as compared to a total cable replacement. To study the propagation characteristics of PD due to electrical treeing, the frequency-dependent property of material should be considered. To do that, one needs to realize that it is the intrinsic values of complex permittivity and conductivity for the materials that are important, and not the measured values. This is due to the fact that the propagation factor γ consisting of attenuation constant α and propagation constant β depends on intrinsic values, not on their measured values. However, it is impossible to do the on-site measurement for the cables. Even in laboratory, due to the low permittivity of XLPE, the fringing effect cannot be fully ignored even with a guard electrode (standard three-electrode configuration) and at the same time, the high permittivity of semiconducting material will introduce the dimensional effect. Thus, an effective and more flexible method is needed, which will be suitable for samples of different configurations.

Purely research work will be focused in this thesis.

2.2 Review on electrical treeing phenomena in XLPE cable

In an insulation system, the factors to aging may induce irreversible changes and even have effects on the insulation property. From the practical experiences of XLPE cable, these factors usually include the occurrences of PD, electrical tree, and water tree. HV XLPE cables are manufactured with strict requirement, which make PD seldom occur under normal operating conditions. And 110 kV and higher rated XLPE cables usually operate under 90°C with an enough margin. Thus, only treeing phenomenon is the dominant problem in focus.

2.2.1 Treeing

The phenomenon known as treeing in dielectrics was first described in 1912 [2]. Treeing in extruded dielectric cable insulation is the term that has been given to a type of electrical pre-breakdown deterioration that has the general appearance of a tree-like path through that wall of insulation. This formation is radial to the cable axis and hence is in line with the electrical field. Trees form in insulations such as PE, XLPE, and ethylene propylene rubber (EPR) cables, are considered as two distinct types: water trees and electrical trees. Conclusions in recent research work show that treed cables that are subjected to DC, surges, or impulses have shorter life in service after that application than cables not subjected to those stresses.

Electrical treeing is the first degradation mechanism experienced with polymer insulated HV cable, due to technological imperfections that are difficult to be excluded totally in large scale technical products, there may be local field enhancements up to 100 kV/mm and more, and thus even with average electric fields of 10 or 20 kV/mm a breakdown of a polymeric insulation may occur. While water treeing is a very complex phenomenon involving electrical, physical and chemical mechanisms, whereby foreign substances in the dielectric play the decisive role in the phenomenon, electrical treeing seems to be a basically comparatively "simple" phenomenon involving mainly purely electrical phenomena and gas discharges in a solid dielectric [38]. Water treeing and electrical treeing are usually discussed separately since they have almost nothing in common,

especially in regard to the basic mechanism of the deterioration of the polymer and consecutive phenomena. To make clear of their differences, the water treeing phenomenon is reviewed at first, followed by the focus on the review of studies on the electrical treeing.

2.2.2 Water treeing

Water tree deterioration was first found in 1967 and it is a major cause of long-term deterioration in medium voltage XLPE cables. Water trees are diffuse structures with a bush- or fan-like appearance. Typically they are in the 0.1 to 1 mm size range and are usually "rooted" at an interface between the insulation and another substance. Water trees are known to disappear on drying of the insulation and reappear on rewetting. Vented trees were classified into two types: "blue" water trees appearing blue in color and ordinary "white" water trees. The blue tree was found to be much more harmful than the white water tree, since more electrical trees started at the blue trees which probably involve some specific highly catalytic impurity. The main reason of the harmfulness of the blue tree is its very high electrical conductivity, which is confirmed from the fact that the space charge accumulates only at the interface between the treed and the un-treed regions [39].

It has been speculated in the literature that the factors which might influence initiation and growth of water trees in XLPE insulation include water [40], semiconducting compounds [37], and mechanical strain [41]. The electrical strength of cable susceptible to water trees may drop to a greater degree as a function of temperature [42], AC voltage [43], and impulse voltage [44]. It was reported that weakest point of each cable corresponds to vented water trees from conductor shielding layer [45]. The work of Mashikian and Groeger [6] indicated that water trees in fact are not associated with protrusions. They are associated with ionic impurities at the semicon-dielectric interface. This has been shown by making a rough interface and looking at where the water trees grew. There was no correlation with stress enhancement at reasonable field, and at the "root" of each water tree, there was an ionic impurity.

Many studies have been contucted on water tree deterioration in XLPE insulated power cables, and they have led to improvement of structure and selection of materials for

distribution cables rated from 6.6 kV to 33 kV [46]. Compared to distribution cables, there have been a smaller number of reports on water tree deterioration in HV transmission cables rated ≥ 66 kV [39]. Since manufacturing techniques are stricter for HV XLPE cables (rated 110~220kV) and the cables normally apply the configuration with a metallic radial waterproof layer, water treeing is not an issue any more.

2.2.3 Electrical treeing

Electrical trees are dark, branch-like structures with readily apparent channels. Carbonization is often evident; thus, these trees do not change appearance as noticeably as water trees on drying or wetting. Electrical trees are considered to be associated with the final cable failures and do not exist for a long period of time. Electrical trees are the result of internal electrical discharges that decompose the organic materials. No moisture is needed for this process. The types of electrical tree could be classified as branch-type, bush-type and mixed-type (branch + bush) according to their aspect, on which the PD characteristic are dependent.

Electrical breakdown, which usually begins with electrical tree inception, is a complex process affected by electrical, thermal, chemical, and other processes. Mechanism of electrical treeing is usually divided into two stages: inception and propagation [3]. The first is the incubation period, or the initiation phase, when hardly anything appears to occur in the insulation, and the second is the propagation period, during which partial discharges occur and the tree grows. There are some possibilities to initiate electrical treeing: (1) localized heating and thermal decomposition; (2) internal mechanical stress from manufacturing process [47]; (3) fatigue cracking from polarity changes; (4) small voids; (5) air inclusions around contaminants; and (6) electron injection. The evaluation of tree inception stress by experiment using XLPE block samples has been conducted elsewhere [35]. Voltage profile [48, 49] and temperature [50] have influences on the growths of electrical trees in XLPE cable. The mechanism by which an electrical tree "grows" is only partially understood.

2.3 Review on measurement methods of electrical treeing in XLPE cable

2.3.1 Reported methods for cable testing

In field practice, the techniques for testing the aging status of XLPE cable are gradually developing. For 6 kV rated XLPE distribution cables where water tree deterioration is the main cause of failure, the test techniques consist of "offline" and "online" types. The "offline" type includes: retained voltage, depolarization current, DC leakage current, potential attenuation method (DC); retained charge, DC voltage addition method (DC and power frequency); AC loss current (power frequency); loss factor (tanδ) (ultra low frequency). The "online" type includes: DC component, pulsed electro-acoustic (PEA) method, DC voltage addition method (DC and power frequency), etc. For 22 kV XLPE cables, keeping the same as those for 6 kV cables, while not applying depolarization current, DC component and PEA method. In addition, the methods of DC bias voltage, PD, withstand voltage are applied. It is still under discussion whether it is suitable to transplant current testing methods for 6~22 kV cables, except that PD technique has been confirmed. Thus, only PD measurement is emphasized. Recently, some new diagnostic methods for XLPE cables have been developed; some of them may be applied for HV rated cables, such as electroluminescence (EL) method, oxidation character method. In laboratory, there are also sampling method, gas analyzing method, silicon oil analyzing methods, etc.

The study of electrical trees has two main advantages in comparison with water trees. In the first instance the trees are usually clearly visible and their growth can be observed in situ at the same time as other experimental investigations are carried out. More importantly however the greater degree of degradation requires a larger amount of electrical power and gives rise to a wider range of observable physical effects. Thus the process of electrical treeing has been followed by such diverse techniques as: acoustic emission, current pulse, light emission, electron spin resonance (ESR) and thermally stimulated discharge currents (TSD), thermally stimulated currents (TSC), thermoluminescence and electrode polarity effects, frustrated total internal reflection (FTIR), partial discharges and gas emission. As a result of the data obtained by these

investigations a broad outline for the mechanism of the formation of electrical trees has been established. However, further work is required to clarify some of the details, although it now seems unlikely that the main features will be challenged.

Reported partial discharge measurement methods for electrical treeing include electrical method and nonelectrical methods. Each technique has not only advantages but also limitations. In all these methods, the characterization of PD signal is very important to identify the type of developing treeing.

2.3.1.1 Electrical PD measurement

Electrical stressing of insulation materials can be the cause of the occurrence of PDs that reduce the voltage life of the dielectric. The growth of electric trees is a prebreakdown phenomenon accompanied by PD. If this can be detected, it is possible to arrest the growth of the electrical tree before complete breakdown occurs and to locate the starting point of the breakdown. The prebreakdown PD detection method has been proved effective in identifying the dominant factors that affect breakdown strength for commercial AC voltages [35, 51].

PD tests are applied to an extremely wide range of HV apparatus. They were primarily used by manufacturers as nondestructive tests for quality control or for type approval and proof tests for customer specification [52]. To be recognized as PD, the current induced in the external conductor must be sufficiently large to be detected and must occur with a sufficient repetition rate to be recognizable as something other than random noise. The detection of discharges is based on energy exchanges which take place during the discharge. These exchanges are manifested as (i) electrical impulse current, (ii) dielectric loss, (iii) electromagnetic radiation, (iv) light, (v) sound, (vi) increased gas pressure, and (vii) chemical reaction. Discharge detection and measuring techniques may be based on the observation of any of the above phenomena.

2.3.1.2 The conventional PD measuring circuit

Traditionally PD detection was done by narrow-band system (40-400 kHz), but lost some useful information due to the high frequency characteristic of PD [53]. Wide-band PD measurement developed later [54] can extract a large amount of information from

acquired PD. Identification of the kinds of defect generating PD, as well as noise rejection, is thus made easier [55]. The conventional PD measurement method is called ERA method as proposed by Electrical Research Association, UK [56]. The layout of this method is shown in Figure 2-1.

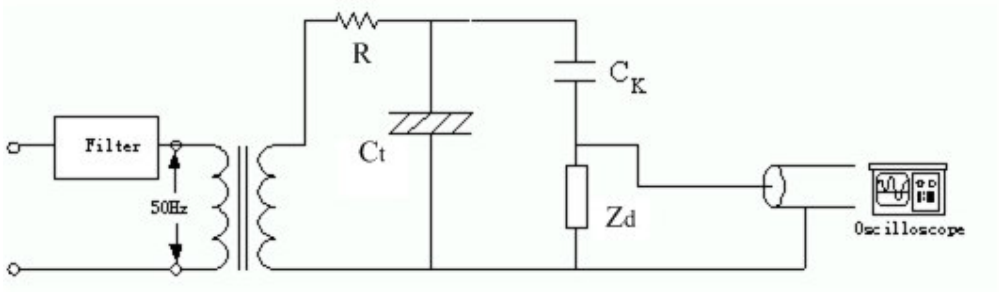

Figure 2-1 Circuit Layout for PD measurement

A PD of magnitude q in a test object (C_t) generates a high-frequency pulse of height Δu in the detection circuit (Z_d) due to the discharge free coupling capacitor C_k. The resistor R blocks the path of PD to the 50 Hz HV source. 50 Hz HV will be mostly dissipated across C_k and high frequency PD will be mostly dissipated across Z_d for measurement. The relationship between Δu and q can be easily derived. In the above layout of this off-line test, the test object is to be isolated from the connected power network. Also discharge free HV source and PD coupler are needed. That makes it difficult for industrial user [57].

PD detection in a distributed transmission line differs fundamentally from that for a lumped element. For example, calibration works differently for the two cases. Since the industry is primarily interested in measuring PD in the interconnected power network, nowadays more efforts have been made to online measurement in the restructured energy market. When PD couplers are permanently installed around the cable, on-line tests can be performed without any interruption of the operation [58]. During the tests, PD signals were measured and acquired by means of a PRPDA (phase resolved partial discharge analyzer) system [59], and the obtained data were off-line processed by means of software.

In general, electrical tree initiation in most solids takes hours to years at realistic stresses. As a result, a tree is not likely to initiate and be detected during PD measurements

performed for the purposes of quality assurance. As well, electrical treeing-induced PD can be of very small magnitude until minutes before failure. Thus PD-based measurements of electrical treeing are of much greater interest to researchers than to practitioners [52, 60].

2.3.1.3 PD sensors

The bandwidth of the electromagnetic waves emitted from PD is very wide and ranges up to GHz [55]. The coupler acts as a HV isolator, and high pass filter allowing high frequency PDs to be detected by a suitable instrumentation at low voltage. Most widely used ones are: capacitive couplers [61], Rogowski coils [62], and high frequency current transformer (HFCT) [63]. The radiated PD microwave signal is sensed with antenna, and passes through preamplifier. Furthermore, a down-converter may be used in the system to shift the center frequency without changing the distribution of the frequency spectrum. The PD signal would damp quite fast in the air. The sensitivity of this method depends on the placement of the sensor.

2.3.1.4 PD detector

All PD detection circuits need use certain device to convert current impulse to voltage pulses, such as a detection impedance [64], a transimpedance amplifier or a FET probe. The detection impedance can be either R with stray capacitance C in parallel or RLC (resistor, capacitor, and inductor parallel connection) type [65]. The shape of the original PD gets altered by the detector frequency response [53]. In ERA units, this measuring impedance is followed by a step-up ferrite transformer to get an optimal signal-to noise ratio and isolation [66]. It is then filtered and amplified for display. In old PD measuring units, the bandwidth of detectors is usually in a few hundred kHz. With modern digital system, higher frequency band width up to 1 GHz can be measured and then it can be de-noised [67].

2.3.1.5 Display of PD activity

Extracted PDs with phase information are displayed as shown in Figure 2-2 (a) in conventional ERA system [56]. After amplification, the discharge pulses are modulated on the ellipse representing 20 ms AC cycle with the corresponding phase/time

information. The repetitive AC cycle is divided into 360 degrees. Using calibrating markers, the peak pulse magnitude is measured.

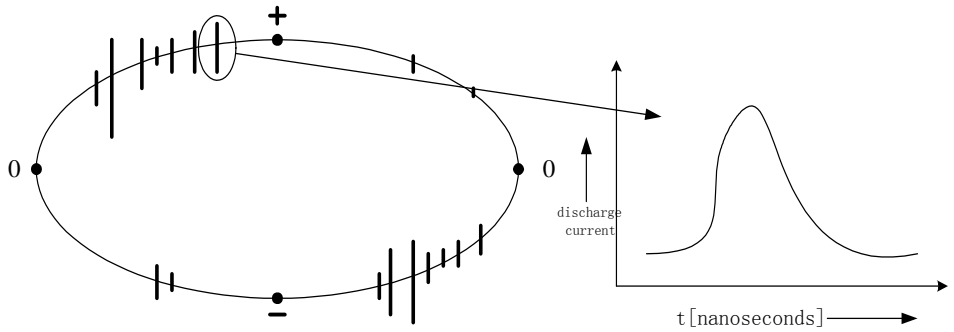

(a) (b)

Figure 2-2 Methods of PD detection: (a) Conventional display using elliptical time base; (b) Zoomed single pulse

2.3.1.6 PD location methods

The location of a PD source through the measurement of traveling wave phenomena can be based on measurements from one or both ends of the cable [68]. The spectrum of the current pulse at the site of a discharge contains a wide range of frequencies. The distorted transmitted signal at the measuring terminals may be considered as comprising of a series of components of different frequencies each of which is related to the form of the PD source, its location and electrical parameters of the cable [19]. Commercially available cable PD locating instruments are designed with 10 MHz bandwidth [69]. International standards use a comparative measurement to locate PD using the calibration signal. Five sources of error relevant to PD location in long lengths of solid dielectric cable have been distinguished [69]. PD source location in a cable system can be achieved in different ways. The most common options are: (a) time-domain reflectometry analysis (TDR), (b) arrival time analysis, (c) frequency-amplitude analysis.

2.3.2 Non-electrical methods

The non-electrical phenomena used for discharges detection are chemical transformation, gas pressure, heat, sound and light. Non-electrical methods can be used for detecting the presence of discharges, but cannot be used for measuring the discharge magnitude.

2.3.2.1 Acoustic PD measurement

The detection of discharges by ear is an old and established method. If there is a sudden release of energy within a solid structure, the energy will be dissipated in the form of elastic waves. This is very material dependent, i.e. the high frequency acoustic attenuation of the material between the PD and the listening device. Thus the sensitivity cannot be generalized. Usually a narrow band of about 30~50 kHz is chosen (just above the audible spectrum, which covers 20 Hz to 20 kHz). Much of the environment noise is in this frequency range is less important; at higher frequencies the attenuation of the sound signals would be too large.

In recent times, acoustic emission (AE) technology is recognized as an effective tool for non-destructive testing and material evaluation. Excellent results were obtained by detecting ultrasound [70-72]. Several ultrasonic detection systems are available commercially. The most important components of the acoustic emission instrumentation system are the integrated pre-amplifier with sensors [72]. The sensors are piezoelectric transducers which convert the acoustic signal into corresponding electric signals.

The acoustic method is an excellent aid for trouble-shooting, when performing electrical discharge tests. It uncovers disturbing discharges, such as corona at high-voltage leads or unwanted surface discharges. It has the advantages that observations can be made in the presence of large discharges; furthermore, a reasonable degree of location can be obtained by moving the ultrasonic transducer along the sample. However, its application in the HV field, as a condition monitoring system is limited [72]. The drawback is that the discharge magnitude cannot be measured and the sensitivity is insufficient, usually 100 pC or more. The PD signal would damp quite fast in the air. The directional sensitiveness of this method depends on the placement of the sensor. The acoustic approach is merely used to locate the site of the PD.

2.3.2.2 Light detection

In some situations, light detection is most sensitive [52]. There are two totally different phenomena which should not be mixed, i.e., luminescence without PD and light caused by PD.

A. Electroluminescence (EL)

It has been established that prior to electrical tree inception, light is emitted at points of electrical stress enhancement in the polymer. This light is not due to PD but due to the phenomenon of EL. EL can occur when the excited species return to their ground states or the electrons and holes recombine at the recombination centers in the polymer. EL depends on the quantum efficiency with which carrier recombination causes photon generation, which is not well known or understood. Polymeric insulation subjected to voltages below the EL inception level does not degrade, while the insulation held above that level always develops electrical trees. The intensity of EL is at least two orders of magnitude lower and the spectra of EL are different from the light emission of PD. EL is also emitted prior to the conversion of a water tree to an electrical tree [5].

It now seems clear that EL at typically very low levels precedes the onset of detectable PDs in time during continuous AC application [73]. Under certain condition, EL can also occur from the surface of the insulation, as well as, without any voltage application when the polymeric insulation is held at high temperature [74, 75]. Therefore it should be noted that the EL observed is the energy released from the solid and not used for damage formation. Furthermore, oxygen also plays a very crucial role in the degradation process. Decreasing the concentration of oxygen in the polymer increases the time to tree inception. Photostabilizers added to the polymer can retard the photodegradation of the polymeric insulation and help to prolong the life of the high voltage cables.

EL detection is a powerful technique to detect polymeric degradation prior to electrical tree inception and was successfully employed in the development of the 500 kV XLPE cable [35]. A sophisticated setup is required to detect the faint light of EL. To resolve the spectra of EL, especially for ultraviolet (UV) detection, a good optical focusing system is essential. But the technique is sensitive enough to reveal charge injection, space charge

accumulation, and insulation degradation prior to PD inception. The EL technique can determine the effect of space charge during charge injection under AC, DC, and impulse voltage as well as evaluate additives used in the polymeric insulation of distribution and transmission class underground cables [73-76].

The advantages of the EL technique are that unlike PD, it does not cause erosion of the insulation. The ageing can be stopped as soon as tree inception occurs, and this reduces the possibility of electrical breakdown, which can damage other sensitive equipment. A high EL inception voltage does not necessarily imply a longer time to tree inception, and long-term ageing tests with EL monitoring are required. The degradation only occurs in a small volume at the semicon tip, and the material in and around the degraded region can be further analyzed with other techniques.

B. Light emission caused by PD

It is well known that the tree propagation process is associated with discharge luminescence. Light emission detection in the visible and UV range during electrical breakdown is a powerful tool in the study of the initiation processes which lead to PD activity as well as the relationship between PD activity and the spatial and temporal development of electrical trees [77, 78].

The measurement for light emission was reported using CCD camera and photomultiplier [79-81]. The parameters extracted for light emission images included: luminous quantity, length [82, 83], intensity [81, 84-86], radial extent [79, 87], area growth [12, 88-91], and fractal dimension [85, 92].

Light detection is an excellent auxiliary method for partial discharge detection and provides a sharp location at a good sensitivity, and is unaffected by electrical disturbances in the test circuit. These techniques can complement more conventional electrical PD detection where only the integrated PD activity within a tree is monitored. Photographic records usually are made, which had the additional advantage that it is a simple method: any household camera can be used. A sensitivity of at least 1 pC can be reached. More sophisticated pieces of apparatus like photomultipliers or image converters are mainly used in physical research; sensitivities at least 0.01 pC can be obtained. However, light

detection has great disadvantages as well: (1) it detects only discharges that are visible from outside the sample, which set limit to inner discharge detection only suitable for transparent media; and (2) it shares the drawback, with other nonelectrical methods, that the discharges magnitude cannot be measured.

2.3.2.3 Dielectric response (DR) measurement

To identify water tree degraded XLPE cables or oil-paper cables with high moisture content, diagnostic tests based on DR were used [93].

In time domain, the DR appears as polarization current, depolarization (discharge) current [46], recovery voltage spectrum [46, 94], discharge voltage and isothermal relaxation current. In the frequency domain, the amplitude and phase of both applied sinusoidal voltage and current through the test object at different frequencies are measured to obtain the impedance, then the diagnostic parameters such as complex permittivity or complex capacitance, followed by the calculation of the dissipation factor $\tan\delta$ [46, 95].

As off-line methods, there are reported measurements of complex permittivity or complex capacitance and consequently $\tan\delta$ and/or total harmonic distortion in the loss current at power frequency, DC leakage current, polarization current and DC transient response current, return voltage, and potential decay after charging. As on-line methods, measurement of $\tan\delta$ and/or DC component in AC charging current, DC superposition current, and insulation resistance are applied [93].

Although bulk properties such as dielectric loss per cycle, $\tan\delta$ and capacitance change are useful pointers to the condition of the insulation, their sensitivity to local defects is limited and can not identify the mechanism and location of developing fault.

In the subsequent sections of this chapter, a summary of the review of the existing theory of PD and current research work on cable insulation diagnostics is presented in order to explore the new areas for further research.

2.4 Review on partial discharges due to electrical treeing in XLPE material

2.4.1 Current PD theory

Why is partial discharge a "hot" topic? The reason is that it is so easy to do “bad” work: seemingly easy PD collection as well as many easily uncared-for things. PD is a localized electrical discharge partially bridging the electrodes within an insulation system. PD can occur in solids, liquids, and gases in ways which will not cause the device to fail a HV withstand test. Yet PD will eventually cause failure in most systems, possibly years after the system is placed in service.

2.4.1.1 Types of PD in insulating material

The term "PD" includes a wide group of discharge phenomena: internal discharges may occur in voids of solid or liquid dielectrics, surface discharge appears at the boundary of different insulation materials, corona discharges occur in gaseous dielectrics if strong inhomogeneous fields are present and the continuous impact of discharges in solid dielectrics forms discharge channels known as treeing [52].

Treeing-induced PD occurs on a nanoseconds scale, often with several peaks in a waveform separated by less than 1 ns. These multiple peaks are thought to be the result of the discharge cascading down multiple tubules within the structure. The mechanism by which a discharge within the tubules of an electrical tree causes a PD pulse in the external system is essentially the same as for void discharge.

2.4.1.2 PD sources

From a practical point of view, PD occurs when some form of electrical activity within the system results in a rapid change of the electric field configuration which causes a current to flow in a conductor connected to the external world [52]. The most common sources of PD are floating components, corona, and voids. Electrical trees can initiate from metallic stress enhancements (as from an asperity on an electrode, a "point" from a semiconducting layer protruding into the dielectric, etc.) or from a void within the dielectric as a result of void discharge.

2.4.1.3 Stochastic characteristics of PD activity

The statistical variability in various properties of PD such as amplitude, shape and time interval of the pulsating PD for the same inception voltage is caused by statistical and formative time lags. It is also verified that ion densities, or surface charges generated during a previous PD event can influence both the local field strength and the release rate of the PD initiating electron. The statistical time lag is influenced by the rate at which free electrons are released into the high-field region of a PD site. It also depends on the probability that an electron can initiate a PD event. Several electron release processes are recognized able to contribute to PD inception, in addition to photo-ionization of the gas by external radiation. The dependency of the rate of the electron release to the local field strength is stronger when the predominant release mechanism is the detachment of negative ions. The statistical time lag modifies the initiation and growth of a discharge making it a probabilistic process in nature. Whatever the physical mechanism of the electron generation and the cause for the polarity asymmetry of the charge is, the amplitude and the frequency of the PD pulse vary depending on the number of available electrons.

2.4.2 Pre-processing of PD signals

Noise associated with PD pulse measurement hinders the use of the latter in predictive maintenance [96]. Many researchers have already proposed to de-noise PD signals using different approaches such as finite impulse response filters (FIR), infinite impulse response filters (IIR), and wavelet multi-resolution analysis. FIR and IIR filters theory of operation is mainly relying on the ability to characterize all spectral information beyond a certain frequency or below a certain frequency threshold to noise or the ability of eliminating certain frequency bands from the signal under consideration. Because of spectral leakage from edge effects and picket fence effect, the signal is not likely to be conveniently limited to certain bins while noise is confined exclusively to the remainder. In practice, the signal/noise separations in the FIR/IIR filters are incomplete.

Wavelet multi-resolution analysis depends on decomposing the signal into successive frequency bands, then, applies either soft\hard threshold to the coefficients in these bands (levels) and then reconstructs the signal which is supposed to be with reduced noise. The

application of wavelet multi-resolution analysis for de-noising PD signals faces a number of challenges such as the choice of the mother wavelet, the choice of the level of multi-resolution analysis, and the method of threshold. More research is still required to acquire an adaptive scheme for de-noising the PD signal. This adaptive scheme should adapt itself according to the type and levels of the existing noise for different practical applications of partial discharge detector.

2.4.3 Developed techniques for PD feature extraction

Lack of experts on PD pulse patterns necessitate the use of automated analysis of PD pulses in order to monitor the ageing and insulating material defects. Automated analysis entails two main steps: feature extraction and pattern classification. This section and the following one introduce a brief description regarding the research effort in order to tackle this timely topic.

The random nature and vast amount of PD data are characterized by different PD patterns. They are pattern of PD distribution, trend analysis and difference in individual PD pulse shapes. Many PD characteristics such as discharge magnitude, energy and repetition rate are monitored to study the severity of the discharge which can be related to the performance of the insulation. In addition to various derived parameters and stochastic properties, phase angle and time/voltage interval (Δt / Δu) distribution of the PD are now widely used for the assessment and service performance in existing units.

2.4.3.1 Derived parameters

The various derived parameters are summarized in reference [56].

A. The apparent charge - The apparent charge of PD is that charge which, if injected instantaneously between the terminals of the test object would momentarily change the voltage between its terminals by the same amount as the PD itself. When the PD occurs in the insulation, the pulse charge measured at the two electrode ends of the sample is called apparent charge. The apparent charge is not equal to the amount of local PD discharge which cannot be directly measured. Using calibrator, the measured apparent charge is calibrated in terms of pC. By using simple capacitive model and if the voltage

change in the void of capacitance C_c is ΔU_c, the discharge q_c from the void is given by (2-1):

$$q_c = \Delta U_c (C_c + \frac{C_a C_b}{C_a + C_b}) \tag{2-1}$$

Equation (2-2) indicates that the relationship between the apparent charges (q_a) and the actual discharge quantity (q_c).

$$q_a = \frac{C_b}{C_b + C_a} q_c \tag{2-2}$$

where, C_a is capacitor with the electrical field lines outside the cavity, C_c the cavity capacitance, and C_b two capacitors with electrical field lines starting or ending at the cavity walls.

B. Repetition rate - The PD pulse repetition rate (n) is the average number of measured PDs per second over a selected period. In practice, only pulses above a specified magnitude or within a specified range of magnitudes may be considered. The results are sometimes expressed as cumulative frequency distribution curves of PD magnitudes to see the trend of PD activity.

C. PD inception voltage - The PD inception voltage is the lowest voltage at which pulses are observed in the test arrangement when the voltage is gradually increased from a lower value at which no such discharges are observed.

D. Other Characteristic Parameters - Besides the above three main parameters, other characteristic parameters, such as the average discharge current, the quadratic rate, the discharge power, and PD extinction voltage etc. are recommended for characterization.

q_a, n and PD inception voltage are the most basic characterizing parameters of the existence and severity of PD activity. They indicate only PD activity qualitatively but they cannot characterize the type of PD.

2.4.3.2 Pulse sequence distribution

Discharge phase based information is the first and most frequently used identification parameters and is used in $\varphi - q$, $\varphi - n$ and 3D $\varphi - q - n$ analysis [97]. The PD occurrence is studied with its peak or average magnitude (q) in a selected y-window size, the

averaged phase angle of that x-window at which it occurs (φ) and the number of its occurrence in a limited q window range. Some of the analyzed pulse height distributions are [56]:

A. q_m-φ [65, 98] : The $q_m - \varphi$ pattern is used to evaluate the PD maximum amplitude distribution. It is known as the maximum pulse height distribution. The maximum of peak PDs at the same phase window from a series of 20 ms data is extracted and the statistical distribution of q_m with φ is evaluated for PD identification.

B. q_{ave}-φ [99, 100]: The $q_{ave} - \varphi$ pattern is used to evaluate the mean pulse height distribution. Instead of taking the peak in that φ window, the measured "n" peak pulse heights are averaged and the statistical distribution of q_{ave} with φ is evaluated. The pattern $q_{ave} - \varphi$ represents an accumulated result of the behavior of PD.

C. φ-n or **q-n** [60, 64, 65, 87, 89, 101, 102]: This distribution is known as pulse count distribution. The number of pulses with a certain magnitude range (q) is counted from 20 ms data distribution. This count in each discharge level window is also studied with "φ".

The PD pulse distribution in the form of $\varphi - q - n$ analysis is the classical method followed widely in all the International Standards for identification of the types of PD. The understanding of PD distribution requires experience. They give out the features by a visual distribution method, which may be difficult to make a judgment in a quantitative way. Further quantificational analysis method is needed.

The PD pulse distribution in 20 ms period is evaluated by superimposing a finite number of repetitive cycles PD data. The shape of these distributions can be quantified by statistical operators. Thus there is the visual recognition of discharges by an automated computer-aided classification system. With the acquired PD patterns (including the 3D patterns), features can be extracted out by surface fitting method.

2.4.3.3 Statistical features

A collection of sequential PD pulses that evolves in time according to probabilistic laws forms a time series. For pattern recognition purposes, the information contained in the discharge shape distributions is quantified using statistical operators.

A. Skewness (S_k) [16, 53, 103] describes the asymmetry of the distribution with respect to a normal distribution. It is defined as

$$S_{\mathrm{k}} = \frac{\sum (x_i - \mu)^3 \times P_i}{\sigma^3} \tag{2-3}$$

where x_i is the recorded value, P_i is the probability of appearance for that value, μ is the mean value and σ is the variance as defined in equation (2-4):

$$\sigma^2 = \sum (x_i - \mu)^2 \times P_i \tag{2-4}$$

For a symmetric distribution, $S_k = 0$, if it is asymmetric to the left, $S_k > 0$, and if it is asymmetric to the right, $S_k < 0$.

B. Kurtosis (K_u) [16, 53, 103] represents the sharpness of the distribution with respect to the normal distribution:

$$K_u = \frac{\sum (x_i - \mu)^4 \times P_i}{\sigma^4} - 3 \tag{2-5}$$

If the distribution has the same sharpness as a normal distribution, $K_u = 0$. If it is sharper than normal, $K_u > 0$; if it is flatter, $K_u < 0$.

C. Cross-correlation factor (cc) [10, 53, 103, 104] describes the difference in shape between the pattern distributions of the positive and the negative half-cycles:

$$cc = \frac{\sum x_i y_i - \sum x_i \sum y_i / n}{\sqrt{[\sum x_i^2 - (\sum x_i)^2 / n][\sum y_i^2 - (\sum y_i)^2 / n]}} \tag{2-6}$$

A value of $cc = 1$ means 100% shape symmetry, $cc = 0$ means total asymmetry.

D. Asymmetry (Asym) [53] is the quotient of the mean level of PD in the negative and positive half-cycles:

$$Asym = \frac{Q_s^- / N^-}{Q_s^+ / N^+} \tag{2-7}$$

The asymmetry can vary between -1 and 1. A value of -1 indicates that there is only a distribution in the positive half of the voltage cycle. A value of 0 shows that the distributions in the positive and negative half voltage cycles are of equal sizes.

With the statistical parameters, the shape of PD occurrence distributions in 20 ms can be quantified by values. Different PD patterns have different characteristic values. The recognition no longer relies on the operator's experience on visual justification. However, it is difficult to use in situations with multi PD sources occur simultaneously. Also there are a number of statistical parameters to compare and make a decision. Additional tool like neural network with these statistical parameters is needed for identification.

2.4.3.4 Weibull distribution

Weibull distribution is used to predict the failure analysis and failure forecasts with small number of data samples. Recently PD sources are recognized using Weibull processing [7, 16, 105, 106]. Using measured PD pulse height (q) cumulative distribution on laboratory test samples, discharge sources are identified from the scale and shape parameters of the Weibull distribution:

$$F(q) = 1 - \exp[-(\frac{q}{\alpha})^{\beta}] \tag{2-8}$$

$$F(q_i) = \frac{\sum_{j=1}^{i} n_j}{N_T} \tag{2-9}$$

The Weibull shape parameters, α and β are the scale and the shape parameters respectively. The parameter α is related to the mean charge quantity associated to a single PD pulse and corresponds to probability of 63.2% in the distribution while β is associated to the data dispersion. These parameters can be estimated by means of the maximum likelihood (ML) method and the quality of fitting can be checked by means of the Cramer-von Mises (CvM) test.

Different types of PD have different *q*-cumulative *n* distribution. Fitting the shape after scaling, type of PD can be identified. This method can be extended to identify multi PD sources [107]. It is a complex statistical method of prediction and difficult to link with the physical mechanism of the type of PD.

2.4.3.5 Inter voltage (Δu) / Inter time (Δt) distribution

A. Δu distribution

This method analyses the distribution of difference in successive PD magnitude of the sequential pulses. Since ions are left in the dielectric, a PD can affect the subsequent next discharge. Therefore, there will be inter-relations between the neighboring pulses [89, 108]. Since different PD patterns have different discharge mechanisms, different PD patterns may have different Δu patterns. It is a good method to know inter-relationship between the pulses in sequence of different PD patterns. In the case of only a few discharge events per cycle of the applied voltage the parameter Δu is very efficient and allows to distinguish clearly whether the partial discharge signals are generated by only one or more local defects, an information that is very helpful for a reliable diagnosis. Even with only one type of defect a small change in the height of the measuring voltage may significantly influence the discharge phenomenon [109]. But it may be difficult to cope with multisource discharges. If two non-correlated pd-sources are active simultaneously, characteristic changes in the Δu / Δu -pattern occur.

B. Δt distribution

In addition the time difference Δt between consecutive discharges is a very significant parameter, too. In a cavity of given size, increase in the applied voltage does not change the amplitude of the discharge but increases the frequency of the recurrence of PD [110]. Δt depends not only on recovery time but also on time lag for the electron [111]. The elimination of "multiple discharge pulses" together with the use of the parameter Δu / Δt reveal very useful additional information [109].

2.4.3.6 Pulse shape features

Nowadays, there is a great increase in number of papers concerning the characterization of individual waveform of PD [112]. The PD waveform exhibits the feature of transient wide-band signals in a few hundred nanoseconds time duration. Unlike the narrow-band detection, the wide-band detection records nearly the true shape of the wave for characterization. It can discover the mechanism and internal details of the PD waveform. But it needs high resolution and large storage.

A. Cross-correlation method

Identical discharges with the same mechanism can be identified by calculating the cross-correlation of the respective time domain signals. Equation (2-10) is used to calculate the cross-correlation of two digital data with i and j defining the selected two single PD and n as the total number of sampled points of the single pulse.

$$\rho_{ij} = \frac{\left|\sum_{m=1}^{n} f_i(m) f_j(m)\right|^2}{\sum_{m=1}^{n} f_i(m)^2 \sum_{m=1}^{n} f_j(m)^2} \tag{2-10}$$

After collecting the random occurring single pulses, this method can be used to group the pulses with high correlation value. This method is verified by the laboratory measurements. An extension of this method is the determination of correlation coefficient of linearly related variables. A simple calculation can indicate that the results will be the same as equation (2-8) even if the scaling factor differs between the selected variables. With the correlation method, auto classification can be achieved by grouping the identical pulses. But it requires more sampled points on single PD.

B. Equivalent *F*-*T* plane

The quantities, equivalent frequency F and duration T defined in [113] provide an intuitive and compact representation of the detected signals in an $F-T$ plane [16, 114]. By means of simple and quite fast procedure. The PD-pulse signals having similar shape can be synthesized in well defined areas of the $F-T$ plane. As with any technique of data compression, this procedure brings to a loss of information regarding PD shape, but the procedure here adopted is considered a good compromise between complexity of

computations and real-time requirements. Moreover, appropriate time pointers allow associating each PD pulse with its transformation in $F-T$ plane. Through these pointers, once the fussy classifier has performed the classification, it is possible to identify a specific PD pulse in the acquired PD pulse sequence and reconstruct a 3D plot for each cluster of PD signals.

2.4.3.7 Features based on signal processing algorithms

A number of signal processing transforms such as Wavelet transform, Fourier transform (FT), and Walsh transform have been applied to characterize PD measurements. These transforms can be utilized effectively for characterizing PD signals provided that pre-processing and filtering of noise remove most of the existing imposed noises.

A. Fourier transform

In higher band frequency, it will be possible to distinguish PD patterns in different phase, since different PD patterns in 20 ms and single PD have different frequency components [104, 115]. Fast Fourier transform (FFT) analysis and PD distribution are applied to PD identification. It has a special feature for extracting the average spectral intensities of recorded signal. However, the weak point of FFT is that the information of the time domain would be lost. And also in the frequency domain, statistical analysis need cope with the random characteristics. If one uses spectrum analyzer, random sampling with limited sampled points may result in more error.

B. Wavelet

Fourier transform assumes that the signal is stationary, but PD signal is always a transient non-stationary nano-second period signal. To overcome this deficiency, a modified method, short time Fourier transform, known as Wavelet transform has broadened the study of PD into both time and frequency domain simultaneously [63]. The advantage of wavelet method is the wavelet function matches the characteristics of PD. PD signal rises sharply and appears in a localized region in the time domain. By decomposing the signal with different filters at various levels, the associated noise may be separated from the PD signal. De-noising on PD is implemented by this method [17, 18, 116].

2.4.3.8 Features based on image processing algorithms

The phase-resolved 3D pattern can be considered as an image. Several attempts to utilized image processing algorithms to extract the distinctive features of these PD images have been conducted. Texture analysis algorithms, fractal theory based algorithm, principal components transformations and wavelet-based image decomposition have been utilized to characterize the constructed PD image. However, they have a limited success in dealing with the characterization of PD signals because of the level of complexity involved in their computations.

Fractal geometry is used to describe the parameters associated with PD patterns [12, 84, 85]. The most normally used image is the three dimensional pattern of $H(\varphi, q, n)$, which provides the relationship between the phase, the discharge quantity and number of occurrence. It is also a method to study the tree shaped PD. Only two fractal features, the fractal dimension and lacunarity are used in this method to identify the difference of various PD patterns. It can describe $\varphi - q - n$ distribution by only 2 parameters, but is difficult to explain by the discharge theory.

2.4.4 Developed techniques for pattern analysis and classification

All the different classifiers proposed for automated classification of PD can be categorized as: distance classifiers, statistical classifiers, artificial neutral network (ANN)-based classifiers, fuzzy logic based classifiers, decision trees and data mining classifiers, and combined classifiers [96].

2.4.5 Modeling

The aim of PD modeling is to provide theoretical support for physical interpretations. The discharge theories should be used in the modeling. The theories interpret the microsecond processes of discharges based on the collision ionization theory and influx discharge theory. The physical model of the PD is also complex due to the complex physical processes of electron generation. But different types of discharges are controlled by similar physical process to a large degree. This permits an efficient unified modeling approach.

Many equivalent circuits for partial discharge simulation have been proposed [117]. In the process of establishing the model, the dimensional reasoning should be used, which consists of defect geometry, discharge structure and involved materials. The model should incorporate the inception voltage, inception delay, measurable charges, statistical characteristics and the distribution over the AC phase. Parameters computed include field, current density, charge density, power density, and force density [118]. It provides the basis for a simulation of random sequences of PD pulses. A simple model has been presented to determine approximately the discharge path in electrical devices by an iterative finite element method (FEM) procedure [119]. The model in [120] considers channel conductivity, charge transport, and electric field redistribution during propagation of the discharge along the channels. It has been used for numerical investigation of temporal-spatial and electric characteristics of the partial discharges in capillaries and electrical trees exposed to AC voltage in needle-plane geometry. An algorithm for solid dielectric breakdown simulation based on cellular automata (CAs) is presented with a point-plane electrode arrangement [121, 122].

2.5 Review on modeling analyses of space charge accumulation and electric field distribution

2.5.1 Introduction

The critical issue of system quality and reliability demands the understanding of failure and aging mechanisms by diagnosing, evaluating, and modeling appropriately selected properties of the electrical insulation polymer and its interaction with other components within the insulation system. The complexity of modeling dielectric failure arises from the fact that there are many factors, known or unknown, at play like a “black box” system displaying the inputs composed of controlled stress variables and a multitude of uncontrolled stochastic factors. The stochastic property of every component and mechanism convolves to form the resulting output. The objective of the engineer is to model only the effect of the applied stress variables on the response variable of the output by assuming an ideal dielectric that is completely homogeneous. For practical purposes, such an assumption has some limitations to its application, although it simplifies the problem significantly. It is clear that many assumptions about the system's components

are necessary to simplify the analysis. Modeling the practical insulation system that is far from ideal, while also bridging the gap to the purely theoretical treatments, utilizing available technology and statistical tools for conducting and analyzing cost and time-effective experiments, are all dimensions of the problem. Most approaches so far have been empirical, while theoretical models struggle to account for the stochastic nature of any factors that convolve to cause failure in practical systems. Approaches to modeling breakdown in the literature have been either via mathematical (semi-empirical) curve fitting of experimental and in-service data, or via theoretical studies of degradation mechanisms as summarized in Figure 2-3 [123].

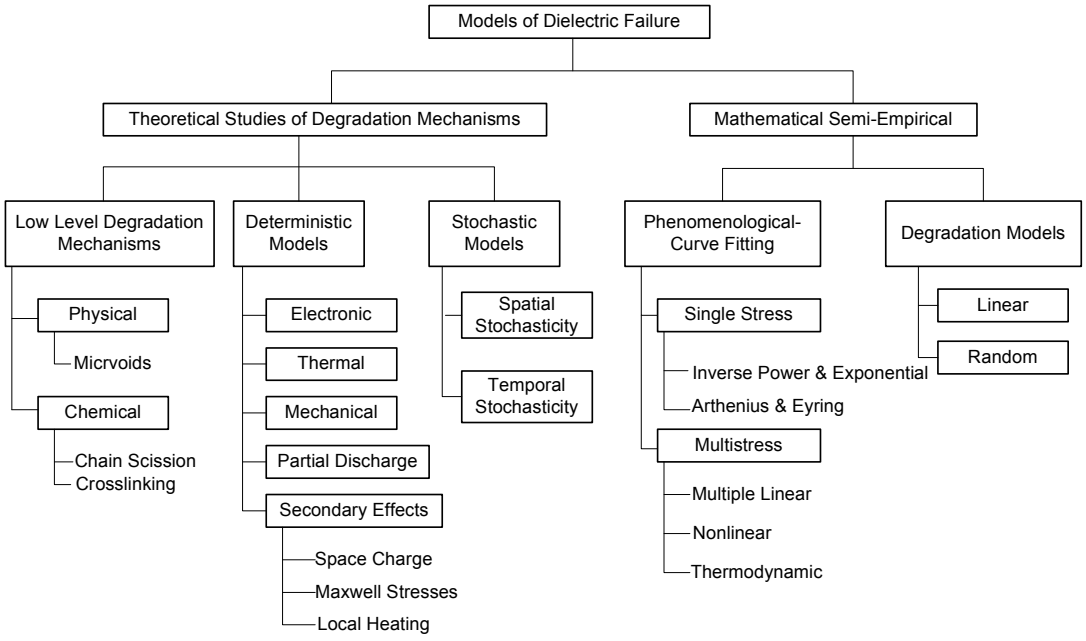

Figure 2-3 Models of dielectric failure [123]

The significant influence of thermal heating on dielectric aging is a troubling and complex problem, especially at higher temperatures.The developing description of the conduction processes in PE and, by association in other insulating polymers, is complex but it is clear that a full account must be taken of the morphology and of the interactions between mechanical and electrical properties.

2.5.2 Morphology of polyethylene

The consideration of the models for conduction and breakdown of crystalline and amorphous insulating solids was proposed by Fröhlich [124], von Hippel [125], van Roggen [126] and others more than 50 years ago. Polymers such as semi-crystalline PE were included as examples of amorphous solids but it is now clear that for PE in particular a much more complex morphology is involved than was contemplated at the time. This morphology is the key factor in determining conduction processes in the polymer and electrical and mechanical properties become closely related.

Two interrelated structures exist in the polymer with contrasting electrical and mechanical properties; crystalline ribbon-like lamellae of ordered chains, and a surrounding amorphous phase where the chains are in various degrees of disorder and fluctuating configuration (Figure 2-4 [127]). The chains are covalently bonded and strong but the interchain forces dominating the amorphous phases are of much weaker secondary character. Tie molecules extending from one lamella across the amorphous phase to enter adjoining lamellae provide longer range intermediate forces to hold the two systems together.

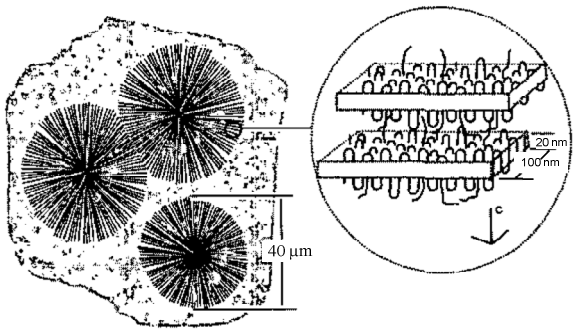

Figure 2-4 Morphology of semi-crystalline PE showing spherulitic arrays of lamellar crystallites consisting of ordered chains in an amorphous background [127]

The lamellar ribbons, radially disposed in tuft-like spherulites, define the amorphous phases between them and determine the conductive paths through the spherulites. To a large extent, they also appear to determine the breakdown paths. It has indicated that the electrical strength of polymers may be ranked in the order of their cohesive energy

density, i.e. in terms of the energy needed to disrupt the secondary amorphous phase bonding.

It is instructive to summarize the conductive paths in diagrammatic form as in Figure 2-5 [127]. The strength of these various transport paths in a spherulite will depend, to a marked degree, on the orientation of the lamellae (and consequently the amorphous spaces) with respect to the field direction. The geometry is such that only a proportion of the lamellar and amorphous paths of a particular spherulite will be suitably oriented to take advantage of the field. Although the space between the spherulites is considered to be generally amorphous it is likely to contain some small embryo lamellae and spherulites. Positive charge (hole) transport is likely to be very restricted by lack of long-range chain orientation but electron movement in interchain spaces should continue and, with reduced constraints imposed by spherulite structure could be more strongly influenced by the field. Molecular ions largely excluded from the lamellae will be directed along the amorphous inter-lamellae radial paths of the spherulites and will continue less constrained in the interspherulite spaces. Molecular ions may contribute to low field conduction, but high field conduction is probably dominated by electrons. Crystalline PE has a band gap of about 10 eV. Thus it seems unlikely that very much conduction takes place within the crystalline region. Recent results from computational quantum mechanics suggest that conduction takes place at the interface between the amorphous and crystalline regions and/or in the amorphous region. Fitting conduction data results in a mean separation between "traps" of 2.8 nm, which is about 25 carbon atoms along a backbone, and the traps are in the range of 0.8 eV deep. These parameters are also consistent with the measured SCLF and the threshold field for nonlinear conduction. The BIG question, which no one has been able to answer, is what the source of these "traps" (or barriers) is.

An advantage of the extended lamella in spherulitic form is that one of the surface paths for spurious leakage current, which was of concern in the earlier work, is eliminated. Moreover, the range of electric fields that might be expected across lamellae in a practical sample of PE under high stress is likely to encompass those fields for which negative resistance was found for the single crystal. It is interesting that negative resistance can be related to trap controlled mobility. The development of such a property at certain fields in

spherulites could, in upsetting the local field and charge distribution, be a mechanism contributing to failure.

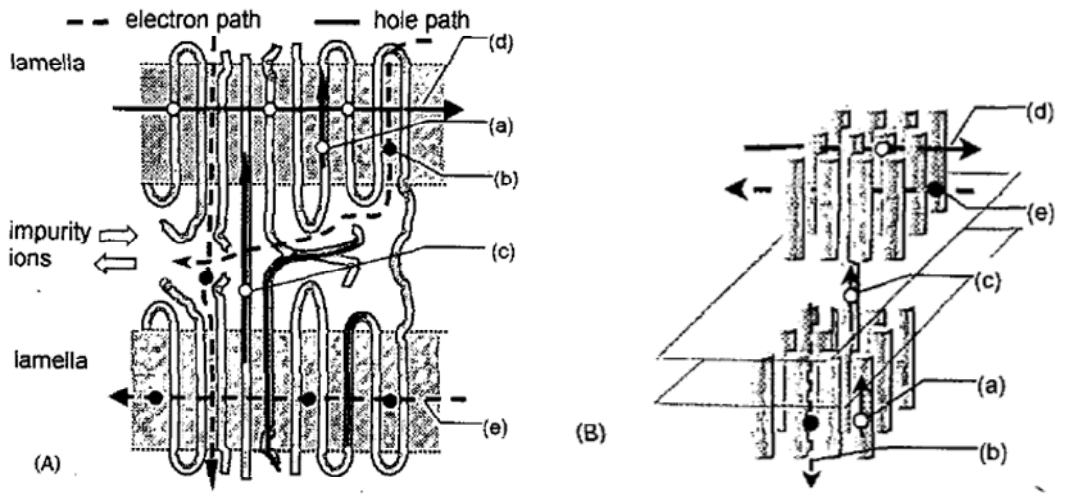

Figure 2-5 Elementary conduction paths in semi-crystalline PE, shown diagrammatically in alternative versions [A] and [B] which offer different perspectives of these processes [127]. Paths are for (a) intrachain holes; (b) interchain electrons; (c) interchain, intrachain holes via tie molecules; (d) hole and (e) electron tunneling in a *b* crystal direction in the lamellar plane.

A particular feature of PE that should be emphasized is the dynamic nature of its morphology. The clearly observed α, β and γ relaxations, indicating thermally induced segment fluctuations, interact with electrical processes in several ways; not least through the direct electromechanical forces generated by E^2. Along the various paths described above there will be fluctuating energy barriers to charge motion and fluctuating trapping energies. At any time, a significant fraction of the charge carriers will be trapped in the environment of relaxing segments.

The key features determining PE morphology is the habit of the lamellar crystal. The habit is reflected in the mechanical and electrical properties of the semi-crystalline solid. It would be highly profitable to return to examine its fundamental properties again in some detail with the advantage of present day microtechniques, thus belatedly continuing the pioneering work begun by Arend van Roggen [126]. However, it should be noted that

details of morphology may not be all that important, and the conduction properties depend more on universal phenomena such as chemical impurities, e.g. oxidation, which occurs during manufacture.

2.5.3 Space charge

All discharges are a result of ionization processes as depicted in Figure 2-6 [123], except for electronegative species, and initiated by a few original free charge carriers inherently present in the dielectric or created in a cavity by cosmic ray ionization of gas. Corona (i.e., PD of significant pulse magnitude and repetition rate to generate substantial average current flow) and PD are well known aging drivers in modest field (< 10 MV/μm) AC, AC+DC, and sub-kilovolt pulse transformers, while space charge appears to dominate in DC applications.

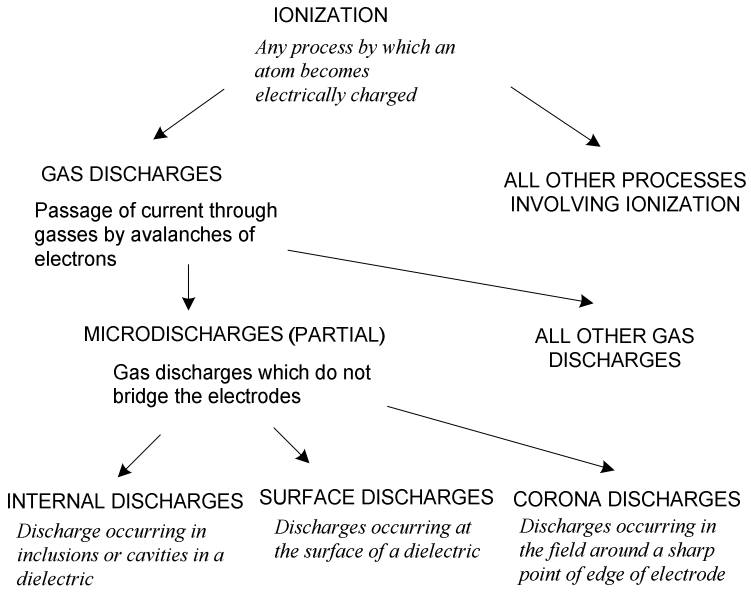

Figure 2-6 Ionization processes and charge formation are illustrative of the types of phenomena that can indirectly influence the aging rate of electrical insulation.

Space charge is well known to distort applied fields especially under DC conditions and to produce locally high fields, leading to dielectric and component aging, and subsequent in-service breakdown, and hence failure. The aging effects are seen in the case of constant stress DC fields as time permits buildup of charge that is either injected homo-charge at electrode-insulator interface, or results from deep trapped bulk charge and

possibly void discharge. These effects are a function of the insulation material itself, the stress environment conditions such as temperature, impurities, and many other factors.

Recently, the development and utilization of several practical and noninvasive methods/ techniques have allowed quantitative analysis of space charge via measurement of an induced current that is directly proportional to the space charge profile. Some of those methods include the pressure wave propagation (PWP) method, piezoelectrically induced pressure step (PIPS) method, the pulsed electroacoustic (PEA) method, the thermal pulse (TP) method, the thermal step pulse (TSP) method, and the laser intensity modulation (LIM) method. These techniques allow further insight into the possible operating mechanisms leading to breakdown. Further research into that area, especially at the nanoscopic level, is needed to understand and model how space charge affects prebreakdown processes leading to dielectric failure.

2.5.3.1 Charge injection

Charge carriers under the influence of a high electric field can be injected into the dielectric material from the surface of an electrode as well as due to PD inception. These carriers are transported through the dielectric, and are captured at the opposing electrode. Charge injection is not an impulse breakdown process, but is a continuous conduction phenomenon similar to intrinsic or extrinsic conduction, except the origin of the carriers is entirely external to the dielectric, and the current increases much faster than linearly with the electric field. Two types of injection processes that have been specifically identified and described are Schottky and Tunnel injections [127]. For example, the charge generation is supposed resulting from injection at the electrodes according to a Schottky law, being for electrons and holes [128],

$$j_e = AT^2 \exp\left(-\frac{ew_{ei}}{k_B T}\right)\exp\left(\frac{e}{k_B T}\sqrt{\frac{eE}{4\pi\varepsilon}}\right) \tag{2-11}$$

$$j_h = AT^2 \exp\left(-\frac{ew_{hi}}{k_B T}\right)\exp\left(\frac{e}{k_B T}\sqrt{\frac{eE}{4\pi\varepsilon}}\right) \tag{2-12}$$

where j_e and j_h are the fluxes of electrons and holes at cathode and anode, respectively, T is the temperature, $A = 1.2\times10^6$ $\mathrm{Am^{-2}K^{-2}}$ is the Richardson constant, and w_{ei} and w_{hi}

are the injection barriers for electrons and holes. Regardless of the physics at the electrode-dielectric interface, the result is a current density in the dielectric that can approach a space charge-limited condition, wherein the electric field at the injection site is reduced to a small value by the proximity of space charge.

Because charge injection is a field-controlled process, the current density will be the maximum at the high field sites. The conduction path follows the electric field vector in dielectrics. If the charge injection process can become established during the rise or fall times of voltage transients, the reduction of the electric field would increase the PD inception voltage. This hypothesis has been supported by laboratory experiments.

2.5.3.2 Charge transport modeling

More than fifty years after the publication of the early work on conduction and dielectric breakdown of solids, concepts derived from semiconductor physics have been transposed to the case of insulating solids including polymers. Alternative descriptions have been proposed as well. The last twenty years have been marked by the publication of excellent review papers [127, 129-132] summarizing the physical concepts available to describe charge transport in the field of atomistic and macroscopic modeling. Enormous steps forward have been achieved as regards computing facilities and our ability to spatially map the space charge, quantitatively, inside dielectric materials. In spite of this, the researchers are still unable to describe quantitatively the electrical response of these materials. There is still no agreement on how to describe charge transport and there is still some controversy as regards the applicability of semiconductors physics to the case of disordered insulating materials.

Two factors are considered as fundamental in providing possibilities for developing sound models of charge transport, by using the basis of fundamental knowledge that has been accumulated in the previous years, and by coupling up-to-date techniques in experiments and in simulation. There are some common features for charge transport models. Even when neglecting dipolar processes and diffusion one generally has to solve the following coupled equations considering a 1D problem along the spatial coordinate x, whatever the model used:

transport equation: $$\frac{j(x,t)}{q} = \mu E(x,t) n(x,t) \quad (2\text{-}13)$$

Possion's equation: $$\frac{\partial E(x,t)}{\partial x} = \frac{\rho(x,t)}{\varepsilon} \quad (2\text{-}14)$$

continuity equation: $$\frac{\partial n(x,t)}{\partial t} + \frac{1}{q}\frac{\partial j(x,t)}{\partial x} = s(x,t) \quad (2\text{-}15)$$

where j is the transport current associated with each kind of carrier of density n and charge q, μ is the mobility, E is the applied field, and ρ is the net density of charge.

2.5.3.3 Space charge-limited field (SCLF)

The calculation of the space charge distribution in a technical polymer dielectric is in general an intractable problem. Fortunately the situation becomes much simpler at high fields of the order of the breakdown field. The mobility of thermal charge carrier in polymers is very small ($<10^{-6}$ $cm^2/(V\cdot sec)$) and controlled by disorder localization and traps. Band mobilities are only expected at fields $E \geq E_c$ which are able to sustain the kinetic energy of the charge carrier above the mobility edge. The critical field E_c is smaller but of the same order as the breakdown field. Thus if a sufficiently high voltage is applied then a space-charge cloud is formed with the dielectric time constant of the system and space charge-limited field (SCLF) is determined to a very good accuracy by the condition that $\sigma(E_{\lim}) = \varepsilon * \omega$. The SCLF is not stable in time but will slowly smear out on a time scale. The concept of SCLF is simple and makes it possible to compute the space charge density $\rho(x)$ without any parameters (mobilities, trap densities, etc.) except E_c . This allows to compute $\rho(x)$ analytically for simple geometries and to draw quantitative conclusions with regard to models for dielectric aging, but such analytical computations are generally not quantitative and they certainly will not predict power dissipation accurately.

The concept of SCLF is fundamental to thinking about dielectrics at very high fields. The idea is that if the material becomes effectively a "metal" above a certain field, then the field within the material is limited to this field. In a pioneering discussion of this concept, by Hibma and Zeller [133, 134], they base their analysis on the assumption that the space charge-limited field is fixed, and in highly inhomogeneous field geometry, the SCLF does

not increase with applied voltage above the critical voltage at which the SCLF is reached at the tip of the stress enhancement. This assumption corresponds to a material in which the conductivity goes from a very small value to essentially infinity at the space charge limited field. For this assumption, the field on the surface of a stress enhancement is independent of the applied voltage. Thus, above the threshold voltage, application of Gauss' Law to the stress enhancement surface will result in a surface charge that is independent of applied voltage. In reality, the field at the stress enhancement surface does increase slowly as a function of applied voltage above the critical voltage as the transition between low and high conductivity is not abrupt.

The SCLF model as developed by Zeller and coworkers provides some very useful analytical approximations [133]. For example, in spherical coordinates and assuming concentric spheres, the radial space charge density can be evaluated from Gauss' Law and the assumptions of the theory with the result that

$$\rho(r) = \frac{2\varepsilon_r \varepsilon_0 E_c}{r} \tag{2-16}$$

for $r_0 < r < r_{sc}$, where r is the inner spherical radius and r_{sc} is the radius of the SCLF charge region, which is given by

$$r_{sc} = \frac{1}{2}\left(r_0 + \frac{V}{E_c} \right) \tag{2-17}$$

Next the needle is approximated by a hyperbola with tip radius r_0. The tip-plate distance d □ r_0 and the angle between the asymptote of the hyperbola and the tip-plate axis is $\sqrt{r_0 / d}$. An exact analytical solution for the SCLF is not possible. It is possible, however, to give an analytical approximation to the SCLF which yields $E = E_c$ on the tip-plate axis in the space-charge region. Outside the axis, E is smaller. This approximation does not lead to serious errors in the tip region. The charge density on the tip-plate axis is given by (r_0 □ d)

$$\rho(x) = \frac{2\varepsilon_r \varepsilon_0 E_c}{x + r_0} \tag{2-18}$$

where x is the distance from the tip and the radius r_{sc} is defined by

$$r_{sc}\left[1+\log\left[\frac{4d}{r_{sc}}\right]\right]=r_0+\frac{2V}{E_c} \tag{2-19}$$

These equations are very useful in thinking about problems, but they are for idealized conditions which do not occur in practice and usually cannot be used for quantitative work.

2.5.4 Temperature rise

Electrical trees grow as a result of discharges in the tree channel. Such discharges result in sudden changes in the field at the tip of the tree. When the field at the interface between a conductor and the dielectric exceeds a "critical field", space charge forms in the dielectric to limit the field as a function of frequency or time constant [135-137]. This space charge formation results in substantial current densities, electromechanical forces, and power dissipation [118, 138-141] which, in various combinations depending on operating conditions, contribute to electrical tree initiation.

Three models have been explored which are at opposite reasonable extremes for field and temperature dependent conductivity of polyethylene and the rational. The first very useful model (equation (2-20a)) has been published in [118] for which $\sigma(E)$ is proportional to $\exp(|E|)$, while for the last two models (equations (2-20b) and (2-20c)), $\sigma(E)$ is proportional to $\exp(\sqrt{|E|})$, specifically,

$$\sigma_1(E,T)=\frac{62.64}{|E|}\exp\left(\frac{-6946}{T}\right)\exp\left(1.1408\times10^{-7}|E|\right) \qquad (a)$$

$$\sigma_2(E,T)=\frac{2.025\times10^{-6}}{|E|}\exp\left(\frac{-4066}{T}\right)\exp\left(2.103\times10^{-3}\sqrt{|E|}\right) \qquad (b) \tag{2-20}$$

$$\sigma_3(E,T)=\frac{1.12\times10^{-5}}{|E|}\exp\left(\frac{-6946}{T}\right)\exp\left(6.307\times10^{-2}\sqrt{|E|}\right) \qquad (c)$$

where T is in K and E is in V/m. The results obtained [138] are not highly dependent on the model used.

The SCLF concept allows to calculate the local heating in the growth region of a PD channel [133]. For a sinusoidal voltage of the form $V(t) = V_0 \sin(\omega t)$, the stationary temperature rise near the high field electrode (needle tip) is given by

$$\Delta T(r_0) = 4f \frac{\varepsilon_r \varepsilon_0}{\kappa} F_c^{\,2} r_0^{\,2} \times \left\{ \frac{r_{sc}^{\,2}}{r_0^{\,2}} \left[\log\left(\frac{r_{sc}}{r_0} \right) - \frac{1}{2} \right] + \frac{1}{2} \right\} \tag{2-21}$$

where κ is the thermal conductivity and is f frequency.

Temperature rise can only be ignored at small tip radii. These results are in general agreement with the transient nonlinear finite element simulations with coupled thermal and electric fields [138] and justify the above assertion that very high field phenomena can only occur on a microscopic basis.

2.5.5 Electromechanical factors

In addition to the temperature rise, substantial electromechanical forces occur at the tip as a result of the action of the electric field on the space charge injected into the dielectric. These electromechanical forces can result in mechanical stresses which are greater than the yield stress of the dielectric at elevated temperatures.

A.A.Griffith started his work around 1920 to consider the energy required for propagation of a crack. The formation of a PD channel requires a formation energy W_f. W_f contains a surface energy term and a plastic deformation energy term. Under normal circumstances the plastic deformation term is dominating and the surface energy may be neglected. The initiation or growth of a PD channel leads to a release of electrostatic energy W_{es}. Growth is energetically possible only if

$$\frac{\partial W_f}{\partial x} \leq \frac{\partial W_{es}}{\partial x} \tag{2-22}$$

where x is the growth coordinate and the derivative is to be taken at the growth front. The basic advantage of the fracture mechanics model is that it is always correct independent of the specific mechanisms which determine either the channel formation energy or the electrostatic energy gain for channel propagation. Thus a unifying concept can help include combined electromechanical and purely mechanical stress fields and thermal, chemical, and plasma mechanical effects on the channel formation energy, etc.

The SCLF model allows to treat these effects in terms of numbers and not just in words [133]. The electro-mechanical stress on the dielectric surface next to the inner spherical electrode can be written as

$$\sigma(r_0) = 2\varepsilon_r \varepsilon_0 F_c^{\,2} \log\left(\frac{V}{2F_c r_0} + \frac{1}{2}\right) \tag{2-23}$$

where r_0 denotes the inner (needle tip) radius. The expression is very useful for the study of the mechanical stability of the dielectric systems, for example as related to micro channel initiation by the electrostatic force under lightning impulse conditions.

2.6 Review on high frequency response of XLPE cable

2.6.1 Theories of PD propagation

Telegrapher's equations are the core of usual transmission-line theory (TLT), as shown in equation (2-24). The telegrapher's equations can be understood as a simplified case of Maxwell's equation:

$$\begin{aligned} \frac{\partial^2}{\partial t^2} V &= \frac{1}{LC}\frac{\partial^2}{\partial x^2} V \\ \frac{\partial^2}{\partial t^2} I &= \frac{1}{LC}\frac{\partial^2}{\partial x^2} I \end{aligned} \tag{2-24}$$

The cable propagation constant is:

$$\gamma(\omega) = \alpha(\omega) + j\beta(\omega) \tag{2-25}$$

where $\alpha(\omega)$ is the frequency dependent attenuation parameter, $\beta(\omega)$ the frequency dependent phase parameter ($\beta(\omega) = \omega / v$ for lossless, non-dispersive propagation with matched impedances at both ends).

In almost every case, PD is a predecessor to breakdown of polymer insulation. Using sensitive PD detection, defects can often be detected during field testing, prior to breakdown. Capacitive, inductive, galvanic, or directional coupling methods are available for sensing PD. With the knowledge of the propagation velocity through the cable and the time delay between the signals observed to the left and to the right of a cable, an estimate of the PD location can be given.

Shielded power cables can be considered as lossy transmission lines. Propagation losses occur in power cables when pulses propagate through them. All the materials that make up a cable, namely core and metallic screen conductors, semi-conducting screens and insulation contribute to the propagation characteristics of the cable. The propagation characteristics are the attenuation and phase velocity. The high frequency attenuation of the cable causes the peak amplitude of a PD pulse, as well as the pulse energy, to decrease as a function of distance propagated.

2.6.2 Current study on high frequency response in shielded power cables

XLPE cables have a very low dielectric loss factor, tanδ at power frequency so that one might expect very low losses also at high frequencies. However, the XLPE cables incorporate the semiconducting layers and significant high frequency losses are caused by the propagation of radial electric displacement current (which increases with frequency) through the resistance of these layers [19]. The ability to detect and locate a PD source is limited by attenuation of the high frequency PD pulses as they propagate through the cable. Therefore it is necessary to understand the high frequency response of such cables.

The most basic HF loss mechanism in solid dielectric cable was identified in 1982 by Stone and Boggs [142] as caused by the radial capacitive current passing through the conductor shield (screen) and ground (insulation) shield layers. In 1984, Weeks and Diao [143] treated the problem through Maxwell's equations, a much more complicated approach that yields the same result. The mechanisms of HF loss was further explored in [144]. HF loss in shielded power cables is caused by a range of phenomena including the following:

- Skin effect losses in the conductor that increase roughly as the square root of frequency and tend to be important at relatively lower frequencies (<1 MHz).

- Dielectric losses in the insulation that increase roughly in proportion to the frequency and, therefore, become more important at relatively HF. For some types of cables with relatively large dielectric loss at HF (PILC and some EPR dielectrics), this loss mechanism can dominate at frequencies in the MHz range.

- Eddy current losses in the conductor caused by current spiraling down the concentric neutral wires or Cu tape shield. In the case of the latter, this loss is probably significant, especially in field-aged cable, where the resistance between lapped tapes has increased as a result of corrosion. In the case of concentric neutral wires, the pitch is so long that this effect appears to be negligible.

- Losses caused by the radial capacitive current passing through conductor and insulation shield layers. For dielectrics with relatively low loss at HF, such as XLPE, this loss mechanism often dominates in the MHz range. This loss is a strong function of the dielectric constant of the shield and the conductivity of the shield, both of which may be a function of frequency. But the radial capacitive current is constant, as it is determined by the capacitive impedance of the insulation. Part of it passes through the capacitance of the shields, and part of it flows through the resistance of the shields. Only the latter causes HF loss in the cable. The lower *C* (or the smaller the dielectric constant of the shields), the greater *R* for maximum loss and the greater the maximum loss in the shield [19, 145]. This is a major source of HF loss for XLPE shielded power cable.

- Radial capacitive current passing circumferentially through the insulation shield to reach a neutral wire. Thus, the smaller the number of neutral wires, the greater the HF loss (all other factors being equal). The combination of the radial displacement current and circumferential displacement current can dominate losses at HF, especially for smaller numbers of neutral wires and/or large cable diameters. The effect of radial displacement current in the shields has never before been computed or discussed.

The high frequency losses are dependent on the dielectric constant and the conductivity of the semiconducting layers [24, 144, 146]. Works in [21, 147, 148] have shown that the semiconducting layers have a dominant role on the propagation characteristics at high frequencies, with propagation velocity and attenuation being especially affected. A viable high frequency model for simulation was constructed in [148]. The semiconducting layer increases the conductor impedance, and thus, the attenuation constant is increased, and the propagation velocity and the characteristic impedance are decreased for a coaxial

mode but the inter-phase mode of propagation is not affected. A transient voltage is attenuated more and its oscillating period becomes greater than those on a cable with no semiconducting layer. The effect of the semiconducting layer impedance on the wave-propagation characteristic and the transient voltage is rather minor when the layer thickness is small and the resistivity is high, and the semiconducting layer effect is dominated by its admittance.

2.6.3 Determination of electrical cable parameters

Already in [142] it was discovered that for solid insulated cables only considering the effect of losses in the conductors and in the insulation itself was inadequate to calculate the losses at high frequencies. The losses in the semi-conducting layers also have to be incorporated in the model. Modeling was further developed in [143], where a comprehensive study of the effects of cable design parameters and surrounding earth was undertaken. Study of the semi-conducting materials themselves and their influence was further pursued in [19] and [21] among others. The state of the art is reported in [144] and [22]. In [149], two high frequency cable models are presented. The approximate model makes separation of the various loss sources possible and permits quick and easy quantification of them. By its analytical closed form approach, the approximate model facilitates parametric study and enhances the understanding of how cable design parameters influence the propagation characteristics. Akihiro Ametani [21] developed an impedance formula of a two-layered conductor based on a conventional circuit theory. The formula being expressed as a combination of existing impedance formulas of a cylindrical conductor, the impedance of a cable having a semiconducting layer is easily evaluated by an existing computer program for calculating cable parameters. Naima Oussalah [150] developed analytical expressions which characterize the PD pulse propagation in a typical shielded power cable for both symmetric and asymmetric PD pulses for an attenuation constant which increases linearly with frequency, as is normally the case for shielded solid dielectric power cable. Besides these analytical methods, a numerical electromagnetic method, finite difference time domain (FDTD) method was applied specially for cable joints [61]. This facilitates determining through computation the output signal of the sensors for various PD locations within the cable.

Up to present, various permittivity measurement methods have been applied in experiment for different materials. Samples were placed in a shielded capacitor-like measurement cell [25]. A high frequency measurement technique was developed [27]. To extract the complex constitutive parameters of individual layers of a multilayer sample, S-parameter waveguide measurements were developed [26]. A systematic approach based on a genetic algorithm (GA) was also proposed to recover the frequency dependence of material properties starting from S-parameters measurements [151]. The frequency and temperature dependent properties of semiconducting layers of medium and HV cables was studied by a designed broadband measurement set up [28].

However, current permittivity determination methods put much requirements as well as limitations on both measurement and calculation. Since electrode measuring system has much influence on the veracity of result, measurements for permittivity determination can only be carried out in laboratory for well-defined samples. On-field measurement for real cable system is still not yet practical. To find a flexible solution, the field-circuit theory is to be used here, which has been applied to determine intrinsic complex permeability and permittivity of Mn-Zn ferrite core used the conventional two-parallel-electrode configuration [30]. The new method is expected to be suitable for different applications.

2.7 Planned research work

The objective of this research is the characterization of XLPE insulation material of HV XLPE cable.

At the first stage, it is planned to develop a computer controlled digital data acquisition system with multi channels to simultaneously record the PDs due to electrical treeing phenomenon. Dielectric response measurement which was usually applied for study of water treeing will be implemented with the PD measurement. In addition, taking use of the transparent property of PE, optical observation is also planned to record the tree formation.

As a second stage of research, it is planned to test the data acquisition in the laboratory with known samples at different rising rates of applied voltage and different aging time at constant HV. Using the above, enough good original data will be collected for the

characterization. And several effective signal processing techniques are to be applied to analyze and characterize the electrical treeing.

At the third stage of this project, electric field and space charge distribution will be analyzed by simulation technique. Starting from the analyses for the geometry factors of needle-plane electrode system, through transient analysis in respect of nonlinear conductivity of polyethylene and different applied voltage waveforms, space charge accumulation and electric field distribution will finally be studied at the macroscopic scale based on bipolar charge transport model.

At the last stage of analysis, a new method is to be developed to determine the intrinsic permittivity of XLPE cable materials. Besides semiconducting material, XLPE is also considered here, since there is no special attention being paid to the intrinsic permittivity of XLPE material in high frequencies. Even though the frequency-dependent property of XLPE is not the dominant like semiconducting material, pure research will be done to verify the efficiency of the to-be-developed method. Since fringing effect of low-permittivity material like XLPE is the main factor to introduce error, new method should be able to solve or avoid such problem. At the same time, semicon as a kind of high-permittivity polymer must have the dimensional effect in high frequency measurement, which should be paid attention to by the new method, since the semiconducting layer has been verified to play an important role in high frequency response of XLPE cable.

Chapter 3 Electrical Treeing Phenomena in XLPE Material

3.1 Experimental setup

3.1.1 Introduction

The first objective of my research is to detect and characterize the PDs due to electrical treeing in XLPE material. Section 2.3 describes various PD measuring techniques. In the laboratory, it is found that electrical method using directly coupled HV coupling capacitors can measure PD buried in HV power supply with harmonics. Electronic interfaces for amplification and recording with maximum sampling points are developed. In this section, the technical details related to the selected measurement method are described.

The electrical method is selected for the measurement, since it can directly give the information, i.e. the discharge quantity of the discharge activities. The quantity of the discharge can be used for further analysis. A high resolution rate is achieved to acquire the complete PD pulse without losing any details. Firstly, it can retain the high frequency information, which will contribute in analyzing the PD propagation. PD can be measured by different types of couplers. A pure resistor coupler is used for PD coupling in laboratory measurement. It is with high frequency response. Since a capacitive coupler gives a wide bandwidth response, it is also used in laboratory. The PD detection system consists of four blocks: (i) the wide bandwidth sensor, (ii) the wide bandwidth preamplifier with transient protection, (iii) the filter, and (iv) the data acquisition and processing system. The original PD signal may be distorted at various parts and care must be taken to extract the original features for analysis.

It is well known that due to the growth of electrical treeing, the internal insulation structure of needle-plane electrode system will change. Dielectric response measurement can evaluate the variation of real and imaginary dielectric constants (ε' and ε'') of insulating materials with frequency. Additionally, it is well known that during PD growth, visible light emits from the tree growth volume and refractive index will change.

IDA200^{TM} Insulation Diagnostic System [152] is applied to carry out the dielectric response measurement iteratively with PD measurement.

Using a digital CCD camera of continuous recording, this measurement was also carried out. And treeing formation was observed by a microscope.

The main flow chart is shown in Figure 3-1.

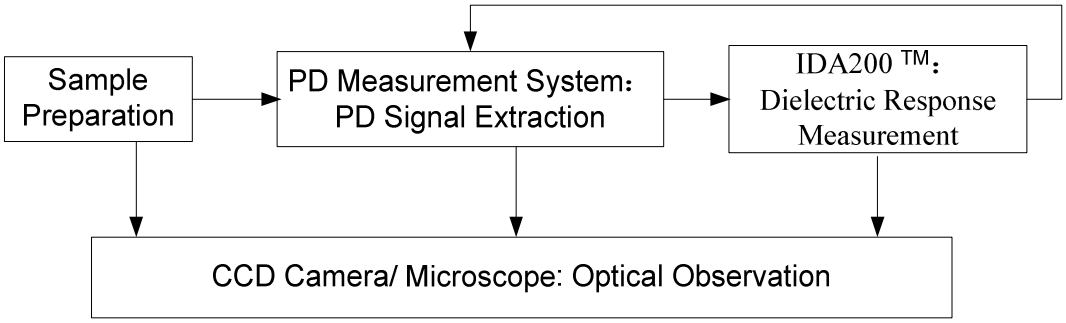

Figure 3-1 Block diagram of measurement system

3.1.2 Laboratory measurement system

3.1.2.1 Fabricated laboratory samples

Electrical treeing is the main long term insulation failure process, where void formation at a region of high electrical stress enhancement (tree initiation) is followed by the growth of fine erosion channels due to partial discharge activity (tree growth). Little is known of the physical processes which lead to void formation. However, electrical field enhancement is likely to occur around material defects, conducting impurities or molded-in metal inserts. The bulk of the published data uses the needle-plane geometry to model a simple conducting defect and to produce the high electrical fields necessary for quick tree initiation.

Before describing the preparation procedure for laboratory samples, one fact should be noted. In a cable, the stress enhancement usually occurs as the result of an asperity on the semiconducting layer, which is a stress enhancement in a quasi-homogeneous field. In laboratory studies, the needle-plane electrode system creates a highly inhomogeneous

field which is extremely high, but not Laplacian, at the needle tip. One would not expect tree growth under those two conditions to be at all similar, especially as that in cable may occur slowly over years while that in laboratory sample is occurring in minutes.

In laboratory, to simulate the serious situation in XLPE material where electrical treeing is possibly growing, typical needle-plane electrode is applied to initiate electrical trees in solid polymeric insulation [7]. In Figure 3-2, laboratory XLPE samples are prepared from the new cut pieces of 230 kV XLPE cable insulation, while PE samples are made of manufactured polyethylene product. Cubical sized samples are prepared after splicing. A heated needle-HV electrode is inserted at the center of one-side of XLPE cubical sample; while in PE, the needle is inserted after drilling because the PE sample is harder than XLPE sample and a heated needle is unpractical to be inserted in PE. And epoxy resin is used to fill the space between needle and XLPE / PE. The epoxy is a 1:1 mix of resin and hardener by weight and the specimens are cured at room temperature during 24 hours. The opposite plane is coated with thin silver paint for grounding. Caution is taken to avoid cavity, corona and surface discharges by using pure and clean material, avoiding sharp edges in air. The sample is immersed in silicon oil. The sample's surface length is kept long enough to avoid the surface discharge. The tests are made at a temperature of 22℃±2℃.

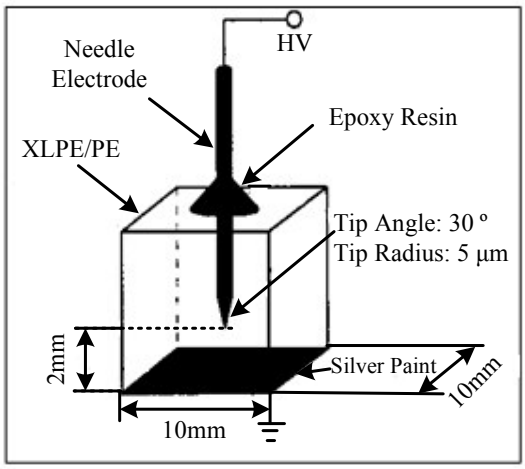

Figure 3-2 PD sample with needle-plane electrode configuration

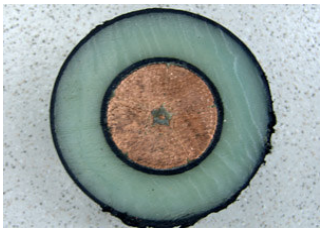

(a) Cross-section of XLPE Cable (230 kV)

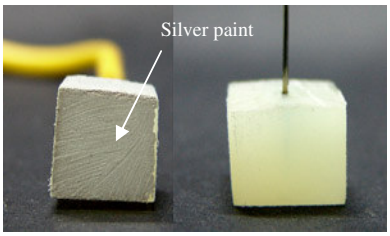

(b) XLPE Samples

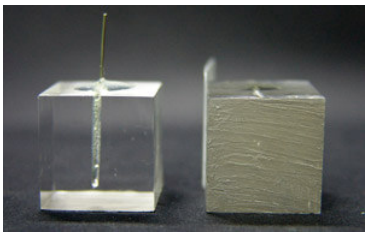

(c) PE Samples

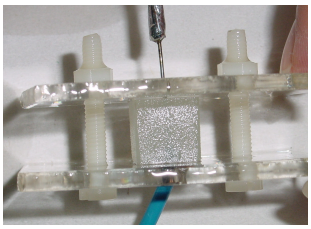

(d) XLPE sample with leads

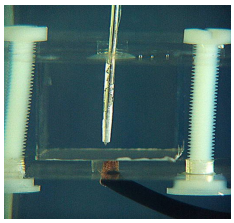

(e) PE sample with leads

Figure 3-3 Fabricated XLPE and PE samples

3.1.2.2 PD measurement

The detailed layout for PD laboratory studies is shown in Figure 3-4 and Figure 3-5. A HV discharge-free transformer (single phase 230 V / 100 kV) controlled from LV winding with a controller and HV indicator is used as PD energizing source [153]. In order to protect the equipment from the breakdown discharge, a water resistor of 3 MΩ (as shown in Figure 3-5 left) at the corona-free high voltage rail is used to limit the 50 Hz current from HV transformer and the PD current from sample flowing to HV transformer. A standard HV coupling mica capacitor (C_k) of 105.2 pF / 100 kV acts as a coupler which is absolutely free of any discharge. As the PD detector, the detection impedance (Z_m) is composed of a 1 kΩ non-inductive resistor which is shunted by an over-voltage protection, a 90 V spark gap to prevent over-voltages at the sensitive input of the detector. The selection of Z_m is important. A 50 or 75 Ω resistor is usually selected in high

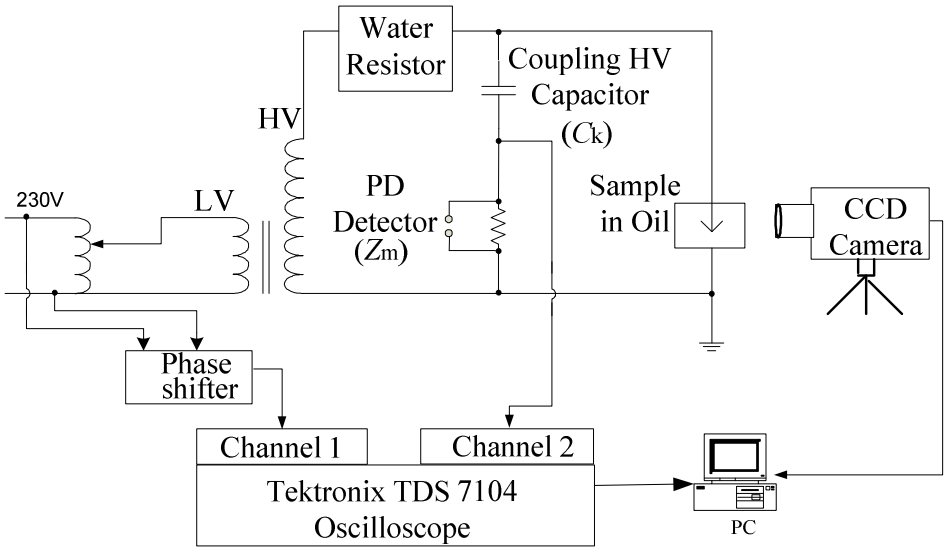

Figure 3-4 Schematic diagram of PD measurement setup

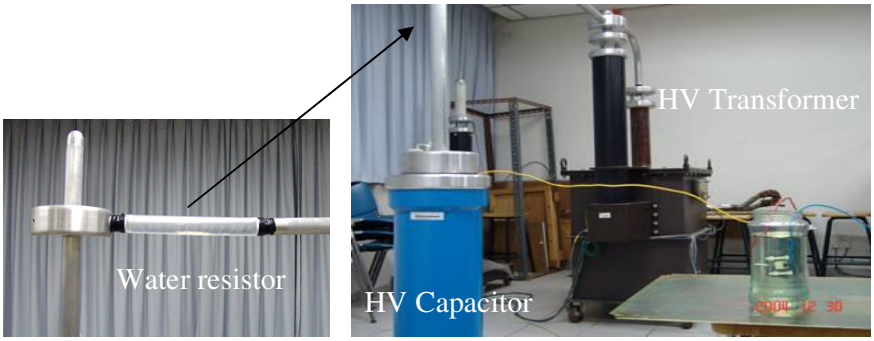

Figure 3-5 Photograph of PD measurement setup

Figure 3-6 Testing equipments: (L) Panel of Tektronix TDS 7104 Digital Phosphor Oscilloscope; (M) HV series control unit; (R) Phase shifter panel

frequency measurement system. However, the lower cutoff frequency of the RC high-pass measurement system is higher with larger resistance. Due to the relatively low frequency content of the electrical-tree PDs which is shown in single-pulse analysis in

following sections, a higher resistance is needed in this system. Although a 1 MΩ detector matches the 1 MΩ input impedance of oscilloscope, its inductance cannot be ignored. Considering not much reflection coefficient, 1 kΩ resistor is selected for Z_m. To reduce external interference, the specimen and electrometer are kept inside an electromagnetic-interference (EMI) cubby. The HV power supply is controlled by a control unit (as shown in Figure 3-6 middle) outside the cubby. Necessary interface to the oscilloscope has been designed by using 1.2 meter-50 Ω coaxial cables (RG58C/U coaxial cable) and high frequency probes (BNC connectors) with low capacitance and high impedance. A 4-channel digital Tektronix oscilloscope TDS7104 [154] (as shown in Figure 3-6 left) with maximum sampling rate of 10 GS/s and bandwidth of 1 GHz is applied for time domain recording. The minimum recoded voltage signal can be 1 mV and the maximum can be 100 V. Reference sine wave signal collected from the power supply is regulated by using a single-phase phase shifter (as shown in Figure 3-6 right) and fed into another channel of oscilloscope. Necessary Labview software routines are developed to control the GPIB controlled oscilloscope and to acquire the data with proper settings using computer. The collected data are stored and analyzed using developed MatLAB software [155]. In addition to measuring the electrical pulses, the tree shape is monitored periodically by recording in situ the image of the tree with a video camera and a long-range microscope.

A. Noise figure and phase shift adjusting

The vertical noise of oscilloscope (i.e. baseline noise) is evaluated as the noise potential level at the minimum vertical scale (V/div). For Tektronix 7104, its minimum vertical scale is 1 mV/div with 1:1 probe. The noise figure of oscilloscope is shown in Figure 3-7. It contains 50 Hz content with low amplitude of 0.7 mV and a DC offset of -0.7 mV, as shown in Figure 3-7 (middle). After removing the signal of power supply by using a Butterworth low-pass digital filter, the white noise level is lower than 2 mV, as shown in Figure 3-7 (below).

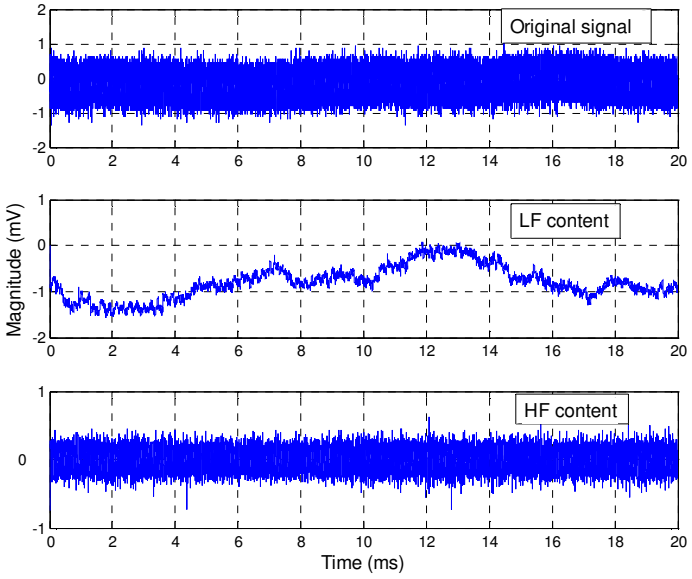

Figure 3-7 Noise figure of oscilloscope: (top) original background without signal; (middle) 50 Hz content; (bottom) white noise

Since PD analysis requires a proper phase reference, a calibrated phase shifter output is recorded with PD measurement. This phase shifter is energized from the same 230 V power supply for generating a pure 50 Hz sinusoidal waveform. To calibrate the phase, a 47 pF capacitor is used to replace the 1 kΩ resistor in Figure 3-4 in order to get a capacitive divider with a ratio of 3.2 ($=V_{in}/V_{out}$). Pure sine wave as the LV reference is fed from the phase shifter into channel 1 of oscilloscope. And the voltage across the 47 pF capacitor is input into channel 2 of oscilloscope. Then the phase of phase shifter is adjusted until the waveform peaks are matched. Thereafter, the pure sine wave signal in channel 1 is used as the standard phase reference signal. Again, by simple alternating of the coupling capacitor and the PD sample, grounded and ungrounded test samples can be tested with maximum sensitivity. The amplitude of actual reference signal is 2 V (peak), but the magnitude of reference sine wave will be rescaled in each figure to fit the dominant signal.

The harmonic content in laboratory power supply distorts 50 Hz waveform as shown in Figure 3-8. Besides the 50 Hz content, the 3rd, 5th, and 7th harmonics are notable. The harmonic content varies with time slightly. The background noise of laboratory system is shown in Figure 3-9. The magnitude of white noise is below 20 mV.

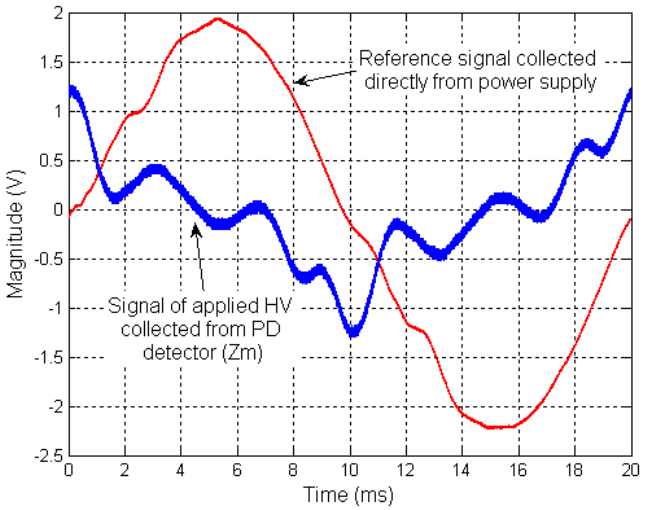

Figure 3-8 Phase shift of 50 Hz power supply collected from PD detector (Z_m): (red) reference; (blue) applied HV=15 kV(rms)

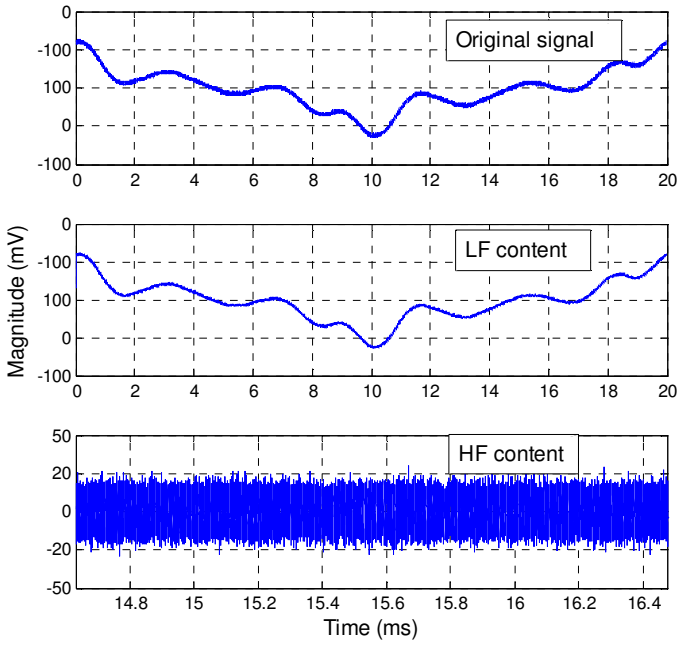

Figure 3-9 Background noise at 15 kV(rms) without occurring PDs: (top) original background without signal; (middle) 50 Hz content; (bottom) white noise

Normally the harmonic will not be so heavy, and we found the filter's bandwidth may not be wide enough. Therefore, we choose to collect the raw signal with full information, but to do this, harmonic has to be collected as well as PD signal.

B. Limitation

The maximum HV rated current and voltage of transformer are 100 mA (rms) and 100 kV (rms) respectively. The 50 Hz phase shift in charging current introduced by the 1 kΩ resistor and coupler will be in the range of 90°.

A non-inductive resistor of 1 kΩ is applied in testing and its inductance is very low even at high frequency. For comparison, a 50 Ω resistor is also measured. From the measured impedance up to 40 MHz by using HP89410A as shown in Figure 3-10, the equivalent circuit parameters of these resistors can be calculated. The detail is shown in Figure 3-11, where the serial inductance is 0.2 μH and the parallel capacitance is 1.8 pF for the 1 kΩ resistor, while 0.35 μH and 10.5 pF for the 50 Ω resistor respectively. The bandwidths of hese two types of circuits are simulated in PSpice as shown in Figure 3-12. The lower cut-off frequency is 1.5 MHz for 1 kΩ-resistor circuit, while 15 MHz for 50 Ω-resistor circuit. Especially, a band-pass effect occurs for the 50 Ω-resistor circuit, i.e. there is a resonance around f=28 MHz. Although normally 50 Ω or 75 Ω is used to collect relatively high frequency content, to avoid the inductance effect, and to match the impedance of coaxial cable, for this study of PD characterization, the PDs due to electrical tree have been found with relatively long rise times and durations (the dominant content of PDs is lower than 20 MHz), and the original information need to be collected as much as possible. Thus the selection of 1 kΩ resistor as the PD detector is initially decided.

Two types of sampling rate are applied in measurements for different purposes. For group PD analysis in time domain, since only the distribution of φ-q-n is the focus, 20 ms data window is recorded with 5 Mega points/s with a resolution of 200 ns/point. Normally, 20 data files are collected continuously. For single pulse analysis, 20 ms data window is recorded with 100 Mega points/s with a resolution of 10 ns/point. This resolution enables to record single PD with at least 128 points in order to obtain the relative information of pulse waveform. 10 data files at most are collected. Two channels are used in the laboratory measurement to simultaneously record PD signal from PD detector and reference signal from the phase shifter.

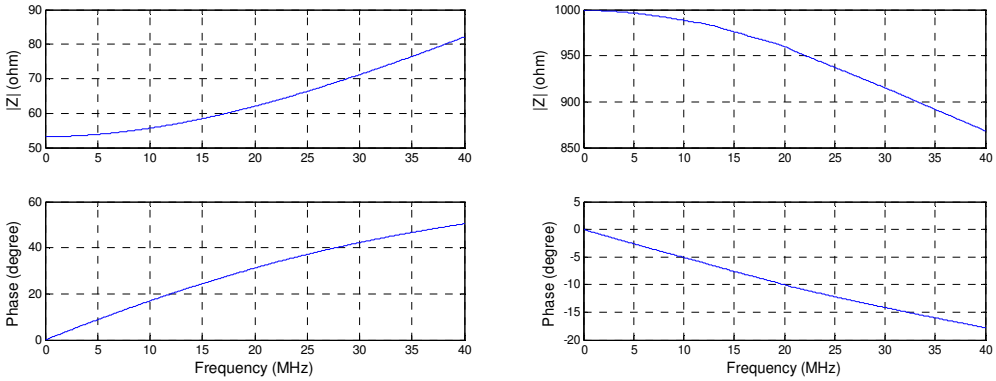

Figure 3-10 Impedance of PD detectors (Z_m, non-inductive resistors): (L) 50 Ω; (R) 1kΩ

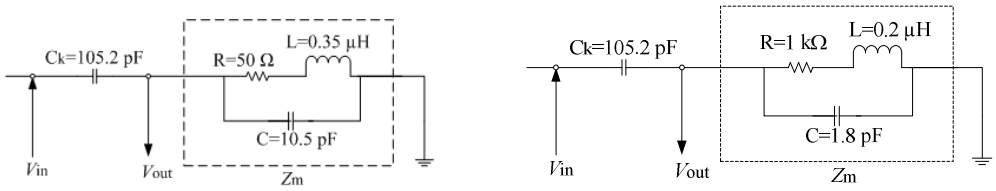

Figure 3-11 Equivalent circuit parameters of PD measurement circuit: (L) 50 Ω; (R) 1kΩ

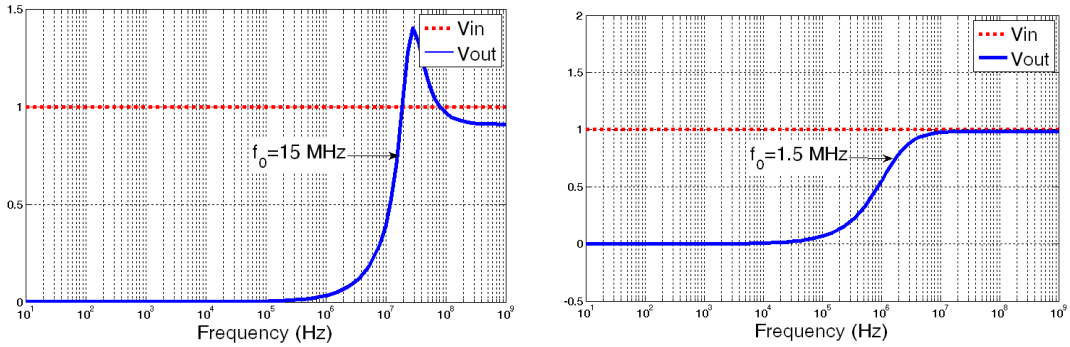

Figure 3-12 Transfer function of the measurement circuit: (L) 50 Ω; (R) 1kΩ

C. PD calibration and effect of detection resistance

The peak value of the highest impulse indicated at a peak voltmeter is calibrated in picocoulombs before the test, so that it serves as a picocoulomb meter. Calibrator for partial discharge measurement KAL451 (100 pC, 1 V, rise time (10~90 %): typically 20ns; max 50ns) [156] is installed across the tested sample to input single-pulse signals. The method of calibration across the test object (without applied HV) is the most accurate method and corresponds to the actual physical process [156]. The PD impulse from the

calibrator runs in the same direction and along the same path of the PD impulse originating in the test object. In order to make sure the best sensitivity of the partial discharge measurement achieved, the resistor value of Z_m is selected and the performance in sensitivity is compared with using a commercial high frequency current transformer ("HFCT" in short, IPEC/HVSL^{TM} HFCT CAE 140/100, transfer impedance T_r: 4.2-4.6 mV/mA (5 %), frequency response: 100 k~20 MHz, typical rise-time response: better than 20 ns), because the impulse collected by HFCT will occur without 50 Hz power supply signal and its dominant harmonics, which make it convenient to confirm the impulse occurrence. As shown in Figure 3-13, the HFCT is installed encompassing the connection cable between C_k and Z_m. Signals can be simultaneously collected without electric contact with the Z_m circuit, thus the existence of HFCT will not interfere much the performance of PD detector. The output signal and reference signal are collected in the same way as in PD measurement shown in Figure 3-4. And suitable resistor will be selected for latter measurement after considering the effect of the resistance.

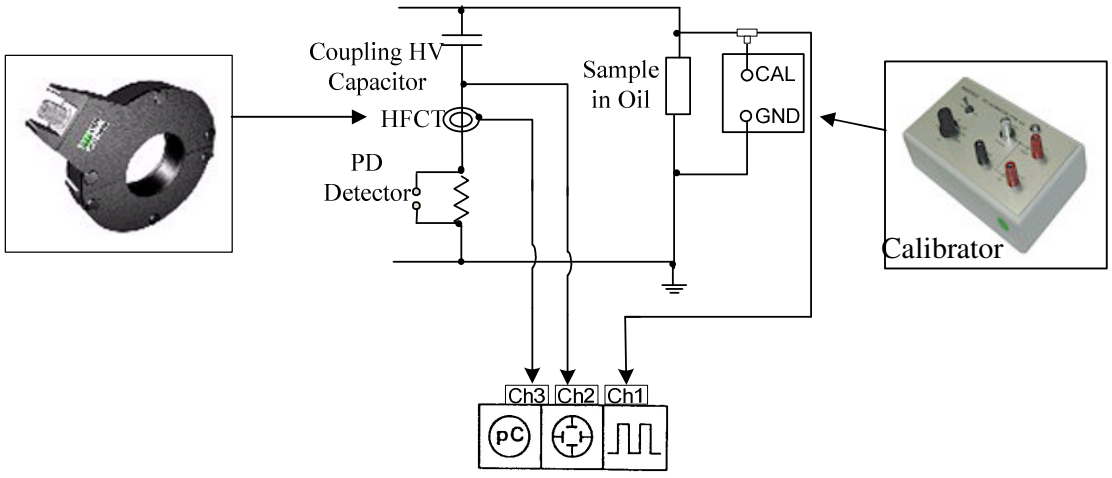

Figure 3-13 Circuit with calibrator and HFCT

Although a 1 kΩ resistor is used in the measurement setup as shown in Figure 3-4, in this section, the performances of 50 Ω and 1 kΩ (symbol "R") resistances for PD detector Z_m is compared, while the tap resistor of the HFCT is 1 kΩ (symbol "CT"). When a 1 kΩ resistor is used, the oscilloscope will be set 1 MΩ input impedance. Instead, if a 50 Ω resistor is applied in order to match the connected 50 Ω coaxial cable, the input impedance of oscilloscope is set as 50 Ω. Without applying power supply at the LV side

of the transformer, that is, no HV source for the sample under test, the collected signals from calibrator, resistor divider, and HFCT (through Channel 1, 2 and 3, respectively as shown in Figure 3-13) have different responses as shown in Table 3-1. The peak magnitude decreases nonlinearly with resistor value due to the nonlinear property of this calibration. The maximum output of resistor divider Z_m is 660 mV according to the case of "R-1k-CT-1k" (1 kΩ for both Z_m and HFCT tap resistor), which have a response higher than that of "CT-1k" by over 14 times. The installment of HFCT has a slight influence to Z_m , i.e., the response of "R-1k-CT-1k" is larger than "R-1k" by about 10 % due to the mutual inductance of HFCT to the PD detection circuit. And the ratio of response of "R-1k" to "R-50" is about 4. The minimum detectable charge for "R-1k" is 2 pC, while it is only 5 pC for "R-50". Therefore, the sensitivity of "R-1k" is better than that of "R-50". This is the theoretical sensitivity. As the background noise is not over 20 mV when HV is applied, those PDs over that level can be detected. Thus the system with a 1 kΩ detector can practically detect PDs of 5 pC at least.

Table 3-1 Calibration of PD sensors

Charge (pC)	R-1k(-CT-1k)	(R-1k-)CT-1k	R-1k	R-50
200	660	42.8	616	156
100	344	23.6	312	82
50	184	11.6	158	44
20	96	5.2	66	20
10	40	3.4	38	14
5	26	×	22	8
2	12	×	12	×

Checking the impulse distortion as shown in Figure 3-14, where "R-1k " is shown in the top two graphs (a) and (b), and "R-50" is shown in the bottom two graphs (c) and (d), there is no significant change in rise time (always about 20 ns) of the impulse except the fall time. From the calibration, it can be found that the high-frequency (up to 50 MHz) response of the system with either 50 Ω or 1 kΩ is satisfactory. However, by using 1 kΩ

resistor in circuit, the PD detector may collect more information for single pulse with higher sensitivity, since the detection circuit will behave as a high-pass filter, whose cut-off frequency ($f_c = \frac{1}{2\pi RC}$, where R is equivalent resistance and C equivalent capacitance) is much lower for higher R value. Moreover, by applying the 1 kΩ detection circuit, 50 Hz charging current is modulated on PD enabling the extracting of the phase reference, which is convenient to extract the information of phase angle of PDs.

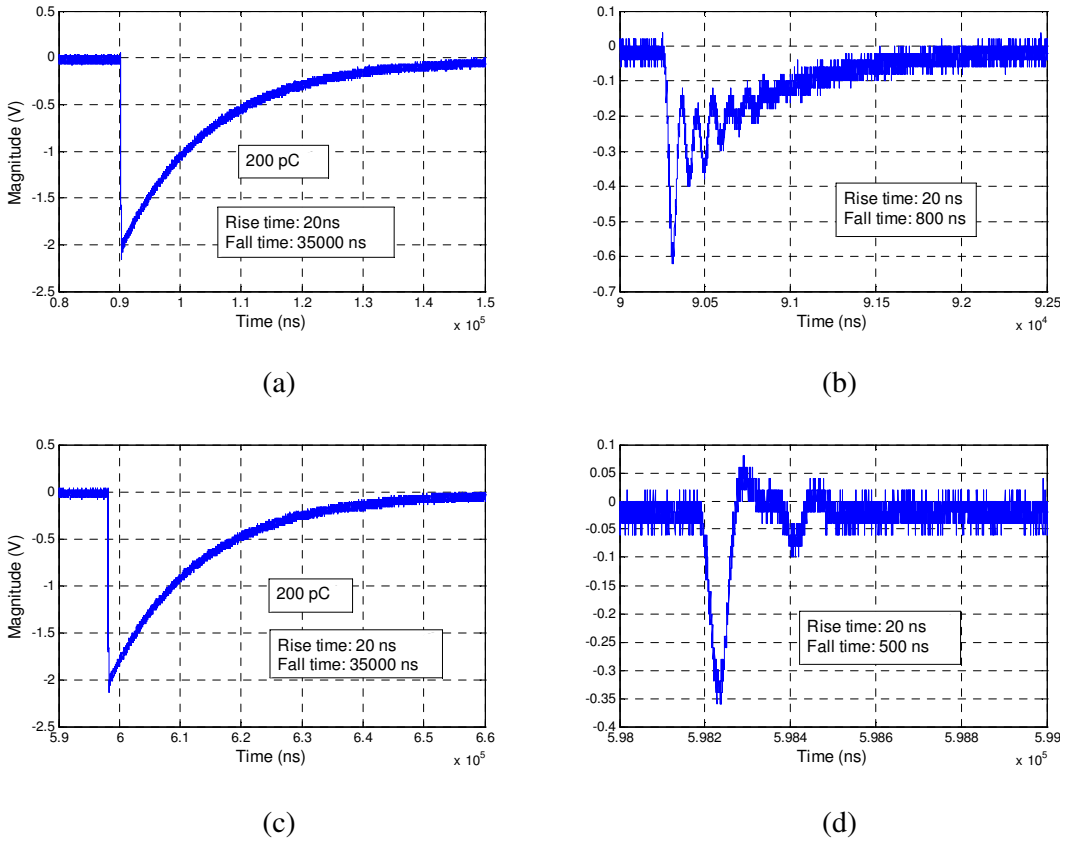

Figure 3-14 Comparison of impulses collected by using resistive PD detector and RFCT: (a) and (b) 1kΩ; (c) and (d) 50 Ω; (a) and (c) input; (b) and (d) output

Table 3-2 Sensitivity of PD sensors in testing

	Applied voltage (rms)	H_{qmax} by Z_m	H_{qmax} by HFCT
R-1k-CT-1k	5 kV	46.6 mV	2.45 mV
	10 kV	52.1 mV	2.68 mV
R-50-CT-50	5 kV	7.58 mV	0.9 mV
	10 kV	17.8 mV	1.1 mV

After removing the calibrator, the sensitivities of PD sensors are compared again by applying the voltage of 5 kV (rms) and 10 kV (rms) and the selection of 1 kΩ PD detector (Z_m) will be double-confirmed. HFCT is also applied here to facilitate making sure the PD occurrences. The maximum magnitude of PDs (H_{qmax}) collected by using either resistive detector or HFCT at each level of applied voltage is shown in Table 3-2. The occurrence of the strongest response in the case of "R-1k-CT-1k" confirms the former selection.

The $\varphi - q$ distributions of PDs collected by using resistive detector and HFCT at 5 kV(rms) and 10 kV(rms) are shown in Figure 3-15. The 50 Hz content has been filtered. It is similar to the results which were obtained without applying HV: not much difference in phases of PD occurrence and obvious distinct magnitudes between the PDs detected by using resistive detector and HFCT. The PD occurrence by using Z_m of 1 kΩ resistance is significant above the background noise level, while the result by using a 50 Ω resistor is not as satisfactory as the former. Therefore, the 1 kΩ-resistance Z_m is confirmed to be applied in the further PD testing. And additional amplifier is not necessary since the PD signal is evident to be extracted from the raw data. Furthermore, possible bottleneck in frequency or dynamic properties from the amplifier in the measurement system need not to be taken into account.

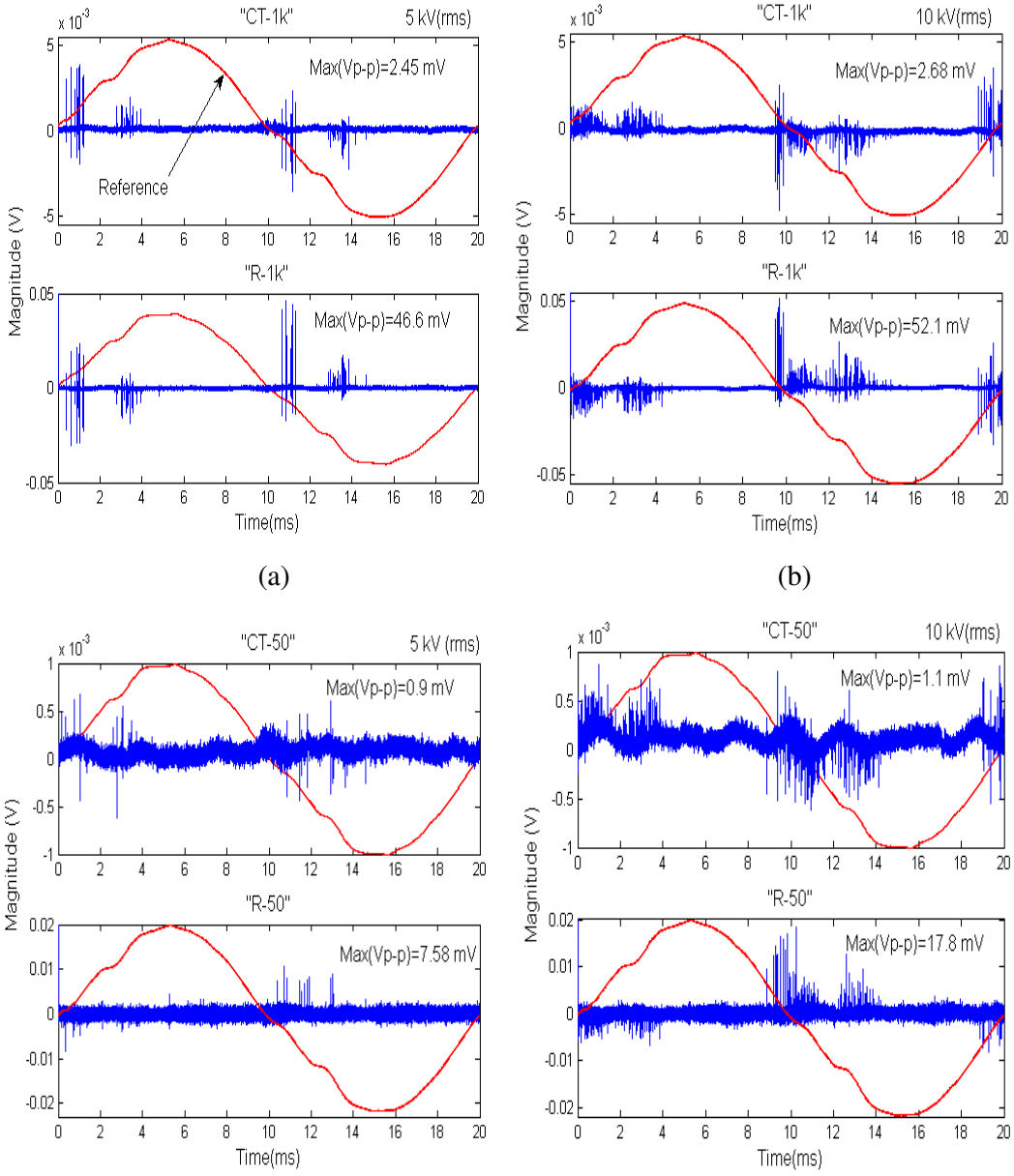

Figure 3-15 Comparison of PD distribution with applied voltage of 5kV and 10kV: (a) and (b) for "R-1kCT-1k; (c) and (d) for "R-50-CT-50"; (a) and (c) at 5 kV(rms); (b) and (d) at 10 kV(rms)

3.1.2.3 Dielectric response measurement

The IDA200^{TM} Insulation Diagnostics System [152] is shown in Figure 3-16. The available AC test frequency is from 0.001 Hz to 1 kHz with a variable voltage level up to

140 V (peak). The electrical parameters at a given frequency can be expressed in the form of a lumped equivalent circuit like a parallel connected RC network. Since the measured capacitance (C_p) of test sample is smaller than the lower capacitance limit of IDA200^{TM} (C_{min}= 40 pF), a ceramic capacitance of known 68 pF is connected in parallel with the sample so as to meet that requirement. A test voltage level of 30 V is applied considering the withstand voltage of that 68 pF capacitor. The measured parameters are parallel equivalent capacitance (C_p) or resistance (R_p), and loss angle (tanδ). The selected frequency range is 0.01 Hz to 1 kHz, since the property changes gradually in the range from 0.001Hz to 0.01Hz but the testing time spends more than 10 hours for 0.001 Hz-1 kHz while only about 10 minutes for 0.01 Hz-1 kHz. In order to avoid the slow change of sample in oil, testing time cannot be too long. Moreover, at frequencies as low as 0.01 Hz, there is already obvious deviation between each kind of property curves measured at different treeing procedures. In addition, too long time will also introduce other influences of decaying.

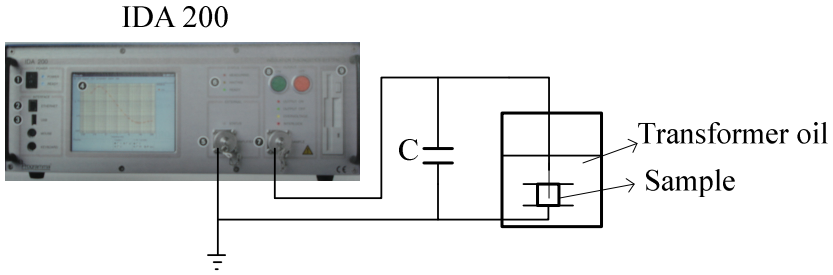

Figure 3-16 Dielectric response measurement setup

Two measurements, one for the 68pF capacitor itself (suffix "0") and the other for the test sample in parallel with the 68pF capacitor (suffix "m"), are made in order to solve the problem of instrument limitation. Making use of equation (3-1), the dielectric parameters of test sample (no suffix) can be determined:

$$\begin{cases} C_{pm} = C_{p0} + C_p \\ R_{pm} = R_{p0}R_p/(R_{p0}+R_p) \\ \tan\delta_m = 1/(\omega C_{pm}R_{pm}) \end{cases} \Rightarrow \begin{cases} C_p = C_{pm} - C_{p0} \\ R_p = R_{pm}R_{p0}/(R_{p0}-R_{pm}) \\ \tan\delta = 1/(\omega C_p R_p) = (R_{p0}-R_{pm})/[\omega(C_{pm}-C_{p0})R_{pm}R_{p0}] \end{cases} \quad (3\text{-}1)$$

3.1.2.4 Optical observation

A remotely controlled SONY Cyber-shot DSC-F828 digital camera is installed 15cm away from the sample to avoid HV interference. It provides 7-time optical zooming plus 8.0-megapixel CCD image. It has a recording rate of 15 frames per second and can record continuously for a period of 45 minutes. Thus the light emission from the sample in silicon oil can be shot during the PD measurement. And the final flashover and sparks formed during the tree growth may be also traced. Feeble light emitted during tree formation can also be recorded.

Besides, a Nikon optical microscope with a magnification up to 80 is also applied to observe the detailed growth of tree in the test sample after its removal from HV set up.

3.2 Laboratory experimental results

3.2.1 Test modes

It is planned to study the growth of electrical treeing by lifting the applied voltage level at different rates or keeping a constant applied voltage during the degradation of specimen till to breakdown. Experiments are conducted in three modes. HV applied to the needle is raised in the way as shown in Figure 3-17. For all testing modes, the linearly-voltage-rising time T_{rise}= 2 min until the applied voltage reaches the expected HV level V_i. During the data-saving time $T_{save} \approx$ 2 min, PD occurrences are recorded. In the mode of "TEST-1**"**, the applied voltage V_i is increasing from 2.5 kV (rms) to 10 kV(rms) by a voltage-rising step V_{step0} =2.5 kV (rms), then increasing by each step V_{step1} =1 kV (rms), and kept at each level for a voltage-keeping time T_{keep1} =10 minutes till the samples break down ("RATE 1" = 1 kV per 10 min); in the mode of "TEST-2**"**, from 2.5 kV (rms) to 10 kV(rms) similar to "TEST-1" V_{step0} =2.5 kV (rms), but then V_{step2} = 2 kV (rms) and T_{keep2} = 60 minutes ("RATE 2" = 2 kV per 60 min); in the mode of "TEST-3**"**, the applied HV level V_i is always kept at 20 kV (rms) ("CONSTANT" = 20 kV).

The procedure is continuing until the test sample break down. By these three testing modes, the roles of high electrical stress and aging time in inducing electrical trees and PD that lead to breakdown are evaluated.

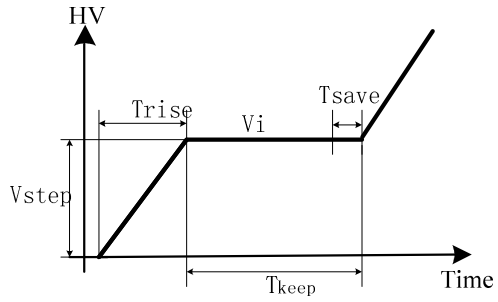

Figure 3-17 The sketch showing the time intervals used in test and PD measurement modes

Before each testing and after each step of PD measurement in **TEST-1**, **TEST-2** and **TEST-3**, off-line dielectric response measurements are carried out for the samples under test. Variations of those parameters (parallel-equivalent capacitance, parallel-equivalent resistance, and loss angel tangent) with frequency, i.e. the curves of $C_p \sim f$, $R_p \sim f$, and $\tan\delta \sim f$ are monitored before and after the tree growth.

Totally more than 5 XLPE and PE samples respectively were tested and good repetition was found.

3.2.2 Selection of signal processing techniques

Following the development of experimental setup, PD signals are collected. Since in laboratory condition and for ideal sample, the de-noising problem needs not much attention to and a low-pass Butterworth digital filter is applied to extract the 50 Hz component. After de-noising, the statistical PD occurrences in 20 ms with 20 waveforms are analyzed for group PD distribution after phase referencing.

To identify the type and number of PDs, several signal processing methods are applied. The first three of them are applicable for group PDs; the others for single PD.

The first method, $\varphi - q - n$ analysis, gives out the relationships in every aspect of discharge quantity, number and phase. This analysis is the most direct method and all the details can be investigated, which provides a basis for further analysis. With different discharge patterns, such as $q_{\max}$ q_{mean} and q_n, the characteristics can be fully described.

As the detailed information has been obtained, we also need to know the overall distribution by a few key parameters. Therefore the second method, the Weibull distribution is deduced, whose advantage is that it can cope with multi-source discharge.

The third method, the $\Delta u - \Delta t$ method, is intended to discover the internal relationship between neighboring pulses for further analyzing the details of individual pulses. It is more close to the initial discharge condition in discharge mechanism.

Finally it comes to the single pulse analysis, which is the trend for PD analysis, since it can extract the detailed information from the PD pulse waveform and contain more information of character and discharge mechanism. As the advantage, there is no need for knowledge of the number of PD sources. Therefore it can cope with several unknown discharge types simultaneously. As popular methods, spectrum (FFT) analysis and equivalent-frequency-duration analysis are selected in analyzing the single PD data.

Electrical treeing may be studied by several means. Besides the partial discharge technique, dielectric response and optical techniques are also adopted as assistant methods. Dielectric response is an advanced tool for insulation diagnosis. Insulation deterioration and degradation change the dielectric responses. It can be measured in different ways. And intermittent light emission is also observed during the partial discharge measurements for both XLPE and PE samples.

3.2.3 TEST-1: Raising applied voltage at "RATE 1" (1 kV per 10 min)

3.2.3.1 Partial discharges

A. Group distribution

In our experiments, the selected XLPE sample broke down at 20 kV (rms), while PE sample failed just when 22 kV (rms) was applied. PDs occur in both half-cycles. PD pulse number and peak magnitude increase with rise in voltage. Typical PD random occurrences in 20 cycles at 5 kV (rms) (treeing initiated), 15 kV (rms) (treeing propagated) and 18 kV (rms) (near breakdown) with phase angle are shown in Figure 3-18 and Figure 3-19. Positive and negative discharges are observed in the treeing [102]. More PDs occur in negative half-cycle as in Table 3-3. The discharges take place around the zero cross of the applied voltage and distribute up to the peak. The magnitude of

positive discharge is slightly higher than that of negative one, especially for PE sample. This means that positive discharges take place in higher voltage and the availability of initial electron for positive discharge is more difficult than for negative discharge [102].

It is obvious that the PD activity for PE sample is more intense than that for XLPE sample. Besides the retardment due to cross-linking, for XLPE sample, the peroxide decomposition products certainly is present, and therefore it can be postulated that the tree inception stress in XLPE insulation is considered to be higher than that in PE material due to the effect of the peroxide decomposition products [35].

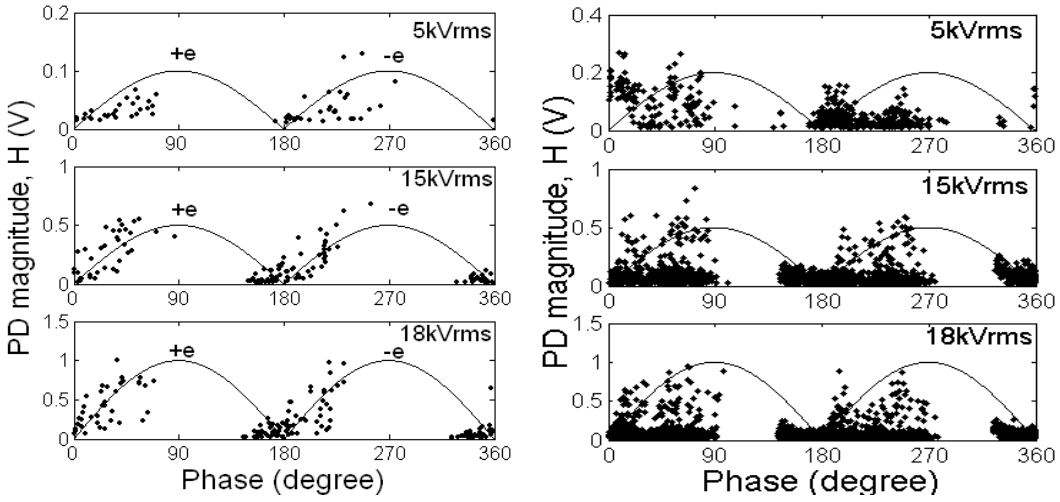

Figure 3-18 PD occurrences in 20 ms in TEST-1: (L) XLPE; (R) PE

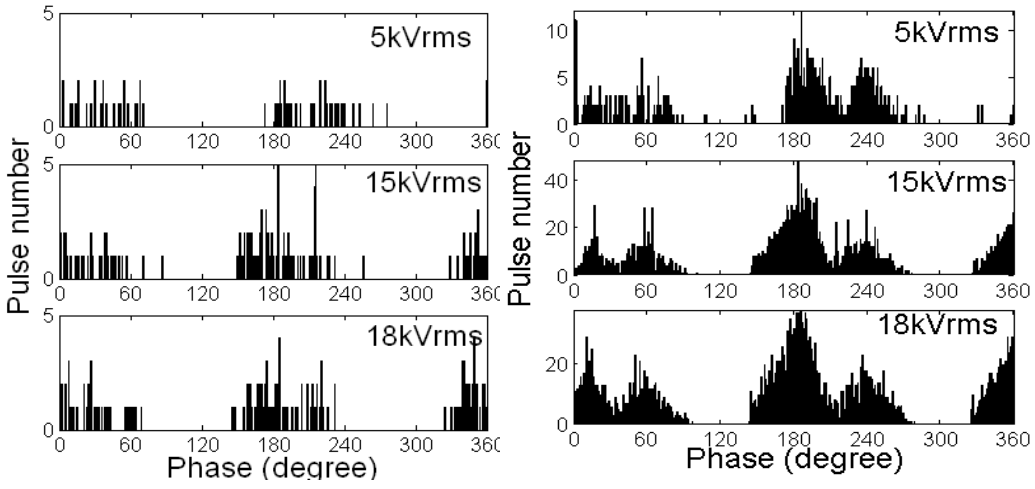

Figure 3-19 Pulse number distributions versus phase in TEST-1: (L) XLPE; (R) PE

Table 3-3 Pulses per 20 cycles at each applied voltage level for XLPE / PE samples

	XLPE			PE		
	5kVrms	15kVrms	18kVrms	5kVrms	15kVrms	18kVrms
Positive pulse	28	59	70	52	426	456
Negative pulse	35	72	80	55	480	495

Pulse activity is seen at all voltage levels in both cycles. More significantly for PE sample, cluster of PD pulses exists with almost constant magnitude at each applied voltage level but increasing with increase in applied voltage. While other pulses occur at HV and their magnitudes are fluctuating. It suggests that the PDs are a combination of two types of cavity-alike treeing discharges. The loose located PDs with high energy possibly occur at the tree channel tips to generate potential branches, while dense and low-energy PDs probably result from the discharge points near the electrode or at the channel walls contributing to the denser tree shape. It is more clearly at low field i.e. HV is 5 kVrms that most of the first type of PDs occur in positive half-cycle and the second type in negative half-cycle. These observations are consistent with a mechanism in which electrical discharges eroding the channel are temporarily extinguished. The first channel contains sufficient positive charge on its sidewalls to extinguish forward discharges, and only electron extraction avalanches on the positive half-cycle can occur [3].

Typical distribution of magnitude (H_q) of PDs with the corresponding number (n) of occurrence is made with 20 sets of 20 ms data as shown in Figure 3-20. Increasing the voltage, range of H_q and n increase. Although it ostensibly indicates the existence of two families of PD pulses with one having low magnitude with maximum n and the other having high magnitude with minimum n, it may well indicate a distribution where most of the PD pulses are "single channel" pulses but a smaller number involve large numbers of channels. Because testing system for grouped PDs has a limited high frequency bandwidth that such multiple channel pulses would show up as larger, single PD pulses.

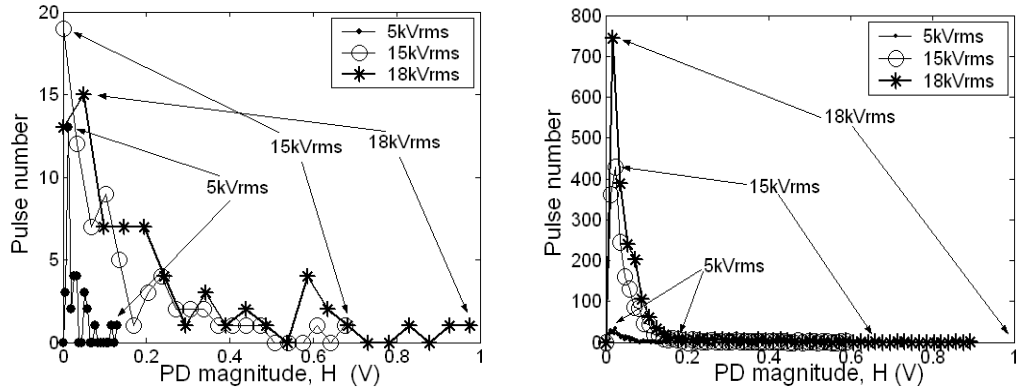

Figure 3-20 Distributions of pulse number versus PD magnitude in TEST-1: (L) XLPE; (R) PE

An analysis of variation of PD magnitude H_q(maximum), H_q(minimum) and H_q(mean) distribution at each voltage level is shown in Figure 3-21. Significant increase in "H_{qmax}" occurs with increase in voltage after 13 kV (rms), especially for PE sample. For XLPE sample, the peak q grows with fluctuation, and a dip appears suddenly and then goes up again until the sample fails. More or less similar behavior is observed for both XLPE and PE samples.

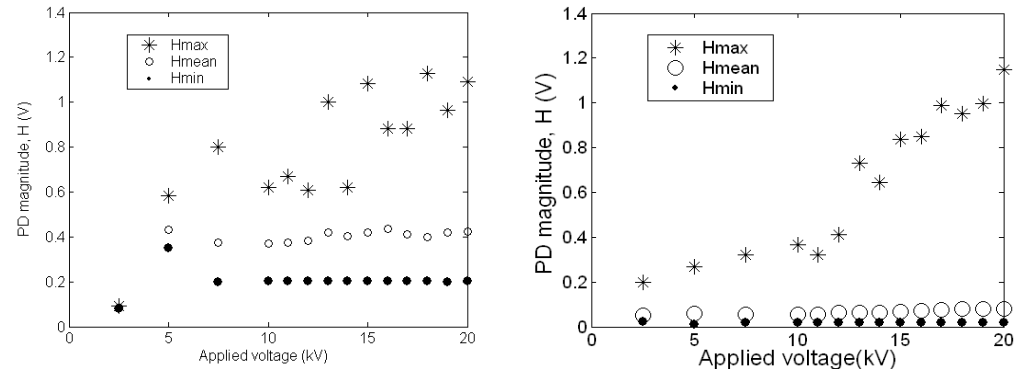

Figure 3-21 Variations of PD magnitude with voltage in TEST-1: (L) XLPE; (R) PE

Cumulative n distribution with H_{qmax} in Figure 3-22 and Weibull analysis with H_q-cum_n data shown as in Figure 3-23 indicate clearly the presence of two treeing phenomena with two sets of fitted α and β values, according to five-parameter Weibull distribution. The major type with high p should be due to micro-void discharge, while the minor type may be of surface discharge, according to the β values, since distinct β values can be used to classify different types of treeing [9]. This is consistent with that shown in Figure 3-24,

where β value of major type changes gradually but that of minor type keeps almost constant along with applied voltage rising. The tail at low possibility may be caused by some low amplitude pulses randomly. They are not following the general rule, since they are affected by testing conditions. It should be also noted that due to the limited high frequency bandwidth special for grouped PDs testing, there is such a possibility that multiple channel pulses would show up as larger, single PD pulses.

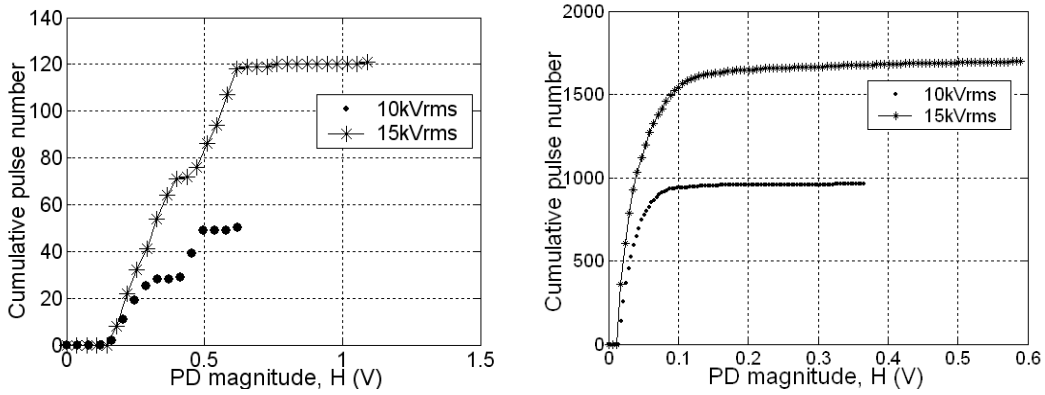

Figure 3-22 Distributions of cumulative pulse number vs. PD magnitude in TEST-1: (L) XLPE; (R) PE

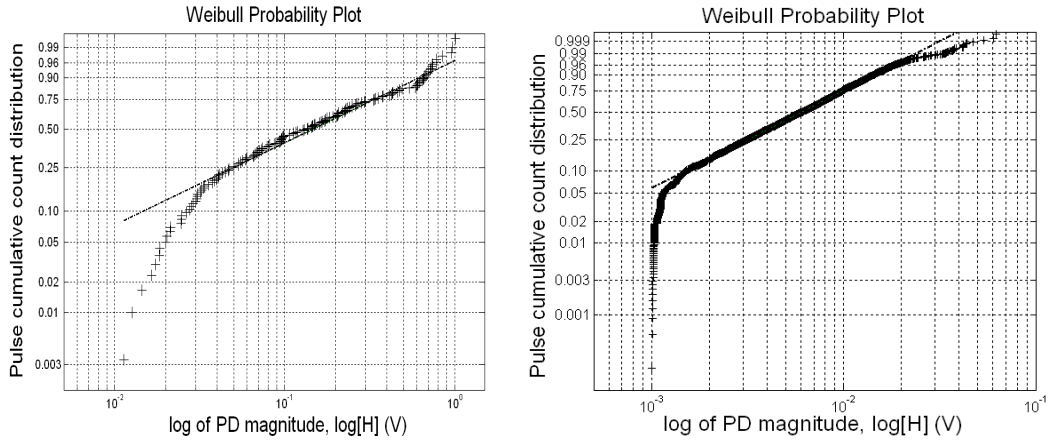

Figure 3-23 Five-parameter Weibull distributions at 18 kV (rms) in TEST-1: (L) XLPE (α_1=0.6618, β_1=3.3723, α_2=0.1184, β_2=1.2678, p=0.7429); (R) PE (α_1=0.0021, β_1=3.9719, α_2=0.0081, β_2=1.4965, p=0.9482)

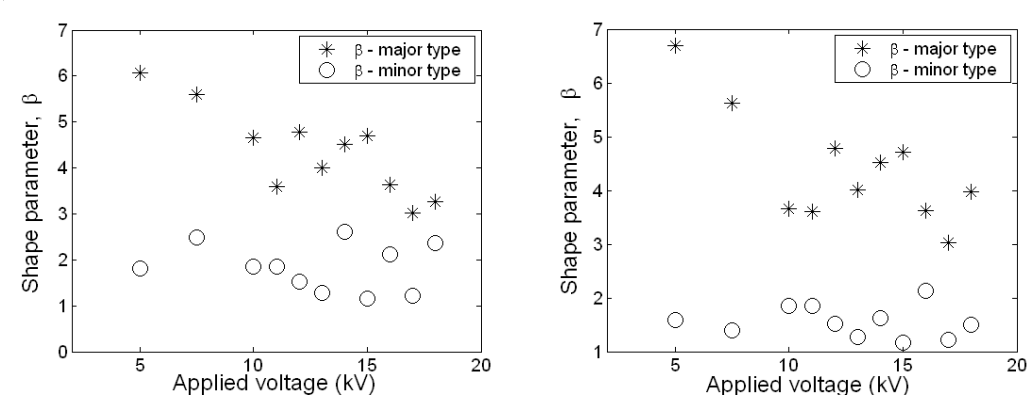

Figure 3-24 Variation of Weibull shape parameters β with applied voltage: (L) XLPE; (R) PE

References [109, 157] suggested the identification of treeing by analysing the time interval (Δt) and peak difference (Δu) between successive PD pulses. The variation of Δt and Δu with applied HV is shown in Figure 3-25. Δt in general decreases and Δu increases with rise in applied voltage. The clusters in Figure 3-25 show that the distribution in Δt is less than 3 ms (XLPE) / 0.6 ms (PE) up to 18 kV(rms), consisting with more pulses in PE than those in XLPE. Also, the range of Δu increases from 0.1 V to 1 V (XLPE) and from 0.2 V to 1 V (PE) with rise in applied voltage. Significant difference in Δt but almost similarity in Δu means that PD occurrence density is higher for PE sample than for XLPE sample. Thus it is verified that the judgment only by PD magnitude is not always the most appropriate measure. Change in Δt can provide new information.

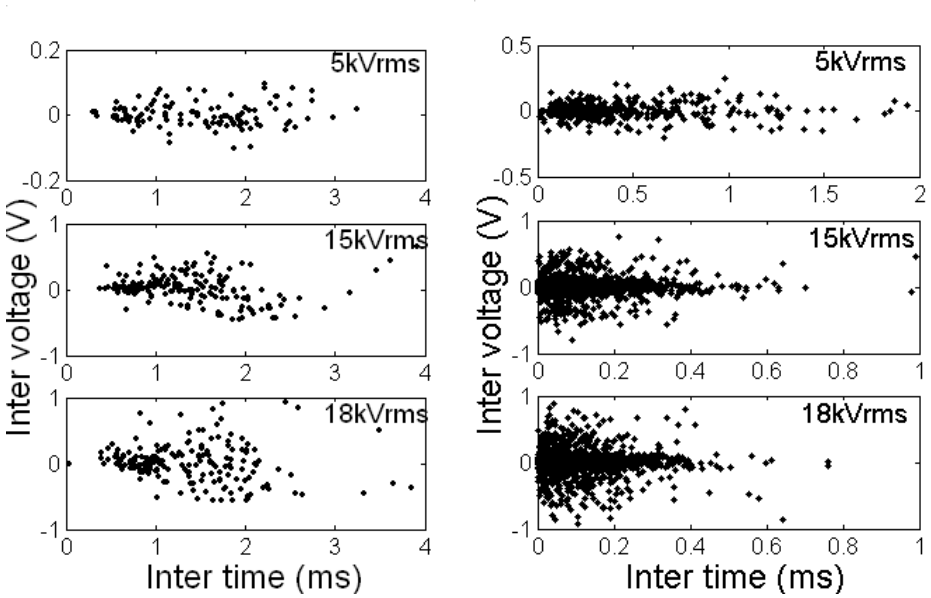

Figure 3-25 Distributions of Δt and Δu of consecutive pulses in TEST-1: (L) XLPE; (R) PE

Typical pulse number distributions with Δt and Δu are shown in Figure 3-26. Peak distribution occurs at low Δt and Δu with high stress indicating the presence of more trees. And the increasing range of Δu indicates the higher energy of discharge under higher stress. The pulse number distributions shown in Figure 3-26 suggest the possible existence of multi-source treeing apart from a dominant one.

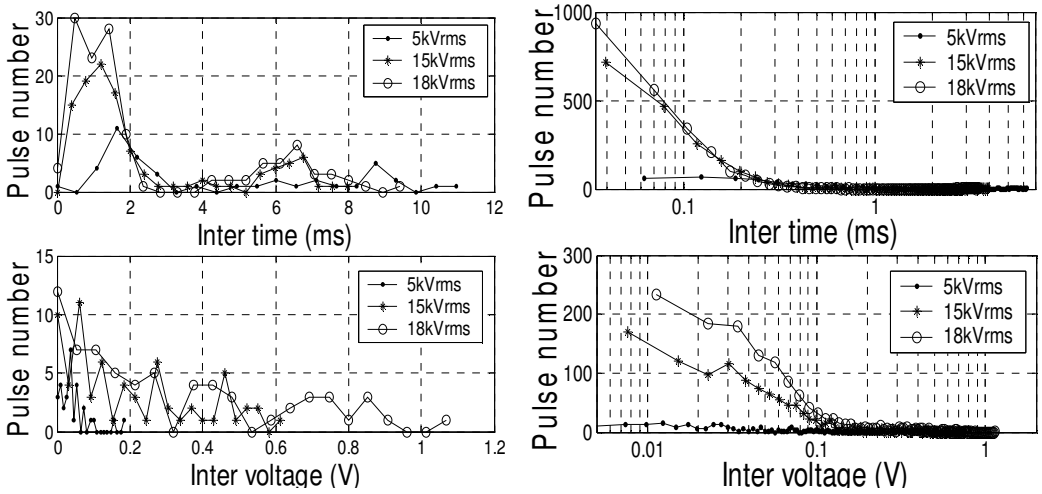

Figure 3-26 Distributions of pulse number versus Δt and Δu in TEST-1: (L) XLPE; (R) PE

B. Single pulse wave shape

It has been recognized that the kind of mechanism generating PD will, in general, produce discharges with different shapes. Likewise, pulse shape may change depending on the position of the defect inside the equipment under test. And noise pulses are often quite distinct from PD pulses [16, 158].

Typical recorded single PD exponential wave shape at 18 kV (rms) with sampled interval of 10 ns is shown in Figure 3-27. The rise and fall times of extracted single PD pulse are analysed. The single PD pulses in both XLPE and PE have a sharp rise time of 70 ns and a tail time of 250 ns. Moreover, it is found that ambient affects these rise and fall times. When the samples are kept in air, the single PD pulse has a very fast rise/fall time; while the pulse width increases if they are kept in silicon oil, implying the role of heat dissipation from the sample.

Treeing-induced PD occurs on a nano-second scale, often with several peaks in a waveform separated by less than 1ns. These multiple peaks are thought to be the result of the discharge cascading down multiple tubules within the structure. The mechanism by which a discharge within the tubules of an electrical tree causes a PD pulse in the external system is essentially the same as for void discharge.

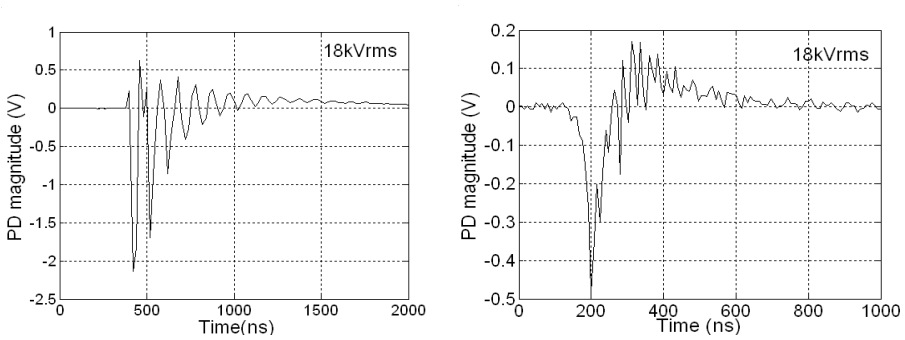

Figure 3-27 Single pulse wave shapes in TEST-1: (L) XLPE; (R) PE

The duration of single PD pulse decreases with the applied voltage as shown in Figure 3-28 (top). Assume a single PD pulse is located at phase of φ with magnitude of H_q (t). Then the single pulse exponential current is integrated in its duration T:

$$\int_0^T \frac{H_q(t)}{R} dt = Q \tag{3-1}$$

where R is the resistance of resistive PD detector.

The calculated variation of exponential PD charge, Q, with applied HV is shown in Figure 3-28 (bottom). In general, Q is found to increase with increase in applied voltage. Each PD pulse may be thought due to discharge in a capillary. Space charge is known to aggregate during treeing growth. Knowing the instant sinusoidal voltage level V(φ), and calculated Q, proportional capacitance C, could be estimated by

$$\Delta C = \frac{Q}{V(\phi)} \tag{3-2}$$

Determined capacitance variation with increase in applied voltage is shown in Figure 3-28 (middle). It varies in a narrow finite range indicating the channels may be more or less identical.

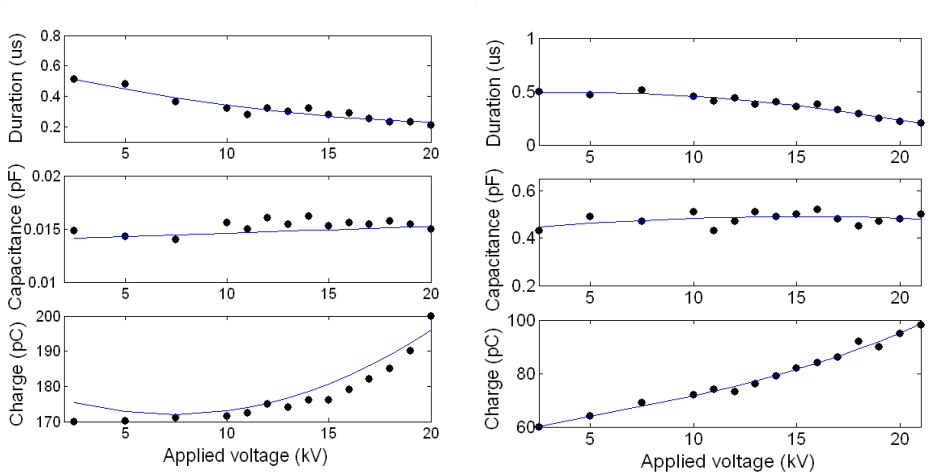

Figure 3-28 Variation of single pulse wave shape in time -domain with voltage in TEST-1: (L) XLPE; (R) PE

FFT analysis of single exponential PD pulses at different HV levels is shown in Figure 3-29. It can be seen that the PD signal has a wide frequency distribution, and spectral energy spreads up to 50 MHz. It indicates that the energy content and range of frequency increases gradually with increase in applied HV. One peak occurs around 10 MHz. The total energy of PD over -20dB congregated below 40 MHz for both XLPE and PE

samples. The results of FFT consist with physical explanation. However it should be noted that this method is most useful to static and periodic signals.

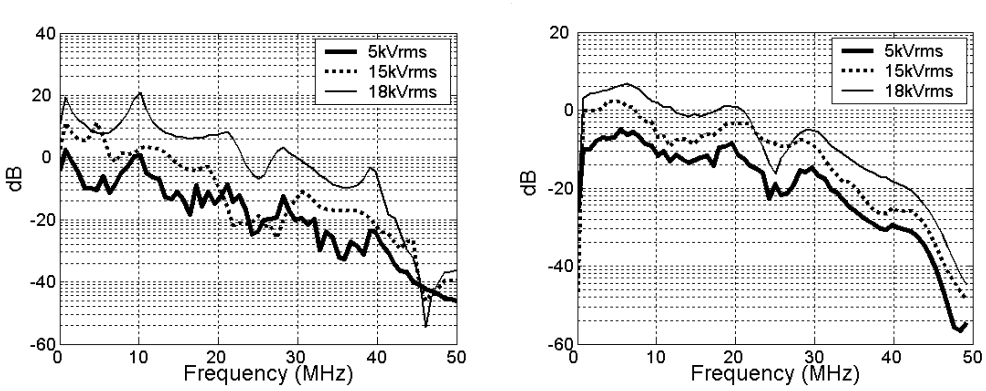

Figure 3-29 Variation of single pulse wave shape in frequency -domain with voltage in TEST-1: (L) XLPE; (R) PE

The cluster of single pulses can be separated according to the signal theory where the equivalent duration T is defined as in equations (3-4), (3-5) and equivalent frequency F as in equation (3-6) [113]. The T and F of single pulses are calculated for positive and negative discharges respectively as shown in Figure 3-30. The single cluster indicates that most of all pulses belong to a similar type, which is coming along with electrical treeing, consistent with Weibull analysis in Figure 3-23. Other pulses outside the cluster circle are possibly random noise and surface discharges. From the F-T plot, it is easy to find the frequency component and duration of single pulses. Positive PDs are scattered farther away than negative ones in the direction of longer T and lower F. Consisting with FFT result, the PDs for XLPE sample converges 5~12 MHz and 200~300ns duration; while for PE sample, they are around 10~13 MHz and 80~100ns duration. It accords with the fact that the PDs in PE sample have higher energy since XLPE material has a better tree-resistance than PE. This technique is also an effective tool for PD type classification and denoising.

$$T^2 = \frac{\int_{-\infty}^{\infty} (t - t_0)^2 x^2(t) dt}{\int_{-\infty}^{\infty} x^2(t) dt} \tag{3-3}$$

where

$$t_0 = \frac{\int_{-\infty}^{\infty} t x^2(t) dt}{\int_{-\infty}^{\infty} x^2(t) dt} \tag{3-4}$$

$$F^2 = \frac{\int_{-\infty}^{\infty} (f - f_0)^2 |X(f)|^2 df}{\int_{-\infty}^{\infty} |X(f)|^2 df} \tag{3-5}$$

By arranging all single pulses in an order of rising *T*, their coefficients of cross-correlation (cc) show a falling trend for both positive and negative discharges, as shown in Figure 3-31. This is an interesting result that most single pulses with low *T* or short duration are similar and they belong to the same type, i.e. discharges due to electric treeing.

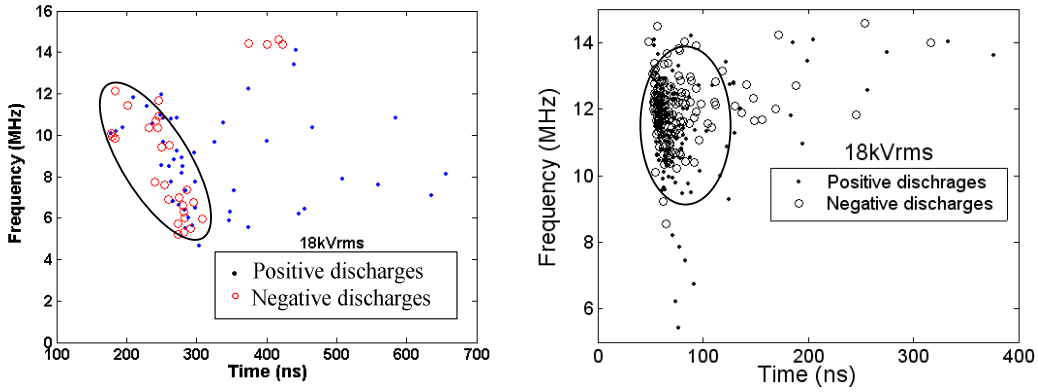

Figure 3-30 Equivalent T and F of single pulses in TEST-1: (L) XLPE; (R) PE

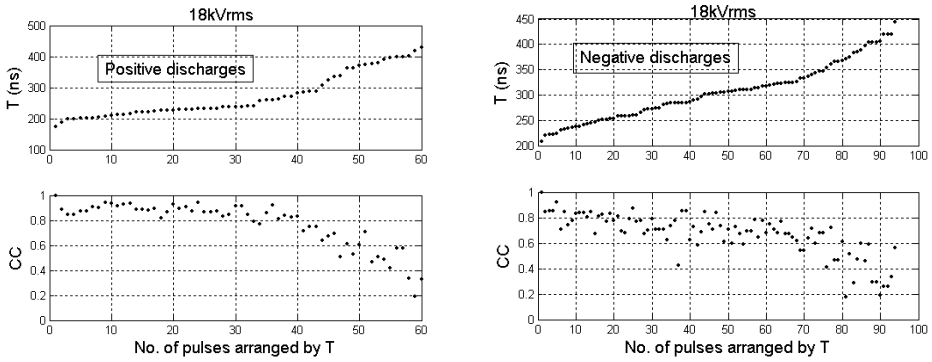

Figure 3-31 Correlation of single pulses for PE insulation in TEST-1

3.2.3.2 Optical observation

In Figure 3-32, the bush tree in XLPE grows to a radius of 250 μm at 16 kV (rms), and the breakdown conical path has a base radius of 700 μm at 20 kV (rms). Intermittent light flashes are observed during testing from highly stressed volume near the tip of needle.

Making use of the transparent property of PE sample, tree formation is observed and recorded by microscope, as in Figure 3-33. Branch trees grow first at relatively low voltage around 5 kV (rms), and then from 10 kV (rms) more branches begin growing near the needle tip, where is the center part of two earliest branches. Around 13 kV (rms), the branch trees become into a bush tree. Continually, it is larger and denser with increasing applied voltage. After the bush tree grows, its size increases slowly. Near the breakdown, new branches should be created which finally go to the ground electrode, since the size of the bush ball seems no much augmentation in volume. However, after the connection channel once comes into being, the destruction to the polymer cannot be deterred. At last, the channel is big and hollow, adhered with carbon decomposition and full of gas product.

Bush-type trees propagate initially like branched trees, but then the formation of new branches from channels close to the electrode rather than the growth tip produces the denser bushy form. During this process discharges continue within the tree with very large acoustic emission (recorded by video), referring to Figure 3-21 (R) where the PD magnitude keeps increasing after 13 kVrms. Once the tree has started to grow the local fields will be strongly dependent upon the space charge and its arrangement, rather than the field intensification of the original point-plane geometry. Possibly therefore the discharge and hence deposited wall charges will increase with applied voltage rather than the initial field [159]. Thus the most likely explanation of the cross-over to a bush shape is that sufficient sidewall charge is generated during the early formation of the tree to cause branch formation from the channel sides, possibly originating at surface pits. The removal or neutralization of wall charge in this way favour the continuation of discharging and the density of the tree channels will increase the magnitude.

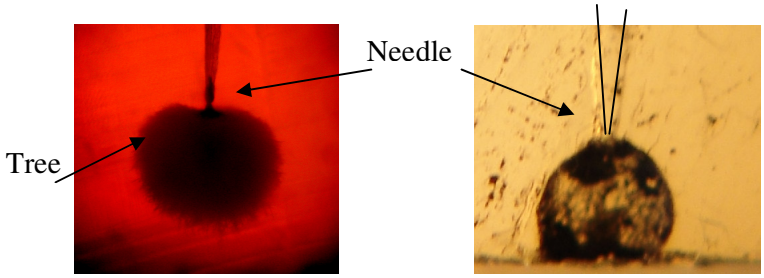

Figure 3-32 Tree formation in XLPE sample in TEST-1: (L) at 16 kV (rms); (R) break down at 20 kV (rms)

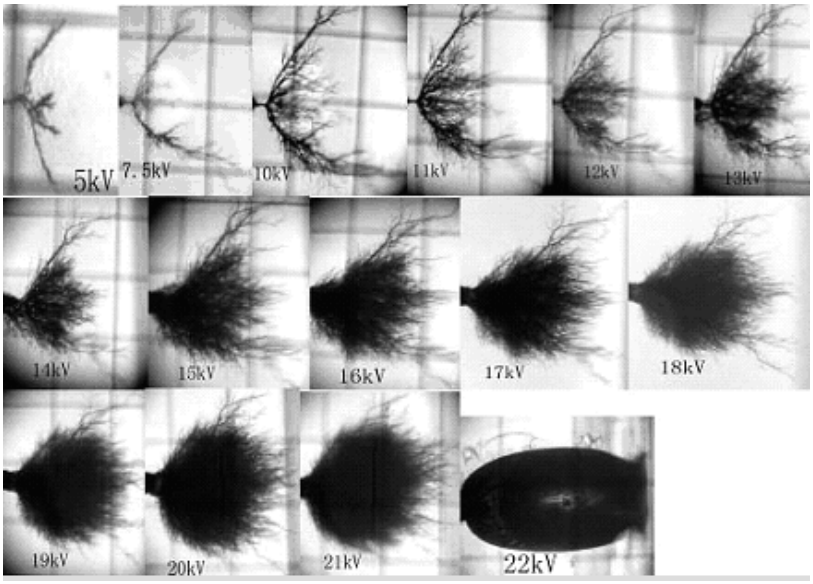

Figure 3-33 Tree formation in PE insulation in TEST-1 (at different voltage with grid of 1mm and magnification factor of 45)

3.2.3.3 Dielectric responses

Dielectric response measurements with the sample kept in oil are made before and after bush tree growth and the results are shown in Figure 3-34. Maximum variation is observed in the low frequency of 0.01 Hz. Parallel capacitance (C_p) decreases significantly and parallel resistance (R_p) increases after treeing. Loss angle ($\tan\delta$) does not change much with reference to the measurement taken before treeing. While after breakdown (BD), C_p increases slightly and R_p decrease significantly resulting significant increase in $\tan\delta$. For XLPE and PE samples, the results show the similar trends, while the C_p of XLPE sample is higher than PE sample, R_p lower and $\tan\delta$ higher.

Increase of wall conductivity is in agreement with the theory of Mason [160] and Densley and Savage [161]. In air discharges in crosslinked polyethylene the experimental work of Gamez-Garcia et al. [162] has shown that oxalic acid may be formed due to the moisture, carbon monoxide/dioxide or oxygen and acetophenone content. Since this forms crystals on the void surface which are semiconducting, the void voltage is reduced and the discharge extinguished. This may be why Wojtas [163] has found that cable material resistivity decreased with aging above a threshold voltage.

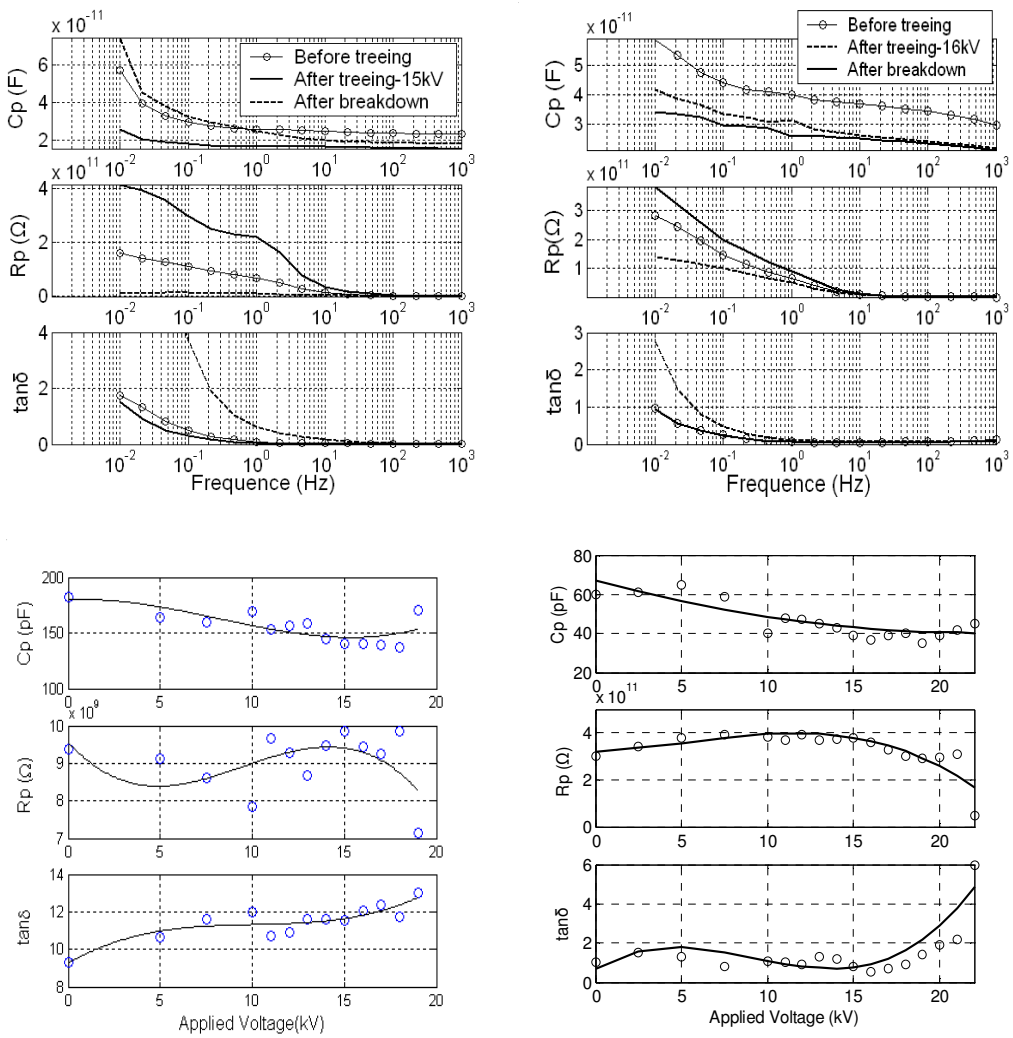

Figure 3-34 Variations of Dielectric responses with frequency and voltage in TEST-1: (L) XLPE; (R) PE

3.2.4 TEST-2: Raising applied voltage at "RATE 2" (2 kV per 60 min)

Aging time and applied voltage are two important factors to initiate electrical trees. Few researchers do study to compare their influences at the same time. In order to find the difference of electrical tree progress, another applied voltage rise rate, RATE 2 (2 kV per 60 min) is used in TEST-2, besides RATE 1 (1 kV per 10 min) in TEST-1. The keeping time of each HV level in TEST-2 is longer than TEST-1, while the jump step between each two HV levels is lower. This means a stronger factor of aging time but a weaker one of applied voltage. This section analyzes whether the treeing growth in TEST-2 is more active than in TEST-1.

3.2.4.1 Partial discharges

Further analyses focus on the data of XLPE sample in this section, since PDs for XLPE and PE samples have similar characteristics although the PD activity in PE sample is more intensive than in XLPE sample, as known from TEST-1. In TEST-2, the XLPE sample failed at an applied voltage of over 30 kV (rms). The PD occurrences are shown in Figure 3-35. The PD magnitude increases steadily with applied voltage, while pulse number distribution with phase angle keeps with little variance. PD patterns of magnitude and pulse number look similar with those of TEST-1, indicating the existence of similar PD mechanism.

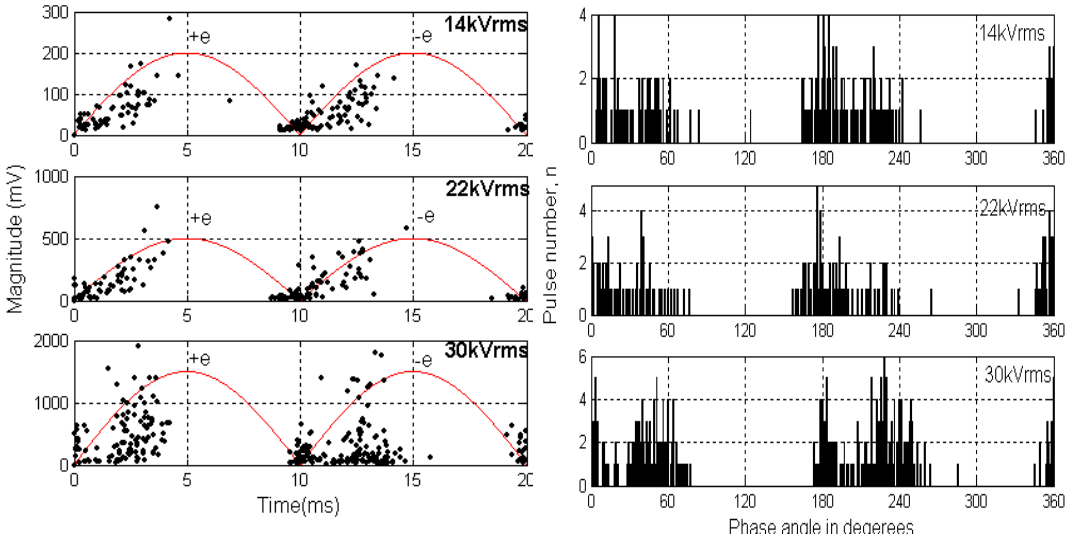

Figure 3-35 PD occurrences in 20 ms for XLPE sample in TEST-2

Variation of H_q with increase in applied voltage is shown in Figure 3-36 (L). In TEST-1, number increases steadily with applied voltage; while in TEST-2, it increases fast only after 20 kV (rms). In Figure 3-36 (L), H_{qmax} increases significantly after 14 kV (rms) indicating the slow growth of trees. The variance of PD pulse number with applied voltage is shown in Figure 3-36 (R). The n increases linearly with applied voltage between 10~14 kV (rms), keeps constant between 14~28 kV (rms), then suddenly drops to a low value of 100, and finally goes up again just before the breakdown at 30 kV (rms). This way suggests the growth of electrical treeing: initiation, propagation followed by a sudden slowdown just before breakdown.

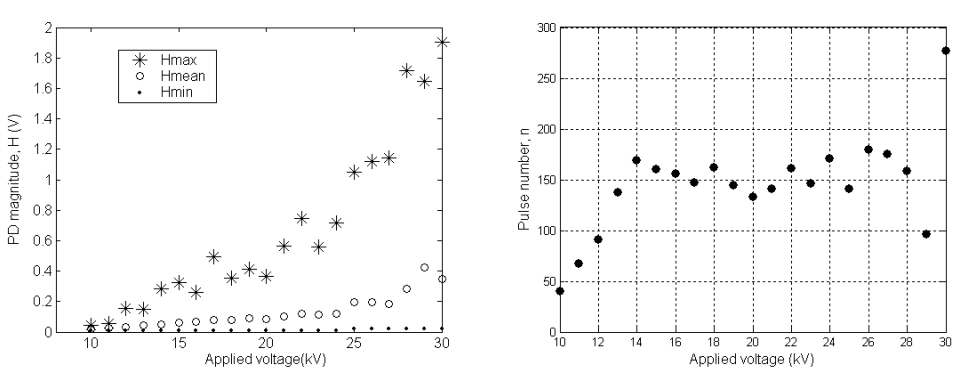

Figure 3-36 Variations of PD magnitude (L) and pulse number (R) with applied voltage for XLPE sample in TEST-2

The cluster with Δu-Δt occurs in a much narrow Δt range of 3 ms at HV, similar to that in TEST-1 (see in Figure 3-25). After linear fitting of q with cumulative n of its occurrences, the Weibull distribution at 30 kV (rms) has a β value of 2.97 and α value of 0.47 suggesting the existence of only one type of discharges as the result of treeing.

For the single pulse analysis, in Figure 3-37, it is found that the single exponential PD pulse has a decreasing duration in the range of 400ns as in TEST-1 (see in Figure 3-27 and Figure 3-28) and higher frequency content in the frequency spectrum of them with increase in applied voltage. Similar to TEST-1 (see in Figure 3-29) where a peak is located around 10 MHz, one peak occurs at 12 MHz in TEST-2. Another small peak occurs between 35~40 MHz.

The equivalent F-T distribution of single pulses is shown in Figure 3-38. A cluster of PDs are converging at the ranges of 230~240 ns / 13~16 MHz for negative discharges. Outside of the cluster circle, other negative discharges are sparsely scattered in 9~16 MHz with duration from 200~380 ns. Positive discharges have lower F and longer T.

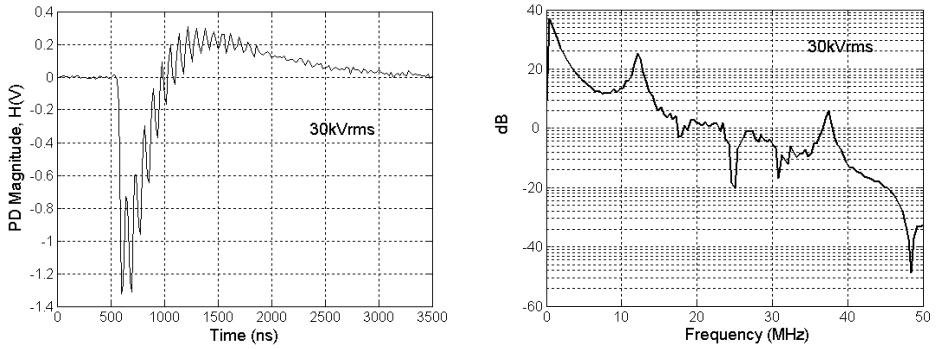

Figure 3-37 Single pulse in time- and frequency- domain for XLPE sample in TEST-2

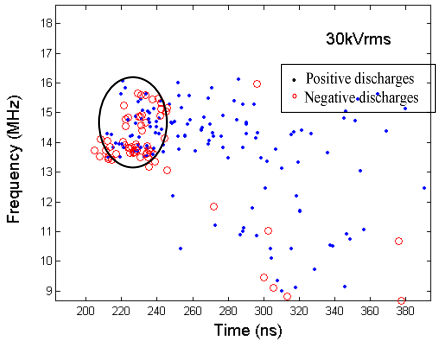

Figure 3-38 Equivalent *T* and *F* of single pulses for XLPE sample in TEST-2

3.2.4.2 Optical observation

In Figure 3-39 (a), branch tree is formed at HV over 15 kV (rms). Bush tree grows in XLPE sample after 20 kV (rms) and measured radius of growth is 500 μm, as shown in Figure 3-39 (b). After breakdown, a hollow path is formed as in Figure 3-39 (c) connecting the needle with the plane electrode, carbon decomposition product accumulated on the channel wall.

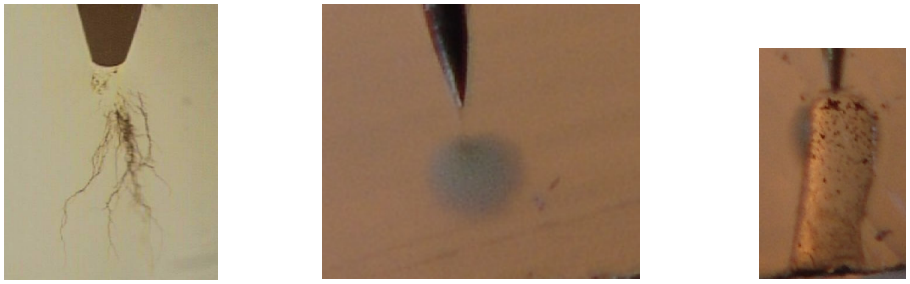

(a) (b) (c)

Figure 3-39 Tree formation in XLPE sample in TEST-2: (a) at 15 kV (rms); (b) at 20 kV (rms); (c) break down at 30 kV (rms)

3.2.4.3 Dielectric responses

In Figure 3-40, the trend of dielectric response results in TEST-2 is similar as in TEST-1 after tree formation. C_p variation is not as significant as in TEST-1 (see in Figure 3-34). And compared with those results of TEST-1, the C_p value is lower, R_p is higher and tanδ is also lower, consisting with the phenomenon that the tree grows slower in TEST-2.

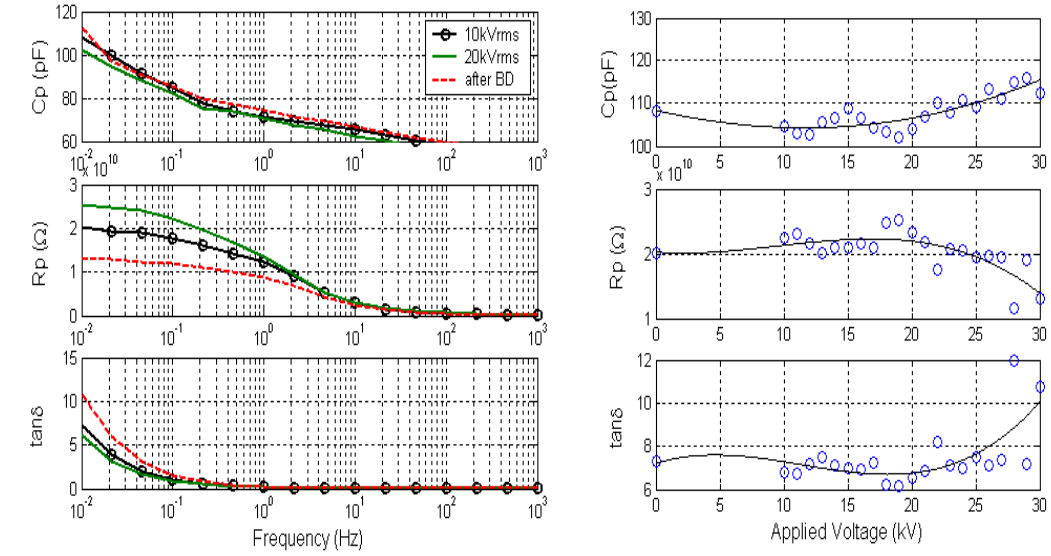

Figure 3-40 Dielectric response measurement for XLPE sample in TEST-2

Compared with the results in TEST-1, the treeing activity in TEST-2 is not as intensive as in TEST-1. Thus, the influence of applied voltage on electrical treeing is stronger than that of aging time. Tree growth is slower in TEST-2 than in TEST-1.

3.2.5 TEST-3: Increasing aging time at CONSTANT HV (20 kV)

3.2.5.1 Partial discharges

The selected XLPE sample broke down after 250 min at constant HV of 20 kV (rms). Its PD occurrence is shown in Figure 3-41. The phase distribution is similar to those of TEST-1 (see in Figure 3-18) and TEST-2 (see in Figure 3-35). As shown in Figure 3-42 (R), the variation of the number of pulses with aging time is very small but a sudden rise

in number is observed near breakdown. Figure 3-42 (L) shows that after linearly increasing for about 100 minutes, peak q is keeping around a constant level with aging time till to breakdown, which is obviously different from that of TEST-2 as shown in Figure 3-36 (L).

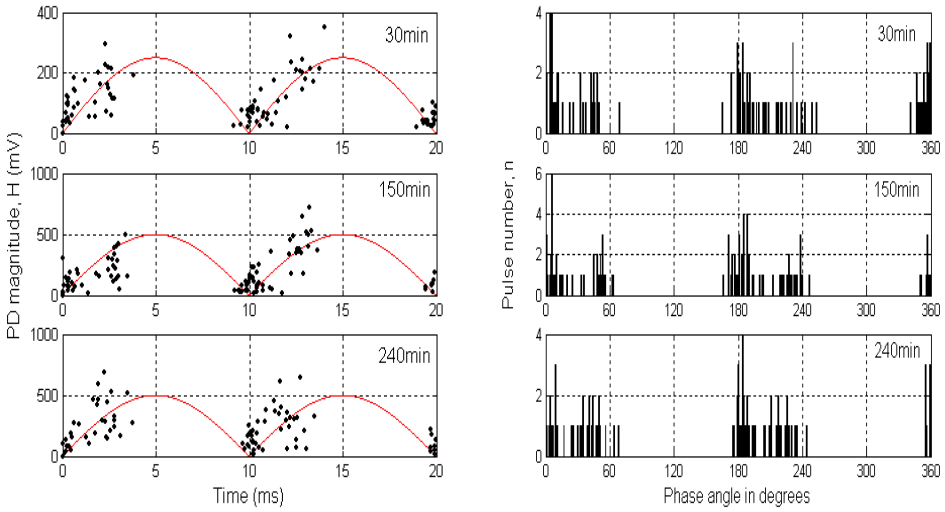

Figure 3-41 PD occurrences in 20 ms for XLPE sample in TEST-3

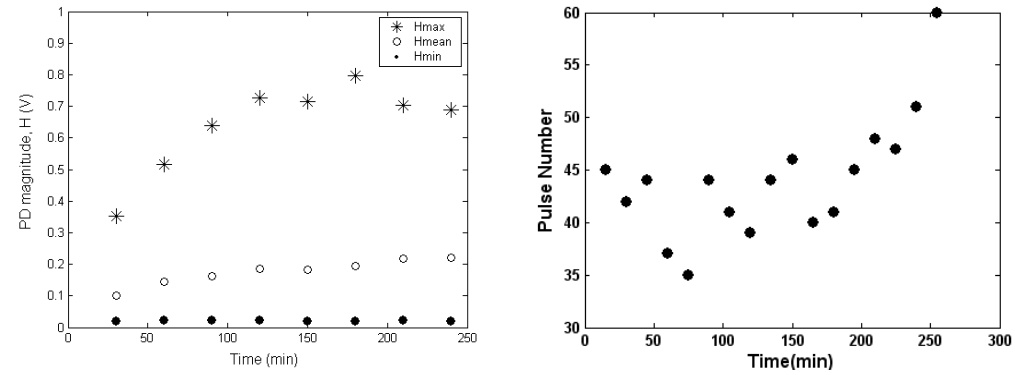

Figure 3-42 Variations of PD magnitude (L) and pulse number (R) with aging time for XLPE sample in TEST-3

The cluster with Δu-Δt always occurs in a very small range of 3 ms, similar to TEST-1 and TEST-2. Weibull analysis also suggests the existence of one main type of discharges resulting from treeing, e.g. one β value of 5.19 and one α value of 0.40 at the 240th minute.

For single PD pulse, as shown in Figure 3-43 and Figure 3-44, the shape of single PD

pulse and its frequency content with peaks in the range of 10~15 MHz and 35~40 MHz do not change much with HV electrical aging time. The pattern is similar as Figure 3-37 (R) of TEST-2 and both of them have a local minimum at 25 MHz. Most positive discharges have scatter T_s of 200~900 ns and F_s of 12~17 MHz. Negative discharges consist of a cluster with 200~300 ns / 13~17 MHz and some other pulses far away. The duration of 200~300ns changes a little with rise in aging time.

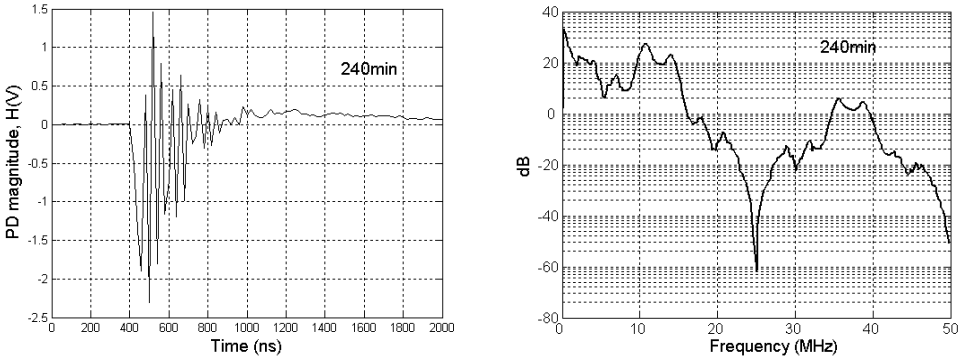

Figure 3-43 Single pulse in time- and frequency- domain for XLPE sample in TEST-3

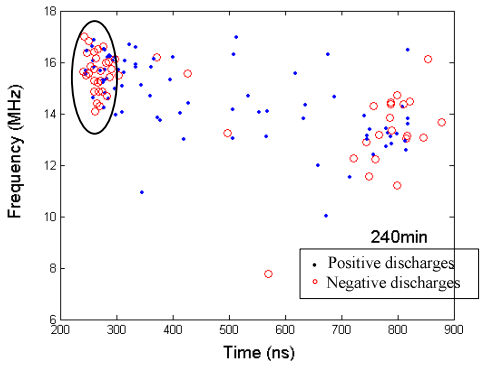

Figure 3-44 Equivalent *T* and *F* of single pulses for XLPE sample in TEST-3

3.2.5.2 Optical observation

Pre-breakdown light flashes appear more at high stress of 20 kV (rms) with the same gap distance and the path length grows gradually with time. For XLPE sample, the light emission is shown in Figure 3-45. For PE sample, a bush-type tree is formed at the very start and grows to a wider radius, as shown in Figure 3-46. The carbonized path in the sample after breakdown indicates that the tree grows in the form of bush whose size is

500 μm in radius and 1 mm in length. More intense intermittent light flashes from needle electrode are observed.

A short video records a series of frames of light emission as shown in Figure 3-47. It takes about 28.53 s for light spot to grow to bridging arc. After the breakdown, the eroded path follows the light emitting path. PD magnitude and number increase significantly, suggesting the existence of bombardment process of electrons and secondary ionization. Gas emission after puncture formation and decrease in light path around 26.67 s suggests the existence of formation of high-pressure gas volume. The number and peak magnitude of PD pulses also decrease. These are the trend indicators of complete failure.

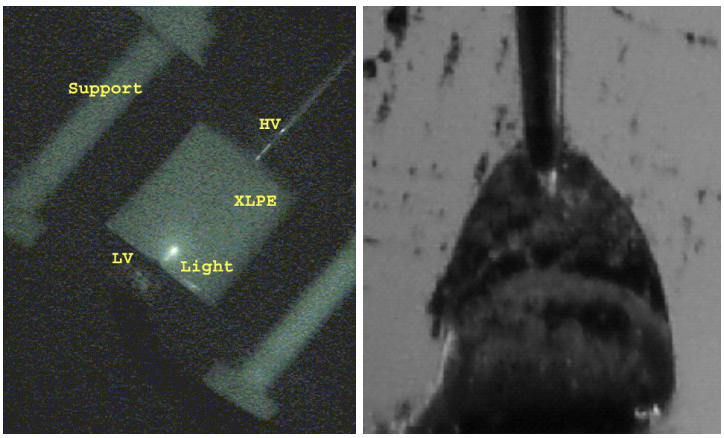

(a) (b)

Figure 3-45 Light emission in XLPE sample in TEST-3: (a) Light emission; (b) BD channel

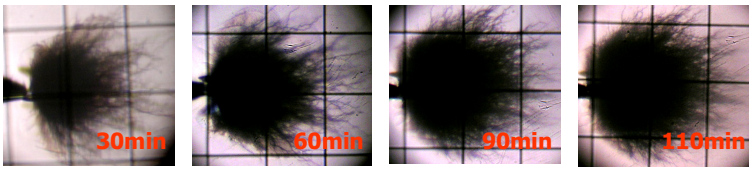

Figure 3-46 Tree formation in PE sample in TEST-3

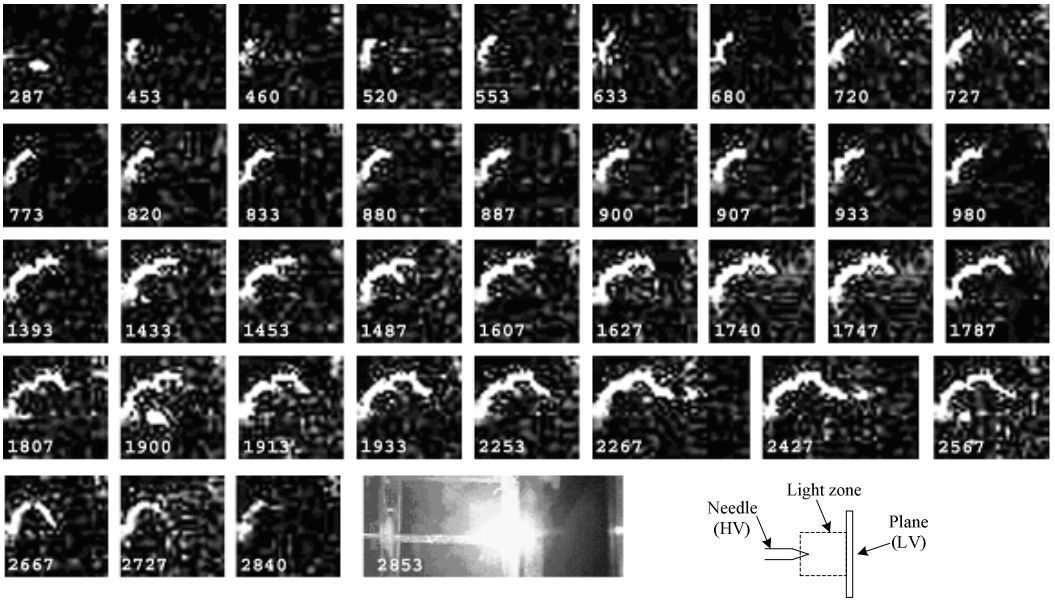

Figure 3-47 Light emission in PE sample in TEST-3 (Frames of recorded pre breakdown light emitting in a period of 28.53 s: the rate of recording is15 frames per second and number on each graph indicates the time)

3.2.5.3 Dielectric responses

With aging time, PDs may generate trees. C_p increases with time of aging. On the other hand, R_p decreases with aging time. Tanδ is found to grow with aging time. These are shown in Figure 3-48. This observation shows the same trend of results of TEST-1 and TEST-2.

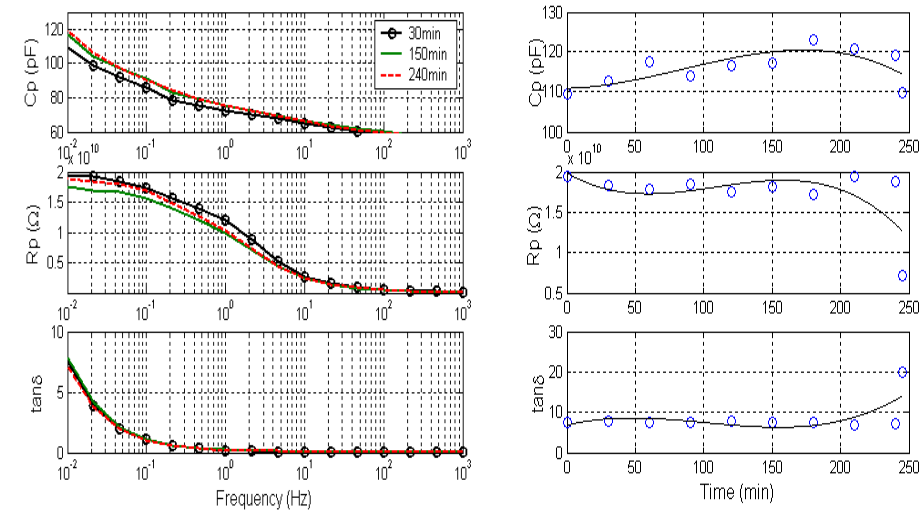

Figure 3-48 Dielectric response measurement for XLPE sample in TEST-3

3.2.6 Comparisons of TEST-1, TEST- 2 and TEST-3

3.2.6.1 Partial discharges

Table 3-4 Comparisons of partial discharge characteristics in three test modes

	TEST-1	TEST-2	TEST-3
φ-q	More Pulses located in negative half-cycle		
n-q	Range of q and n increasing with applied voltage		
	Peak in low range of q	Peak in middle range of q	Peak near breakdown
q-v or q-t	Increasing steadily	Increasing significantly after 20 kV (rms)	Around a constant level
n-v or n-t	Increasing steadily	Increasing after 20 kV (rms)	Very small variation; a sudden rise near breakdown
Δu- Δt	Δt < 3 ms (↓) ; Δu ↑	Δt ~ 3 ms (↓) ; Δu ↑	Δt ~ 3 ms (↓) ; Δu ↑
Weibull (β)	6.1 (5kV (rms)) ~ 3.4 (18 kV (rms))	6.9 (10 kV (rms)) ~ 3.0 (30 kV (rms))	Always around 5
Single pulse (cluster)	Tr <100 ns (↓); T: 200~300 ns (↓); F: 5~12 MHz (↑)	Tr <100 ns (↓); T: 200~300 ns (↓); F:13~16 MHz (↑)	Tr <100 ns (↓); T:200~300 ns (↓); F: 14~17 MHz (↑)

3.2.6.2 Optical observations

Table 3-5 Comparisons of optical observation in three test modes

	TEST-1	TEST-2	TEST-3
Tree size at 20 kV (rms)	~700 μm	~500 μm	~500 μm

Light emission	Observed after 12 kV (rms)	Observed at 30 kV (rms) near breakdown	More densely observed at 20 kV (rms) after 130 min

In TEST-1 and TEST-2, branch tree changes into bush tree after 10 kV (rms) applied, and tree grows faster in TEST-1 than in TEST-2. In TEST-3, bush tree keeps growing slowly with aging time.

3.2.6.3 Dielectric response changes after tree formation

Table 3-6 Comparisons of Dielectric response changes in three test modes

	TEST-1	TEST-2	TEST-3
C_p	↑	↑	↑
R_p	↓	↓	↓
tanδ	↑	↑	↑

3.2.7 Discussion

Because the initiation and growth of electrical tree in insulation systems is a long time process under service conditions, their laboratory investigation requires some form of acceleration. This is most conveniently supplied by the use of needle electrodes to enhance applied fields of kV/mm to nearly MV/mm. Thus the metal electrode in point-plane geometry is used to initiate electrical trees in this study. This geometry fulfil the dual role of high reproducibility combined with field intensification but have the drawback that the polymeric material investigated does not necessarily possess either the physical properties or the morphology that exists in engineered insulation systems.

The mechanism of AC tree initiation appears to be due to localised high electrical gradient. At high localized electrical gradient, degradation at stress enhanced points near electrode and in the cavity is observed in the form of slow growing tree-like structures in XLPE and PE. Tree shape is dependent on applied voltage agreeing with observations [164]. The appearance of larger number of pulses in the negative half-cycle suggests that the ionization process may be due to high energy electrons. Formed space charge may

react with polymer to yield PD pulses in the positive half-cycle and it may be due to attached high-energy charge carriers. Sudden dip in magnitude of pulses with increase in applied voltage as shown in Figure 3-36 suggests that built-up gas pressure limits the tree growth [9, 165]. When a tree approaches close to the counter electrode, its behaviour may be somewhat different [3]. Light emission is observed during the partial discharge measurement. After breakdown, emission of gas bubbles can be observed in a few frames indicating the presence of large volume of gas. Intermittent light emission over a long interval compared to Δt suggests the need of necessary time to build up charge. Tree may be initiated with light emission based on charge and capacitance of the different capillary paths. Observed shape of diffused light emission matches with the outline shape of branch tree. Conical bush tree formed at HV with tip starting from needle tip in the form of tunnel like channel.

In its first stage electrical tree propagation exhibits a decelerating growth rate. Eventually however an acceleration of the propagation rate occurs leading ultimately to failure. Tree propagation is observed to be intermittent in form with bursts of growth decaying to a standstill followed by further growth activity. Subsequent to the formation of the first branch which is a self-limiting process under AC stresses, the inactive periods can be associated with the initiation of tip splitting. Extinction of channel discharges is the reason usually advanced for the cessation of growth. Wasilenko's proposal [166] that a threshold tip field is necessary for the continued propagation of a channel is possibly operative here. Once a number of branches have been formed it is possible for some to be growing while others are inactive, and the individual growth curves of each branch will be subsumed to give a propagation curve appropriate to the overall tree structure. One reason for the temporary cessation of the tree growth may be the lack of a vent to release gaseous decomposition to the external environment [167]. This is particularly the case for bow-tie electrical trees and vented trees at a metallic asperity [167], rather than those initiated at voids [167] or at contaminants in the semiconducting screens of a cable [168]. The final stage of tree growth exhibits an accelerating propagation, corresponding to a runaway development of a tree branch from one of the existing tree tips. Very often this terminal growth is filamentary (channel diameter ~1 μm), jagged but unbranched.

Reported observation [157] suggests the shape of PD as triangular with a rise/fall time in the range of 100 ns with pulse duration of 300ns. In our case, exponential and oscillating single PD wave shapes are observed at all the stress levels as in Figure 3-27. The PD shape may be influenced by the propagation.

Capillary branch and ball-type trees are found to occur at low stress above 5 kV (rms). Recordable light emission does not occur up to about 10 kV (rms). Bush tree in the form of channel is formed at higher stress level.

For the dielectric response measurement, since the samples tested in each mode are not exactly the same due to the unavoidable deviation in the preparation procedure, it does not make sense to compare the absolute value of magnitude of these parameters. Dielectric properties (C_p, R_p and tanδ) change gradually with treeing growth after initiation, while the trends go into reverse ways near breakdown. For example, an inflexion point occurs at 15 kV in the frequency spectrum curve as shown in Figure 3-34. Before that point, branch trees grow gradually and after that point the tree shape changes into a bush type one as shown in Figure 3-33. Therefore, it means that the behaviors of the lumped parameters have a direct relationship with the microscopic physical change in material. This result is useful to monitor the degradation status of insulation system.

Since XLPE and PE have similar characteristics in partial discharge, dielectric response, and light emission, the tree formation observed in PE could help analyze that in XLPE.

Different increase rate of applied voltage and aging time have different influences on the tree growth. Faster rise in HV, which is the combination of higher applied HV level and shorter keeping time at each level, can induce faster growth of electrical treeing and has to be paid more attention. Moreover, aging time for the case with a constant HV applied is also a factor to grow trees and may lead to failure.

3.3 Summary

Partial discharge measurement, dielectric measurement and optical observation were carried out. Experimental setup was developed for laboratory studies. XLPE and PE samples to generate pure electrical trees have been fabricated and the characteristics of

pure PD have been evaluated. The measurements have been implemented for group and single PD analysis to study various PD distributions in time and frequency planes.

Several signal processing methods were used to identify the PD characteristics. For group PD data, φ-q-n distribution is the most direct method and the basis for further analyses. Then Weibull parameters, α and β, were extracted and different PD types can be identified since they have their own characteristic values. Δu-Δt distribution is another effective method and it gives information on every kind of discharge mechanism. They somehow describe initial discharge conditions affected by the former discharge, although internal rules are difficult to achieve. Further analysis was conducted for single PD pulse. Single pulse waveform was recorded in time- and frequency- domain. Equivalent F-T cluster analysis was used to characterize the single pulses. Cross-correlation coefficients of these single pulses were calculated to show the relationships among the pulses.

The effects of rise rate and aging time of applied voltage were analyzed and compared in three test modes: TEST-1 – raising applied voltage at 1 kV per 10 min, TEST-2 – raising applied voltage at 2 kV per 60 min, and TEST-3 – increasing aging time at constant HV. Trees grew differently in these modes in respect of influences of electric field together with aging time. It was found that the trees grew faster in situations with higher voltage rise rate than in those cases with relatively longer aging time but constant voltage. It means that the local electric field is the key parameter of tree growth. The field distribution is affected by some factors. One of them is space charge accumulation in tree channels which may change with stressing time and local field strength. Electric field and space charge density is coupled with each other through the aging time.

Dielectric response parameters, R_p, C_p, and tanδ, were recorded with frequency range from 0.01~1000Hz before and during tree growth and after breakdown. Similar trends although with difference grades (differences in value between the initial samples and the failed ones) were found in all the three modes: C_p varies in a range of 20 pF; R_p drops suddenly before the sample breaks down; tanδ shows a significant increase nearly the final failure. For all the three parameters, an inflexion point occurs on the frequency spectrum curve at the 15 kV in Test 1, 20 kV in Test 2 and after 150 min in Test 3. This is an important behavior and can be used to monitor the condition of insulations. No

research has been carried out using this method for electrical tree analysis, though it has been used in water treeing analysis. This non-destruction measurement can be considered as an assistant to partial discharge measurement.

Tree formation and light emission during tree growth was observed by the video camera as a quick break around the point of the needle. Branch- and bush- type trees were found and bush type trees occurred at higher applied voltage. During the first stage of growth from the needle, the tree is affected by the influence of the needle and the high electrical stress in the area. Several branches grow up and spread toward the ground electrode. In the second stage, the tree is characterized by slow growth with multiple, wide tree channels (bush shape) and a high magnitude of PD which follows an up & down behavior. In this phase of growth, the development of the tree is characterized by "jumps". A branch grows fast and continuously during a short period of time and then stops. Another branch then starts the process is repeated. However, as shown in Figure 3-33, the global progression of the tree is approximately constant. When the tree extends to approximately the ground electrode, the level of PD increases as well as the number and thickness of the tree channels. All the branches grow uniformly until one touches the electrode. After this leading channel reaches the ground electrode and the tree bridges both electrodes, a chain of discharges of large amplitude starts from the ground and broadens the channel in the direction to the needle. As a result, the channels become carbonized and the process continues until another leading channel is formed and so on. The tree approaches the ground electrode. When the tree touches the electrode, large pulses with large width, rise-time and fall-time alternate with regular, small pulses.

Chapter 4 Modeling of Electric Field and Space Charge Distributions in XLPE

In polymeric insulated high voltage cables, the treeing phenomenon in the insulation has been identified as an important factor controlling long-term ageing. However, owing to its complicated nature, the mechanisms involved are not yet fully understood. Experimentally, the study of treeing in actual cables is difficult, tedious, time-consuming limited informative and expensive (e.g. actual service voltage or higher is required, tree growth occurs over a long period of time, and the location of trees is random, requiring considerable time for examining sections of the cables). In order to overcome the problems, a method is used whereby a standard defect is introduced into the bulk insulation to mimic the effect of a contaminant or insulation surface roughness as found in an actual cable. This "defect" concentrates the electrical stress and serves as an initiation site on which the tree growth is more probable. Moreover, the standard defect gives a controlled, reproducible stress concentration.

Generally, there are two kinds of standard defect currently used, i.e. needle-plane and double-needle electrode configurations. These geometries fulfill the requirement of producing high stress intensification (strong divergent stress favors charge injection and tree growth) and repeatable results, such as, typically the characteristic voltage for electrical treeing. Using this technique it has been shown that electrical trees grow not only under AC stresses but also under DC conditions [111], voltage ramps, short circuit, polarity reversal and impulse voltages.

Charges can be injected by the electrodes under the influence of the electric stress through either Schottky injection or tunnel injection processes. Moreover, hetero-charges can result from the presence of impurities contained within the dielectrics and can generate their own electric stress which is superimposed on the applied electrical stress. It can affect the breakdown stress of the insulating materials in terms of aiding or weakening local electric stress. Recent progress in the non-destructive measurement of space charge distribution in the materials and polymeric cables [169, 170] has had a significant impact on the understanding of electric ageing (including electrical treeing), high-field conduction and breakdown phenomena.

Three stages are involved in the development of electrical trees, i.e. inception, propagation and completion. Among many experimental setups used to study the treeing phenomena, those allowing inhomogeneous field condition are widely used, and many models have been developed trying to describe the relevant aging process [118, 171-176] and concomitant partial discharges [120, 171, 177-179]. It is believed that the tree initiation is the most important phenomenon, since most evidences show that the insulation fails sooner or later once an electrical tree is formed, although this is not an established fact at normally engineering voltages and electric field. It has been reported [159] that large variation in time exists in the first stage of development and is generally attributed to the sample preparation causing morphological difference in the material, or space charge accumulation or experimental conditions such as temperature, or void present at the needle tip. Therefore, special attention should be paid to the local stress variations associated with electrode geometries actually employed in the experimental work.

In this chapter, primary studies are carried out firstly on the electric stress profiles of the needle-plane electrode system used for experimental investigation of tree initiation and growth. The effects of diameter of needle, tip angle, tip radius and tip separation on the local electric stress are presented. Based on that, the initiation and propagation mechanisms of electrical treeing are analyzed by taking into account the effects of conductive particles, gas bubbles around a conductive particle, and two bubbles, one with space charges inside. Furthermore, regarding the nonlinear conductivity of polyethylene, the electric field and space charge distributions is analyzed as well as the influence of voltage waveform. Temperature rise is also calculated by solving an electro-thermal coupling transient problem. Going deeper to macroscopic scale, the space charge accumulation phenomena in insulation bulk is studied based on the bipolar space charge transport model. Since all the developed models are not equivalent because of the lack of enough evidence from current space charge measurements, different assumptions have different explanations for the charge transport phenomena. Two assumptions are applied in the analysis in this project: unique and exponential deep trapping level, respectively.

4.1 Electric field in needle-plane electrode system

4.1.1 Analytical solution

In order to obtain an analytical solution for the needle-plane electrode system, it is assumed that the needle has a hyperbolic shape. The derived formula for the electric stress at the tip of the needle is given by [180]

$$E_{tip} = \frac{2U(1+\frac{r}{d})^{\frac{1}{2}}}{r\ln(\frac{r+2d+2d^{\frac{1}{2}}(d+r)^{\frac{1}{2}}}{r})} \tag{4-1}$$

where U is the potential at the needle, r the tip radius of the needle and d the distance between the needle tip and the plane electrode. In the cases where $d >> r$, the above equation can be further simplified as "Meson's Formula":

$$E_{tip} = \frac{2U}{r\ln(1+\frac{4d}{r})} \tag{4-2}$$

The above equation (4-1) or (4-2) has been widely used to calculate the maximum stress at the needle tip. It should be noted that this is the space charge free "Laplacian" field, which is not relevant to tree initiation, as charge is injected and space charge is formed at high levels (~3000 C/m^3) around the tip. In practice, it is very difficult to prepare hyperboloid shaped needles resulting in considerable deviation from the ideal. The parameters associated with needles used for high voltage insulation material testing vary from laboratory to laboratory. For example, the diameter of the needles, Φ, have varied from 0.685 mm to 1.0 mm; the radius of the needle tip, r, from 1 μm to 100 μm; and the separation distance, d, from 0.5 mm to 10 mm. Moreover, the tip angle is typically 30°. Apart from the wide range of needle geometries, the deviation from the hyperboloid shape may cause errors in the estimation of actual electric stress using equation (4-1) or (4-2). This has not been realized until recently where numerical methods have provided a different value of electric stress at the needle tip. The finite element method (FEM) of analysis has the advantage of geometrical flexibility, e.g. it is possible to include a greater density of elements in regions where stress and geometry vary rapidly.

4.1.2 Numerical modeling

The accuracy of the FEM technique can be improved by increasing the number of elements, which is realized by decreasing the solver residual and percent error in software, e.g. COMSOL Multiphysics® v3.4. But the computation time has to be considered at the same time when the result is acceptable. Owing to the Z-axis symmetry of the needle-plane electrode system considered, it can be solved as a two-dimensional axis symmetrical problem as shown in Figure 4-1. HV, typically 10 kV is applied to the needle electrode and the base dielectric material (XLPE) is grounded. The needle electrode and ground electrode are set as "perfect conductor", and background "polyethylene" has a relative permittivity of 2.3. The conditions for other boundaries are defined as balloon or DV, i.e. normal derivative of potential. Both the Dirichlet and Neumann boundary conditions are used.

A major consideration in any electric stress analysis is the placement of the far-field boundary which is desirable an infinite distance. However, compromise has to be made between the computation cost and the accuracy to confine the solution in a reasonable space. In Figure 4-1 the calculated stress at the tip will change little with the size of space boundary, if the ratio of AE / BC >3.5 and the ratio of EF / d >1.5 [180]. All the results in the following sections are computed with the same boundaries.

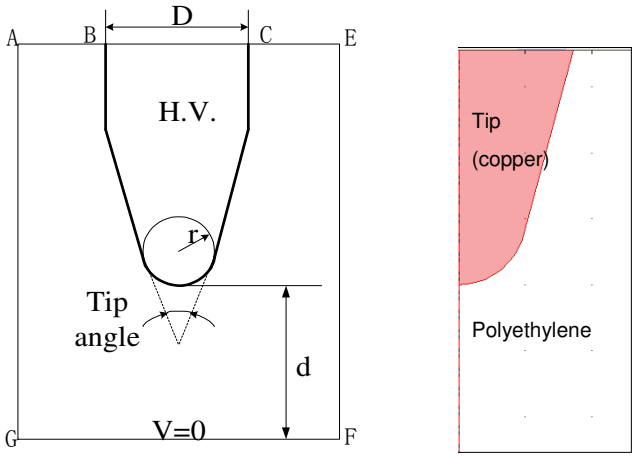

Figure 4-1 Model used for electric stress computation: (L) Geometry; (R) draw mode in COMSOL

4.1.3 Without space charge ($\rho = 0$)

The highest stress only occurs at the tip of the needle. And the maximum stress at the tip will change with different geometries of the needle. The dependency of the electric stress on the following parameters is studied: D - diameter of the needle; θ - angle of the needle tip; r- radius of the needle tip; d – distance between the needle and the plane.

A. The influence of diameter (D)

Figure 4-2 illustrates the variation of electric stress at the needle tip with varying diameters of needle. It can be seen that the diameter of needle has little influence on maximum electric stress, especially for the diameter with higher value.

B. The influence of tip angle (θ)

The variation of electric stress at the needle tip with different tip angles is shown in Figure 4-3. An approximately linear relationship is found and the slope is larger for the needle with smaller diameter and steeper tip.

C. The influence of needle radius (r)

The variation of electric stress with varying needle radius is shown in Figure 4-4. The electric stress at the needle tip, calculated by equation (4-1) changes dramatically with the change in tip radius. The result by finite element method also shows the trend. However, the electric stress values obtained from equation (4-1) are generally higher than the values obtained by finite element method, particularly when the tip radius $r < 5\,\mu\text{m}$.

D. The influence of distance between the needle tip and the plane electrode (d)

Figure 4-5 shows the relationship of the electric stress at the needle tip and the distance from the needle tip to the plane electrode. The values obtained from the calculation by equation (4-1), and finite element method also give a noticeable difference in electric stress. There appears a cross-over point between two curves for two methods, before which the finite element method gives a higher value than equation (4-1), and after which the finite element method gives a lower value. The difference clearly demonstrates that the hyperbolic shaped needle used in the analytical solution is not a good representation

of needles used in the experimental work.

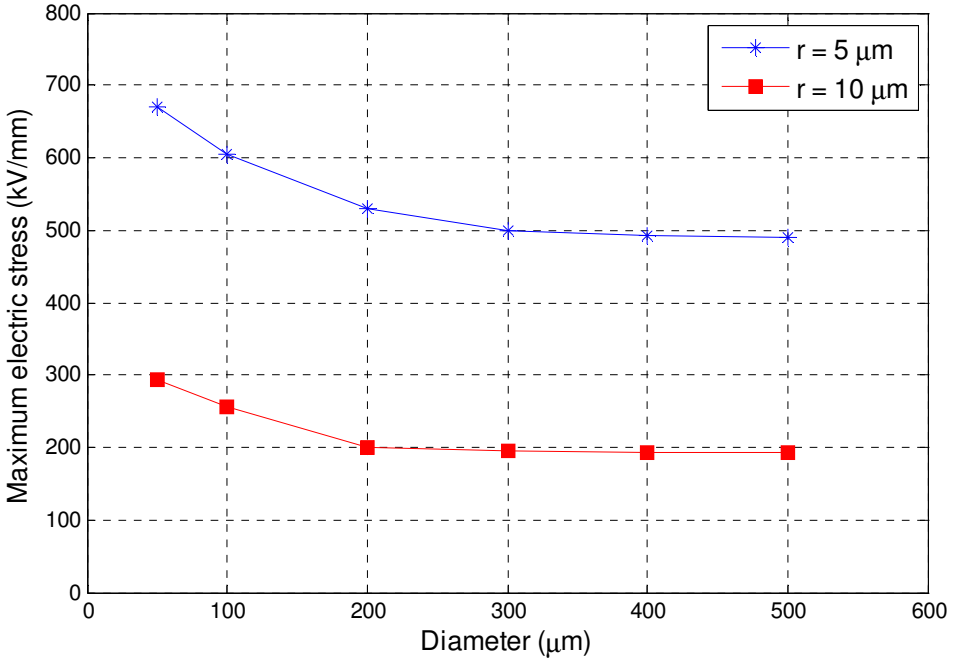

Figure 4-2 Electric stress vs. diameter of the needle (θ =30º and d=2mm)

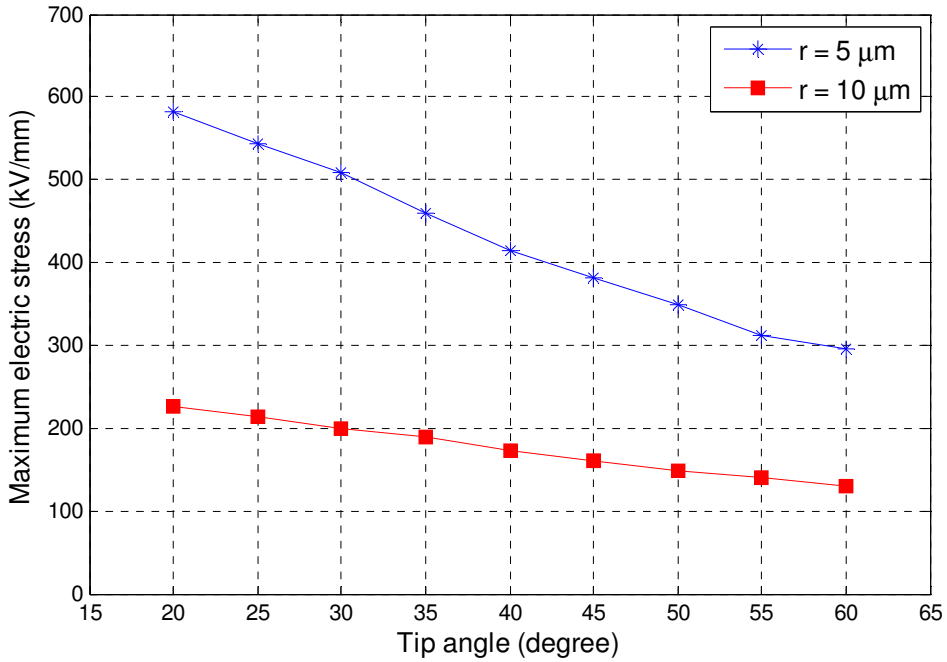

Figure 4-3 Electric stress vs. tip angle of the needle (D=300μm and d=2mm)

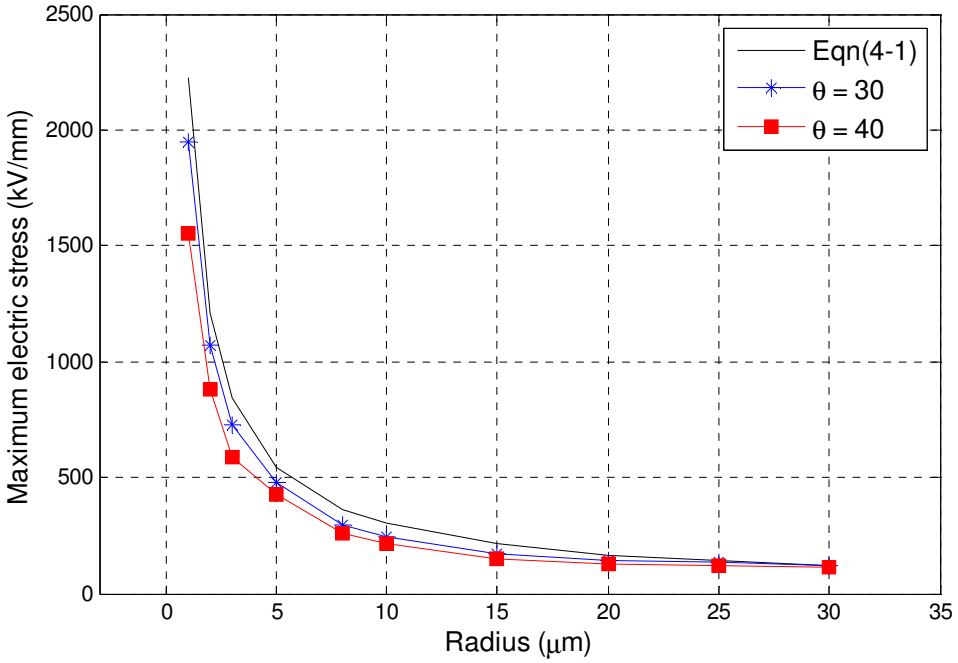

Figure 4-4 Electric stress vs. tip radius of the needle (D=300μm and d=2mm)

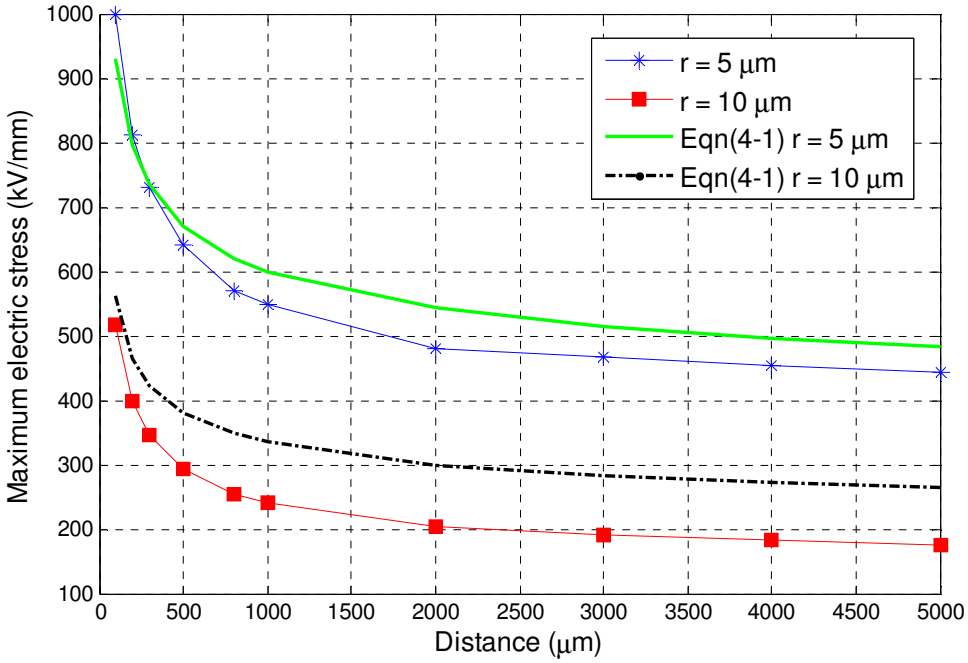

Figure 4-5 Electric stress vs. distance between needle and plane electrodes (D=300μm and θ =30°)

4.1.4 With space charge ($\rho \neq 0$)

It is well known that space charge plays a very important role in dielectric aging and breakdown. Space charge can distort applied fields and to produce locally high fields, leading to dielectric and component aging, and subsequent in-service breakdown, and hence failure, as described earlier in this work. The aging effects are seen in the case of constant stress DC fields as time permits buildup of charge that is either injected homo-charge at electrode-insulator interface, or results from deep trapped bulk charge and possibly void discharge. These effects are a function of the insulation material itself, the stress environment conditions such as temperature, impurities, and many other factors.

The apparent field necessary for tree initiation at a needle tip, calculated from the applied voltage ignoring space charge, may exceed the breakdown strength of the material by an order of magnitude. Therefore, homo-charge must be present around the needle tip reducing the total effect field to much lower level. Also the distinct difference between the tree initiation voltage for a positive and negative stressed needle attributes to space charge effects. Both electrons and holes are considered to be injected into polymer dielectrics. The time for space charge formation is determined by the dielectric time constant and the rate of change of the applied voltage. Space charge measurement using the pulsed electro acoustic (PEA) method [181] has shown that the injected charges tends to be trapped reasonably deep in polymeric material used for cable insulation. These deep traps may originate from the interface between crystalline and amorphous regions of the polymer as well as additives [127]. The level of injected space charge is determined by the potential barrier formed at the interface between the electrode and dielectric material. The barrier is governed by electro physical properties of the interface such as the work function of the electrode metals or semiconductors, and surface traps of the dielectric. Additives and gas phases may affect the work function and surface traps.

The contacts between electrodes and PE are of considerable importance in controlling the amount and distribution of charge in the polymer, and consequently in influencing electrical strength and aging processes. In the case of PE, it should be emphasized that these contacts never can be uniform on the scale of the polymer morphology. In addition, in the majority of experimental situations, the electrode is metal and covered with oxide

or other contact impurities. In practical situations, such as HV cables, the interface is even more difficult to characterize. However, one needs bear in mind that trapped charge in cables seems to be closely associated with the electrodes. With the assistance of present techniques, space charge injected via the needle electrode now can be measured by several methods. The radius of the space charge boundary R can be derived by using $R = r(1+V/V_c)/2$ which is based on the field-limited space charge model, where V is the applied potential and V_c the onset potential for injection [182]. It has been reported [164] that the injecting distance of the space charge into the material varies from 5 to 60 μm. To simulate the presence of space charge, two models have been developed so far: space charge is assumed to be confined to a cylindrical region or a spherical region around the needle tip. Before going to study on the "real" space charge model, a fictitious model is analyzed at first: the space charge is assumed to be uniformly distributed in the confined region. And the spherical space charge model is recommended as the best suited one for the needle-plane electrode system [183], as shown in Figure 4-6.

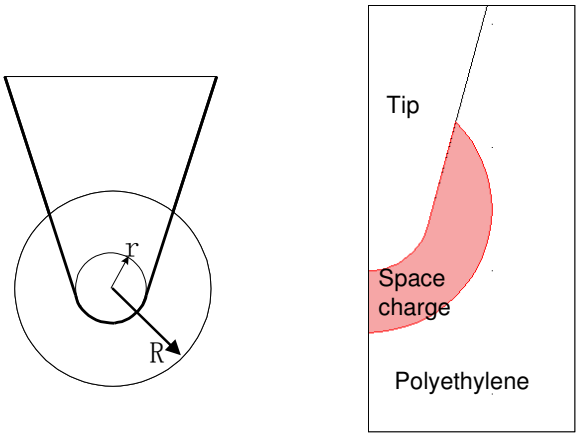

Figure 4-6 Charge confined in spherical region: (L) Geometry; (R) model in COMSOL

A. The influence of charge density (+*q*)

It is temporally assumed here that space charge is uniformly distributed in the confined spherical region, although its value is difficult to quantify. However, its maximum charge density occurs when the total effect field stress at the needle tip approaches zero, since the role of homo-space charge is to reduce the total effective field, and any further increase in space charge density will result in the reversal electric stress. With increasing space charge density, the maximum electric stress moves from the needle tip to the edge

of the space charge region. Figure 4-7 shows the effects of space charge occurrence on the electric field distribution.

The potential barrier formed at the interface between the electrode and dielectric material influences the level of injected charges. The barrier is governed by electrophysical properties of the interface such as the work function of the electrode metals or semiconductors, and surface traps of the dielectric. Additives and gas phases may affect the work function and surface traps. Figure 4-8 shows the dependence of electric stress on the magnitude of space charge density. All the maximum electric stresses shown in Figure 4-8 occur at the needle tip and a linear relationship holds until the point where further increase in the space charge density will lead the shift in the location where the maximum electric stress from the needle tip to the edge of space charge region.

B. The influence of radius of the charge confined spherical region (*R*)

The extent of the space charge region from the needle tip varies considerably. This may depend on several factors such as the applied voltage, the morphology of the material, temperature, etc. Figure 4-9 shows the effect of size of the space charge region on the maximum electric stress. The effect on maximum charge density is also illustrated in Figure 4-9. Although the charge density required to bring the electric stress at needle tip to zero decreased with increasing charge region, the total charge in this region increased, based on the relationship of $Q = \pi R^2 \cdot q$.

C. The influence of space charge with reversal polarity (-*q*)

It has been reported that electrical treeing can be also initiated when the space charge with reversal polarization exists, implying additional high stress may occur due to the presence of space charge [184]. In order to simulate the reversal effect of space charge on electric stress, the sign of the applied voltage or the space charge can be reversed. And the result is shown in Figure 4-10. Unlike the case of homo-charge where the maximum electric stress occurs either at the needle tip or the edge of space charge region depending on the charge density, here the maximum electric stress always occurs at the needle tip due to the hetero-charge. And the maximum electric stress with reversal polarization effect is significantly higher than that with homo-charge. The electric stress increases

with the increase of either charge density or area of the space charge region (sometimes termed the injecting distance). The maximum stress increases linearly with charge density with the slope which is increasing with the increased region size of the injecting charge.

D. The effect of applied voltage (*V*) on electric stress and charge density

The injection level of space charge is associated with tree initiation voltage in some cases. The relationship between the maximum electric stress and the maximum charge density whose further increase will result in the electric stress at needle tip to be zero via applied voltage is shown in Figure 4-11. It is obvious that two linear relationships have been obtained, and the slope may change with different configuration.

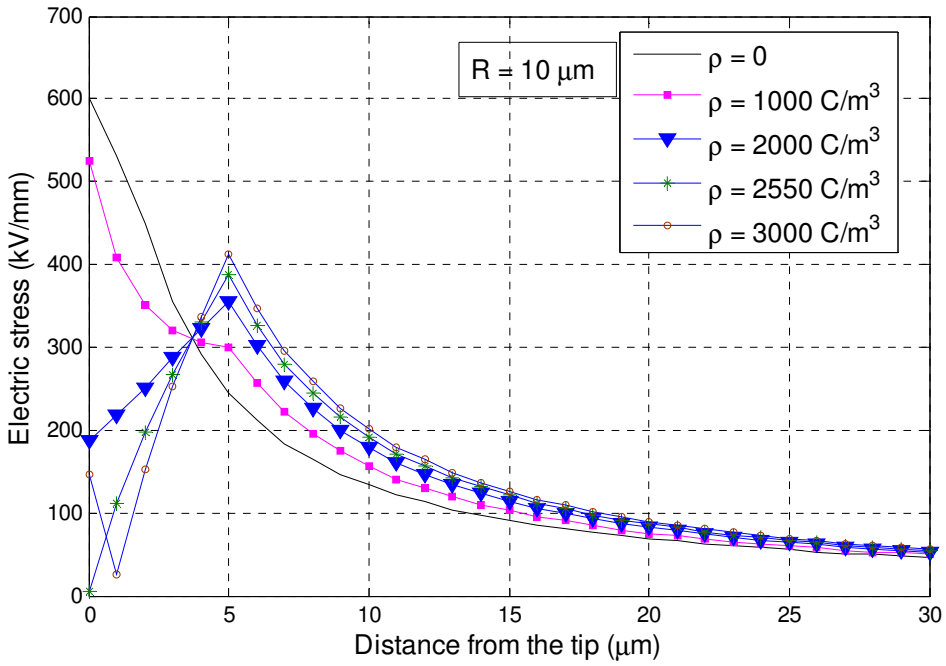

(a)

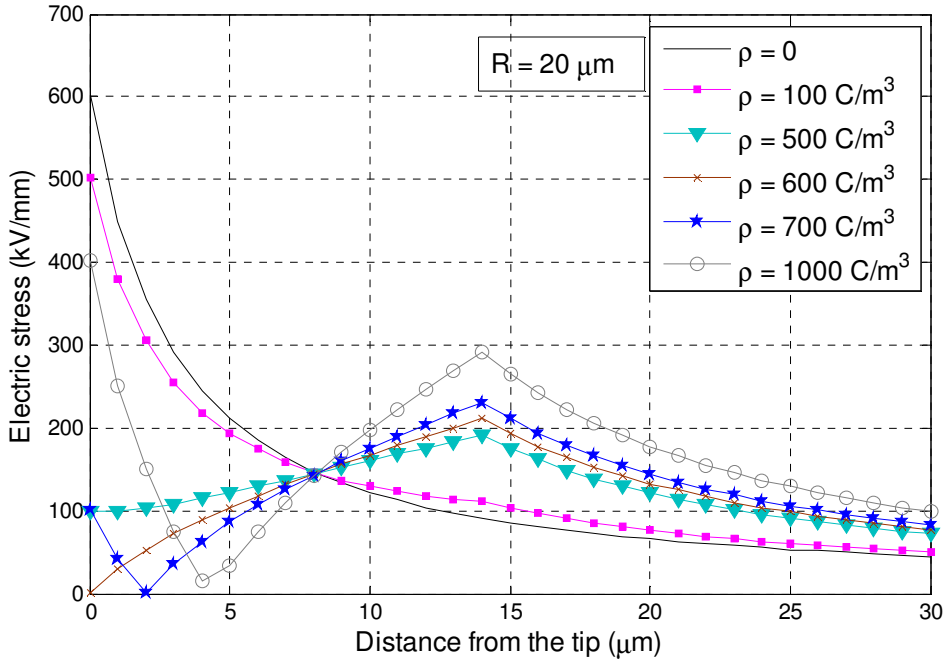

(b)

Figure 4-7 The electric stress changes owing to the presence of space charge: (a) R=10μm; (b) R=20μm (D = 50μm, θ = 30º, d = 2mm, and r = 5μm)

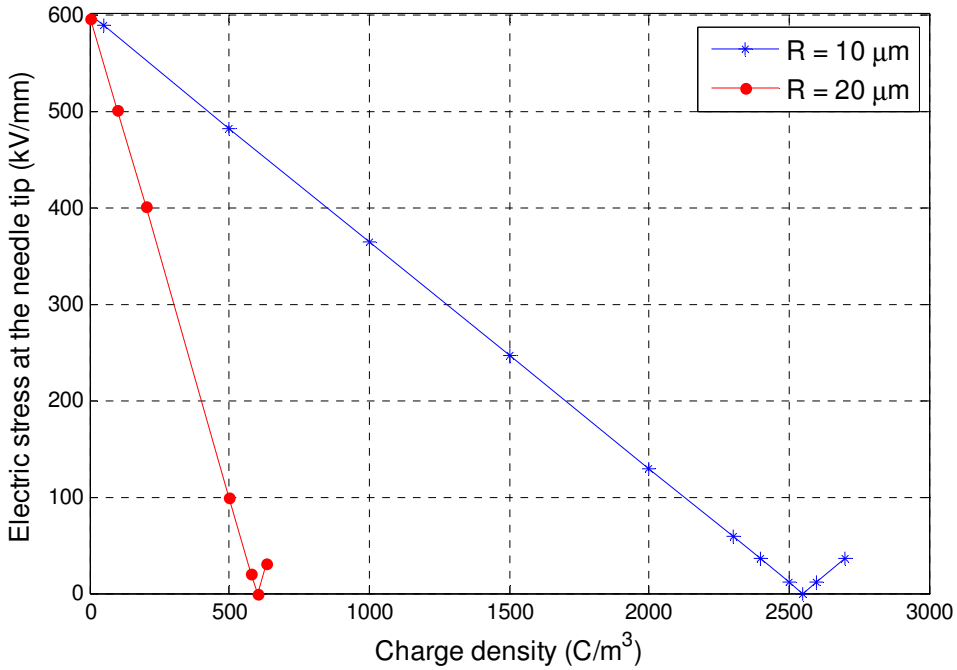

Figure 4-8 Dependence of electric stress on charge density (D = 50μm, θ = 30º, d = 2mm, and r = 5μm)

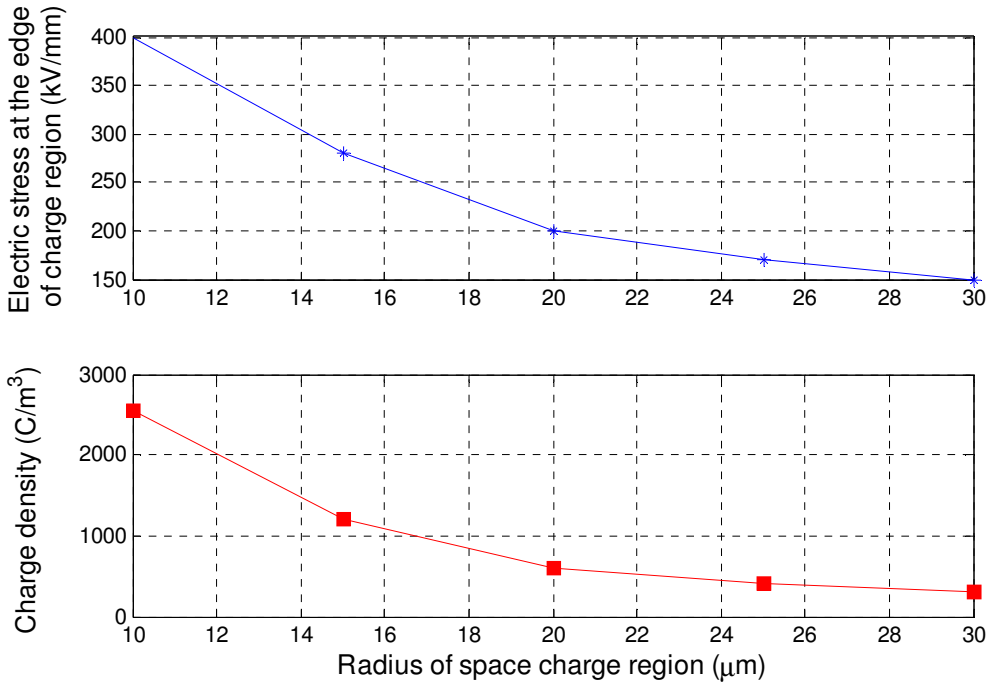

Figure 4-9 Effect of the size of space charge region: (top) on electric stress; (bottom) on charge density (D=50μm, θ =30º, d=2mm, and r =5μm)

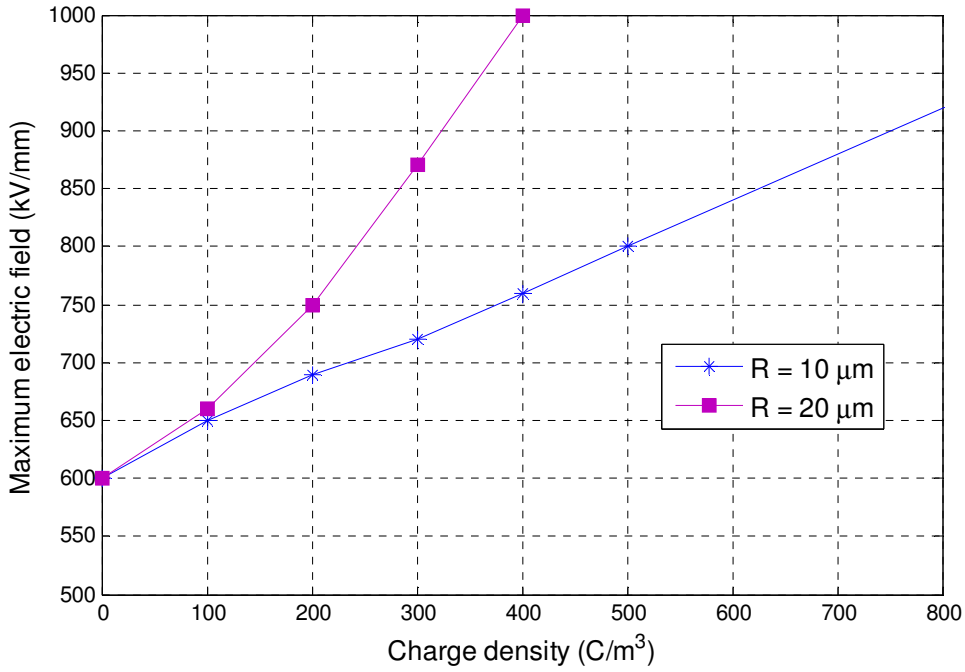

Figure 4-10 Effect of space charge with reversal polarization on electric stress (D=50μm, θ =30º, d=2mm, and r =5μm)

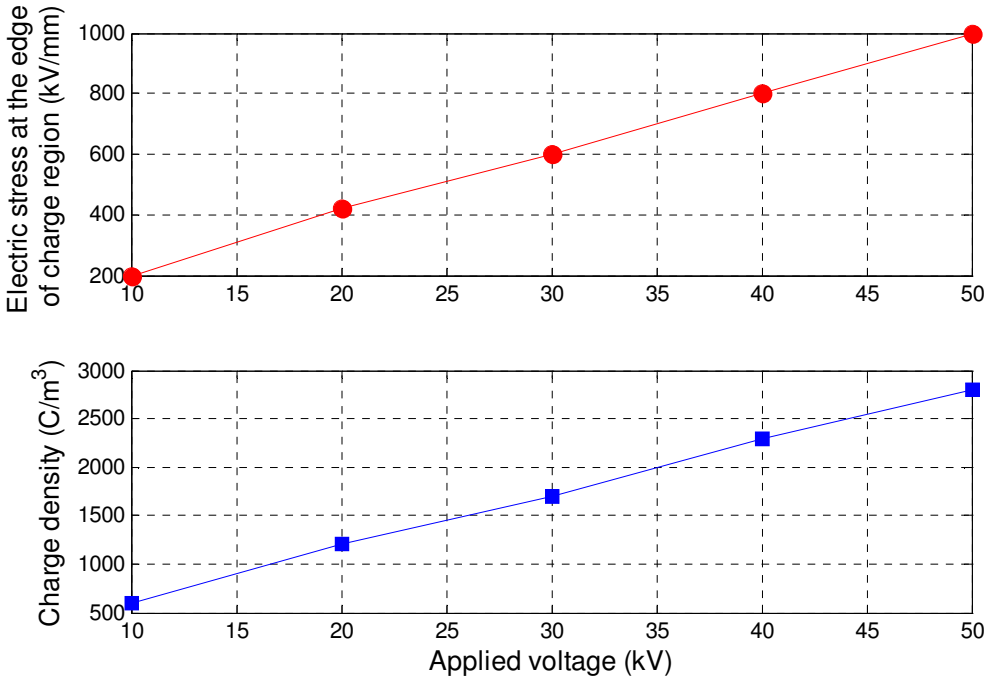

Figure 4-11 Effect of the size of space charge region: (top) on electric stress; (bottom) on charge density (D=50μm, θ =30º, d=2mm, and r =5μm)

4.2 Three cases of electrical tree growth

To simulate the distribution of electric field under the condition of treeing, some parameters were assumed: applied voltage U=10 kV, the radius of needle tip r =50 μm or 100 μm, and the distance from needle tip to ground d=2 mm. Attempts to simulate electrical tree structures are aimed at elucidating those factors in the propagation dynamics which determine the tree shape [3]. Based on Mason's formula as equation (4-1), when $d > 10r$, the E_{max} required for the tree growth can be estimated.

The E_{max} has a linear relationship with voltage U for known dimensions. Similar to the results obtained by using the boundary element method (BEM), the electric stress values obtained by equation (4-1) are generally higher than the values obtained by the FEM method, particularly when the tip radius is less than 5μm [180]. However, as the electrical trees are growing from the needle to the plane electrode, the actual distribution of electric field would change gradually, considering the conductivity of channels and the effect of

space charges. Equivalent circuit method can not efficiently indicate the details at microscopic level, and stochastic model is too complex to separate the influence of each factor from the whole structure.

For efficiency and simplicity, the treeing growth model is abstractly categorized into three cases. They are analyzed here and help investigate the fundamental mechanisms in respect of trees initiation and propagation.

4.2.1 The effect of a conductive particle

Typical examples for those defects possibly leading to treeing are electrode protrusions (representing the defects at insulating / semiconducting interface in practical, since charge injection from field enhancement tips is shown to be the first step in a series of pre-treeing events.), and floating conductive particles (impurities in insulation bulk as probable tree-initiation locations) as well as the assumed conductive tips of electrical tree channels (due to carbon products cumulated on channel walls, which may result new channel growth combined with space charges or high energy carriers if some conditions are satisfied, e.g. the electromechanical force is high enough to overcome the yield stress of insulating polymer). A needle tip, a conductive particle, or a conductive part of a tree channel can be represented by a conductive or metal ball with tens of micron in radius. If this tiny ball has high voltage potential, as shown in Figure 4-12, the highest electric stress occurs at its surface which is the nearest to the ground, and the electric stress profiler changes dramatically along with the distance away from that point toward the plane electrode. Assuming the conductive particle has a potential of 10 kV(rms), the maximum electric stress is 4.5×10^7 V/m for the particle with a radius of 50μm and 2.8×10^7 V/m for that of 100μm. This illustrates that the smaller radius of this ball, e.g. the sharper needle tip, would cause a more serious convergence of electric field. That is why in general trees are initiated from the point electrode of the point-plane configuration. Metal splinter embedded in insulation may affect the inception voltage, because it has sharp edges around which the local field may be high enough to initiate electrical discharges. During the propagation of trees, conductive thermally-decomposed carbon products have also such impact to distort the electric field distribution. For a cable joint, if there is a conductive impurity particle and unfortunately it is at high voltage potential,

it may act as the convergence point of electric stress, thus electrical trees may be initiated there.

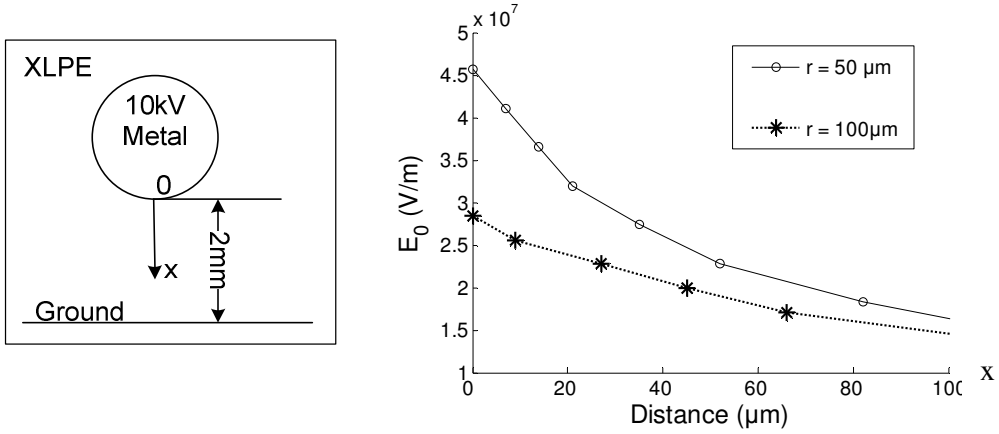

(a) (b)

Figure 4-12 Electric field distortion of Case A - one metal/conductive particle in XLPE: (a) Model of Case A; (b) electric field distortion caused by a high-potential metal / conductive particle *i*-th different radius *r* in XLPE insulation (E_0 is the electric stress).

4.2.2 The effect of gas bubbles around a conductive particle

Trees growing from the larger voids can be clearly distinguished from electrical trees due to metal needles, however small voids of 2 μm or less are not easily detectable and would allow for tree inception fields below the DC breakdown value. A comparison between needles and needle cavities shows that the time to inception is reduced when the cavity is present and that is probably also the case if cracks exist adjacent to the needle. These observations almost certainly reflect the greater ease of generating a destructive discharge/avalanche in gaseous contents of a void or craze than in the polymer.

Similarly, since the channels of electrical trees are proved hollow, for simplicity, they can be considered as a sequence of bubbles or voids. Compared with the electric stress distribution in Case A (r =50 μm), the influences of the size of bubble and its position around a conductive particle were analyzed as shown in Figure 4-13. If the bubble is bigger, the point with maximum electric stress will move farther forward to the ground. For the bubbles with radii of 20 μm and 50 μm in Figure 4-13 (b), the locations of maximum stresses are around 40 μm and 100 μm, respectively. In other words, E_{max} moves to the point of the bubble's edge nearest to ground. The location of a bubble,

however, has a slight effect on the electric field, even though the bubble with bigger angle (θ) or farther away from ground could slightly ease the stress concentration. As shown in Figure 4-13 (c), regardless of the angle, 0°, 45° or 90°, the maximum stress location is always at the surface of the bubble which is the farthest point from that conductive particle. Therefore it is not the location but the size of a bubble that can significantly influence the distribution of electric field. The electric field distortion may become more serious due to either the E_{max} point nearer the ground or the bigger-size bubbles generated in tree channels. Thus trees will be continually growing more easily. In addition, any bubble contacting with a conductive particle such as carbon product attached on the channel may produce a new site with higher electric stress and nearer to ground, given that the conductive particle has a high enough potential. Such hopeful new-born point can possibly initiate a new channel of trees.

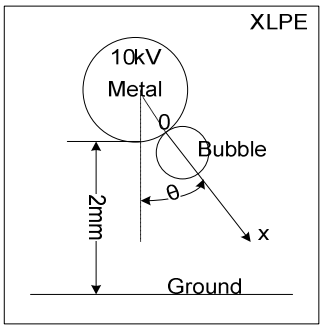

(a)

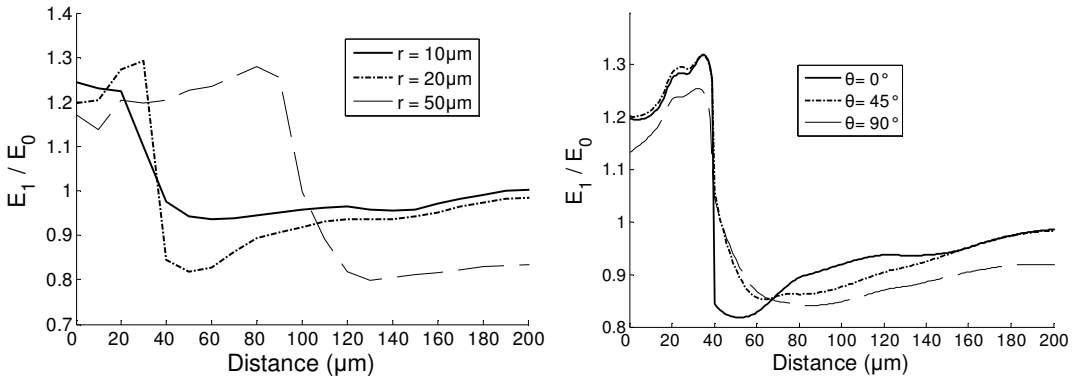

(b) (c)

Figure 4-13 Electric field distortion of Case B-one metal particle & one bubble in XLPE: (a) Model of Case B; (b) electric field distortion caused by a bubble with different radius, r μm, contacting with a 50 μm-size conductive particle at high voltage potential; (c) the

influence of bubble position, θ on field distortion (E_1 is the actual magnitude of electric stress).

Partial discharges occur in the gaseous contents of microscopic voids when the field exceeds a threshold value depending upon the void size and gas pressure (about 3×10^6 V/m in the largest air-filled voids at atmospheric pressure). Erosion of the internal surfaces of the void by high energy ions and molecules produced in the discharge may be followed by the formation of a filamentary pattern of channels penetrating the polymer. This defect then acts as an electrical tree with repetitive discharges causing it to grow, possibly amalgamating with other such discharge centers and eventually initiating a runaway breakdown process.

4.2.3 The effect of two bubbles, one with space charges inside

When electrical trees are examined in detail it is found that they consist of connected channels (i.e. hollow tubules) a few microns in diameter, with branches tens of microns long. The walls of the channels are not always carbonized and only weakly conducting. To model it, let two micro bubbles are located consecutively, in one of which space charges are assumed uniformly distributed, although it is not realizable in practice. It is similar to the situation that partial discharges burst in the channels of trees. As shown in Figure 4-14, the electric stress at the center of the bubble, either 50 μm- or 100 μm-bubble is zero, since the space charges are uniformly distributed in the bubble. And the location with the highest electric stress is exactly the nearest-to-ground point of that bubble, e.g. x = 100 μm and 200 μm, respectively. The accumulation of space charges in insulation can influence the distribution of electric field. The external field is distorted by the internal field due to space charges and they superpose each other to produce the effect field. The electric stress is intensified at the parts of each tree channel where the space charges build up, thus electrical trees grow continually or new branches are generated. It is more evident in bush-branch trees of solid dielectrics, where the bush tree appears to act as a secondary electrode which initiates a branch-type tree from selected tips (sites) on its surface rather from a metal electrode [3]. Furthermore, there is also a reciprocal influence between two different paths of trees. During branch-type trees are changing into bush-type trees, the increase rate of tree size slows down, but the density becomes higher.

Regarding the properties of the model, it shall be noted that it does not cover all physical aspects, among which are the formation of space charges and specific conductivity of tree channels. Additionally, it should be mentioned that the simulations are in a 2D range, whereas the experiments take place in a 3D volume.

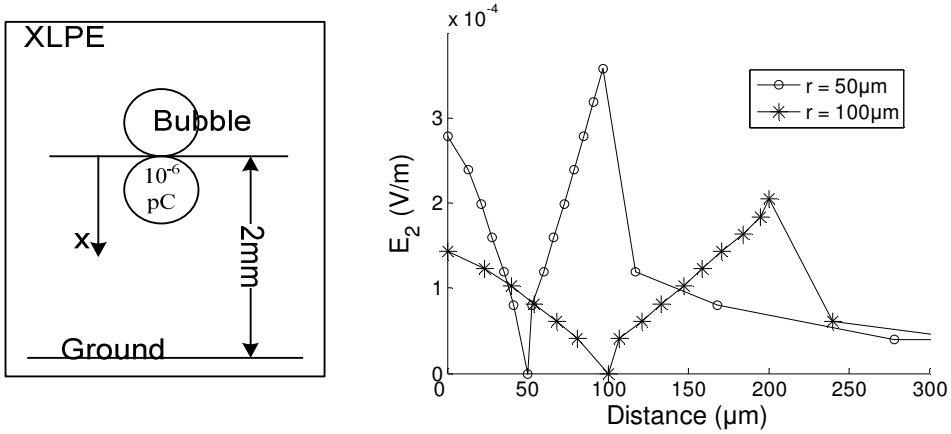

(a) (b)

Figure 4-14 Electric field distortion of Case C - two bubbles, one of which containing space charges: (a) Model of Case C; (b) electric field distortion caused by space charges in bubble (no external electric field, E_2 is the actual magnitude of electric stress).

4.3 The influence of nonlinear conductivity

So far, the conductivity of XLPE is considered as a constant independent of the field. However, it is not true in practice. In order to simulate accurately in high field dielectric, the function for the conductivity vs. electric field must be reasonably accurate in the region of space charge-limited field (SCLF). S. Boggs [132] has contributed a lot on the formula description of conductivity of polyethylene. In his research, comparing the measured charge with the computed charge as a function of applied voltage provides a way to gain insight into the field-dependent conductivity over a range of field [185]. Thus, three typical equations for conductivity which results in about the same SCLF (field at which $\sigma(E,T)=\varepsilon\omega$) are applied in the following simulation, corresponding to equation (2-20) (a) to (c). Rewrite them here:

$$\sigma_1(E,T) = \frac{62.64}{|E|}\exp\left(\frac{-6946}{T}\right)\exp\left(1.1408\times10^{-7}|E|\right) \quad (a)$$

$$\sigma_2(E,T) = \frac{2.025\times10^{-6}}{|E|}\exp\left(\frac{-4066}{T}\right)\exp\left(2.103\times10^{-3}\sqrt{|E|}\right) \quad (b) \quad (2\text{-}20)$$

$$\sigma_3(E,T) = \frac{1.12\times10^{-5}}{|E|}\exp\left(\frac{-6946}{T}\right)\exp\left(6.307\times10^{-2}\sqrt{|E|}\right) \quad (c)$$

Normally the electric field is solved through time stepping with a time dependent applied voltage. During this process, the charge on one of the electrodes is computed using Gauss' Law. Those data can be obtained which are dependent on the conductivity as a function of field and even temperature over a range of field near the SCLF. In COMSOL, the electric field $E(r,z)$ is coupled by the temperature $T(r,z)$ through the power dissipation $P = J \cdot E$, i.e. two analysis modules are selected to do the transient finite element computation for electric field distribution and thermal diffusion in an axial symmetry (2D) dimension.

To do the electro-thermal coupled transient nonlinear finite element analysis, the dielectric is modeled with thermal property parameters for typical polyethylene, i.e. mass density of $920\,\text{kg/m}^3$, heat capacity of $2170\,\text{J/(kg}\cdot\text{K)}$, and temperature-dependent thermal conductivity of $0.335 - 8.75\times10^{-4}\cdot(T-293)\ \text{W/(m}\cdot\text{K)}$. The heat capacity and density can also be made temperature and/or electric field dependent, which is useful for example to accommodate a phase transition such as melting of the crystallites of XLPE around $100\ ^{\circ}\text{C}$. However, the latter two parameters will be set as a constant in this work.

Thus, the following computation should satisfy

$$\begin{cases} -\nabla\cdot\partial(\varepsilon_0\varepsilon_r\nabla V)/\partial t - \nabla\cdot(\sigma\nabla V - \vec{J}^e) = 0 \\ \rho C_p \partial T/\partial t - \nabla\cdot(k\nabla T) = Q \end{cases} \quad (4\text{-}3)$$

in sub domain, where V is electric potential, ε_r relative permittivity, σ electric conductivity, J^e external current density (zero assumed here), ρ mass density, C_p heat capacitance, k thermal conductivity, and Q heat source ($= E\cdot J = \sigma E^2$).

And the boundary conditions are

$V = V_s$ on the needle tip;
$V = 0$ at the ground electrode.

where V_s is the applied voltage in each analysis.

4.3.1 Space charge-limited field (SCLF)

The concept of space charge-limited field (SCLF) is fundamental to thinking about dielectrics at very high fields [132]. In the pioneering study by Hibma and Zeller [134], they base their analysis on the assumption that the space charge-limited field is fixed, and in a highly inhomogeneous field geometry, the SCLF does not increase with applied voltage above the critical voltage at which the SCLF is reached at the tip of the stress enhancement. This assumption corresponds to a material in which the conductivity goes from a very small value to essential infinity at the space charge-limited field, i.e. the conductivity form as shown in equation (2-20). For this assumption, the field on the surface of a stress enhancement is independent of the applied voltage. Figure 4-15 confirms such assumption under "DC" conditions which is realized by waiting a relatively long time i.e. 300 s after a step voltage (1 s rise time) is applied on the needle electrode. With different applied DC voltage but same equation of conductivity, the electric field is limited to around 240 kV/mm near the needle tip for the predefined model (needle tip radius $r = 5\,\mu\text{m}$). And the details of conductivity has little influence on the electric field as can be seen in Figure 4-16 where the differences of electric stress and SCLF range are not so much as 25%. Thus, above the threshold voltage, application of Gauss' Law to the stress enhancement surface will result in a surface charge that is independent of applied voltage.

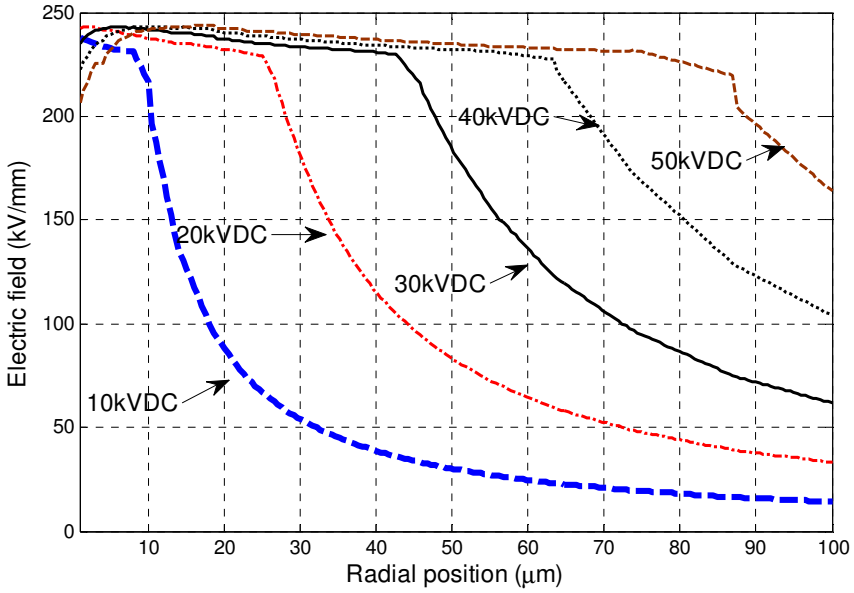

Figure 4-15 Electric field vs. radial position for the conditions: needle tip radius $r = 5\,\mu\text{m}$ and conductivity $\sigma = \sigma_1$

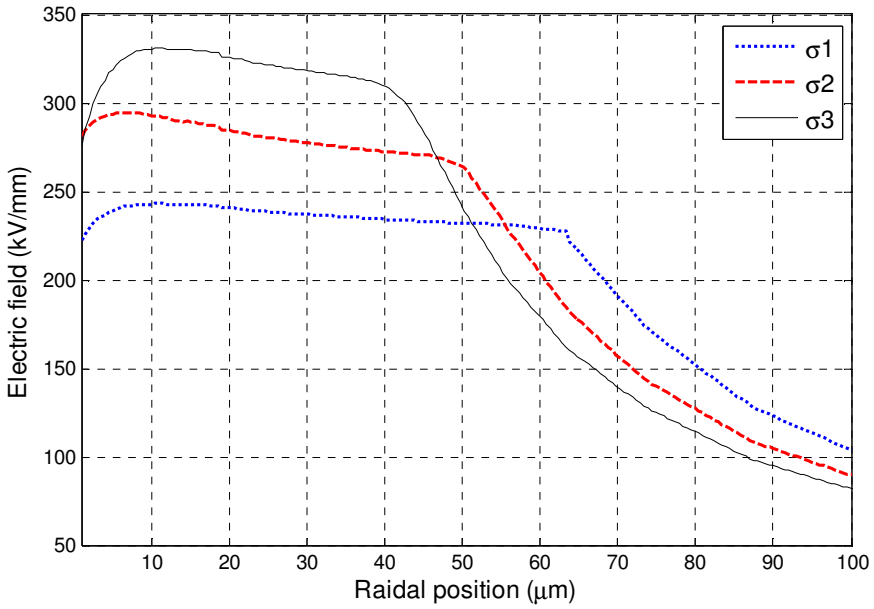

Figure 4-16 The influence of conductivity on the electric field distribution when 40 kVDC is applied at the needle electrode

4.3.2 Triangular waveform

In reality, the field at the stress enhancement surface does increase slowly as a function of applied voltage above the critical voltage as the transition between low and high conductivity is not abrupt. If the field distribution is computed accurately using transient nonlinear finite element analysis and realistic models for the field-dependent conductivity even coupled with thermal effect later, the charge on the tip region of a stress enhancement can be determined through application of Guass' Law. In computation, the electric field with space charge effect (Poisson's Equation) is considered as the composition of the Laplace field (Laplace's Equation) and the field induced by space charge. While the space charge-limited field does not increase as a function of the applied voltage, the radius to which the space charge-limited field extends from the stress enhancement does increase with the applied voltage.

To analyze the time-dependent effects of rising and falling of applied voltage at the needle tip, similar to the analysis in charging and discharging phenomena, a simple voltage waveform with linearly rising and falling part is considered. Here, it is called "triangular" waveform. This triangular waveform can be defined by

$$\begin{cases} V = \dfrac{V_p}{t_0} \cdot t & 0 \le t < t_0 \\ V = V_p - \dfrac{V_p}{t_0} \cdot (t - t_0) & t_0 \le t \le 2t_0 \\ V = 0 & t > 2t_0 \end{cases} \tag{4-4}$$

where V_p is the peak value of applied voltage and t_0 is the transition time of rise part and fall part of the applied voltage. Here, $t_0 = 5\,\text{ms}$.

Figure 4-17 shows the SCLF independent of the waveform peak besides the increasing SCLF radius with increased voltage of triangular waveform, similar to the situation under "DC" condition. Figure 4-18 shows the calculated space charge distribution corresponding to the Poisson's equation where the electric field is obtained from the difference between the total electric field as shown in Figure 4-17 and the Laplace field. The critical voltage or threshold voltage, V_c for SCLF is lower than the applied voltage

value before *t*=2.5 ms, i.e. lower than ½ of V_p, because at the time of 2.5 ms, there has already occurred SCLF as shown in Figure 4-19. Figure 4-20 shows the transient nonlinear finite element simulation results of the electric field distribution due to the space charge polarity reversal under the unipolar pulse. At the most near point $(r, z) = (0, -2\,\mu\text{m})$ to the needle tip, the electric field polarity reverses from +200 kV/mm to -200 kV/mm after the time of $V = V_p$, while it is reversed to a lower anti-polar field at farther position. This indicates that if the applied unipolar voltage is more than twice the threshold voltage for the SCLF, then as the voltage drops, the field at the tip reaches the opposite polarity SCLF, at which point the high carrier mobility will result in reversal of the space charge in the region of SCLF.

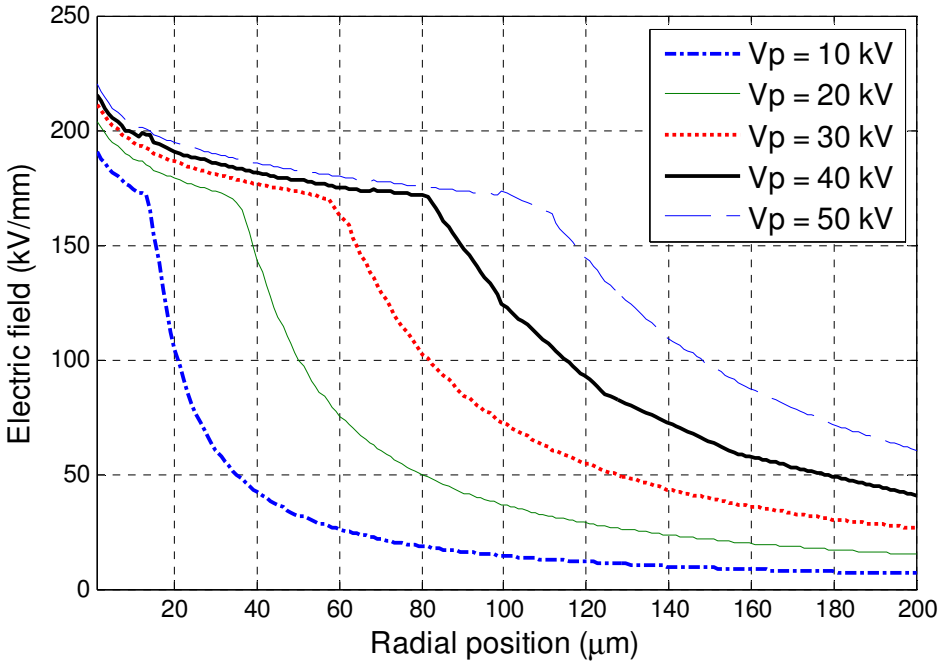

Figure 4-17 The electric field distributions at the times of $t = t_0$ for various V_p

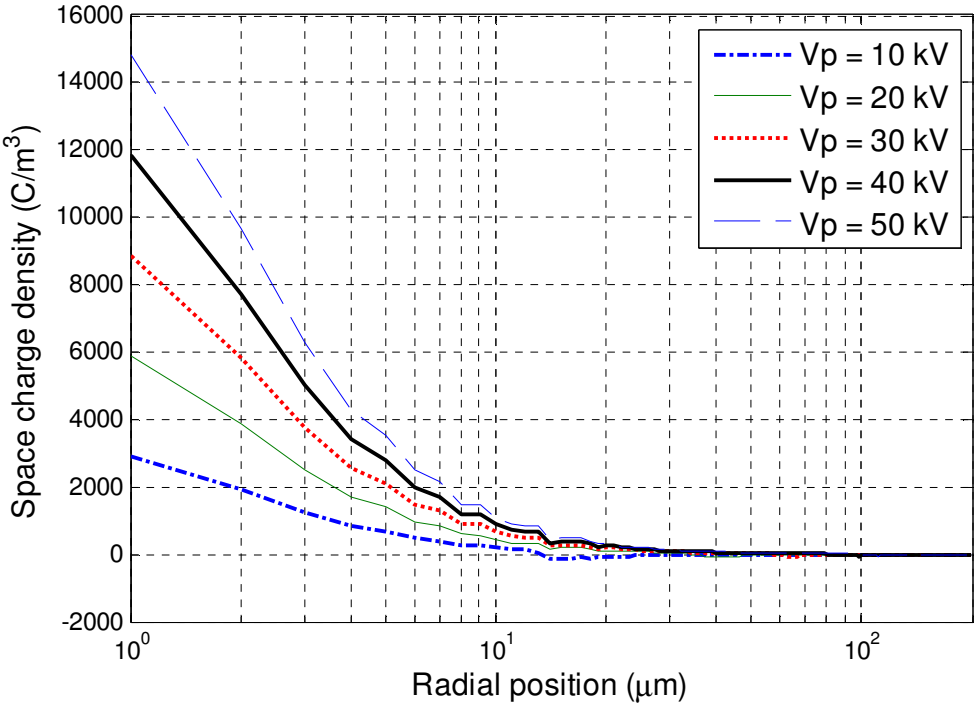

Figure 4-18 The space charge distribution at the times of $t = t_0$ for various V_p

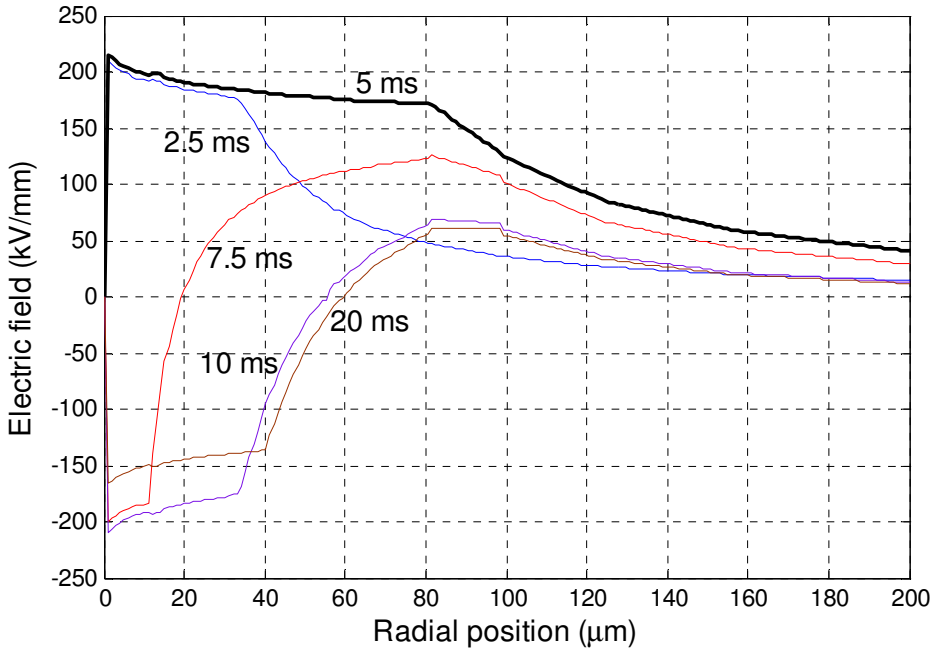

Figure 4-19 The electric field distribution vs. radial position at different time, t ($V_p = 40\,\text{kV}$ and $t_0 = 5\,\text{ms}$)

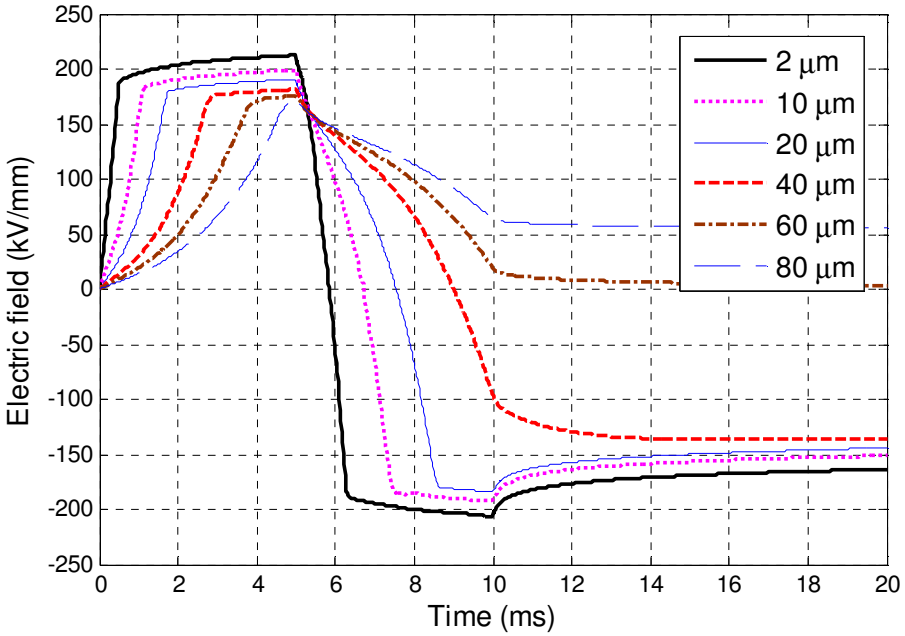

Figure 4-20 The electric field vs. time for various radial positions on the axis of symmetry ($V_p = 40\,\text{kV}$ and $t_0 = 5\,\text{ms}$)

4.3.3 AC waveform

Extending the triangular (unipolar) waveform to the situation of a sequence of continuous sine wave, the AC sine (bipolar) waveform of power frequency is defined by

$$V = Vp\sin(2\pi ft + \varphi_0) \tag{4-5}$$

where $V_p = 40\,\text{kV}$, $f = 50\,\text{Hz}$ and $\varphi_0 = 0$.

Applying the AC waveform at the needle tip, when the SCLF is reached, charge starts to be injected from the needle tip into the dielectric. The electric field "pushes" this charge away from the needle tip which causes a force on the dielectric. The force is normally negative, meaning that the force is away from the high field electrode. Figure 4-21 and Figure 4-22 show that the charge reverses most quickly near the needle tip, and the field reversal spreads out therefrom. As shown in Figure 4-23, because the field reverses before the space charge density does in each half cycle, the force density reverses, as well. For a bipolar waveform, the field at the needle tip reverses from the SCLF to that of the opposite polarity. This is followed by charge transfer from the tip which causes the

space charge density to reverse from the tip outward. Thus at some points in this process, the space charge and force at the tip will be of one polarity, while the space charge and force at some distance away from the tip will be of the opposite polarity. Figure 4-24 shows the reversal procedure of space charge density which is a little earlier than the timing of 10ms when the polarity of potential at the needle tip is being reversed. The force reverses near the needle tip before the force further away from the needle tip is going to reverse, which will place the polymer in tension. Under AC conditions, this sequence of events repeats every cycle and causes a complex, time dependent mechanical stress distribution within the dielectric which undoubtedly plays a role in cavity formation at the tip of stress enhancement as the polymer is weakened by bond scission resulting from interaction with UV photons and hot electrons [133].

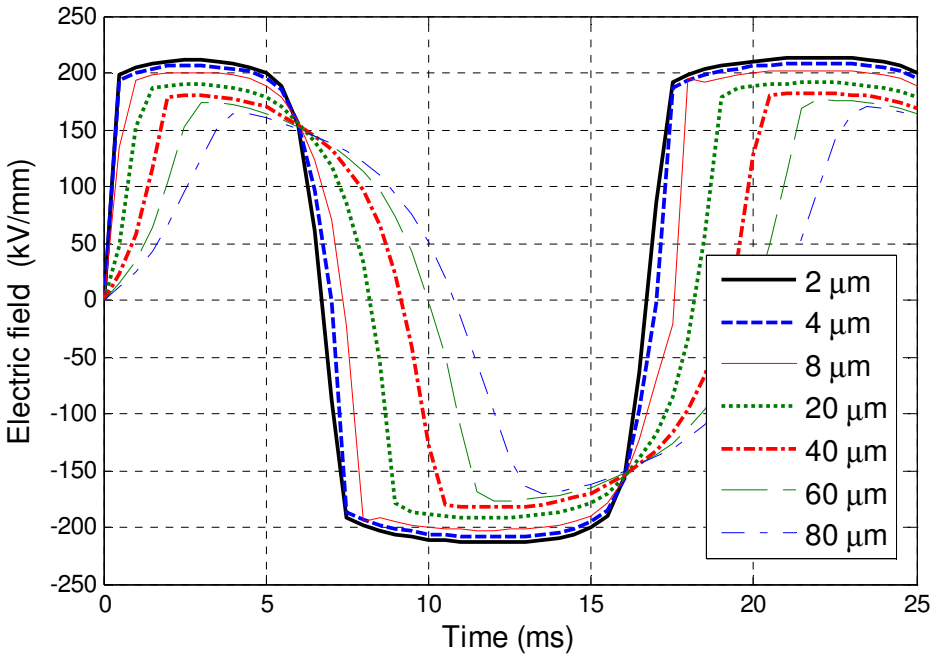

Figure 4-21 The electric field vs. time for various radial positions from the needle tip ($r = 5\,\mu\text{m}$) to ground electrode

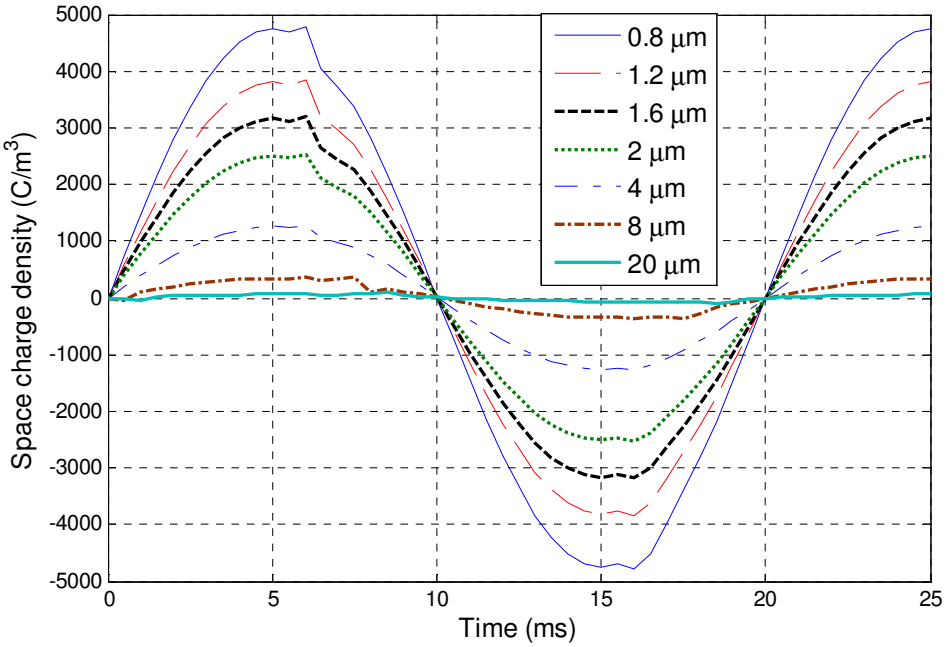

Figure 4-22 The space charge distribution vs. time for various radial positions from the needle tip ($r = 5\,\mu\text{m}$) to ground electrode

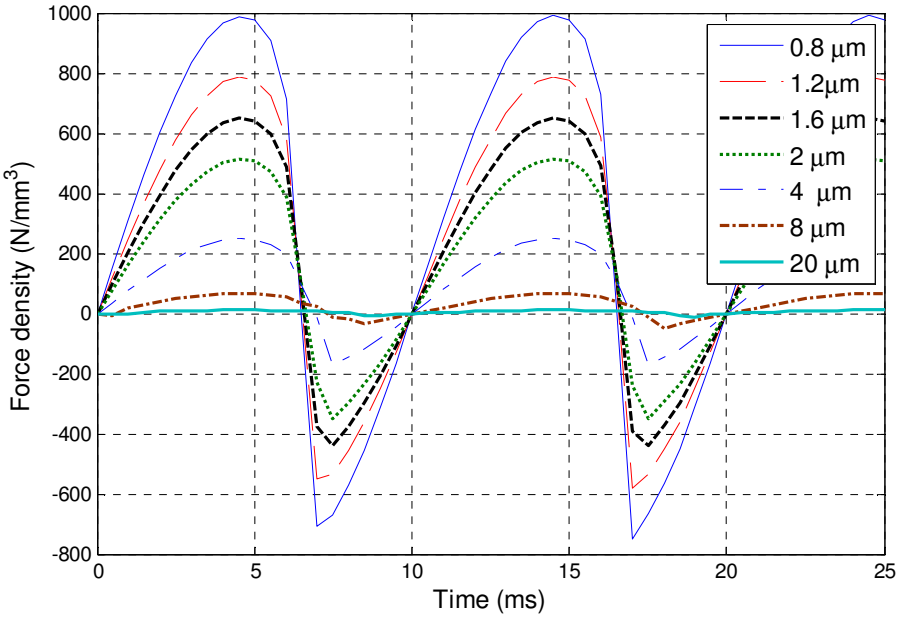

Figure 4-23 The force density vs. time for various radial positions from the needle tip ($r = 5\,\mu\text{m}$) to ground electrode, which is the product of electric field in Figure 4-21 and space charge density in Figure 4-22.

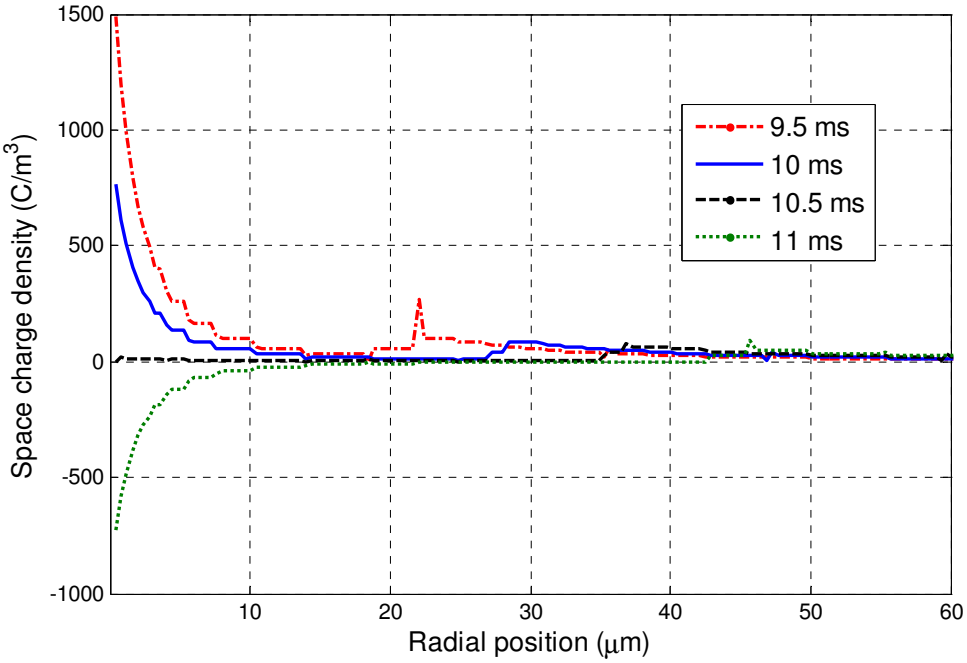

Figure 4-24 The polarity reversal of space charge with the polarity reversal of electric field

4.3.4 Temperature rise

So far, the temperature effect is ignored since the temperature rise is too small to be considered for ms scale waveform because the power frequency scale is long enough for thermal diffusion to limit the temperature rise to lower than 1K for the 5 μm needle tip. Thus to make the temperature effect become substantial, high frequency waveform is specially applied. Three voltage waveforms have been investigated: a) a step wave with rise time of 10 ns (10% to 90%); b) a step wave with rise time of 100 ns (10% to 90%); and c) a step wave with rise time of 1200 ns (10% to 90%) which is to simulate a standard lightning impulse with a rise time of 1.2 μs (10% to 90%) and a tail of 50 μs (to 50% amplitude). All the three waveforms can be defined by [138]

$$V(t) = \frac{V_p}{2}[1 + \tanh(\frac{t}{0.45 \times t_r} - 3)] \tag{4-6}$$

where V_p is the peak voltage and t_r is the rise time in seconds. Here, $V_p = 40\,\text{kV}$ in order to keep consistent with former computations, and $t_{r1} = 10\,\text{ns}$, $t_{r2} = 100\,\text{ns}$ and

$t_{r3} = 1200$ ns . $\sigma(E,T)$ is a function of electric field and temperature as in equation (2-20). In COMSOL, the electric field $E(r,z)$ is coupled by the temperature $T(r,z)$ through the power dissipation $P = J \cdot E$.

As shown in Figure 4-25 and Figure 4-26, different equations of conductivity cause no much difference for the temperature rise, meaning that the equation detail will not influence the temperature effect very much. Peak temperature always occurs somewhat off the tip, as the metallic needle acts as a heat sink. With the time, the temperature increases rapidly even about a rise of 30 K in 15 ns and up to almost 100 K in 100 ns, which is the situation for a 5 μm-radius effect. The total power dissipation is relatively independent of the pulse rise time. However, for waveforms with different rise time, the 10 ns-rise time waveform results a maximum temperature rise of about 100 K, 90K for 100 ns waveforms and 70 K for 1.2 μs waveform, indicating that the maximum temperature rise drops slower for the waveform with a longer rise time, which has a relationship with the limited power diffusion speed. Then consider the needle tips with different radii, as shown in Figure 4-27, the defect with a larger radius (10 μm) can cause a lower temperature rise. Note that the significant temperature rise is likely to cause a shock wave in the polymer. Change of 100 K in 10 ns must have a substantial mechanical impact. For the case, the mechanical stress is dominated by thermal expansion rather than field-induced forces, and can reach to the value which is comparably with the yield stress of XLPE [133].

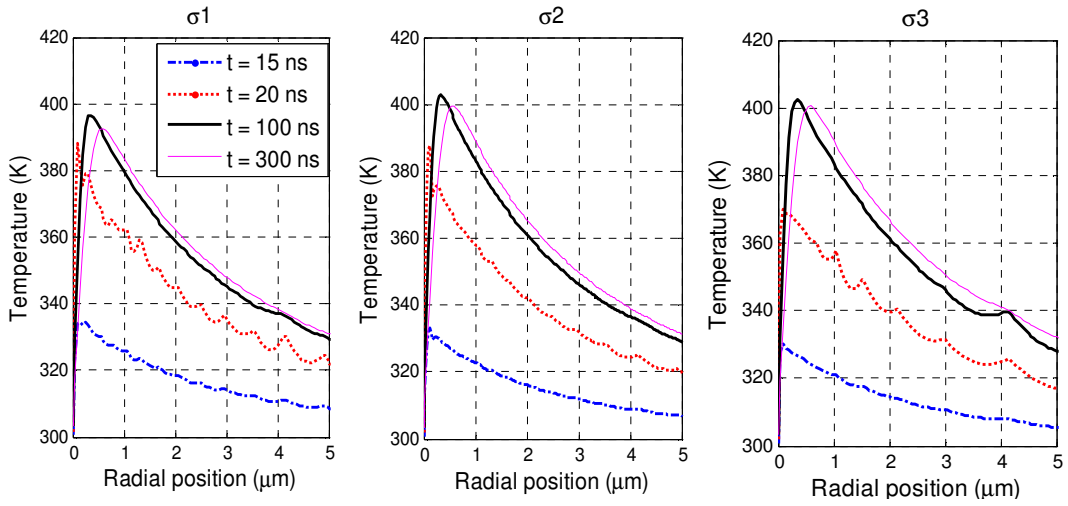

Figure 4-25 The temperature profiles on axis at various times during application of a 10 ns-rise time step wave for $\sigma(E,T)$ corresponding to equations (2-20) (a)-(c)

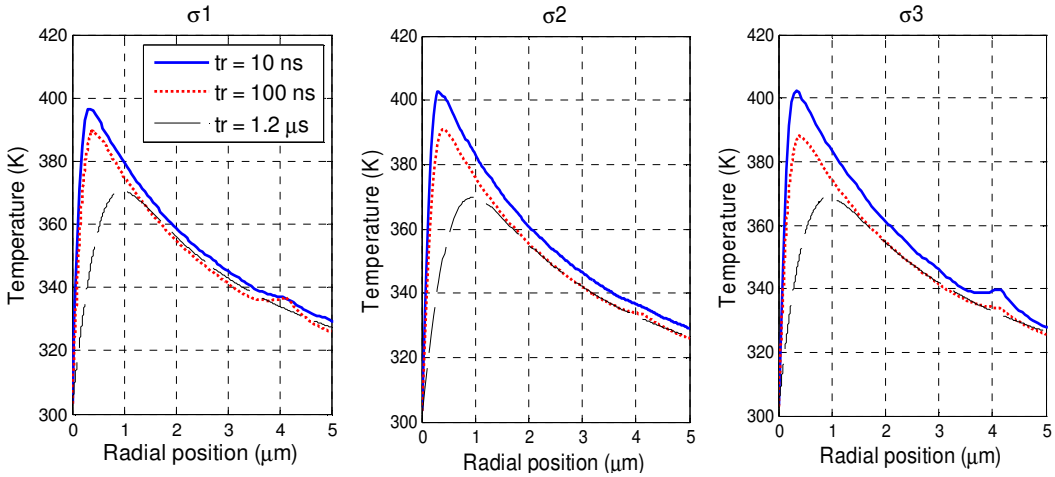

Figure 4-26 The temperature profiles near maximum temperature rise on axis for waveforms with rise times of 10 ns, 100 ns and 1.2 μs for $\sigma(E,T)$ corresponding to equations (2-20) (a)-(c)

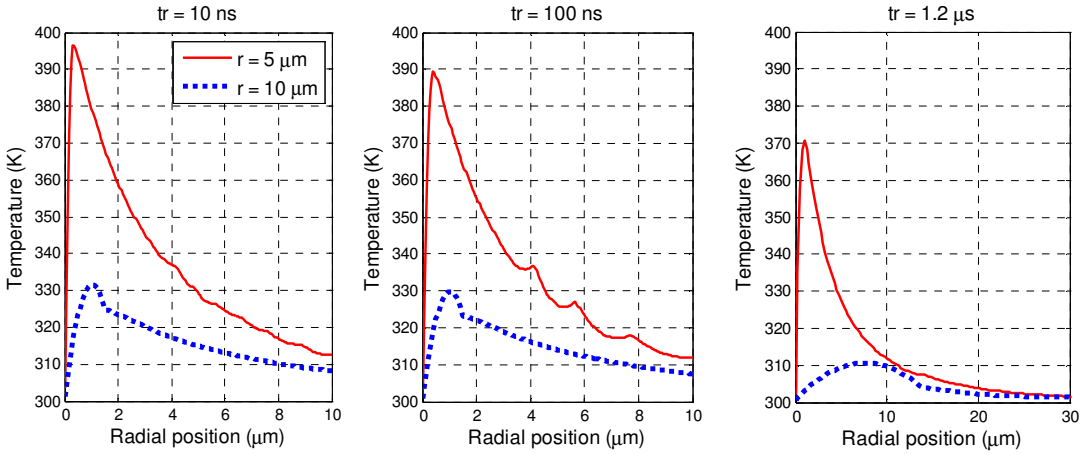

Figure 4-27 The temperature profiles near maximum temperature rise vs. radial position on axis for various tip radii of 5 μm and 10 μm waveforms with rise times of 10 ns, 100 ns and 1.2 μs ($\sigma = \sigma_1$)

4.4 Bipolar charge transport

An understanding of space charge accumulation and its link to dielectric breakdown would be a major scientific achievement as well as facilitating the prediction of cable lifetime and the design of better cables. The above discussion demonstrates that the

electric field distribution under highly inhomogeneous field conditions can be predicted with reasonable accuracy from simple, first principle arguments and more accurately through numerical computation. Such predictions are based on a phenomeno-logical model of conduction. The theoretical description of high field conduction is based on "hopping theory" which assumes "traps" in the range of 1 eV deep with a mean separation in the range of 3 nm. Nevertheless, the space charge accumulation and the related trapping-detrapping phenomena are still poorly understood. Over recent decades, a great deal of effort has been expended in developing experimental tools for space charge characterization [184, 186] in measuring space charge profiles [169, 181] or in identifying the different kinds of charges [73, 187]. Meanwhile, only a few attempts have been made to provide some model description of these experimental results [188-192]. Polyethylenes are semi-crystalline materials, with complex chemistry, and with ill-defined trapping and conduction processes. The approach to develop electrical transport modeling associates experiment and numerical simulation [189, 192, 193] from molecular to macroscopic scale [129]. The glaring deficiency in present understanding is a theoretical basis for such "traps". One possibility is that the random variation in backbone separation in the amorphous region of a polymer provides the barriers at the relevant density which limit conduction.

The approach aims at modeling charge transport phenomena in a synthetic insulator largely used in the high voltage area: polyethylene. The aims are to account for the internal distribution of field as a function of stress, which could be used in the future to feed aging models, since, whatever the aging scenario considered, the local field is an important parameter. The transport model must be able to account for the distribution of electric charges (and of electric field) in non-stationary situations. The approach must be general enough to be applicable to a wide variety of insulators.

The nature of charge carriers in polyethylene is generally approached by considering two kinds of phenomena: the transport of electrons and holes through localized states in the forbidden gap, and the transport of ionic charges due to migration of charge species that are not chemically linked to the macromolecules [3, 129]. The wide variety of phenomena at play and the small amount of data and tools for describing it are really

severe handicaps for modeling transport. In this section, bipolar charge transport phenomenon is analyzed regarding to different hypotheses on the trap distribution.

4.4.1 Bipolar charge transport model

At high fields, the carriers are almost certainly electrons. Given the fact that XLPE is symmetric with regard to positive and negative voltage on a guarded needle tip to space charge densities of at least 3000 C/m^3, there must be plenty of charge available in the polymer and without charge injection. However, in this computation, the free carrier concentration at high fields is assumed only dependent on the amount of injection. Injected carriers become trapped and form space charge regions, thus they modify the local fields and the steady-state current. The carrier mobility is low and governed by field-dependent transport between traps. A major difficulty of charge transport modeling lies in the description of carrier mobility. Charge transport within insulating polymers is often described by a hopping mechanism in which carriers move from site to site by getting over a potential barrier. The most widely used principle for describing charge transport in polymer insulation is to consider a trap-controlled mobility. Carriers move within bands and can be trapped in shallow sites in which they are still in interaction with bands. This scheme amounts to considering an effective mobility of the form

$$\mu_{eff} = \mu_b \exp(-\frac{W'}{k_B T}) \tag{4-7}$$

where μ_b is the band mobility and W' is the depth of shallow traps. This formalism was initially proposed by Mott and Gurney [194]. The approach is justified by the existence of two kinds of traps in polyethylene: conduction sites due to topological disorder and trapping sites related to chemical disorder, the respective depths being more than 1 eV apart.

The cells used for computation are shown in Figure 4-28. The Cell Type A is applied for a typical two-parallel electrode system, which is widely used in charge transport modeling [189, 192, 193]. The applied voltage will provide a uniform electric field as the initial condition. The 1D model with such cell is set up in a rectangular coordinate system, where x is a component of (x, y, z). Referring to the applications of such cell in 1D modeling for coaxial cables [195] and needle-spherical electrode system [196], a new

type of cell, Cell Type B, is designed especially for the needle-plane electrode geometry where stress concentration will occur near to the anode (needle electrode). Since the distance of two electrodes (2 mm) is very large compared to the radius of needle tip (5 μm), the plane electrode can be considered as a curved shape with an infinite radius. It is realized in a cylinder coordinate system and the x denotes the r component of (r,ϕ,z). Note that the distance between the needle and plane electrodes is 2 mm, and the cell length is 5 μm less for the sake of simplification.

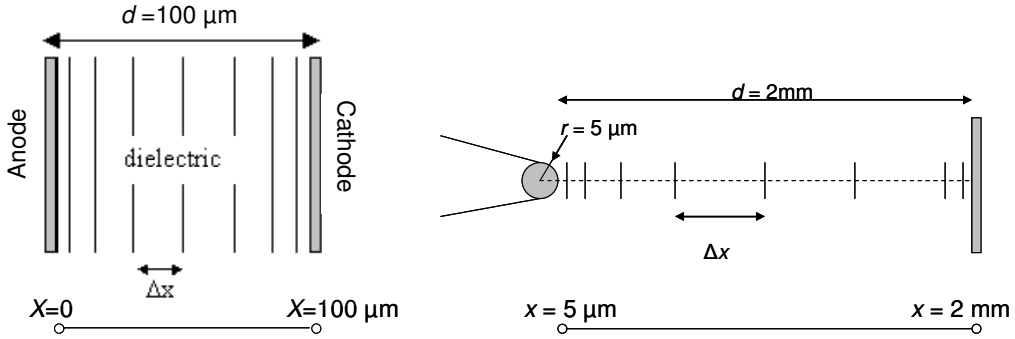

Figure 4-28 Schematic representation of a cell, divided into several elements Δx, tightened next to the electrodes: (L) 1D cell for a parallel electrode geometry (Cell Type A); (R) 1D cell for a coaxial (or needle-plane) electrode geometry (Cell Type B)

The equations describing the behavior of charge carriers, through a one-dimensional (1D) time and space dependent total flux $j(x,t)$ and neglecting diffusion are the following:

Transport equation: $$j(x,t) = \mu E(x,t)\rho(x,t) \tag{4-8}$$

Possion's equation: $$\frac{\partial E(x,t)}{\partial x} = \frac{\sum \rho_i(x,t)}{\varepsilon} \tag{4-9}$$

continuity equation: $$\frac{\partial \rho(x,t)}{\partial t} + \mathrm{SGN}(\rho)\frac{\partial j(x,t)}{\partial x} = s(x,t) \tag{4-10}$$

where μ is the mobility of carriers, ρ the density of mobile species, E the electric field, x the spatial coordinate, t the time, s the source term, and ε is the dielectric permittivity. $\mathrm{SGN}(\rho)$ is 1 for holes and -1 for electrons.

In the following models, we have considered that current originates only from transport of injected carriers. Dipolar contributions have not been dealt with because polyethylene

is normally a weakly polar material, and hence this contribution is expected to be low. Furthermore, current space charge measurement techniques (i.e. PEA) provide limited evidences to support the developed models, attempting to explain space charge accumulation and transient currents by a single process may be misleading. Hence, several approaches are tried in following parts.

4.4.2 Unique deep trapping level ("Model I")

Conduction and trapping clearly cannot both be predicted in a frame where only one energy level is considered. In this approach, the principle of an effective mobility is integrated that encompasses transport phenomena related to shallow traps. Trapping in deep traps is not accounted for in this approach. This approach, which has already been described in several papers [128, 188], is depicted in Figure 4-29.

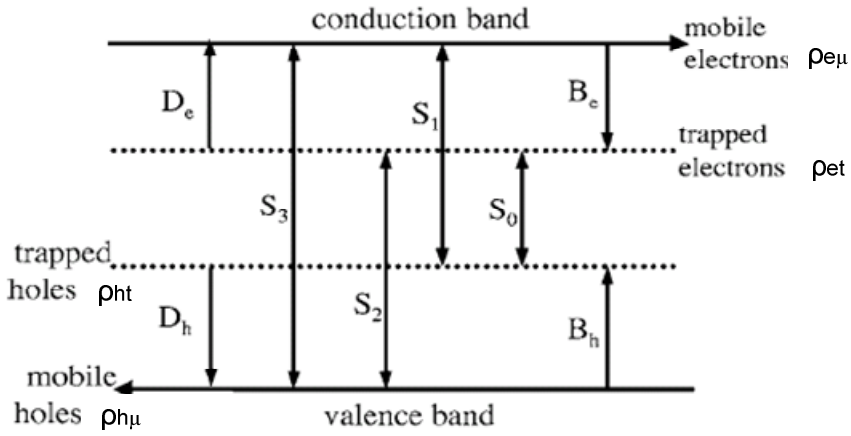

Figure 4-29 Schematic representation of the conduction and trapping coefficients for bipolar charge transport with assumed unique deep trapping level

Trapping phenomena responsible for long lasting space charge are described by a unique deep trapping level [188, 190]. For mobile (or trapped) electrons and holes, the continuity equation is solved as the following set of partial differential equations [128, 189]:

$$\begin{aligned}
&\frac{\partial \rho_{e\mu}(x,t)}{\partial t} - \frac{\partial j_e(x,t)}{\partial x} = -S_1\rho_{ht}\rho_{e\mu} - S_3\rho_{h\mu}\rho_{e\mu} - B_e\rho_{e\mu}(1-\frac{\rho_{et}}{\rho_{0et}}) + D_e\rho_{et} \\
&\frac{\partial \rho_{h\mu}(x,t)}{\partial t} + \frac{\partial j_h(x,t)}{\partial x} = -S_2\rho_{et}\rho_{h\mu} - S_3\rho_{h\mu}\rho_{e\mu} - B_h\rho_{h\mu}(1-\frac{\rho_{ht}}{\rho_{0ht}}) + D_h\rho_{ht} \\
&\frac{\partial \rho_{et}(x,t)}{\partial t} = -S_2\rho_{h\mu}\rho_{et} - S_0\rho_{ht}\rho_{et} + B_e\rho_{e\mu}(1-\frac{\rho_{et}}{\rho_{0et}}) \\
&\frac{\partial \rho_{ht}(x,t)}{\partial t} = -S_1\rho_{ht}\rho_{e\mu} - S_0\rho_{ht}\rho_{et} + B_h\rho_{h\mu}(1-\frac{\rho_{ht}}{\rho_{0ht}})
\end{aligned} \tag{4-11}$$

The coefficients S_i are the recombination coefficients, B_e and B_h are trapping coefficients for electrons and holes, respectively, $\rho_{e\mu}$ and $\rho_{h\mu}$ are mobile electron and hole densities , ρ_{et} and ρ_{ht} are trapped electron and hole densities, and ρ_{0et} and ρ_{0ht} are the trap densities for electrons and holes, respectively. The net charge density is:

$$\rho = \rho_{h\mu} + \rho_{ht} - \rho_{e\mu} - \rho_{et} \tag{4-12}$$

The de-trapping probability is defined by a de-trapping coefficient, for each species, which is of the form:

$$D_{(e,h)} = v\exp(-\frac{w_{(e,h)}}{k_B T}) \tag{4-13}$$

where v is the attempt to escape frequency, which has been set to $k_B T / h = 6.2\times10^{12}$ s^{-1} at room temperature, T is the temperature, and w is the de-trapping barrier.

Injection at the electrodes follows the Schottky law for electrons and holes:

$$\begin{aligned}
j_e(d,t) &= AT^2\exp\left(-\frac{ew_{ei}}{k_B T}\right)\exp\left(\frac{e}{k_B T}\sqrt{\frac{eE(d,t)}{4\pi\varepsilon}}\right) \\
j_h(0,t) &= AT^2\exp\left(-\frac{ew_{hi}}{k_B T}\right)\exp\left(\frac{e}{k_B T}\sqrt{\frac{eE(0,t)}{4\pi\varepsilon}}\right)
\end{aligned} \tag{4-14}$$

where $j(d,t)$ and $j(0,t)$ are the fluxes of electrons and holes at the cathode and anode, respectively, T is the temperature, $A = 1.2\times10^{-6}$ Am^{-1}K^{-2} is the Richardson constant, d is the inter-electrode spacing, and w_{ei} and w_{hi} are the injection barriers for electrons and holes.

Assuming no extraction barrier, the extraction fluxes are:

$$\begin{aligned} j_e(0,t) &= \mu_e E(0,t)\rho_{e\mu}(0,t) \\ j_h(d,t) &= \mu_h E(d,t)\rho_{h\mu}(d,t) \end{aligned} \tag{4-15}$$

No charge is assumed in the insulation bulk before field application ($t \le t_0$). The initial parameterization of the model has been done using values as shown in Table 4-1.

Table 4-1 Definition of Model I parameters controlling dynamic charge interactions [128]

Parameter		Value
B_e	Trapping coefficients	$0.10\,\mathrm{s^{-1}}$
B_h		$0.20\,\mathrm{s^{-1}}$
S_0	Recombination coefficients	$4\times10^{-3}\ \mathrm{m^{-3}C^{-1}s^{-1}}$
S_1		$4\times10^{-3}\ \mathrm{m^{-3}C^{-1}s^{-1}}$
S_2		$4\times10^{-3}\ \mathrm{m^{-3}C^{-1}s^{-1}}$
S_3		0
w_e	De-trapping coefficient	0.96 eV
w_h		0.99 eV
μ_e	Mobility	$1\times10^{-14}\ \mathrm{m^2V^{-1}s^{-1}}$
μ_h		$2\times10^{-13}\ \mathrm{m^2V^{-1}s^{-1}}$
ρ_{0et}	Trap density	$100\,\mathrm{Cm^{-3}}$
ρ_{0ht}		$100\,\mathrm{Cm^{-3}}$
w_{ei}	Barrier height for injection	1.27 eV
w_{hi}		1.16 eV

There are difficulties to solve the group of partial discharge equations (PDEs) as equation (4-11): the vibration due to the fluid-dynamic feature of the model; the possibility of minus result of specie density (absolute value used in the computation). These problems may make the solution non-converged. Several numerical methods have been developed, such as Leonard QUICKEST scheme [197]. However, these methods can only be realized by writing personal codes. In this study, the simulation is successfully realized in COMSOL Multiphysics® v3.4, where 1D Poisson's Equation module, and 1D Convection and Diffusion module are applied. Since the latter module is specially used for fluid-like dynamic problem, there is an Artificial Diffusion function to help solve the tough problems for the charge transport model, where the default setting is applied: Streamline diffusion (Petrov-Galerkin / Compensated).

Five unknowns in total are computed: electric potential, mobile electron density ($\rho_{e\mu}$), trapped electron density (ρ_{et}), mobile hole density ($\rho_{h\mu}$) and trapped hole density (ρ_{ht}). Mesh is an especially important step for solving such model. Producing appropriate mesh can effectively help model to reach convergence in shortest time and limited space. Here the mesh is made finer nearer to each electrode and the element length is shorter than 0.1μm. Transient analysis is carried out. The time step is set as 0.001s and can be automatically regulated by the solver depending on the variation rate in the computed parameters. Considering the model's parameterization condition that Schottky injection in only good at lower fields below 100 kV/mm [3], the initial electric field due to applied voltage is always kept around 60 kV/mm field.

For the model with a cell of type A in Figure 4-28 ("Model I.A"), 6 kV is applied at the anode electrode (boundary 1: x=0) and cathode electrode (boundary 2: x=100 μm) is grounded. For mobile holes, Neumann boundary condition or "flux" is set for boundary 1 (point 1) according to equation (4-14); "convective flux" is set for boundary 2 (point 2); vice versa for mobile electrons. Figure 4-30 shows the electric field distortion with the stressing time. Figure 4-31, Figure 4-32, Figure 4-33 and Figure 4-34 show the density distributions of electrons and holes, mobile and trapped, respectively. Since the effective mobility of positive species (holes) is assumed larger than that of negative species (electrons) by five times (seen in Table 4-1), the holes distribution spreads to near the cathode and meet the negative charges there within 10 s. The negative charges are moving slowly and limited in a small range of 30 μm around the cathode. And the change in the negative charge distribution is becoming non-significant after 100 s. With time, the trapped species, negative or positive, tend to accumulate gradually, while the mobile species reduces as they are transporting toward the other electrode. It can be seen that a steady state will be reached in a long time. Figure 4-35 shows the net charge density distribution. Since the trapped species are dominant for electrons and holes, the total charge density are growing until the steady state is arrived after 100 s.

For the model with Cell Type B in Figure 4-28 ("Model I.B"), cylinder coordinate should be applied in Poisson's equation. That is, to multiply the diffusion coefficient and source term by a parameter x. In order to make the maximum initial electric field be around 60 kV/mm, the potential at anode is set to 2 kV. Other settings are similar to those of Model

I.A. This case is the special derivation of Model I.A where applied electric field distribution is concentrate seriously near the anode. Figure 4-36 and Figure 4-37 show the electric field distortion and net charge density, respectively. It can be seen that the electric field is decreasing near the anode due to the increasing net charge density with stressing time. Due to the rather low electric field near the cathode, there is almost no electron injected from the cathode. This trend consists with the occurrence of the field-limited space charge. And with stressing time, the increase rate is slowing down and going to reach a steady state in a long enough aging time. This model shows the long time feature of charge transport phenomena in polymers. In addition, this model can be applied to account for other phenomena: the recombination process of mobile electron and trapped holes ($S_1\rho_{ht}\rho_{e\mu}$) is shown to be associated with electroluminescence; and total current density shows the current-time characteristics of space charge-limited currents, etc.

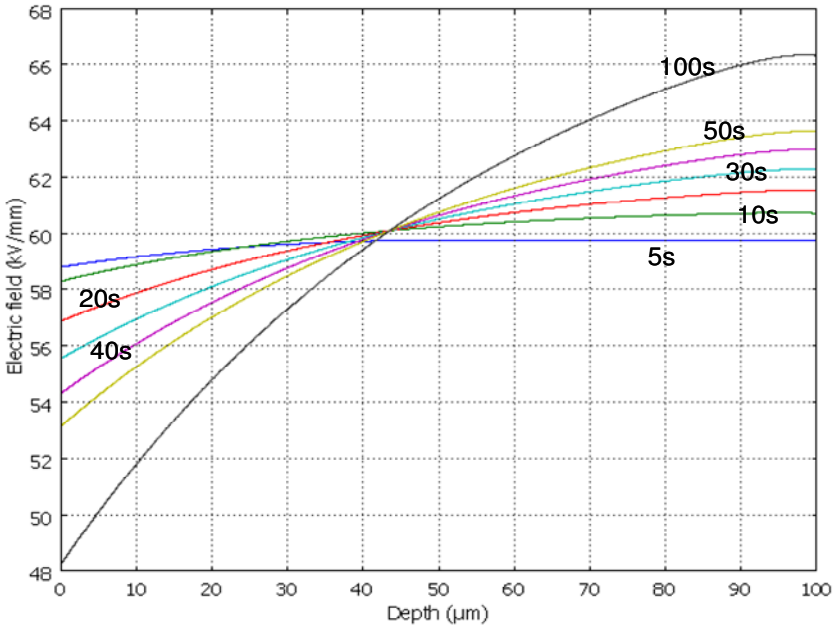

Figure 4-30 Electric field profiles at different times (Model I.A)

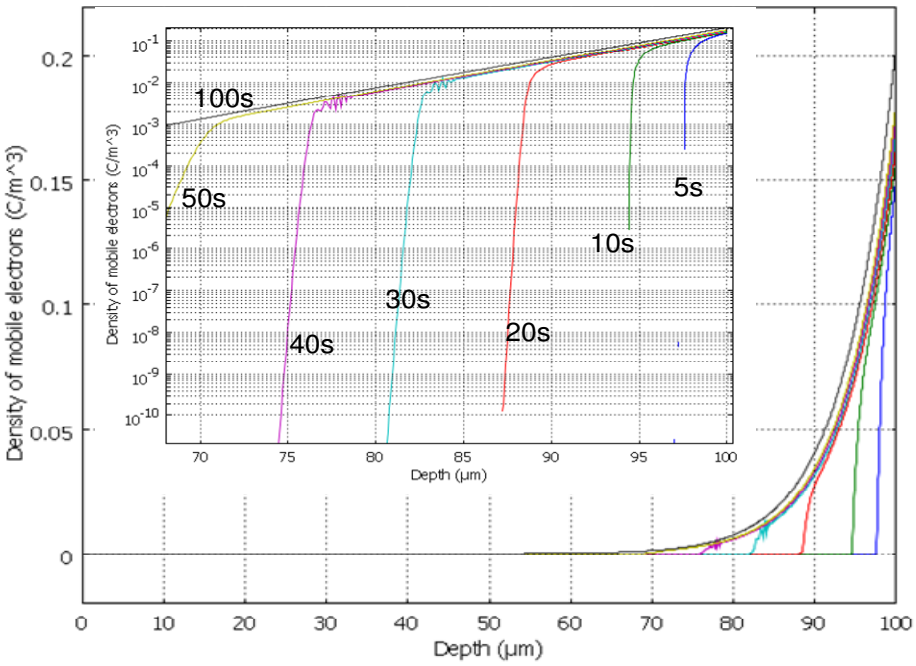

Figure 4-31 Density profiles of mobile electrons at different times (Model I.A)

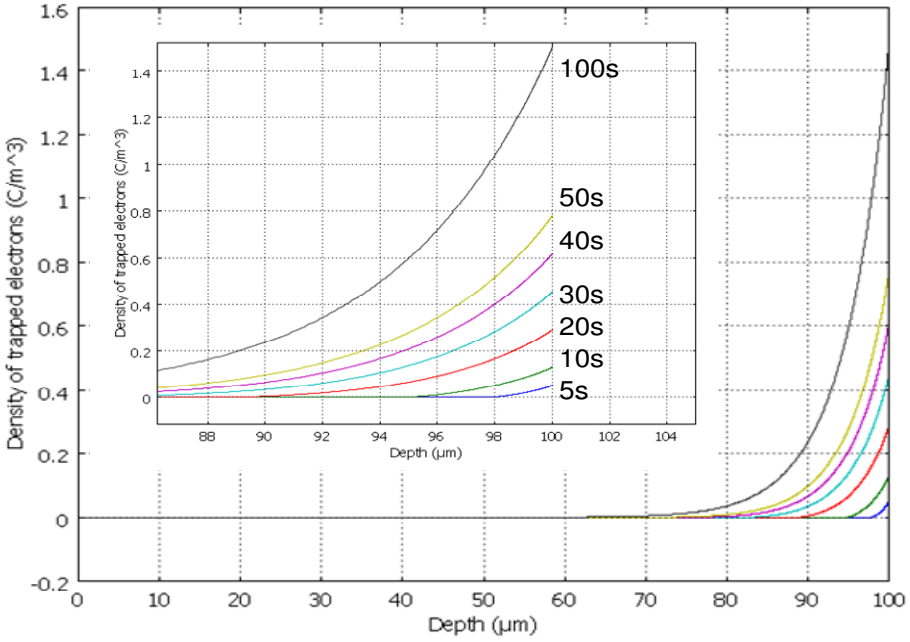

Figure 4-32 Density profiles of trapped electrons at different times (Model I.A)

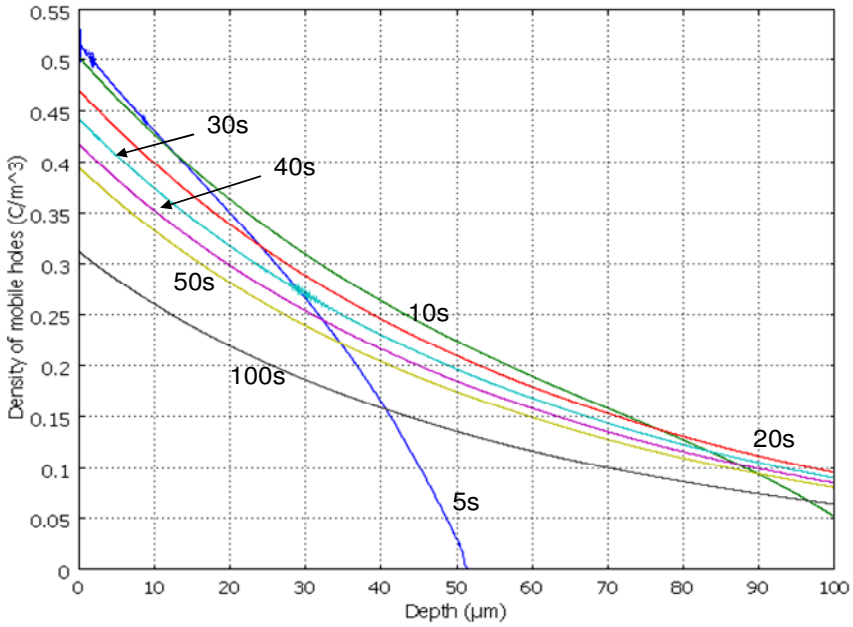

Figure 4-33 Density profiles of mobile holes at different times (Model I.A)

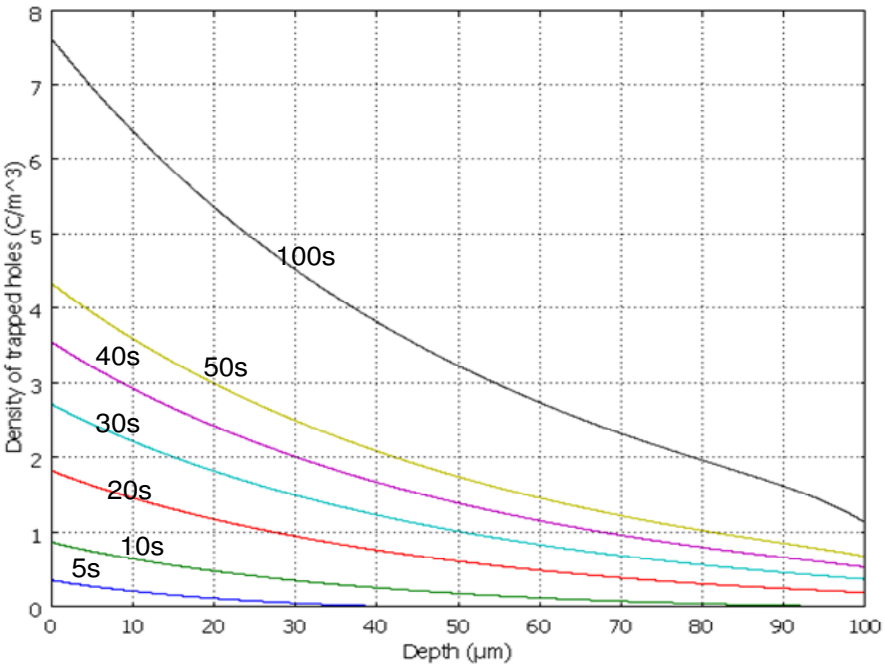

Figure 4-34 Density profiles of trapped holes at different times (Model I.A)

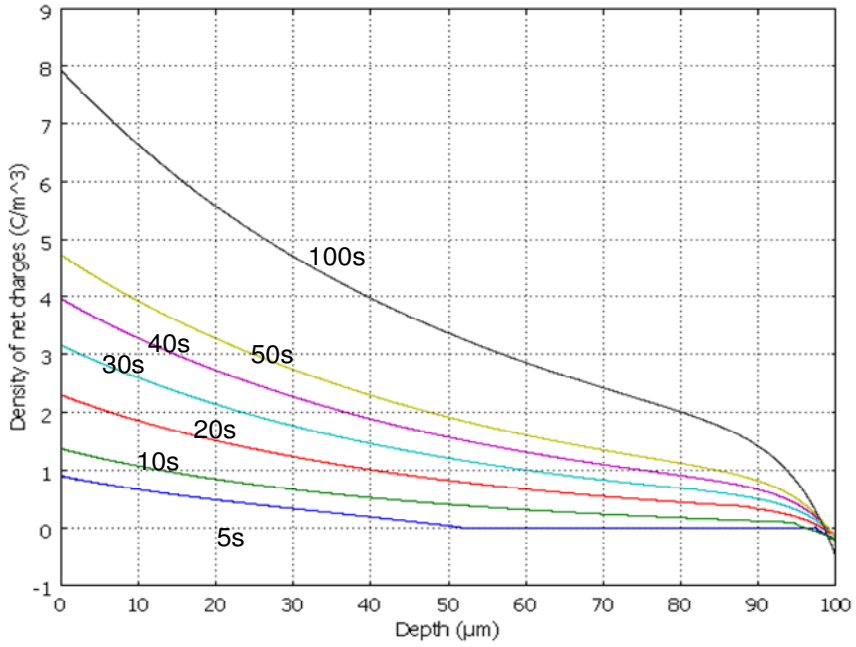

Figure 4-35 Net charge density profiles at different times (Model I.A)

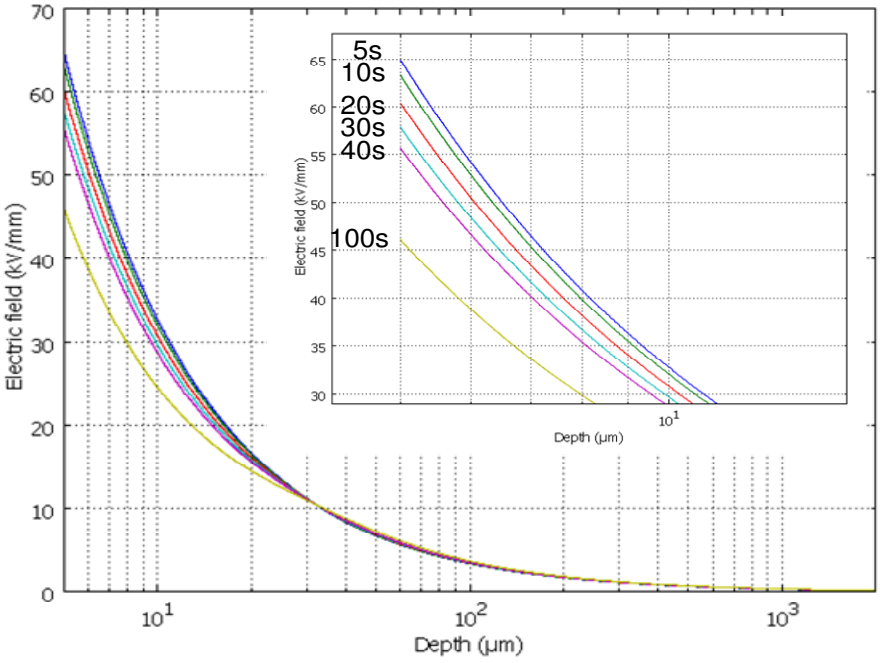

Figure 4-36 Electric field profiles at different times (Model I.B)

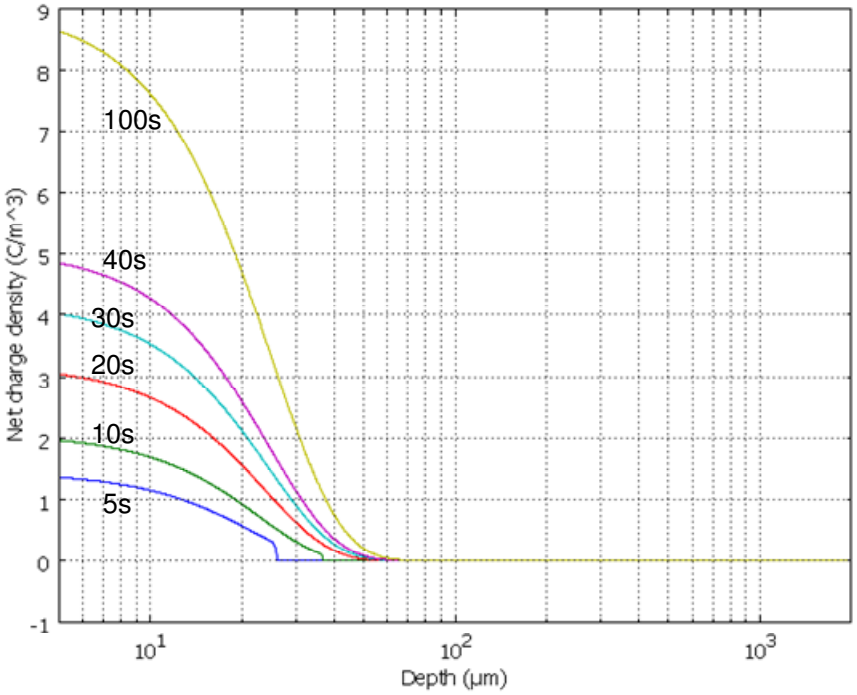

Figure 4-37 Net charge density profiles at different times (Model I.B)

4.4.3 Exponential trapping level ("Model II")

The main feature of this model is that an exponential distribution of trap densities is considered and that the same ensemble of carriers moves site to site and participates in deep trapping. For the sake of simplification, charge recombination has been excluded. Thus the source term in equation (4-10) is null in this case.

Traps are supposed to be filled from the deepest levels upwards [192]. The trap density distributions (Figure 4-38), respectively, for electrons and holes, characterized by a shape parameter T_0, the pre-exponential factor N', and maximum trap depth Δ_m:

$$N_{(e,h)t} = N'_{(e,h)} \exp(-\frac{\Delta_{(e,h)}}{k_B T_{0(e,h)}}) \qquad (\Delta \le \Delta_m) \tag{4-16}$$

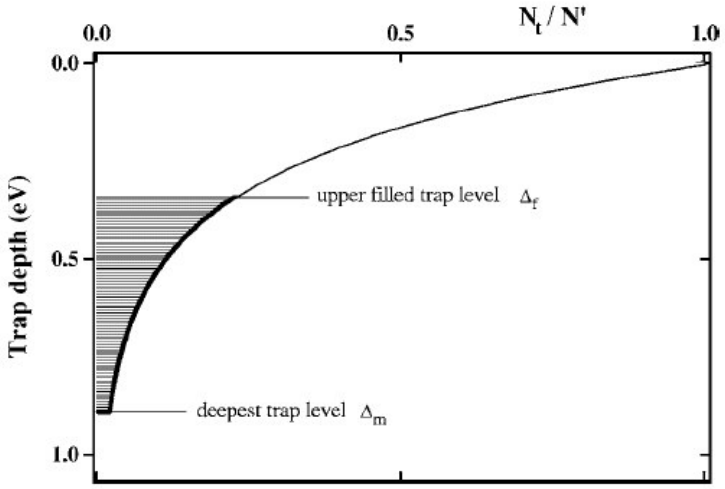

Figure 4-38 Exponential distribution of trap levels for one kind of carriers (The upper filled level Δ_f is variable as a function of time and space)

In this model, the hopping charges essentially come from the highest filled trap state at a depth Δ_f, and the resulting mobility has the form [192]:

$$\mu = \frac{2vd}{E}\exp(-\frac{\Delta_f}{k_B T})\sinh(\frac{eEd}{2k_B T}) \tag{4-17}$$

Using the relationship between ρ and Δ_f:

$$\rho = \int_{\Delta_f}^{\Delta_m} N_t(\Delta) d\Delta \tag{4-18}$$

which gives

$$\Delta_f = k_B T_0 \ln\left[\frac{\rho}{eN' k_B T_0} + \exp(-\frac{\Delta_m}{k_B T_0})\right] \tag{4-19}$$

equation (4-17) becomes:

$$\mu(E) = \frac{2vd}{E}\left[\frac{\rho}{eN' k_B T_0} + \exp(-\frac{\Delta_m}{k_B T_0})\right]^a \sinh(\frac{eEd}{2k_B T}) \tag{4-20}$$

When $T \square T_0$, only a fraction ρ_f of the total carrier density ρ is involved in transport, corresponding effectively to carriers trapped at an energy within $k_B T$ in respect to Δ_f [192, 198]:

$$\rho_f = \frac{\rho}{1+a} \text{ with } a = \frac{T_0}{T} \tag{4-21}$$

The average inter-site distance d is related to the trap density according to:

$$d = (N' k_B T_0)^{-\frac{1}{3}} \left[1 - \exp(-\frac{\Delta_m}{k_B T_0}) \right]^{-\frac{1}{3}} \tag{4-22}$$

No charge is assumed in the insulation bulk before field application ($t \le t_0$). The initial parameterization of the model has been done using values as shown in Table 4-2.

Table 4-2 Definition of Model II parameters controlling dynamic charge interactions[128]

Parameter		Value
T_{0e}	Shape parameter of the distribution function	2×10^4 K
T_{0h}		2×10^4 K
N'_e	Pre-exponential term of the distribution function	10^{46} $m^{-3}J^{-1}$
N'_h		10^{46} $m^{-3}J^{-1}$
Δ_{me}	Maximum trap depth	0.608 eV
Δ_{mh}		0.534 eV
w_{ei}	Barrier height for injection	1.27 eV
w_{hi}		1.16 eV

Similar to the Model I.A, the two-parallel electrode geometry (Model II.A) is analyzed at first. Differently, only three unknowns are computed: potential, mobile electrons (ρ_{ef}) and holes (ρ_{hf}). Figure 4-39 shows the evolution of electric field profiles as a function of stressing time. After 1 s, a significant distortion of the field is observed. The electric field is getting to be maximal near the cathode at $t = 10$ s and decreasing from then on due to the flow and co-existence of negative and positive charges. A quasi-steady state is reached in the relatively short time and then the distribution is changing slowly non-significantly. Density profiles for positive and negative charges are shown in Figure 4-40 and Figure 4-41, respectively. Positive charges (holes) have larger mobility than negative charges (electrons). Thus positive charges are distributed forward much faster to the cathode than the negative charges to the anode. This is related to the model parameters such as the barrier height to injection and the trap depth. From Figure 4-40, it can be seen that positive charge distribution has spread to the cathode around 10 s, which means that two types of species meet at that time. A peak occurs in the negative charge density profile also around 10 s, which in combination with positive charges results in the obvious drop of electric field near the cathode. The peak value for both positive and

negative charges are keeping constant before they meet. This consists with the model assumption that a fraction of total charges contribute to transport as mobile charges, while the dominant part are trapped with a constant maximum deep trap depth. Figure 4-42 shows the interaction of negative and positive charges with time.

Through the similar transferring procedure from Model I.A to Model I.B, Model II.B is set up just by multiplying the diffusion coefficient and source term by a parameter x in Model II.A and thus modifying the 1D cell from Type A to Type B. The high potential is regulated to 2 kV in order to obtain a maximum initially applied electric field at the same order as in Model II.A. Due to the locally concentrated electric field distribution, serious distortion is shown near the anode in Figure 4-43. This model shows the feature of space charge-limited field. At $t = 12\,\mathrm{s}$, the field in the space charge accumulating zone is almost limited to a constant value, lower than 3 kV/mm. From then on, the field distribution will be only change at the border of the zone (around $x = 70\,\mu\mathrm{m}$), since the charge density is constant within that zone and the charge distribution range spreads slowly until reaching the future steady. The main reason to this phenomenon is the injection of net charges as shown in Figure 4-44, which is the algebraic sum of positive charges (holes) and negative charges (electrons). According to the assumption of exponential deep trapping level, the trapped charges is with same shape profiles but neatly one thousand or $a\,(=T_0/T)$ times larger in magnitude. Figure 4-45 and Figure 4-46 show the mobile positive and negative charge density, respectively. Positive charges are injected from anode gradually from $t = 0^+$. They move forward to electrode with reducing magnitude and slower speed. Since the electric field is too low, there is no obvious negative charge injection phenomenon. After 10 s, there are negative charges injected also from the anode, and hetero-charges accumulate showing the effect of polarity reversal. The density of mobile negative charges, a small fraction of total negative charges, grows to a steady value of around 3.8 $\mathrm{C/m^3}$. From then on, the net charge density is keeping at about -150 $\mathrm{C/m^3}$. With stress time, the charge spreading speed slows down and the total charges seem to be limited in a certain range around the anode. The magnitude of electric field increases from the initial value to the maximum of 25 kV/mm and then drops to an almost uniform value in the charges distributed range.

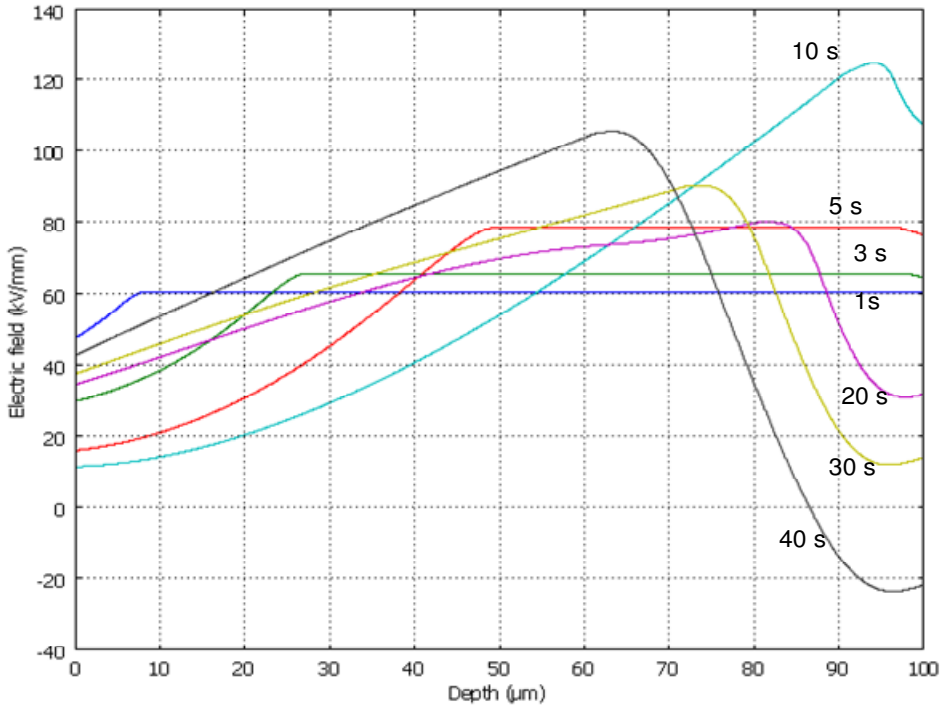

Figure 4-39 Electric field profiles at different times (Model II.A)

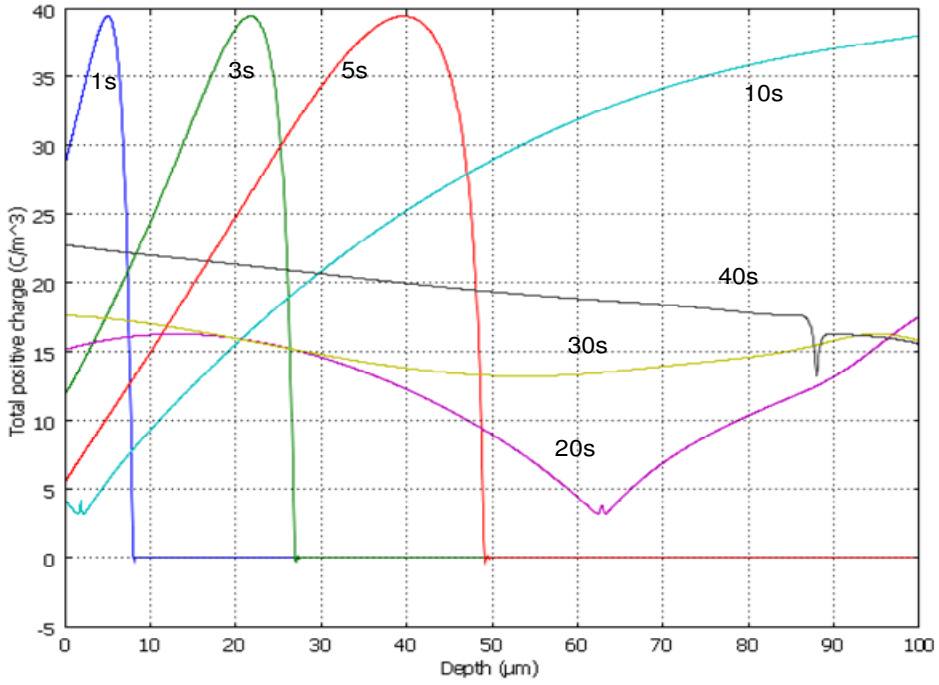

Figure 4-40 Positive charge density profiles at different times (Model II.A)

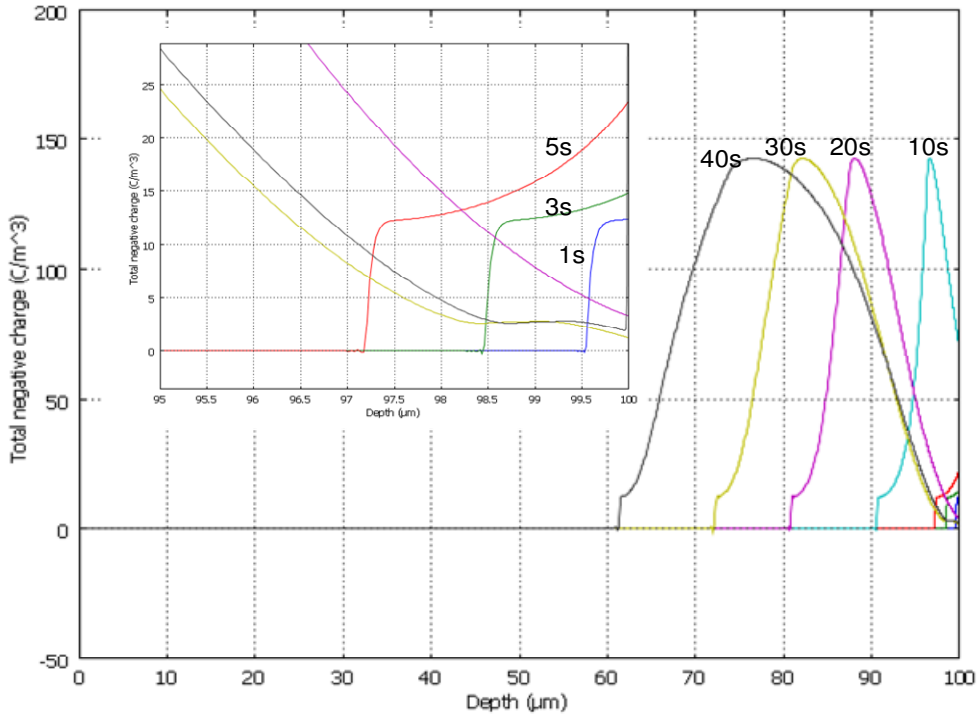

Figure 4-41 Negative charge density profiles at different times (Model II.A)

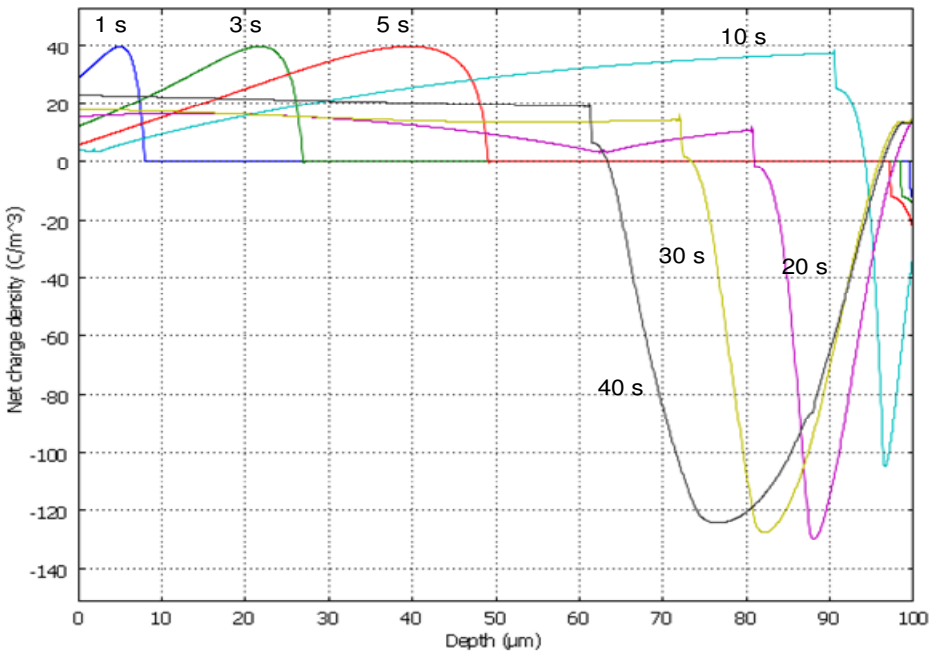

Figure 4-42 Net charge density profiles at different times (Model II.A)

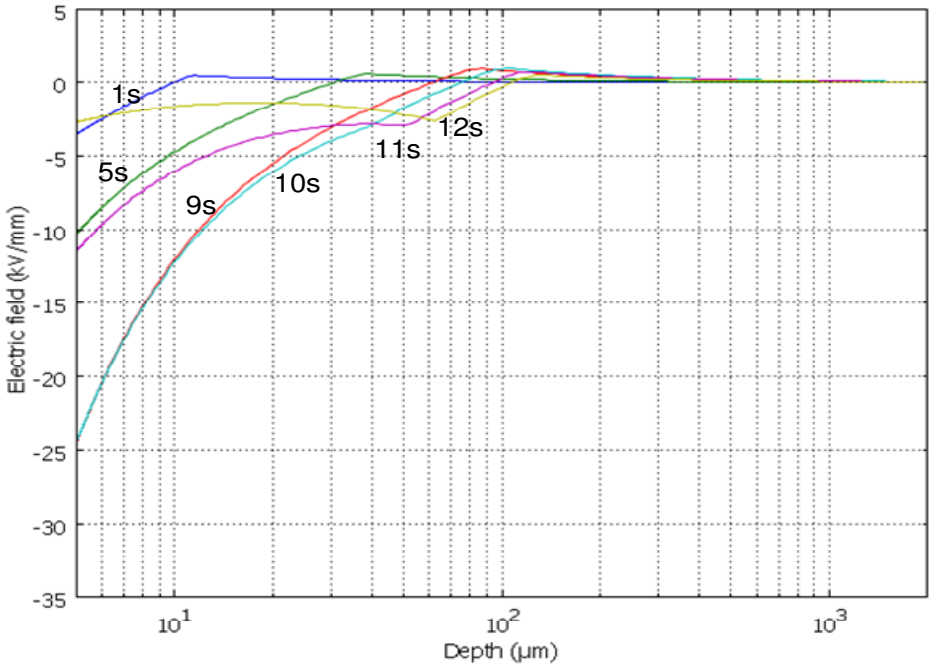

Figure 4-43 Electric field profiles at different times (Model II.B)

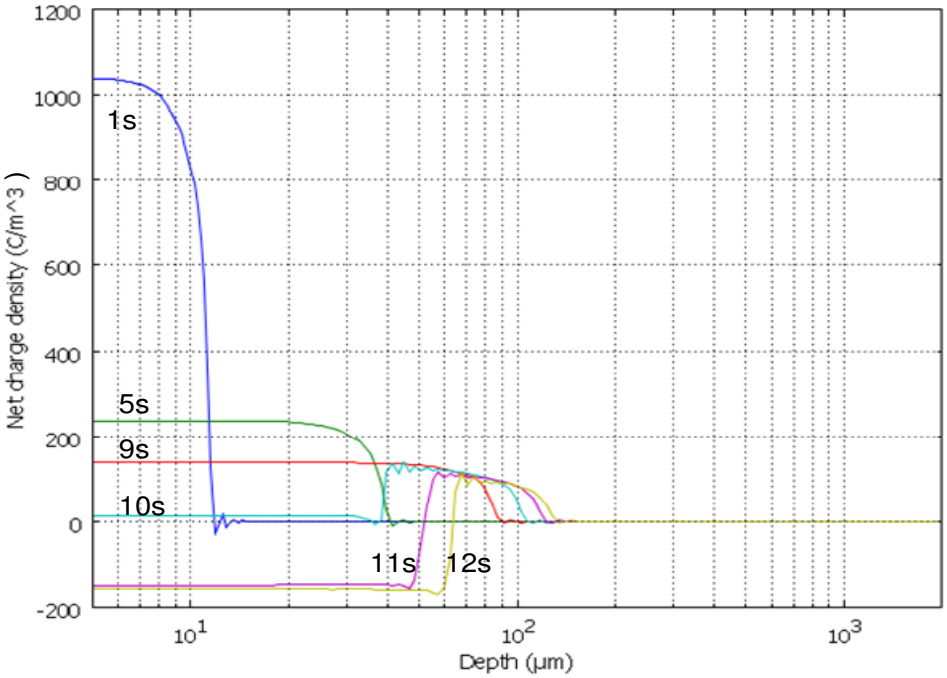

Figure 4-44 Net charge density profiles at different times (Model II.B)

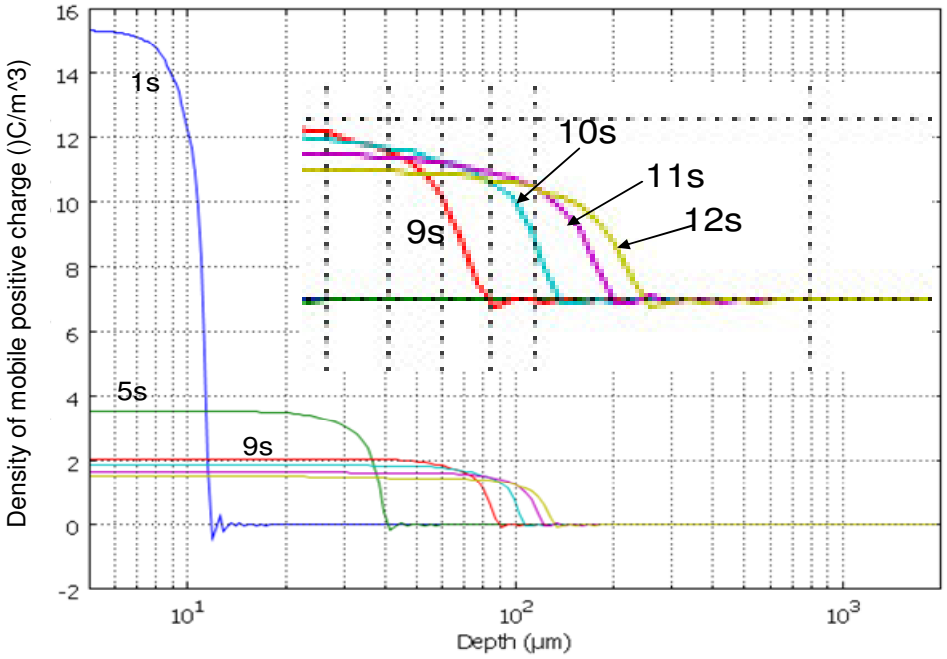

Figure 4-45 Mobile positive charge density profiles at different times (Model II.B)

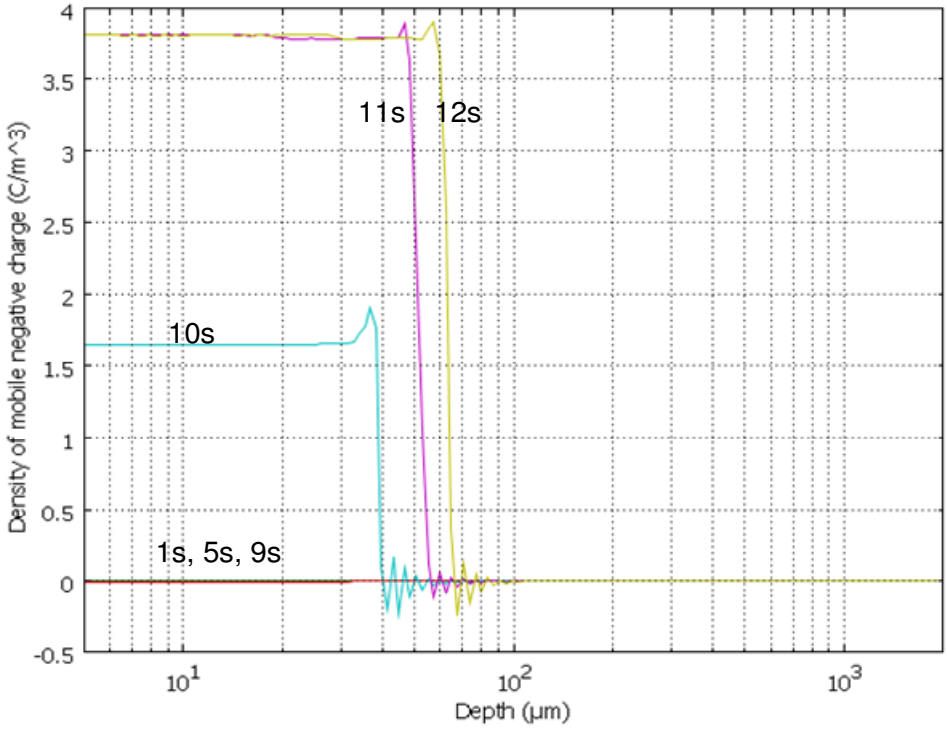

Figure 4-46 Mobile positive charge density profiles at different times (Model II.B)

4.5 Summary

At first, the needle-plane electrode geometry was analyzed in respect of electric field distribution. Two-dimensional static-electrical problem was proposed and a representative model was set up. The influences of some parameters on the electrical field in this system were considered, including needle diameter, needle tip angle, needle radius, and distance from needle to plane. The diameter of needle has little influence on maximum electric stress, especially for the diameter with higher value. A linear relationship is found and the slope is higher for the needle with smaller diameter and steeper tip. The electric stress at the needle tip changes dramatically with the change in tip radius. Although this hyperbolic shaped needle is not a perfect representation of needles used in experimental work, these analyses are still good enough to compare the influences of these configuration parameters.

In addition, a modified model was set up to analyze the space charge effect. It is demonstrated that the charge density, charge polarization, and charge confined in spherical region also do play roles, which are not negligible, in the field distribution. Maximum charge density occurs when the total effective field stress at the needle tip approaches zero. A linear relationship holds until the point where further increase in the space charge density will lead the shift in the location of the maximum electric stress from the needle tip to the edge of space charge region. Although the maximum charge density decreases with increasing charge region, the total charge in this region increases. And the maximum electric stress with reversal polarization effect is significantly higher than that with homo-charge. The maximum electric stress always occurs at the needle tip. Additionally, two approximately linear relationships were obtained between the maximum electric stress and the maximum charge via applied voltage.

Furthermore, three cases of electrical tree growth were analyzed by using FEM method: the effect of radius of conductive particles; the effect of gas bubbles around a conductive particle; and the effect of two bubbles, one with space charges inside. In the model, a metal ball is used to simulate the needle tip or conductive particle in insulation material, a bubble is the micro representation of the tree channel. The electric field distribution was

calculated in each situation and the initiation and propagation conditions of electrical trees were analyzed.

The nonlinear conductivity, which has dependences on the field and temperature, is necessarily considered in the analyses for electric field distribution and space charge buildup. Making use of COMSOL Multiphysics® software, the electric field is computed coupled with thermal effect by using nonlinear transient solver and different waveforms of voltage input. The space charge-limited field is decided in quantity, and the transient space charge buildup is found to grow gradually along the radius direction. The temperature rise is also found significant when fast-rise waveforms are applied. The rise magnitude is affected by some factors such as needle tip radius.

Since the space charge density has an important influence over the electric field distribution and thus to the insulation condition, the space charge accumulation phenomena need to be better understood. So far, limited models have been developed. And they are not equivalent regarding the space charge buildup within the insulation and the transient currents, since current space charge measurement techniques prevent the full evidence of these developed models. At the macroscopic scale, the popular model, bipolar charge transport model, is essentially founded upon a composition of Poisson's equation, continuity equation and transport equation. And in this study, two typical assumptions are applied: unique and exponential deep trapping level, respectively. Without applying the traditional techniques which are programming based on some developed numerical methods, COMSOL Multiphysics® software is successfully applied to solve the tough problem. This problem is solved by taking advantage of specialized modules which are good at solving the fluid-like dynamic problem. For this study, a 1D multiphysics problem is at first computed for the parallel electrode geometry. And then, the needle-plane electrode system is analyzed by transferring the coordinate system from the rectangular one into a cylinder one. The total charge density is considered as the algebraic sum of densities of electrons and holes, mobile and trapped, respectively. The density of each species can be calculated with the stressing time and thus these models show certain features which can be used to explain the charge transport phenomena. Due to the larger mobility of positive charges (holes) compared to negative charges (electrons), the positive charges move faster forward the cathode and meet negative

charges near the cathode. And thus the electric field is distorted according to the space charge accumulation. The distortion is especially more serious near the anode for the models with a cell of type B. With the stressing time, a steady state is expected to be reached finally. Although these models cannot fully explain the phenomena of bipolar space charge transport, the model with the first assumption can show the long time decaying and the other model with the second assumption has the features of transient field-limited space charge buildup.

Chapter 5 Determination of Intrinsic Permittivity of XLPE Cable Materials

5.1 Field-circuit coupled method to determine intrinsic permittivity of XLPE material

The XLPE-insulated cables consist of a copper or an aluminum conductor (inner conductor), a semiconducting layer extruded over the inner conductor, an XLPE-insulation, an outer semiconducting layer, a metallic wire screen or aluminum sheath and an outer polyethylene sheath. The influence of the semiconducting layers on the PD propagation has been widely studied [19-21]. Its permittivity is verified as frequency-dependent. This is a common property for any dielectric material when the frequency band is sufficiently wide, as it is for XLPE material. Thus, it may not be sufficiently accurate to assume the same permittivity value of XLPE at 1 MHz as that at 1 GHz. Investigating the frequency-dependence of XLPE material is meaningful since partial discharge pulses contain a wide range of frequency components. Until now, various permittivity measurement methods have been used in experiment [24-30] for different materials. A field-circuit coupled method was introduced in [30] to tackle the dimensional effect that occurs in a material with high permittivity and conductivity simultaneously or a material with high permittivity and permeability simultaneously.

To understand the high frequency response of such cables, one needs to realize that it is the intrinsic values of complex permittivity and conductivity for the materials that are important, and not the measured values. According to the theory given by [31], the measured permittivity of a material may differ significantly from its intrinsic value if there is a dimensional effect in it or if the fringing effect becomes pronounced, such is the case with the two-parallel-electrode method. Illustration and enhanced research can be found in [28, 30] and [32, 33], where an air-filled capacitor is studied. Compared to the relative permittivity of semicon, the relative permittivity of XLPE insulation is very small, usually around three. Fringing effect is for sure significant when the conventional two-parallel-electrode method is used to measure permittivity. Even with a guard electrode, the energy stored in the ambience may still not be ignored.

This section presents a field-circuit coupled method to contravene the deviation of measured value from the intrinsic one due to fringing effect, which can effectively take into account the energy stored in the ambient and thus correct the measurement error. It has no limitations on the dimensions of test samples and fixtures, and also a guard electrode will not be required.

5.1.1 Development of mathematical model

The concentric cylindrical structure is a typical one of HV (230 kV) XLPE as depicted in Figure 5-1.

This is an electrostatic problem where the electric field E and potential φ are governed by the following two equations respectively:

$$\vec{E} = -\nabla\varphi \tag{5-1}$$

$$\frac{\partial^2\varphi}{\partial x^2} + \frac{\partial^2\varphi}{\partial y^2} + \frac{\partial^2\varphi}{\partial z^2} = 0 \tag{5-2}$$

Because of the axial symmetry of the model, the electric field distribution is independent of variable z, and the solution can be carried out by analyzing a Laplace equation in any meridian plane cylindrical coordinate system. For simplicity, a rectangular coordinate system is applied as shown in Figure 5-2. Hence equation (5-2) can be reduced to

$$\frac{\partial^2\varphi}{\partial x^2} + \frac{\partial^2\varphi}{\partial y^2} = 0 \tag{5-3}$$

AC voltage source is applied to the top of the XLPE cable segment, and the bottom surface is grounded, as indicated in Figure 5-2. Due to the axial symmetry, just for the right part of cross-section, the Dirichlet boundary conditions for equation (5-3) are

$$\begin{cases} \varphi\big|_{\Gamma_1} = |U| & (\Gamma_1 : R_1 < x < R_2,\ y = d) \\ \varphi\big|_{\Gamma_1} = 0 & (\Gamma_2 : R_1 < x < R_2,\ y = 0) \end{cases} \tag{5-4}$$

Since the electric field strength is rather weak in the air far from the XLPE, the Neumann boundary condition for equation (5-3) is

$$\frac{\partial\varphi}{\partial n}\Big|_{\Gamma_5} = 0 \quad (\Gamma_5 :\ x = \infty,\ y = \infty) \tag{5-5}$$

Due to the continuity of electric flux density at the interface of XLPE and air,

$$\begin{cases} \varepsilon_1 \dfrac{\partial \varphi}{\partial n^+}\Big|_{\Gamma_3} = \varepsilon_2 \dfrac{\partial \varphi}{\partial n^-}\Big|_{\Gamma_3} & (\Gamma_3 :\ x = R_2, 0 < y < d) \\ \varepsilon_1 \dfrac{\partial \varphi}{\partial n^-}\Big|_{\Gamma_4} = \varepsilon_2 \dfrac{\partial \varphi}{\partial n^+}\Big|_{\Gamma_4} & (\Gamma_4 :\ x = R_1, 0 < y < d) \end{cases} \tag{5-6}$$

where ε_1 is the permittivity of XLPE and ε_2 is the permittivity of air.

Equation (5-3) with its boundary conditions as shown in equations (5-4)-(5-6) can be solved numerically.

The solution was obtained by ANSOFT simulation tool "MAXWELL". The convergence can be reached by iteration where the convergence criteria are set as following: error=1%, energy error=0.8% and delta energy=0.9%. Several hours are needed to accomplish the accurate solution.

Figure 5-3 illustrates the distribution of electrical equipotential curves in both XLPE material and the ambient. The fringing effect can be inferred from these distributions since in the ambient, the difference between neighboring equipotential lines are obvious.

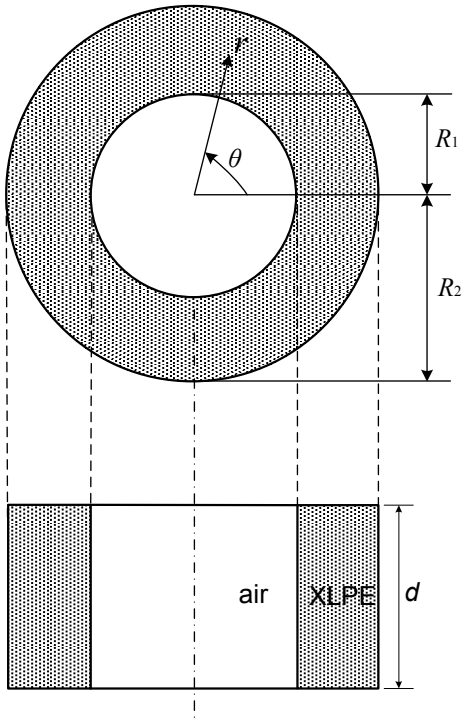

Figure 5-1 The sample configuration of XLPE cable segment

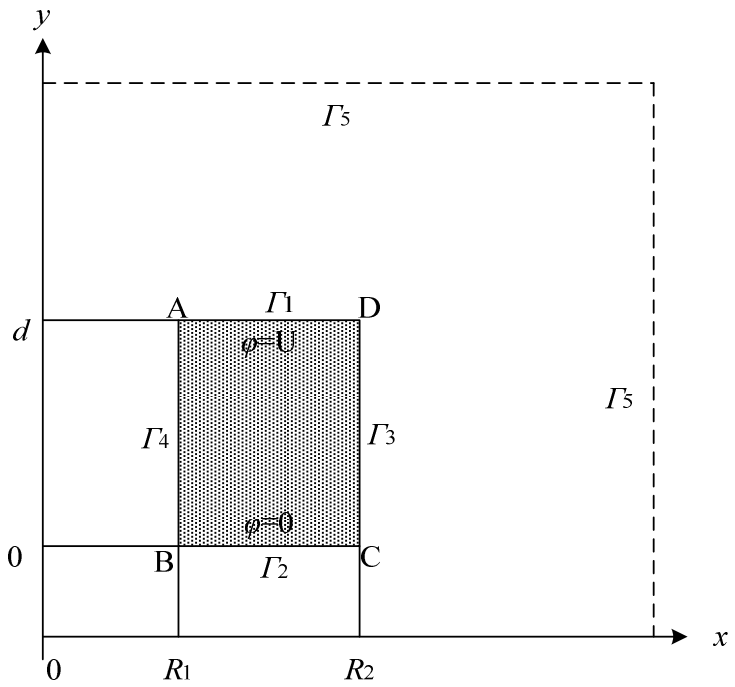

Figure 5-2 The axisymmetric sectional plane of the model

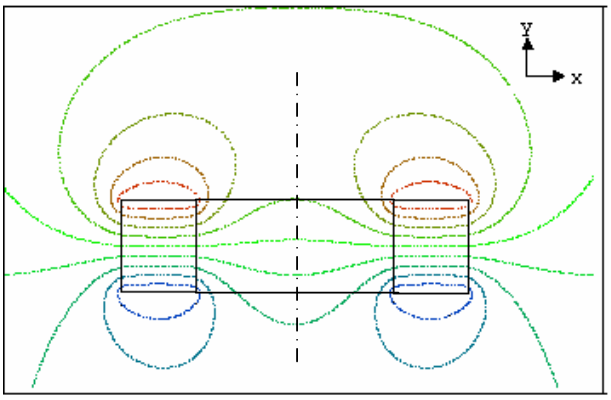

Figure 5-3 The distribution of equipotential curves

To study the relationship between the measurable permittivity and intrinsic permittivity, a field-circuit coupled method is given below.

The complex power supplied to the capacitor can be written as [31]:

$$S = S_E + S_H \tag{5-7}$$

where S_E is the complex power related to the electric field, which is written as [31]:

$$S_E = \iiint (j\omega\varepsilon)^* \left|E\right|^2 dv \tag{5-8}$$

and S_H is the complex power related to the magnetic field which is written as [31]:

$$S_H = \iiint j\omega\mu \left|H\right|^2 dv \tag{5-9}$$

In case of XLPE materials, where the influence of the magnetic field is negligible, the only remaining term to be considered in equation (5-7) is S_E .

The electric field distribution is obtained from MAXWELL. As shown in Figure 5-4, the value of electric field strength is calculated for the discrete grid with a step of delta ("Δ"). $\vec{E}(i, j)$ denotes the electric stress at the point (i, j) , which includes $E_x(i, j)$, $E_y(i, j)$ and $E_z(i, j)$. Due to the symmetry, $E_z(i, j)$ is always equal to zero. Therefore, the real part and the imaginary part of complex power can be expressed as

$$\overline{P_d} = \mathrm{Re}[S_E] = \iiint \omega\varepsilon'' \left|E\right|^2 d\tau = \omega\varepsilon'' \cdot 2\pi \sum_{i,j} \left|\vec{E}(i, j)\right|^2 s(i, j)x(i, j) \tag{5-10}$$

$$\begin{aligned} \overline{Q_e} = \mathrm{Im}[S_E] &= \omega \iiint \varepsilon' \left|E\right|^2 d\tau = \omega\varepsilon' \sum_{i,j} \int_0^{2\pi} \left|\vec{E}(i, j)\right|^2 s(i, j)x(i, j)d\theta \\ &= \omega\varepsilon' \cdot 2\pi \sum_{i,j} \left|\vec{E}(i, j)\right|^2 s(i, j)x(i, j) \end{aligned} \tag{5-11}$$

where, for the part of XLPE,

$$s(i, j) = \begin{cases} \frac{1}{4}\Delta^2 & (i = 1, j = 1 \mid i = m, j = 1 \mid i = 1, j = n \mid i = m, j = n) \\ \frac{1}{2}\Delta^2 & ((i = 1 \mid i = m), 2 < j < n-1 \mid (j = 1 \mid j = n), 2 < i < m-1) \\ \Delta^2 & (2 < i < m-1, 2 < j < n-1) \end{cases} \tag{5-12}$$

The symbols Δ, *i*, and *j* represent grid step, x-position and y-position, respectively as shown in Figure 5-4. And other energy contained in the ambient should also be considered.

AC voltage source is applied in order to include the factor of ω. However, the “AC conduction” solver of MAXWELL only can calculate field in XY plane. To compare the results from models in XY plane and in RZ plane, assuming a DC voltage source

referring to t=0 of $U = 10\angle 0^0$ V, the energy is calculated both in XY plane and RZ plane by "electrostatic" solver. The results are included in Table 5-1. It can be found that the energy in RZ plane is a bit higher than that in XY plane by about 5%. In later calculation, XY plane is applied for field solution by "AC conduction" solver.

Table 5-1 Comparison of energy calculation in different coordinate system

	XY plane		RZ plane	
Energy (J)	$\overline{P_d}$	$\overline{Q_e}$	$\overline{P_d}$	$\overline{Q_e}$
$\Delta = 0.1\,\text{mm}$	1.1743e-13	2.9433e-10	1.2281e-13	3.0904e-10
$\Delta = 0.05\,\text{mm}$	1.1760e-13	2.9441e-10	1.2301e-13	3.0913e-10
$\Delta = 0.02\,\text{mm}$	1.1772e-13	2.9446e-10	1.2314e-13	3.0918e-10

The conventional method of measuring the permittivity is to use two parallel electrodes with a dielectric material sample inserted between the electrodes as illustrated in Figure 5-5 (a). The characteristics of the circuit elements (resistors or conductors, capacitors, and inductors) depend upon the properties of the matter. The principle of the measurement is based on the equivalent circuit of the capacitor as shown in Figure 5-5 (b). The complex field equations bear a relationship to the complex circuit equations [31]. The complex power supplied to a circuit element is:

$$S = \overline{P_d} - j\overline{Q_e} = |U|^2 Y^* = |U|^2 (G - j\omega C) \tag{5-13}$$

where the conductance G accounts for energy dissipation and the capacitance C accounts for energy storage. It should be noted that S is a function of frequency. Thus the designation of an element as a resistor, inductor, or capacitor is, to some degree, dependent upon frequency. One can prove that the equivalent conductance and capacitance can be expressed as

$$G = \omega\varepsilon'' \frac{A}{d} \tag{5-14}$$

$$C = \varepsilon' \frac{A}{d} \tag{5-15}$$

where $A = \pi(R_2^2 - R_1^2)$.

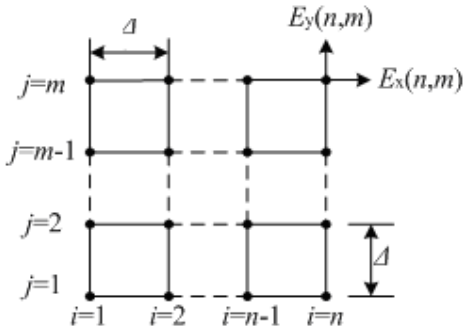

Figure 5-4 The grid configuration for power calculation

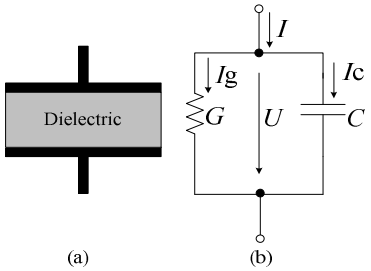

Figure 5-5 A capacitor according to circuit concepts

(a) Physical capacitor; (b) Equivalent circuit

The real and the imaginary parts of the measured complex permittivity of the insulation material can be calculated as

$$\varepsilon'_m = \frac{\overline{Q_e} \cdot d}{\omega\pi(R_2^2 - R_1^2)|U|^2} \tag{5-16}$$

$$\varepsilon''_m = \frac{\overline{P_d} \cdot d}{\omega\pi(R_2^2 - R_1^2)|U|^2} \tag{5-17}$$

According to the electromagnetic theory given in [31], if the material takes the intrinsic complex permittivity of $\varepsilon^* = \varepsilon' - j\varepsilon''$, then the measurable or the value that can be measured from experiments, must be equal to $\varepsilon_m^* = \varepsilon_m' - j\varepsilon_m''$ with ε_m' calculated by equation (5-16) and ε_m'' by equation (5-17).

When an experiment is carried out to measure the permittivity for the material with an assumed intrinsic value of permittivity, the real and reactive powers supplied to the sample under test can be read from the instrument, and according to the electromagnetic

theory given in [31], they should be just the components of power that can be calculated by equations (5-10) and (5-11). Consequently, the two components of permittivity calculated by equations (5-14) and (5-15) represent the experimentally measured (real and imaginary) components of permittivity. If all the complex power is contained inside the material or the power due to the energy stored in ambient is negligible, one can expect that the measured or calculated permittivity is identical to the assumed intrinsic value [31]. However, they are different in practical cases due to the fringing effect, since the energy is not only stored in XLPE insulation material but also in the ambient. Thus the measured value of permittivity differs from the intrinsic value, as it will be illustrated in the following section.

5.1.2 Determination of intrinsic permittivity based on measured value

To compare the measurable with intrinsic value of permittivity, and to study the fringing effect on the measurement error for XLPE material, the following steps are taken:

1) Specify the dimensions, intrinsic permittivity of the sample under study;

2) Calculate the electric field stress by using a given source;

3) Calculate the complex power via equations (5-10) and (5-11), which include power due to the energy stored in XLPE and the ambient;

4) Calculate the permittivity using equations (5-16) and (5-17).

Based on the actual size of a 230kV XLPE cable, the radius parameters are $R_1 = 32\text{mm}$ and $R_2 = 56\text{mm}$. In this model, the length of the cable segment is selected as $d = 30\text{mm}$.

Assuming the intrinsic permittivity and using the formulation in the preceding section, the measurable permittivity from experiment is calculated. For example, for XLPE insulation, we assume the real part of relative permittivity $\varepsilon_r^{'} = \varepsilon' / \varepsilon_0 = 2.25$, and loss factor $\tan\delta = 0.0004$. Based on the formula of $\tan\delta = \varepsilon'' / \varepsilon'$, ε'' is calculated and equals 0.0009. Thus, the intrinsic permittivity of XLPE insulation will be expressed by: $\varepsilon^* = 2.25 - j0.0009$. For the ambient part, the relative permittivity of air is $\varepsilon_{air} = 1.0006$.

Considering that the applied voltage $U = 10\angle 0^0 V$, f = 50Hz, and the grid step is Δ=0.02mm. The complex power due to the electric field *S* can be obtained.

The time-average electric energy, which can be calculated by [199]

$$\overline{W_e} = \frac{1}{2\omega}\mathrm{Im}(S_E) \tag{5-18}$$

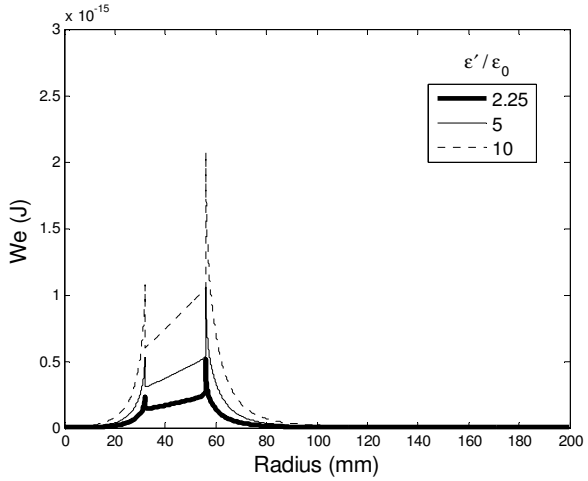

Figure 5-6 The distribution of electric energy in the radius direction along line BC as shown in Figure 5-2

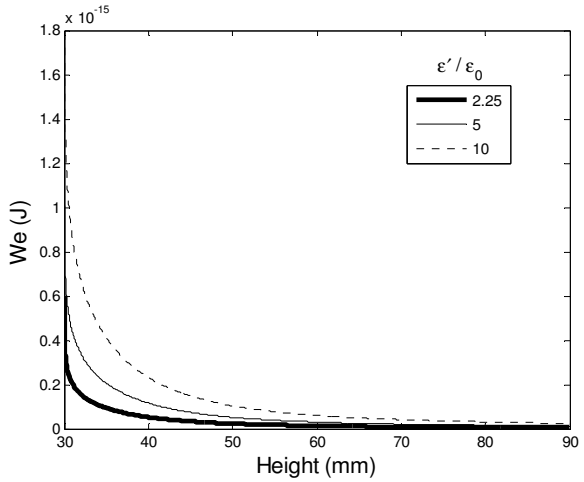

Figure 5-7 The distribution of electric energy in the vertical direction along line BA as shown in Figure 5-2

The energy is $\overline{W_e} = 4.6865\times10^{-13}\mathrm{J}$, and the time-average power dissipation $\overline{P_d} = 1.1772\times10^{-13}\mathrm{W}$, $\varepsilon_c^{'} = 3.7877\varepsilon_0$, $\varepsilon_c^{''} = 0.0009031\varepsilon_0$. It can be seen that

there is a significant difference between the real parts of measurable and intrinsic permittivity, while the values of imaginary part are close to each other. To quantify this difference, errors are defined as follows:

$$error\_\varepsilon' = \left| \frac{\varepsilon'_c - \varepsilon'_m}{\varepsilon'_{in}} \right| \times 100\% \tag{5-19}$$

$$error\_\varepsilon'' = \left| \frac{\varepsilon''_c - \varepsilon''_m}{\varepsilon''_{in}} \right| \times 100\% \tag{5-20}$$

where ε'_m and ε''_m are the real and imaginary parts of the intrinsic complex permittivity, respectively; ε'_c and ε''_c are the real and imaginary parts of the calculated complex permittivity, which are also the values that are measured from experiments if the material takes the assumed intrinsic permittivity.

Figure 5-6 and Figure 5-7 show the distributions of stored energy in both XLPE and ambient air. One can see from these figures that most of the electric energy $\overline{W_e}$ is distributed in the part of XLPE insulation, as expected. However, there is still some energy spreading in the outer space close to the inner and outer surfaces. For a material with higher permittivity, there is higher electric field energy and that energy spreads farther. In far-away space, the energy decays to zero. It is interesting that energy distribution has two peaks at the interfaces of the XLPE material and air, as shown in Figure 5-6. Accumulated space charges could be the cause of this phenomenon.

In the following paragraph, a method is proposed to determine intrinsic permittivity based on its measured value. For simplicity, if only real part of complex permittivity is considered in further analysis, this is acceptable since XLPE cable has very small dielectric loss or ε''_m is very small. However, the imaginary part of complex permittivity is determined by the power loss of dielectrics, and it is actually the toughest task to determine the complex permittivity of XLPE cables. Thus both the real and imaginary parts of complex permittivity are analyzed in the following parts.

Assuming different values of intrinsic permittivity and following the steps listed at the beginning of this section, the corresponding measurable permittivity can be calculated. For samples of the same dimensions as in Section 5.1.1, the intrinsic and measurable

permittivity is drawn in Figure 5-8. The error resulting from fringing effect is calculated and shown in Figure 5-9. The detail values are shown in Table 5-2. It can be noted that the error due to fringing effect especially the error of real part of permittivity (*error_ε'*) is significant and correction to the measured permittivity must be carried out to determine the intrinsic values.

The correction is taken in the following steps: first, according to the value of the measured permittivity, find the point, say Point A, on the vertical axis in Figure 5-8; then draw a line in parallel to the horizontal axis from Point A. This line intersects with the curve at a point, say Point B. Next, from Point B, draw a line in parallel to vertical axis. This line crosses horizontal axis at a point, say Point C. The value at Point C is just the intrinsic value corresponding to the measured permittivity.

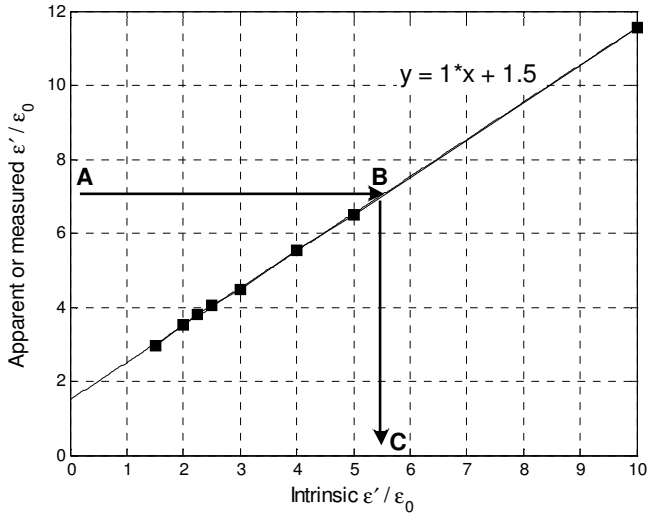

(a)

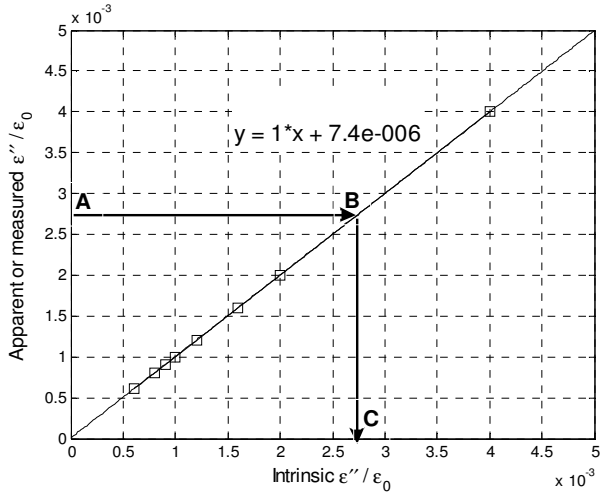

(b)

Figure 5-8 The one-to-one relationship of calculated (or measured) and intrinsic permittivities: (a) Real part; (b) Imaginary part

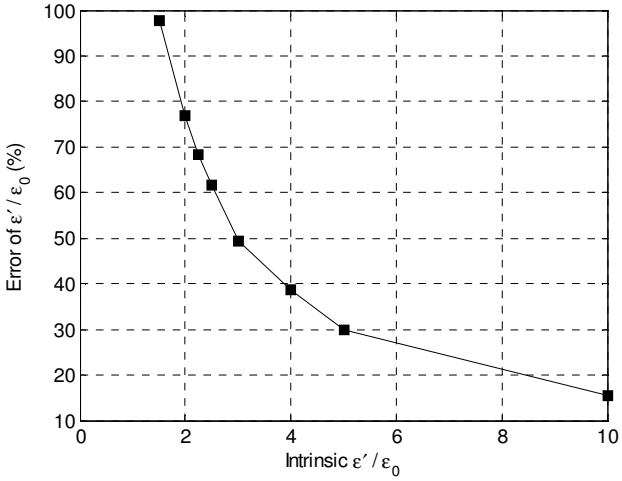

(a)

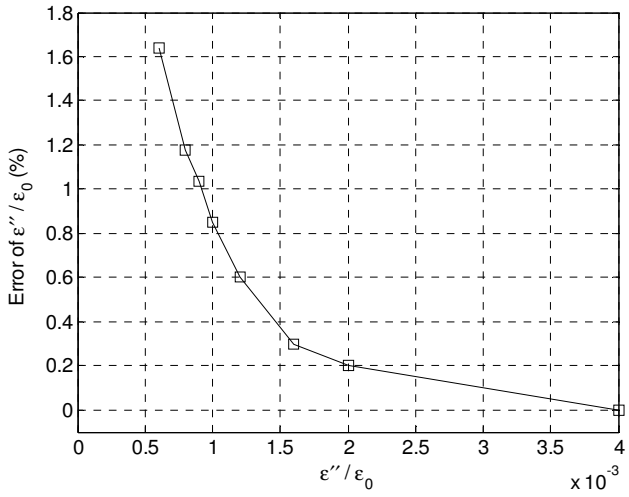

(b)

Figure 5-9 The error between calculated and intrinsic permittivity versus different intrinsic permittivity ($\tan\delta = 0.0004$, and $\varepsilon'' = \varepsilon' \cdot \tan\delta$) : (a) real part; (b) imaginary part

Table 5-2 Detailed values of the measured and intrinsic permittivities

Real part of permittivity			Imaginary part of permittivity		
Assumed intrinsic value (ε'_{in})	Measured value (ε'_{m})	*Error_ε'* (%)	Assumed intrinsic value (ε''_{in})	Measured value (ε''_{m})	*Error_ε''* (%)
1.5	2.9643	97.62	0.000600	0.000610	1.64
2	3.5364	76.82	0.000800	0.000809	1.18
2.25	3.7877	68.34	0.000900	0.000909	1.03
2.5	4.0395	61.58	0.001000	0.001009	0.85
3	4.4816	49.39	0.001200	0.001207	0.60
4	5.5469	38.67	0.001600	0.001606	0.35
5	6.4922	29.84	0.002000	0.002004	0.20
10	11.558	15.58	0.004000	0.004000	0.00

Although the error of measurable imaginary permittivity is rather small, it can also be determined. For samples with different dimensions, curves of measured permittivity versus intrinsic value will change somewhat, yet can be generated in a similar manner. Therefore, intrinsic complex permittivity can be obtained by this type of correction curves.

5.1.3 Modifications on the correction curve

The modification on the correction curve may come with the height and radius of sample, and the size of electrode.

Keeping the fully covered two-parallel-electrode configuration and the sample height d=30 mm, the above two graphs of Figure 5-10 show the error of measurable complex permittivity in those cases when the sample has different inner (R_1) or outer (R_2) radius, e.g. R_1= 44 mm and R_2=56 mm in "Case B". Since the width of coaxial XLPE sample as well as electrode area is different in these four cases (Case A, Case B, Case C, and Case D), the fringing effect is definitely different, which will result in different measurement error. The error in Case A is smaller than in Case B, Case C, and Case D, due to the smaller aspect ratio $b = d / w = d /[2\pi(R_2\text{^}2 - R_1\text{^}2)]$.

Besides, if the sample size contain R_1=32mm, R_2=56mm, and d=30mm, the placement of electrode has also an effect on the difference between measurable and intrinsic permittivity as shown in the below two graphs of Figure 5-10. When the electrode is placed in the middle part of sample (Case F), it is the worst situation. Because XLPE instead air is the ambient around the sample part between the two parallel electrodes, the fringing effect is most serious. The situations of Case E and Case G are better than Case F, since there is only one side of XLPE ambient, yet still worse than Case A. Furthermore, the error of imaginary part of permittivity is rather obvious in Case E, Case F, and Case G compared with Case B, Case C, and Case D. This demonstrates that the size and position of electrode is a very important factor to measurement accuracy.

Figure 5-11 shows the influence of sample height d, while the inner and outer radius and electrode size consisting with those of Case A. It is clear that the error increases monotonically with the height of sample. This is also due to the aspect ratio of electrode

configuration, which influences the fringing effect. From Figure 5-10 and Figure 5-11, the real part of permittivity always shows large error around 100%, while the measurable imaginary permittivity is most believably below 3%, except the cases with incompletely covered electrode.

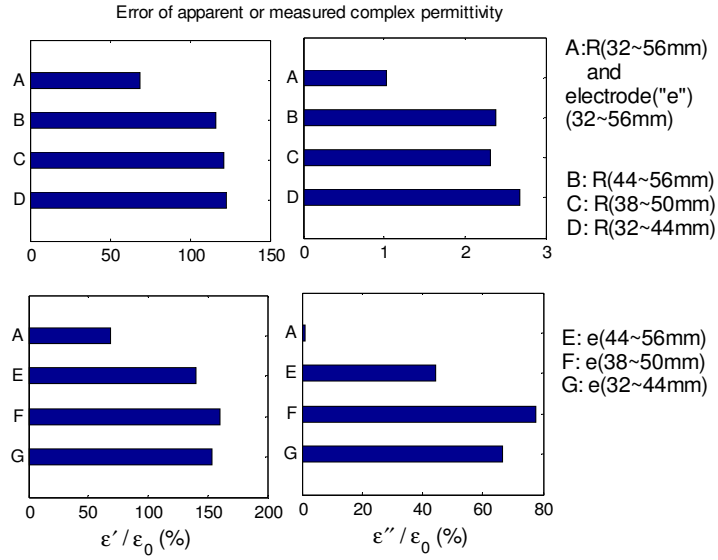

Figure 5-10 The influences of sample radius (cases of B, C, and D) and electrode width (cases of E, F, and G) on the error of apparent or measured complex permittivity. Note: "M($r_1 \sim r_2$ mm)" denotes an inner radius of r_1 mm and an outer radius of r_2 mm.

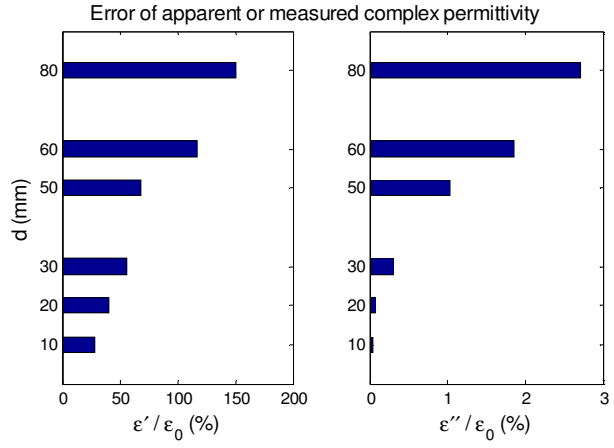

Figure 5-11 The influences of sample height and electrode width on the error of apparent or measured complex permittivity.

5.1.4 Measurement result

To verify the field-circuit coupled method, a simplified measurement is carried out and calculation procedure is preceded as following.

Firstly, an XLPE circular sample is prepared: its diameter D=37mm, its thickness d=2.5mm, and its smooth upper and lower surfaces are painted silver coatings as two parallel electrodes.

Then, on one hand, the impedance of sample is measured by using an impedance analyzer (HP 4294A with 16451B dielectric test fixture) and the real and imaginary parts are shown in Figure 5-12. There is some disturbance at the frequencies below 1 kHz for the real part of impedance, which is difficult to avoid at low frequency in usual experiment. From the two components of measured impedance, the real energy (P_d) and imaginary energy (Q_e) can be obtained by equation (5-13). And then complex permittivity can be determined, as shown in Figure 5-13. This is just the measured value which is influenced by the fringing effect. On the other hand, by assuming a certain permittivity of 2.25-j0.0009, mode matching method [200] or FDTD-converted FDFD method is applied to calculate the electric field energy contained in XLPE sample and ambient. The latter will take a long time to obtain the result, while the former is much faster.

At last, based on the circuit measurement result and field calculation, Newton-Raphson method [201] is applied to determine the intrinsic value of permittivity. Figure 5-14 shows the determined intrinsic permittivity. The real part is around 2.27, while the imaginary part is in the order of 10^{-3}. The values jump significantly at frequencies above 10 MHz, and even negative values come out for the imaginary part. These abnormal values may be resulted from the measurement equipment itself. For comparison, a measurement result by using three-electrode configuration, which is two parallel electrodes with a guard, is also presented in Figure 5-15. It is clear that the result is not as good as the proposed field-circuit coupled method, since the guard cannot remove all the influence of the fringing effect in real measurement.

Among these three results of measured by two-electrode without a guard, measured by two-electrode with a guard, and determined by field-circuit coupled method, real part of

permittivity is influenced significantly, while the imaginary part is always steady. This can be explained by the distribution characteristic of the electric energy stored in XLPE sample and ambient air.

It should be noted that the proposed method has some key steps: 1) carefulness should be taken during the measurement, such as removing the influence of cable inductance, 2) make sure the consistency of mathematics model and measurement configuration.

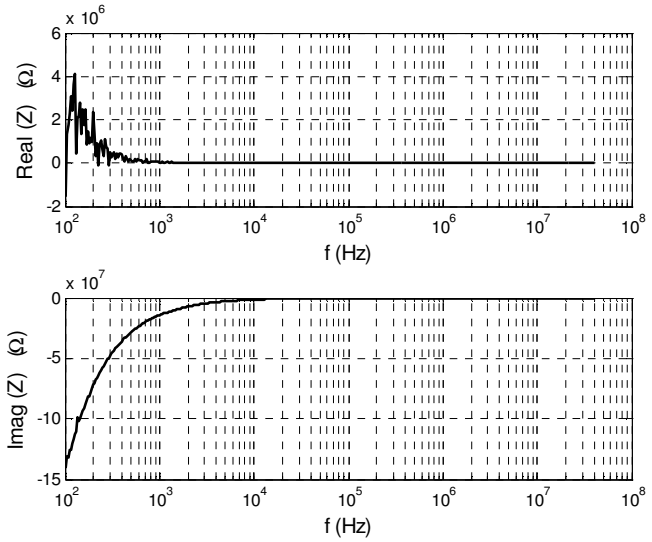

Figure 5-12 Measured real and imaginary parts of XLPE sample's impedance

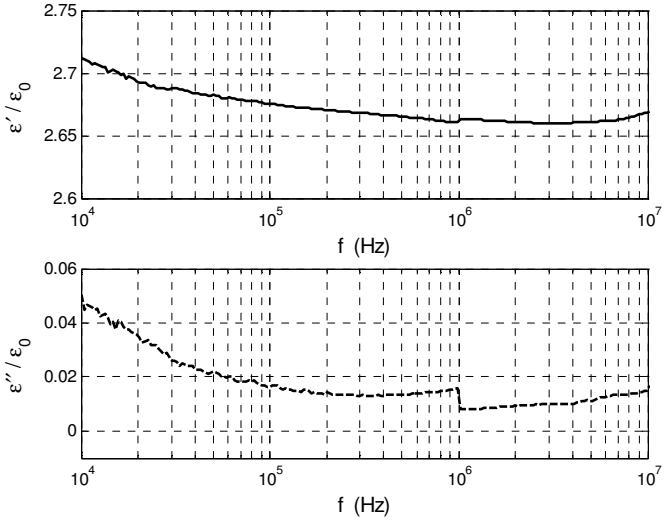

Figure 5-13 The permittivity calculated directly from the measured impedance

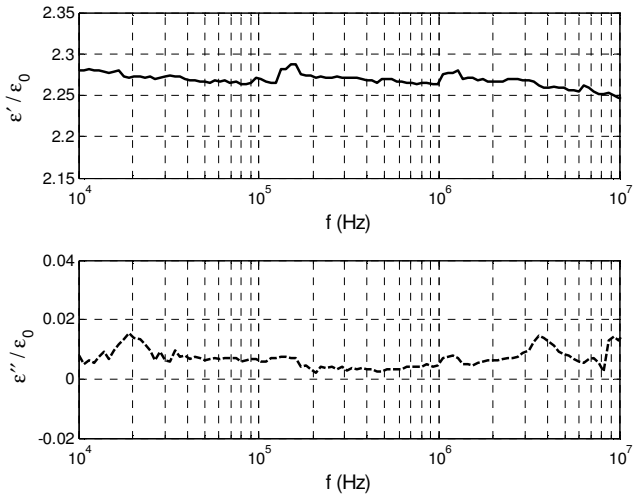

Figure 5-14 Determined real and imaginary parts of permittivity

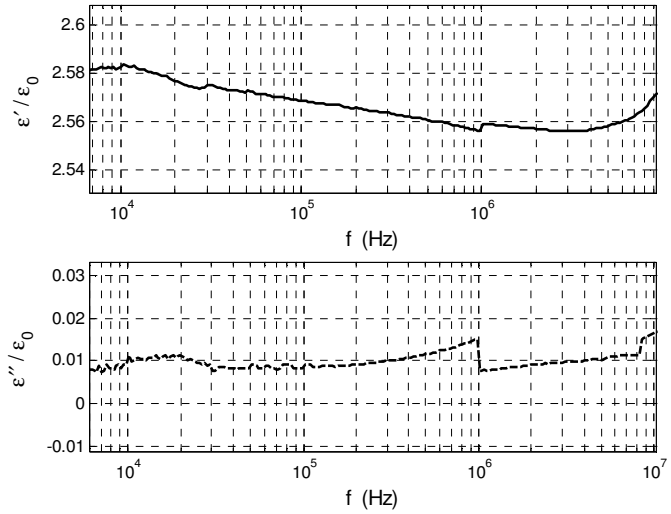

Figure 5-15 The measured complex permittivity by using three-electrode configuration (two parallel electrodes with guard)

In the same way as that for XLPE material, the field-circuit coupled method can be also applied to determine the intrinsic permittivity of semiconducting material.

5.2 Dimensional effects on the measurement of permittivity of semiconducting materials used in HV XLPE cable

One common method to detect PD is the measurement of the radial fields of the PD with sensitive field sensors [202]. In order to design and improve partial discharge field

sensors, an exact knowledge of the propagation characteristics of the cable is needed. Usually these sensors couple PD signals through the outer semiconducting layer. To study the coupling mechanisms and design an effective sensor, it is essential to determine the intrinsic not apparent permittivity of semicon.

The extruded semiconducting layers provide a smooth interface between the conductors and the dielectric avoiding electric field stress enhancement in order to avoid any partial discharges. In HV cables, the interface between the conductors and electrical insulation is made of relatively thin semiconducting layers with extremely high permittivity, which is typically in the range of 20 to 4000 for frequencies from 0.1 to 1000 MHz [28].

As have been demonstrated that dimensional effect occurs in the characterization of other materials, such as Mn-Zn material [203], it is expected that the dimension of the sample will play a role in the measurement of the permittivity of the semiconducting material, due to its high permittivity. So far, no detailed quantitative study has been reported on how much influence the samples' dimensions impose on the measurement of intrinsic permittivity of semiconducting material. This section aims to come to a quantitative conclusion on how much the influence is.

In the following paragraphs, a detailed study, based on a mathematical model, will be carried out to illustrate the influence of sample dimension on the measurement of permittivity of semiconducting material.

5.2.1 Rectangular parallel plate capacitor model of semiconducting layer

Figure 5-16 shows the different layers of a typical XLPE cable. To measure the frequency-dependent properties of semiconducting material, the sample is usually a small part cut from the cable. Its rectangular parallel plate capacitor model under study is shown in Figure 5-17 (a). The top view of the capacitor and the corresponding coordinate system is shown in Figure 5-17 (b).

Figure 5-16 XLPE cable

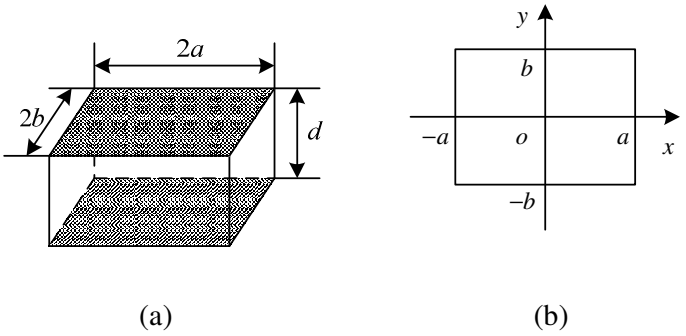

(a) (b)

Figure 5-17 A capacitor model of semiconducting material under study

Due to the high permittivity of semiconducting material, fringing effect of the capacitor can be neglected. The equation governing the electric fields in the capacitor and the boundary condition can be written as below:

$$\frac{\partial^2 E_z}{\partial x^2}+\frac{\partial^2 E_z}{\partial y^2}+\omega^2\mu\varepsilon E_z=0 \tag{5-21}$$

$$E_z=\frac{V}{d},\ (x=\pm a,\ y=\pm b) \tag{5-22}$$

Suppose that the total electric fields is decomposed into the incident electric fields E_0 and the induced electric fields E_i, and let E_0 be V/d which equals the electric fields at the edge of the capacitor electrodes. The above equation and the boundary condition can be rewritten as:

$$\frac{\partial^2 E_i}{\partial x^2}+\frac{\partial^2 E_i}{\partial y^2}+k^2 E_i=-k^2 E_0 \tag{5-23}$$

$$E_i=0,\ (x=\pm a,\ y=\pm b) \tag{5-24}$$

where $$k^2=-\gamma^2=\omega^2\mu\varepsilon \tag{5-25}$$

For the solution of equation (5-23), the green's function satisfying the following Helmholtz's equation is considered first:

$$\left(\frac{\partial^2}{\partial x^2}+\frac{\partial^2}{\partial y^2}+k^2\right)G=-\delta(x-w)\delta(x-v) \tag{5-26}$$

$$G=0,\ (x=\pm a,\ y=\pm b) \tag{5-27}$$

The solution to equations (5-26) and (5-27) is

$$G(x, y \,|\, w, v) = \sum_{m=1}^{\infty} \sum_{n=1}^{\infty} C_{mn} u_{mn}(x, y) \tag{5-28}$$

where

$$u_{mn} = \cos\frac{(2m-1)\pi x}{2a} \cos\frac{(2n-1)\pi y}{2b} \tag{5-29}$$

By substituting equation (5-28) into equation (5-26), the coefficient C_{mn} can be obtained as follows by utilization of the orthogonality of the sinusoids:

$$C_{mn} = \frac{1}{ab(k_{mn}^2 - k^2)} \cos\frac{(2m-1)\pi w}{2a} \cos\frac{(2n-1)\pi v}{2b} \tag{5-30}$$

where

$$k_{mn}^2 = [\frac{(2m-1)\pi}{2a}]^2 + [\frac{(2n-1)\pi}{2b}]^2 \tag{5-31}$$

Thus, equation (5-28) can be rewritten as:

$$G(x, y \mid w, v) = \frac{1}{ab} \sum_{m=1}^{\infty} \sum_{n=1}^{\infty} \frac{\cos\frac{(2m-1)\pi x}{2a} \cos\frac{(2n-1)\pi y}{2b}}{[\frac{(2m-1)\pi}{2a}]^2 + [\frac{(2n-1)\pi}{2b}]^2 - k^2}$$

$$\times \cos\frac{(2m-1)\pi w}{2a} \cos\frac{(2n-1)\pi v}{2b} \tag{5-32}$$

The solution to equation (5-23) with the boundary condition of (5-24) can be obtained by performing the following integration:

$$E_i(x, y) = \int_{-b}^{b} \int_{-a}^{a} G(x, y \mid w, v) k^2 E_0 \, dw dv$$

$$= k^2 E_0 \frac{16}{\pi^2} \sum_{m=1}^{\infty} \sum_{n=1}^{\infty} \frac{(-1)^{m+n}}{(2m-1)(2n-1)} \times \frac{\cos\frac{(2m-1)\pi x}{2a} \cos\frac{(2n-1)\pi y}{2b}}{[\frac{(2m-1)\pi}{2a}]^2 + [\frac{(2n-1)\pi}{2b}]^2 - k^2} \tag{5-33}$$

The electric fields inside the capacitor can be written as:

$$E_z = E_i + E_0 \tag{5-34}$$

The complex power supplied to the capacitor can be written as [31]:

$$S = S_E + S_H \tag{5-35}$$

where S_E is the complex power related to the electric field, which is written as [31] :

$$S_E = \iiint (j\omega\varepsilon)^* \mid E \mid^2 dv = 4d \int_0^b \int_0^a (j\omega\varepsilon)^* \mid E_z \mid^2 dxdy \tag{5-36}$$

and $S_{\mathrm{H}} \approx 0$ due to the rather small permeability $\mu = \mu_0$.

The impedance of the capacitor can be obtained as follows:

$$Z = \frac{\mid V \mid^2}{S^*} \tag{5-37}$$

The current flowing through the capacitor for a given voltage V can be derived as follows:

$$I = j\omega\varepsilon \int_{-b}^{b} \int_{-a}^{a} E_z dxdy = j\omega\varepsilon \int_{-b}^{b} \int_{-a}^{a} (E_i + E_0) dxdy$$

$$= j\omega\varepsilon k^2 E_0 (\frac{16}{\pi^2})^2 ab \sum_{m=1}^{\infty} \sum_{n=1}^{\infty} \frac{1}{(2m-1)^2 (2n-1)^2}$$

$$\times \frac{1}{[\frac{(2m-1)\pi}{2a}]^2 + [\frac{(2n-1)\pi}{2b}]^2 - k^2} + j\omega\varepsilon 4abE_0 \tag{5-38}$$

The impedance of the capacitor can also be written as follows:

$$Z = \frac{V}{I} \tag{5-39}$$

Although the results of equations (5-37) and (5-39) are the same, the efficiency to solve the impedance by using equation (5-39) is apparently much higher than that by using equation (5-37).

5.2.2 Influence of sample's dimensions on apparent complex permittivity

The apparent permittivity could deviate from the intrinsic value greatly. The deviation is due to the distortion of the electric field distribution in the capacitor model, which is the result of dimensional effects. For further illustration of the influence of the sample's dimensions on the deviation, the intrinsic complex permittivity is assumed as that derived from the measured result in reference [28]. The real part of permittivity is referred directly and the imaginary part is deducted by using the relationship of $\sigma = \omega\varepsilon''$ [19].

Five samples are assumed to have the dimensions as in Table 5-3. Blocks 1, 2, and 3 are samples with typical dimensions used in experiments, while Block 4 and Block 5 are assumed as extreme cases. The calculated magnitudes and phase angles of the five capacitors according to equation (5-39) are shown in Figure 5-18 and Figure 5-19, respectively. The complex permittivity can be expressed by the measured impedance of the capacitor as follows [31]:

$$\varepsilon = \frac{d}{j\omega ZA} = -j\frac{dZ^*}{\omega |Z|^2 A} \tag{5-40}$$

The intrinsic complex permittivity and the calculated apparent complex permittivity for the five blocks are shown in Figure 5-20 and Figure 5-21. For the first three samples, the dimensional influence on the apparent complex permittivity can be easily identified in the frequency range above 100 MHz, which is necessary to be recognized since the often seen sub-nanosecond current rise time of PDs in XLPE leads to an optimal bandwidth of 100 to 500 MHz [55].

It should be noted that negative values of the real part of the apparent complex permittivity are found sometimes. Actually, from Figure 5-19, it can be seen that the phase angles can become positive at some frequencies for the block with large cross sectional areas. This illustrates that the capacitor becomes inductive at those frequencies. From equation (5-40) one can see that when the impedance becomes inductive, the real part of the apparent complex permittivity will become negative, as shown in Figure 5-20.

To understand the above phenomenon physically, variation of the electric field distribution in block 5 along the x axis versus frequencies when the applied voltage is fixed at 0.5 V is shown in Figure 5-22. The dimensional resonance at around 26 MHz and the pronounced skin effect above a few hundred MHz are easily identified. Figure 5-23 shows the electric field distribution in block 5 at 26 MHz. It can be seen that the electric field is rather distorted, far from the uniform distributions at low frequencies.

For exact identification of the resonance frequency, variation of the electric fields at the center of the five blocks versus frequencies is shown in Figure 5-24. As one can see from the analysis in the previous section, for a given incident electric field, the electric field distribution in the capacitor is not affected by the thickness, *d*. In other words, for two

blocks with the same upper and bottom faces but different thickness, the measured apparent permittivities are the same. Comparing the resonant frequencies of the five blocks found in Figure 5-24 can lead to the conclusion that both the area ($2a \times 2b$) and the shape (a:b) have influences on the apparent complex permittivity. Generally speaking, for the blocks with the same ratio of a:b, the resonant frequency of the one with larger area of $2a \times 2b$ is lower. For the blocks with the same area of $2a \times 2b$, the resonant frequency of the one with square cross section is lower.

From Figure 5-18, Figure 5-20 and Figure 5-21 , one can see that due to dimensional resonance, the magnitude of the impedance of the block capacitor may have a local minimum value for blocks 4 and 5, not for those of small size such as blocks 1, 2 and 3. A more obvious indication of the existence of the dimensional resonance is the resonant-type phenomena in the real part of the apparent complex permittivity as shown in Figure 5-20 although the maximum of the real part of the apparent complex permittivity usually does not occur at the exact frequency where dimensional resonance occurs, as compared with Figure 5-24.

Since the measurable apparent complex permittivity deviates from its intrinsic value, mathematical methods such as Newton-Raphson method [30], should be adopted to determine the intrinsic complex permittivity from its measured value.

Table 5-3 Dimensions of the five assumed bocks

Block No.	2a (mm)	2b (mm)	d (mm)
1	5	5	2
2	10	5	2
3	10	10	2
4	50	20	2
5	100	100	2

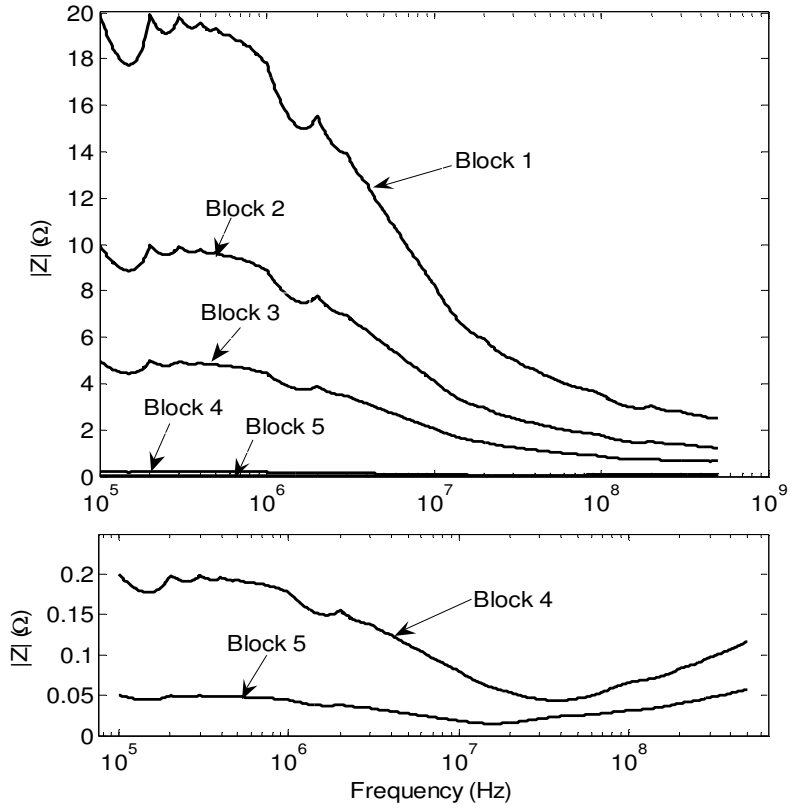

Figure 5-18 Calculated (apparent) magnitude of impedance

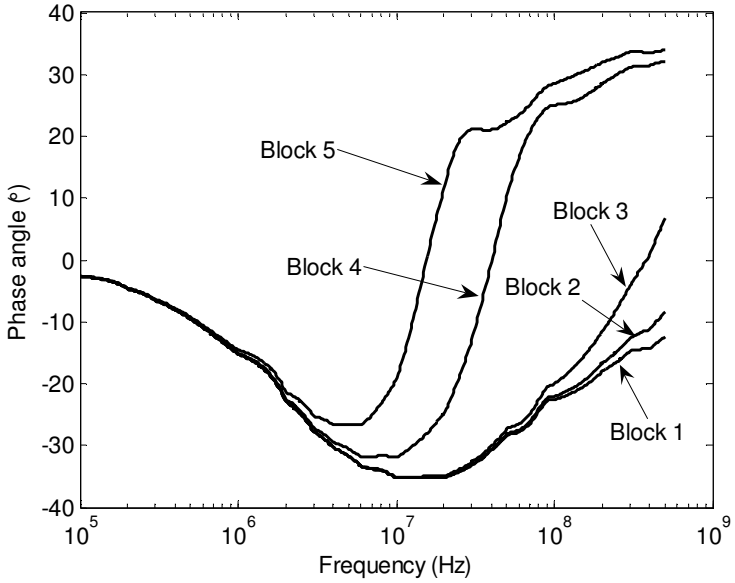

Figure 5-19 Calculated phase angle of impedance

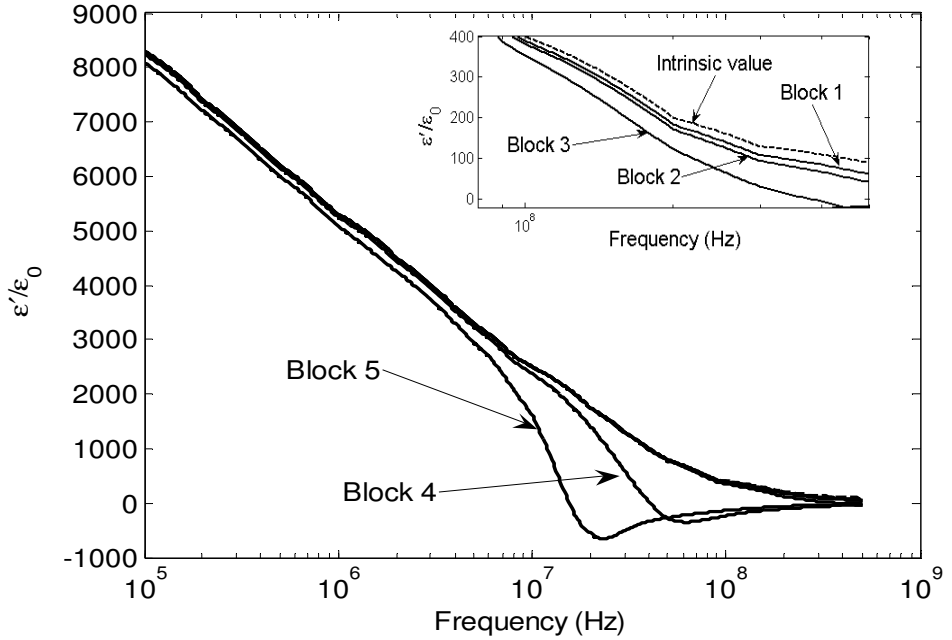

Figure 5-20 Calculated real part of permittivity

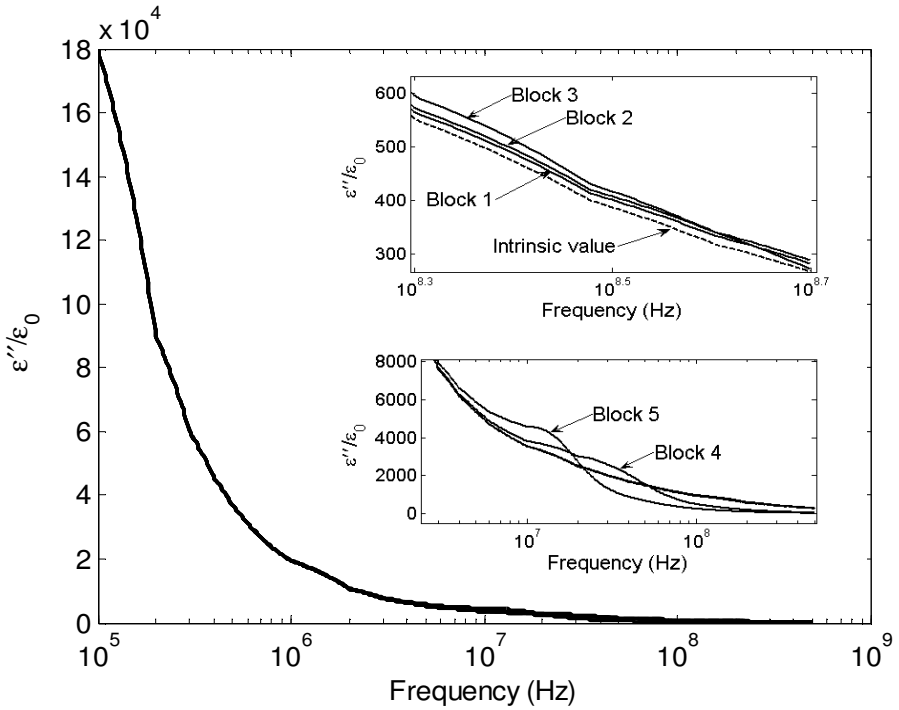

Figure 5-21 Calculated imaginary part of permittivity

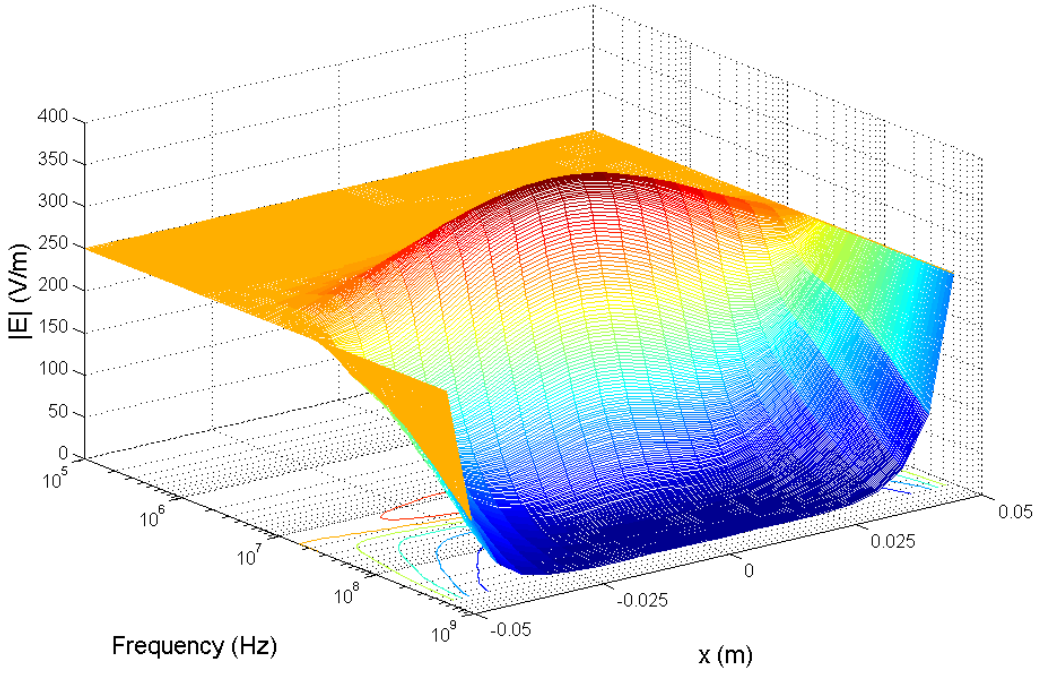

Figure 5-22 Electric field distribution along x-axis at *y*=0 vs. frequency (Block 5)

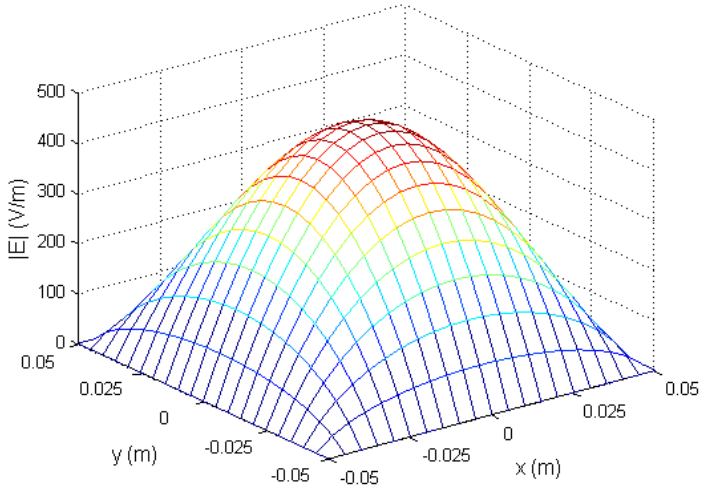

Figure 5-23 Electric field distribution at the frequency where the distortion is the most (Block 5)

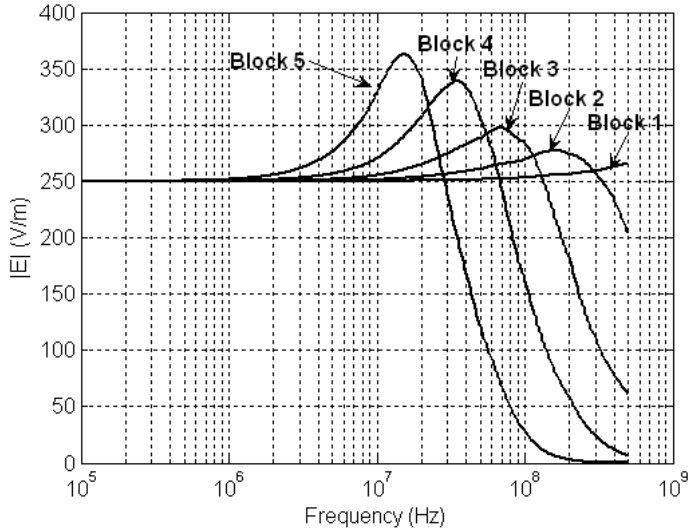

Figure 5-24 Electric field strength at the center (x=0, y=0) of blocks vs. frequency

5.3 Newton-Raphson method to determine the intrinsic permittivity of materials of XLPE cable

A field-circuit coupled method was introduced in [30] to tackle the dimensional effect that occurs in a material with high permittivity and conductivity simultaneously or a material with high permittivity and permeability simultaneously. This method is applied to two-parallel-electrode configuration of XLPE insulation in Section 5.1. And the dimensional effect of semiconducting material of XLPE cable is also studied in Section 5.2. In this section, these two kinds of materials are considered at the same time in two types of models. Newton-Raphson method is applied to find the measured value and therefore to determine the intrinsic value of permittivity based on the measurement result.

5.3.1 Model configuration

A XLPE cable segment is cut from a 230kV XLPE cable. The inner conductor is extracted and the other parts out of outer semiconducting layer are also peeled off. The model is shown as in Figure 5-25. The dimensional parameters of this segment are: h=55mm; a=29 mm; b=32 mm; c=56 mm; d=58 mm.

As known, the complex permittivity satisfies the relation of $\varepsilon^* = \varepsilon' - j\varepsilon''$. This sample consists of two types of materials: XLPE insulation and inner/outer semiconducting layer.

To determine their complex permittivity, there should be four unknown parameters: $\varepsilon_2^{'}$ and $\varepsilon_2^{''}$ for XLPE insulation material, $\varepsilon_1^{'}(\varepsilon_3^{'})$ and $\varepsilon_1^{''}(\varepsilon_3^{''})$ for semiconducting material.

Two-parallel-electrode configuration is usually applied in normal measurement to determine the real and imaginary parts of complex permittivity of certain kind of material. Since two equations can be obtained from each model according to the relations of resistance and capacitance, four equations from two models are needed to determine the complex permittivity of XLPE and semicon. Different models with two-parallel-electrode configuration are shown in Figure 5-26. For Model A, silver paint is coated on the top and bottom cross sections of the XLPE cable segment as two parallel electrodes; for Model B, the surfaces of inner and outer semicon are coated with silver paint as electrodes.

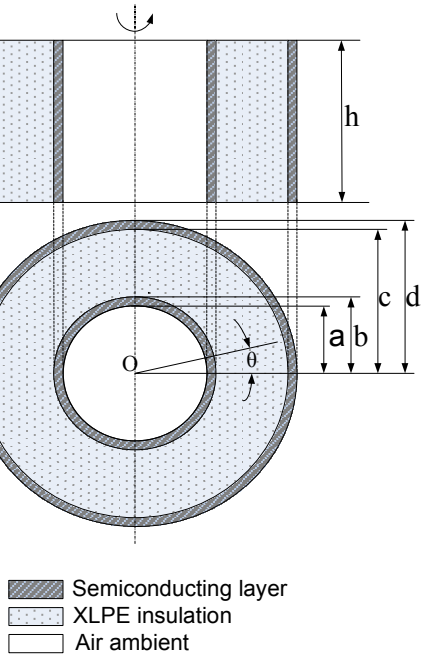

Figure 5-25 Configuration of XLPE cable segment

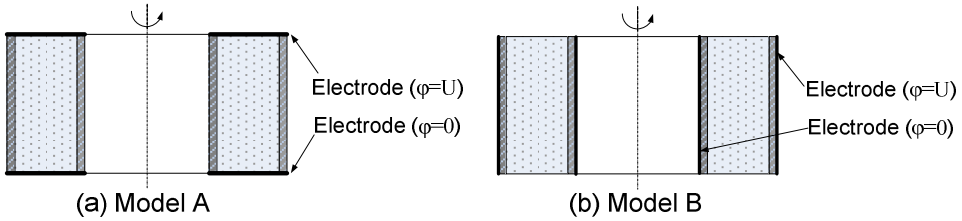

Figure 5-26 Electrode configuration of Model A and Model B

For Model A (with top-bottom electrodes), normal relations of resistance and capacitance are satisfied:

$$\frac{1}{R_{\mathrm{pA}}} = \frac{1}{R_{\mathrm{p1}}} + \frac{1}{R_{\mathrm{p2}}} + \frac{1}{R_{\mathrm{p3}}} \tag{5-41}$$

$$C_{\mathrm{pA}} = C_{\mathrm{p1}} + C_{\mathrm{p2}} + C_{\mathrm{p3}} \tag{5-42}$$

where subscript "p" denotes "parallel equivalent", R_{pA}, R_{p1}, R_{p2}, and R_{p3} (C_{pA}, C_{p1}, C_{p2}, and C_{p3}) is the parallel equivalent resistance (capacitance) of Model A, inner semicon, XLPE insulation, and outer semicon respectively,

$$R_{\mathrm{p1}} = \frac{1}{\omega \varepsilon_1^{''}} \cdot \frac{h}{\pi (b^2 - a^2)} \tag{5-43}$$

$$R_{\mathrm{p2}} = \frac{1}{\omega \varepsilon_2^{''}} \cdot \frac{h}{\pi (c^2 - b^2)} \tag{5-44}$$

$$R_{\mathrm{p3}} = \frac{1}{\omega \varepsilon_3^{''}} \cdot \frac{h}{\pi (d^2 - c^2)} \tag{5-45}$$

$$C_{\mathrm{p1}} = \varepsilon_1^{'} \cdot \frac{\pi (b^2 - a^2)}{h} \tag{5-46}$$

$$C_{\mathrm{p2}} = \varepsilon_2^{'} \cdot \frac{\pi (c^2 - b^2)}{h} \tag{5-47}$$

$$C_{\mathrm{p3}} = \varepsilon_3^{'} \cdot \frac{\pi (d^2 - c^2)}{h} \tag{5-48}$$

Substitute equations (5-43) - (5-48) into equations (5-41) and (5-42), and take note that $\varepsilon_1^{'} = \varepsilon_3^{'}$, $\varepsilon_1^{''} = \varepsilon_3^{''}$ since inner and outer semicon are made of the same material, a new couple of equations can be obtained:

$$\frac{1}{R_{\mathrm{PA}}} = \omega \varepsilon_1^{''} \cdot \frac{\pi (b^2 - a^2 + d^2 - c^2)}{h} + \omega \varepsilon_2^{''} \cdot \frac{\pi (c^2 - b^2)}{h} \tag{5-49}$$

$$C_{\mathrm{PA}} = \varepsilon_1^{'} \cdot \frac{\pi (b^2 - a^2 + d^2 - c^2)}{h} + \varepsilon_2^{'} \cdot \frac{\pi (c^2 - b^2)}{h} \tag{5-50}$$

For Model B (with inner-outer electrodes), the calculation is some more laborious but the line is clear and single. Classic formulas are applied here to calculate those equivalent-circuit parameters. Although they are suitable for infinite-length cable and error will

hence occur for the short cable segment, the Newton-Raphson method can help determine the intrinsic value later.

For semiconducting layers,

$$R_{\mathrm{P1}} = \int_a^b \frac{1}{\omega \varepsilon_1^{''}} \cdot \frac{dr}{2\pi r h} = \frac{1}{\omega \varepsilon_1^{''}} \cdot \frac{\ln(b/a)}{2\pi h} \tag{5-51}$$

$$C_{\mathrm{P1}} = \varepsilon_1^{'} \cdot \frac{2\pi h}{\ln(b/a)} \tag{5-52}$$

$$R_{\mathrm{P3}} = \frac{1}{\omega \varepsilon_3^{''}} \cdot \frac{\ln(d/c)}{2\pi h} \tag{5-53}$$

$$C_{\mathrm{P3}} = \varepsilon_3^{'} \cdot \frac{2\pi h}{\ln(d/c)} \tag{5-54}$$

where $R_{\mathrm{p1}}$and R_{p3} ($C_{\mathrm{p1}}$and C_{p3}) is the parallel equivalent resistance (capacitance) of inner and outer semicon, respectively.

For XLPE part,

$$R_{\mathrm{P2}} = \frac{1}{\omega \varepsilon_2^{''}} \cdot \frac{\ln(c/b)}{2\pi h} \tag{5-55}$$

$$C_{\mathrm{P2}} = \varepsilon_2^{'} \cdot \frac{2\pi h}{\ln(c/b)} \tag{5-56}$$

where R_{p2} (C_{p2}) is the parallel equivalent resistance (capacitance) of XLPE insulation.

Based on the definitions in circuit theory as follow:

$$Z = R_{\mathrm{S}} + \frac{1}{j\omega C_{\mathrm{S}}} \tag{5-57}$$

$$Y = G + j\omega C_{\mathrm{P}} = \frac{1}{R_{\mathrm{P}}} + j\omega C_{\mathrm{P}} \tag{5-58}$$

$$Z = \frac{1}{Y} \tag{5-59}$$

the conversion of parallel equivalent parameter to serial equivalent parameter satisfies:

$$R_{\mathrm{S}} = \frac{R_{\mathrm{P}}}{1 + \omega^2 C_{\mathrm{P}}^2 R_{\mathrm{P}}^2} \tag{5-60}$$

$$C_S = C_P(1+\frac{1}{\omega^2 C_P^2 R_P^2}) \tag{5-61}$$

Thus R_{s1}, R_{s2}, R_{s3}, C_{s1}, C_{s2}, and C_{s3} can be obtained, where subscript "s" denotes "series equivalent".

From the relation of

$$R_{SB} = R_{S1} + R_{S2} + R_{S3} \tag{5-62}$$

$$\frac{1}{C_{SB}} = \frac{1}{C_{S1}} + \frac{1}{C_{S2}} + \frac{1}{C_{S3}} \tag{5-63}$$

and $\varepsilon_1^{'} = \varepsilon_3^{'},\ \varepsilon_1^{''} = \varepsilon_3^{''},$

the following equations can be derived:

$$R_{SB} = \frac{1}{2\pi h\omega}\cdot[\frac{\varepsilon_1^{''}}{(\varepsilon_1^{'})^2+(\varepsilon_1^{''})^2}\cdot\ln\frac{bd}{ac} + \frac{\varepsilon_2^{''}}{(\varepsilon_2^{'})^2+(\varepsilon_2^{''})^2}\cdot\ln\frac{c}{b}] \tag{5-64}$$

$$\frac{1}{C_{SB}} = \frac{1}{2\pi h}\cdot[\frac{\varepsilon_1^{'}}{(\varepsilon_1^{'})^2+(\varepsilon_1^{''})^2}\cdot\ln\frac{bd}{ac} + \frac{\varepsilon_2^{'}}{(\varepsilon_2^{'})^2+(\varepsilon_2^{''})^2}\cdot\ln\frac{c}{b}] \tag{5-65}$$

Colligate equations (5-49), (5-50), (5-64) and (5-65), and replace ε' and ε'' by $\varepsilon_r^{'}(=\varepsilon'/\varepsilon_0)$ and $\varepsilon_r^{''}(=\varepsilon''/\varepsilon_0)$ respectively, a set of equation group is set up as follows:

$$\frac{1}{R_{PA}} = A_1\cdot\varepsilon_{r1}^{''} + A_2\cdot\varepsilon_{r2}^{''} \tag{5-66}$$

$$\omega C_{PA} = B_1\cdot\varepsilon_{r1}^{'} + B_2\cdot\varepsilon_{r2}^{'} \tag{5-67}$$

$$R_{SB} = C_1\cdot\frac{\varepsilon_{r1}^{''}}{(\varepsilon_{r1}^{'})^2+(\varepsilon_{r1}^{''})^2} + C_2\cdot\frac{\varepsilon_{r2}^{''}}{(\varepsilon_{r2}^{'})^2+(\varepsilon_{r2}^{''})^2} \tag{5-68}$$

$$\frac{1}{\omega C_{SB}} = D_1\cdot\frac{\varepsilon_{r1}^{'}}{(\varepsilon_{r1}^{'})^2+(\varepsilon_{r1}^{''})^2} + D_2\cdot\frac{\varepsilon_{r2}^{'}}{(\varepsilon_{r2}^{'})^2+(\varepsilon_{r2}^{''})^2} \tag{5-69}$$

where, the coefficients are:

$$A_1 = B_1 = \frac{\omega\pi(d^2-c^2+b^2-a^2)\varepsilon_0}{h} \tag{5-70}$$

$$A_2 = B_2 = \frac{\omega\pi(c^2-b^2)\varepsilon_0}{h} \tag{5-71}$$

$$C_1 = D_1 = \frac{\ln(d/c) + \ln(b/a)}{2\pi h \varepsilon_0 \omega} \tag{5-72}$$

$$C_2 = D_2 = \frac{\ln(c/b)}{2\pi h \varepsilon_0 \omega} \tag{5-73}$$

The equations (5-66) - (5-69) link the measurable or apparent resistance (R) and capacitance (C) with intrinsic permittivity (ε^*) of materials. With a known frequency (ω) and sample dimensions (a, b, c, d and h), A, B, C, and D can be considered as constant coefficients calculated by using equations (5-70) – (5-73). Thus in mathematics the unknown complex permittivity (ε' and ε'') should be possibly derived from the measurement result (R_P, C_P, R_S, and C_S).

5.3.2 Measurement results

Using HP4195A Network Analyzer, the frequency spectrum of impedance of Models A and B was measured, and is shown in Figure 5-27. Because the aspect ratio of Model A is

$$b_A = h/w = h/[\pi(d^2 - a^2)] = 0.0069,$$

while that of Model B is

$$b_B = (d-a)/[h\pi(a+d)] = 0.0019,$$

the later capacitance configuration is in a better condition. At high-frequency part, the measurement result of Model A shows an inductive trend due to the transition of material or the influence of measurement cable.

From the measured impedance (Z_A or Y_A, and Z_B) of two models, R_{PA}, C_{PA}, R_{SB}, and C_{SB} could be also easily obtained based on the relationship shown as equations (5-57)-(5-59). That is rewritten as

$$\frac{1}{Z_A} = Y_A = \frac{1}{R_{PA}} + j\omega C_{PA},$$

$$Z_B = R_{SB} + \frac{1}{j\omega C_{SB}}.$$

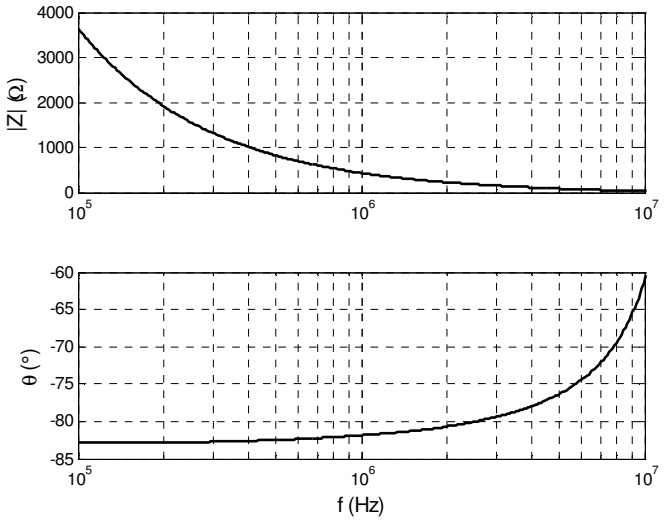

(a)

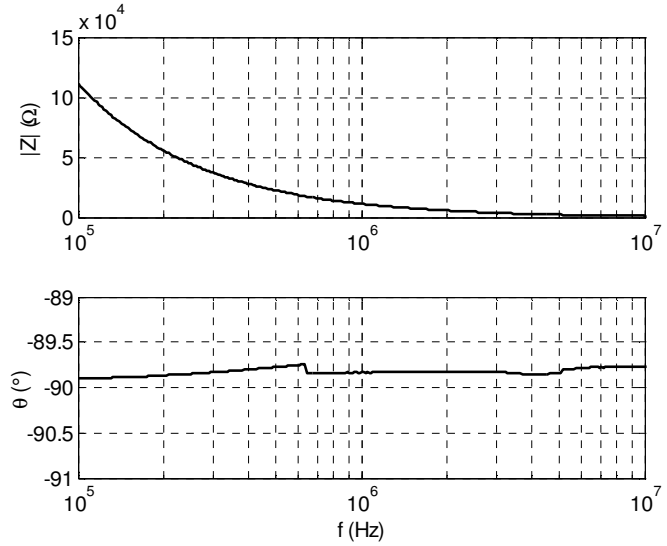

(b)

Figure 5-27 Measured impedance spectrum of Model A (a) and Model B (b)

To determine the unknown apparent complex permittivity $\varepsilon_1^*(=\varepsilon_1^{'}-j\varepsilon_1^{''})$ and $\varepsilon_2^*(=\varepsilon_2^{'}-j\varepsilon_2^{''})$, the Newton-Raphson method (Appendix C) is applied. And the iteration equation of the Newton-Raphson method can be written as equation (5-74):

$$\begin{bmatrix} \varepsilon_{r1}^{'}(n+1) \\ \varepsilon_{r2}^{'}(n+1) \\ \varepsilon_{r1}^{''}(n+1) \\ \varepsilon_{r2}^{''}(n+1) \end{bmatrix} = \begin{bmatrix} \varepsilon_{r1}^{'}(n) \\ \varepsilon_{r2}^{'}(n) \\ \varepsilon_{r1}^{''}(n) \\ \varepsilon_{r2}^{''}(n) \end{bmatrix} - J^{-1} \begin{bmatrix} f_1 - y_1 \\ f_2 - y_2 \\ f_3 - y_3 \\ f_4 - y_4 \end{bmatrix} \tag{5-74}$$

where

$$f_1 = A_1 \cdot \varepsilon_{r1}^{''} + A_2 \cdot \varepsilon_{r2}^{''} \tag{5-75}$$

$$f_2 = B_1 \cdot \varepsilon_{r1}^{'} + B_2 \cdot \varepsilon_{r2}^{'} \tag{5-76}$$

$$f_3 = C_1 \cdot \frac{\varepsilon_1^{''}}{(\varepsilon_1^{'})^2 + (\varepsilon_1^{''})^2} + C_2 \cdot \frac{\varepsilon_2^{''}}{(\varepsilon_2^{'})^2 + (\varepsilon_2^{''})^2} \tag{5-77}$$

$$f_4 = D_1 \cdot \frac{\varepsilon_1^{'}}{(\varepsilon_1^{'})^2 + (\varepsilon_1^{''})^2} + D_2 \cdot \frac{\varepsilon_2^{'}}{(\varepsilon_2^{'})^2 + (\varepsilon_2^{''})^2} \tag{5-78}$$

A_1, A_2, B_1, B_2, C_1, C_2, D_1, and D_2 are the same as in equations (5-70)-(5-73),

$$y_1 = \frac{1}{R_{\mathrm{PA}}} \tag{5-79}$$

$$y_2 = \omega C_{\mathrm{PA}} \tag{5-80}$$

$$y_3 = R_{\mathrm{PB}} \tag{5-81}$$

$$y_4 = \frac{1}{\omega C_{\mathrm{PB}}} \tag{5-82}$$

$$J = \begin{bmatrix} \partial f_1 / \partial \varepsilon_{r1}^{'} & \partial f_1 / \partial \varepsilon_{r2}^{'} & \partial f_1 / \partial \varepsilon_{r1}^{''} & \partial f_1 / \partial \varepsilon_{r2}^{''} \\ \partial f_2 / \partial \varepsilon_{r1}^{'} & \partial f_2 / \partial \varepsilon_{r2}^{'} & \partial f_2 / \partial \varepsilon_{r1}^{''} & \partial f_2 / \partial \varepsilon_{r2}^{''} \\ \partial f_3 / \partial \varepsilon_{r1}^{'} & \partial f_3 / \partial \varepsilon_{r2}^{'} & \partial f_3 / \partial \varepsilon_{r1}^{''} & \partial f_3 / \partial \varepsilon_{r2}^{''} \\ \partial f_4 / \partial \varepsilon_{r1}^{'} & \partial f_4 / \partial \varepsilon_{r2}^{'} & \partial f_4 / \partial \varepsilon_{r1}^{''} & \partial f_4 / \partial \varepsilon_{r2}^{''} \end{bmatrix} \tag{5-83}$$

The initial values for the iteration are $\varepsilon_{r1}^{'} = 8000$, $\varepsilon_{r1}^{''} = 1000$, referred to [28], and $\varepsilon_{r2}^{'} = 2.25$, $\varepsilon_{r2}^{''} = 0.0009$. The calculated measurable result is shown in Figure 5-28. For the part of semiconducting material, although the initial value is far from the calculation result, convergence can still be obtained in few times of iterations. The high permittivity results in high displacement current, which produces high magnetic field. The alternating magnetic field in turn produces a counteracting electric field, which effectively reduces the applied electric field and results in a smaller measured permittivity, as usually known dimensional effect. For the part of XLPE insulation, because the fringing effect has a significant influence, especially for Model B, the error between real parts of the measurable (apparent) permittivity and intrinsic value definitely exists, while the

imaginary part is hardly affected due to the almost no-loss property of ambient air. Therefore, additional work is needed to determine the intrinsic permittivity of the cable segment based on the measured value.

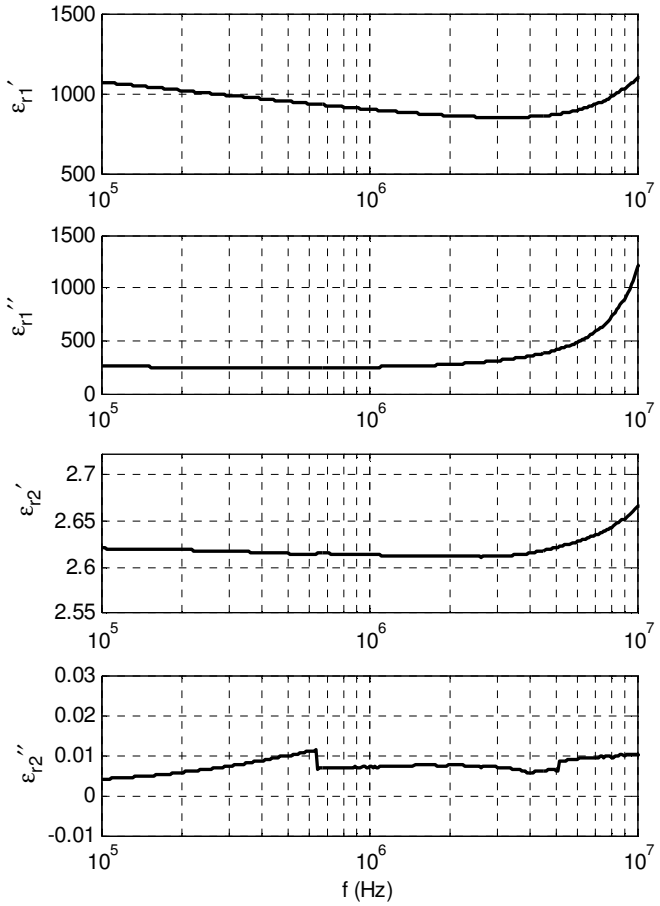

Figure 5-28 Measured complex permittivity for semicon (the top two graphs) and for XLPE insulation (the bottom two graphs).

5.3.3 Newton-Raphson iteration to determine intrinsic value

When an experiment is carried out to measure the permittivity for the material with an assumed intrinsic value of permittivity, the complex powers related to electric field and magnetic field can be read from the instrument, and according to the electromagnetic theory given in [31], they should be just the components of power that can be calculated by equations (5-84) and (5-85):

$$S_{\mathrm{E}} = \iiint (j\omega\varepsilon)^* \mid E \mid^2 dv \tag{5-84}$$

$$S_{\mathrm{H}} = \iiint j\omega\mu^* \mid H \mid^2 dv \tag{5-85}$$

If all the complex power is contained inside the material or the power due to the energy stored in ambient is negligible, one can expect that the measured value is identical to the assumed intrinsic value [31]. However, they are different in practical cases due to the fringing effect, since the energy is not only stored in XLPE insulation material but also stored in the ambient. In this paper, only permittivity is considered and for XLPE material where the influence of the magnetic field is negligible, the only remaining term is S_{E}. As shown in Figure 5-29, the electric field is distributed not only in XLPE cable segment but also in ambient air. The apparent permittivity is calculated by the measured total energy and the sample itself, which will definitely produce a difference from the intrinsic value. Due to the worse condition of capacitor configuration in Model A, it can bring a larger error than Model B.

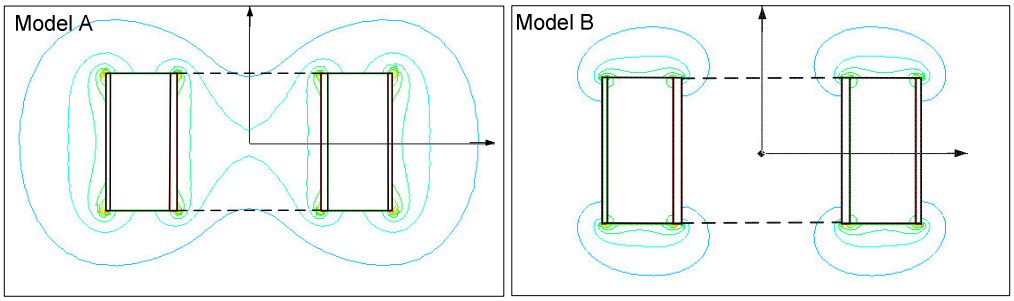

Figure 5-29 The distribution of electric field in Model A and B: (L) Model A (top-bottom electrodes); (R) Model B (inner-outer electrodes)

The intrinsic value should be determined by Newton-Raphson method at each frequency. First set the initial values of iteration based on the measurement result, then use the Newton-Raphson method to find the intrinsic value at that frequency. There is a faster way: using the obtained intrinsic permittivity at former point of frequency to act as the new initial value at the later frequency. In this procedure, it is important and usually difficult to calculate the power stored in the XLPE cable segment and ambient air from the electric field distribution. For simplicity, this task is achieved by Ansoft simulation software "MAXWELL", however, at the cost of time.

The procedure at one point of frequency is shown in the following part.

Set f =10^5Hz. The initial values of iteration i.e. the measured value, x_m, are:

$$x_m = \begin{bmatrix} 1072.8 \\ 2.6199 \\ 262.23 \\ 0.0040721 \end{bmatrix}$$

refer to the measurement result as shown in Figure 5-28.

Rewrite equation (5-74) here:

$$\begin{bmatrix} \varepsilon'_{r1}(n+1) \\ \varepsilon'_{r2}(n+1) \\ \varepsilon''_{r1}(n+1) \\ \varepsilon''_{r2}(n+1) \end{bmatrix} = \begin{bmatrix} \varepsilon'_{r1}(n) \\ \varepsilon'_{r2}(n) \\ \varepsilon''_{r1}(n) \\ \varepsilon''_{r2}(n) \end{bmatrix} - \boldsymbol{J}^{-1} \begin{bmatrix} f_1 - y_1 \\ f_2 - y_2 \\ f_3 - y_3 \\ f_4 - y_4 \end{bmatrix}$$

where

$$f_1 = \mathrm{Re}(S_A(\varepsilon'_{r1}, \varepsilon''_{r1}, \varepsilon'_{r2}, \varepsilon''_{r2})) \tag{5-86}$$

$$f_2 = \mathrm{Im}(S_A(\varepsilon'_{r1}, \varepsilon''_{r1}, \varepsilon'_{r2}, \varepsilon''_{r2})) \tag{5-87}$$

$$f_3 = \mathrm{Re}(S_B(\varepsilon'_{r1}, \varepsilon''_{r1}, \varepsilon'_{r2}, \varepsilon''_{r2})) \tag{5-88}$$

$$f_4 = \mathrm{Im}(S_B(\varepsilon'_{r1}, \varepsilon''_{r1}, \varepsilon'_{r2}, \varepsilon''_{r2})) \tag{5-89}$$

$$y_1 = P_A = \frac{|U|^2 \cos\theta_A}{|Z_A|} \tag{5-90}$$

$$y_2 = Q_A = \frac{|U|^2 \sin\theta_A}{|Z_A|} \tag{5-91}$$

$$y_3 = P_B = \frac{|U|^2 \cos\theta_B}{|Z_B|} \tag{5-92}$$

$$y_4 = Q_B = \frac{|U|^2 \sin\theta_B}{|Z_B|} \tag{5-93}$$

S_A (S_B) is the total electric power in XLPE cable segment and the ambient, P_A (P_B) or Q_A (Q_B) is the measured real or reactive electric power, $|U|$ is the magnitude of applied

voltage, $|Z_A|$ ($|Z_B|$) is the magnitude of measured impedance, θ_A (θ_B) is the phase angle of measured impedance of Model A (B), and J is the same as equation (5-83).

After several iterations, the intrinsic values of permittivity of XLPE and semicon are obtained. The result of detailed iteration procedure is shown in Table 5-4, and the convergence speed can be found in Figure 5-30 that all four procedures achieve convergence in five iterations.

Based on this result, those intrinsic values at higher frequencies can be determined in the same manner. In other words, the obtained result at the lower frequency can be considered as the initial or assumed value in the iteration procedure at the higher frequency. Indeed, for each frequency, the procedure can also be carried out separately maybe at the cost of more times of iterations. However, this method is still very effective.

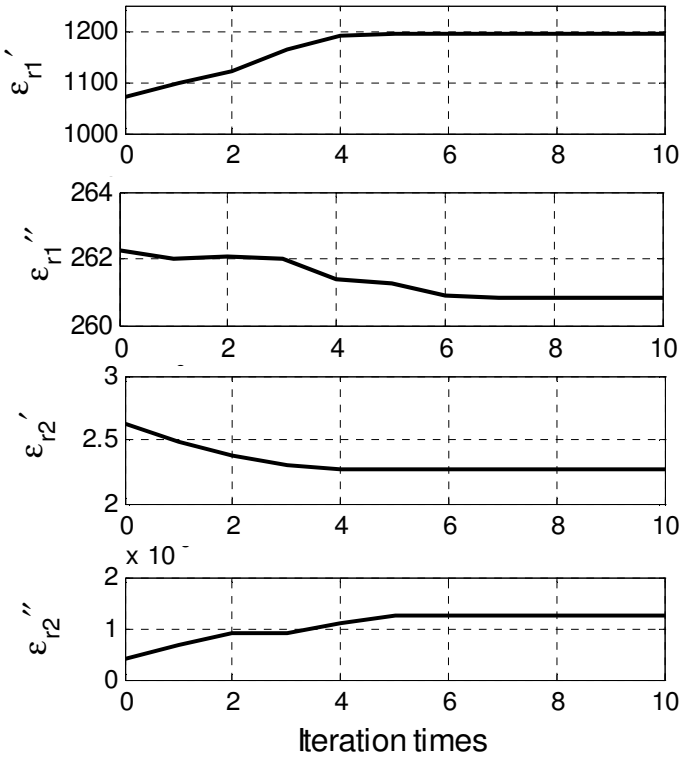

Figure 5-30 Determined intrinsic value of permittivity of XLPE insulation material and semiconducting material

Table 5-4 Determined intrinsic value in iterations

Iteration No.	$\varepsilon'_{r1}/\varepsilon_0$	$\varepsilon''_{r1}/\varepsilon_0$	$\varepsilon'_{r2}/\varepsilon_0$	$\varepsilon''_{r2}/\varepsilon_0$
0	1072	262.23	2.6199	0.00040721
1	1100	262.00	2.4800	0.00065466
2	1120	262.06	2.3700	0.00088472
3	1165	261.99	2.3000	0.00088701
4	1190	261.39	2.2700	0.00108840
5	1194.9	261.28	2.2690	0.0012366
6	1194.9	260.91	2.2690	0.0012366
7	1194.9	260.85	2.2690	0.0012366
8	1194.9	260.84	2.2690	0.0012366
9	1194.9	260.83	2.2690	0.0012366
10	1194.9	260.83	2.2690	0.0012366

5.4 Summary

To overcome the difficulties to apply current methods for practical cables, a more flexible method is presented in this chapter. The permittivity of XLPE is normally difficult to precisely be determined due to the fringing effect and therefore three-electrode geometry is usually necessary. This developed method is firstly verified by carrying out for XLPE material and theoretically practical to any material including semicon. For semiconducting material, the laboratory sample is normally in small size, but the dimensional effect for large size cannot be ignored in future field testing. The new developed method can find out such problem and do quantificational analysis. And this method can also be applicable in a complex situation: the permittivities of XLPE and semicon need to be determined simultaneously.

In Section 5.1, a field-circuit coupled method was introduced and a mathematical model was established to study the difference between the measurable and intrinsic permittivity

of XLPE insulation material. Numerical results demonstrate that due to the fringing effect, significant errors in the measurement of permittivity could be induced, especially for materials with very low dielectric constant, such as for XLPE. The measured permittivity for XLPE is higher than its intrinsic value due to the energy stored in the ambient air, as shown in Table 5-2, especially for real part of permittivity ε'. A curve of measurable permittivity versus intrinsic value was established for XLPE sample with given dimensions. The influence factors like the size of sample and electrode were analyzed. In addition, a simplified measurement was carried out and the intrinsic value of XLPE sample is determined utilizing the methods found in references. The proposed field-circuit coupled method shows obvious advantage over the two-electrode measurement with a guard electrode. Theoretically, it is general to all kinds of materials, such as XLPE as well as semicon. Since this method is able to use a simple two-parallel-electrode geometry, it provides possibility to measure the complex real cable configuration with available simulation tools. Thus the high frequency response can be studied and the PD location technique may develop further.

In Section 5.2, a mathematical model for a capacitor made of semicon in XLPE cable was set up to investigate the dimensional effect in the measurement of its permittivity. The numerical calculation results show that due to extremely high permittivity of semicon, the measurable or apparent permittivity is different from its intrinsic value, when the frequencies are above 80 MHz. The high permittivity results in high displacement current, which produces high magnetic field. The alternating magnetic field in turn produces a counteracting electric field, which effectively reduces the applied electric field and results in a smaller measured permittivity. It is found that the larger the sample, the higher the difference. To minimize the dimensional effect, the dimension of the sample should be kept as small as possible. Newton-Raphson method can be used to determine intrinsic value based on its measured permittivity. The method provided in this section can be used to estimate how small the sample is in order to make the measured permittivity close to or just equal to its intrinsic value.

In Section 5.3, two mathematical models for a capacitor made of XLPE and semicon materials from a 230 kV XLPE power cable was set up to determine the intrinsic value of permittivity. From numerical calculation, the four unknown parameters (real and

imaginary parts of permittivity for these two materials) can be found by iterations based on Newton-Raphson method. Due to the dimensional effect of semiconducting material with high permittivity and the fringing effect of XLPE insulation material with rather small real part of permittivity, the measured or apparent permittivity is different from their intrinsic value. Newton-Raphson method can be used to effectively determine the intrinsic value based on their measured permittivity.

In conclusion, the field-circuit coupled theory combined with Newton-Raphson method could overcome the disadvantages of current permittivity determination methods which require much on measuring instruments, sample dimension, electrode condition, etc. Only if the dimensions of sample can be precisely measured, it is possible to determine the intrinsic permittivity for any sample, since just a two-parallel electrode geometry is needed. The toughest task is to make the computational model resemble the tested sample as much as possible with considering those factors, such as poor contact of electrode with sample surface. The convenience and feasibility of such technique depends on the development of simulation tools and computation methods.

Chapter 6 Conclusions and Recommendations

During the past three-year research period, three parts of work have been conducted. The objectives of this project are presented in the first part; a literature review of the research background and current status is included in the second part; the third part contains the major contributions of this project. And a brief summary of these contributions are listed below:

The developed signal processing methods can be easily applied to characterize the randomly occurring PD pulses due to electrical treeing in XLPE material of HV XLPE power cable. For group PD data, φ-q-n distribution is the most direct method and main qualitative features were extracted using this method. Then Weibull parameters, scale factor (α) and shape factor (β) were extracted and different PD types can be identified since they have their own characteristic values. Cumulative n distribution using q-n data was used for identification. In all the three modes, shape parameter shows decreasing trend over 3, the indicator of usual cavity discharge. Five-parameter Weibull analyses with a large p indicates discharges are mainly belonging to one type. And the changing of β with aging suggests the variance of PD mechanism. Δu-Δt distribution is another effective method and they give related information to every kind of discharge mechanism. It is based on the time (Δt) and magnitude difference (Δu) between consecutive PD pulses. They will somehow describe initial discharge conditions affected by the former discharge, although the clear internal rules will be difficult to achieve. Laboratory studies suggest that Δu in the range of 0.1V to 1V with Δt distribution of 3 ms. When the discharge starts, the volume of cavity will be small and time to charge up will be long due to insulation and the behavior of discharge will be random due to charge distribution on the walls. Further analysis was made for single PD pulse. It is based on single pulse analysis and the developed technique is novel based on the details of single PD wave shape. Single pulse waveform was recorded in time- and frequency- domains. The frequency range is up to 50 MHz, and a large cluster is located around 10~15 MHz, besides those at low frequency and the minor one at 35~40 MHz. Equivalent F-T cluster analysis was also used to characterize the single pulses. The results show that single PD

pulses are most clustered at 200~300 ns / 10~20 MHz. Other positive pulses scatter to larger T while negative pulses to lower F. The values of cross-correlation coefficients of these single pulses also indicate that most PDs are similar and belong to one main type besides a minor type.

Besides the partial discharge technique, dielectric response measurement can be also adopted as a supporting method. No research on using this non-destructive method for carrying out electrical tree analysis has been reported. The frequency spectrums of R_p, C_p, and tanδ recorded in 0.01~1000 Hz during tree growth present similar trends in all the three test modes. And the most important result is that an inflexion point occurs in the near-to-fail part on the frequency spectrum curve for all the three parameters, which is simultaneous with the transferring of tree shape from branch type to bush type. Such results help monitor the condition of insulation.

The effects of rise rate and aging time of applied voltage are analyzed and compared in three test modes: TEST-1 - raising applied voltage at 1kV per 10 min, TEST-2 - raising applied voltage at 2 kV per 60 min, and TEST-3 - constant HV. Trees grow differently in different modes as verified by optical recording. It is demonstrated that the trees grow faster in situations with applied voltages of higher rise rate than in those with longer aging time. This means that the local electric field is the key parameter of tree growth. The changes in electric field induce space charge transport and accumulation in tree channels, and the charge density distribution can simultaneously affect the distribution of local electric field.

For theoretical analyses, a 2D axial-symmetrical electrostatic problem is proposed for a representative model of the needle-plane electrode configuration. The influences of the geometrical parameters on the electrical field distribution are analyzed. In addition, the model is modified to analyze the effect of space charge, such as the influences of the charge density, charge polarization, and charge confined spherical region. Based on that, the initiation and propagation conditions of electrical trees are studied in three cases regarding to the effect of conductive particles; the effect of gas bubbles around a conductive particle; and the effect of two bubbles, one with space charges inside.

In more realistic analyses, the field- and thermal- dependent conductivity of polyethylene is considered in the transient problems with voltage inputs of different waveforms. The electric fields change with stressing time at different radial positions according to the change of space charge distribution. The simulation results agree with the theory of space charge-limited field. In addition, significant temperature rise happens upon fast rising applied voltage.

In order to understand the mechanism of charge transport phenomenon, the bipolar charge transport model is analyzed as a multiphysics problem based on Poisson's equation, continuity equation and transport equation. It is tough to solve such problem (a group of coupled partial difference equations) due to its fluid-like dynamic characteristics. Without programming by traditional numerical methods, COMSOL's specialized modules have been successfully applied in this study. The model's parameterization has involved many other researchers' contribution. And there are two typical assumptions: unique (Model I) and exponential (Model II) deep trapping levels. Besides the traditional 1D computation cell configured in a rectangular coordinate (Type A) is applied denoting a parallel electrode system, a new type of 1D cell is designed for the needle-plane electrode system which is presented in a cylinder coordinate (Type B). The net space charges are considered as the algebraic sum of the species of electrons and holes, mobile and trapped, respectively. The density of each species can be calculated with the stressing time and thus these models show certain features adding to explain the charge transport phenomena. Since there are limited evidences of developed models, the two models are not equivalent. The Model I shows that the proportion of trapped charges increases with time, whereas the Model II shows that the maximum density of trapped charges is constant. As a consequence, Model I predicts a more strongly decaying transient current; Model II has shown some features of transient field-limited space charge buildup as show in former sections.

With the thought of facilitating the study of the high-frequency response of XLPE cable for characterization of PD propagation, the determination of intrinsic permittivity of cable materials has also been paid attention to. Normal laboratory measurement methods put strict requirements on the sample conditions. And in-field testing cannot be replaced by laboratory testing for many reasons. However, the flexible

field-circuit coupled method developed in this research is effective, simple and unlimited by the dimension of sample and the electrode geometry. Although XLPE material is not a dominant contributor in high-frequency loss of cable, the developed method is verified by applying to XLPE. The numerical results from a mathematical model show that the measured (real part of) permittivity for XLPE is higher than its intrinsic value due to the energy stored in the ambient air. A correction curve of measurable permittivity versus intrinsic value is established. The influencing factors like the size of sample and electrode are also analyzed. Taken as an example, a measurement has been carried out and the intrinsic value of XLPE sample is determined utilizing the referred iteration method. The result suggests that the proposed field-circuit coupled method has an obvious advantage over the traditional three-electrode measurement. This method can be carried out only by a measurement even with a simple two-parallel-electrode geometry, which provides the possibility of its application in field. The sources of measurement error, such as electrode loss due to poor contact and equipment instability at high frequency can be taken into account by refining the model in the simulation module. Certainly, such possibility depends on the development of computation methods and simulation tools in order to make it practical for various applications.

Semiconducting material is actually the dominant influence factor of loss at high frequency. The dimensional effect due to its high permittivity is unavoidable and has also been analyzed qualitatively and quantitatively. The numerical calculation results show that the measurable or apparent permittivity differs from the intrinsic value, when the frequencies are above 80 MHz. and the larger the sample, the higher the difference is. To minimize the dimensional effect, the dimension of the sample should be kept as small as possible. And this method can be used to estimate how small the sample is in order to make the measured permittivity close to or just equal to its intrinsic value.

With the idea of field-circuit coupled theory, Newton-Raphson method can be applied to determine the permittivities simultaneously for XLPE and semicon. For example, there are four unknown parameters which can be obtained by applying two capacitor models; one is parallel model and the other series model. Due to the coexistence of the fringing effect and the dimensional effect, the measured or apparent permittivity is

different from the intrinsic value. Newton-Raphson method can be used to effectively determine the intrinsic permittivities based on their measured values which are also obtained by using such iteration method from the measured impedances of two capacitor models.

The knowledge gathered and newly developed techniques have established a basis to undertake future research work on the electrical characterization of HV polymeric power cable. Possible areas are:

- More advanced signal processing techniques need to be developed, such as analyses with other distributions besides *q-n* distribution of PD pulses, and more information to be extracted from the single PD pulse;
- Analyses with considering the interesting differences between PE and XLPE, which can be related to mechanical-morphological properties;
- Analyses with more complicate multiphysics problems where electric field, temperature and other parameters are coupled;
- Studies of other charge transport models and their application in new practical situations;
- Application of field-circuit coupled method for samples with complex structure in laboratory;
- Application of field-circuit coupled method for cables in field;
- Modification of simulation model in order to take into account of more factors of loss.

BIBLIOGRAPHY

[1] R. Bartnikas and K. D. Srivastava, *Power and communication cables: theory and applications*: IEEE Press, 2000.

[2] W. A. Thue, *Electrical power cable engineering*: New York, Marcel Dekker, 2003.

[3] L. A. Dissado and J. C. Fothergill, *Electrical degradation and breakdown in polymers*. London: Ed. Peter Peregrinus Ltd., 1992.

[4] R. Ross and R. Ross, "Inception and propagation mechanisms of water treeing," *Dielectrics and Electrical Insulation, IEEE Transactions on,* vol. 5, pp. 660-680, 1998.

[5] S. S. Bamji, A. T. Bulinski, and R. J. Densley, "Final Breakdown Mechanism Of Water Treeing," *Electrical Insulation and Dielectric Phenomena, 1991. CEIDP. 1991 Annual Report. Conference on,* pp. 298-305, 1991.

[6] M. S. Mashikian and A. Szarkowski, "Medium voltage cable defects revealed by off-line partial discharge testing at power frequency," *Electrical Insulation Magazine, IEEE,* vol. 22, pp. 24-32, 2006.

[7] R. Bozzo, C. Gemme, F. Guastavino, M. Cacciari, A. Contin, and G. C. Montanari, "Aging diagnosis of insulation systems by PD measurements. Extraction of partial discharge features in electrical treeing," *Dielectrics and Electrical Insulation, IEEE Transactions on,* vol. 5, pp. 118-124, 1998.

[8] S. Jiang and D. Kececioglu, "Graphical representation of two mixed-Weibull distributions," *Reliability, IEEE Transactions on,* vol. 41, pp. 241-247, 1992.

[9] A. Contin, G. C. Montanari, and C. Ferraro, "PD source recognition by Weibull processing of pulse height distributions," *Dielectrics and Electrical Insulation, IEEE Transactions on,* vol. 7, pp. 48-58, 2000.

[10] T. Okamoto and T. Tanaka, "Auto-correlation function of PD pulses under electrical treeing degradation," *Dielectrics and Electrical Insulation, IEEE Transactions on,* vol. 2, pp. 857-865, 1995.

[11] E. Gulski and F. H. Kreuger, "Diagnostics of insulating systems using statistical tools," *Electrical Insulation, Conference Record of the 1992 IEEE International Symposium on,* pp. 393-396, 1992.

[12] K. Wu, Y. Suzuoki, and H. Xie, "Sub-fractal structure of single partial discharge in an electrical tree," *J.Phys.D: Appl.Phys,* vol. 33, pp. 2954-2957, 2000.

[13] A. Krivda, E. Gulski, L. Satish, and W. S. Zaengl, "The use of fractal features for recognition of 3-D discharge patterns," *Dielectrics and Electrical Insulation, IEEE Transactions on,* vol. 2, pp. 889-892, 1995.

[14] A. A. Mazroua, R. Bartnikas, and M. M. A. Salama, "Neural network system using the multi-layer perception technique for the recognition of PD pulse shapes due to cavities and electrical trees," *Power Delivery, IEEE Transactions on,* vol. 10, pp. 92-96, 1995.

[15] E. Gulski and A. Krivda, "Neural networks as a tool for recognition of partial discharges," *Electrical Insulation, IEEE Transactions on,* vol. 28, pp. 984-1001, 1993.

[16] A. Contin, A. Cavallini, G. C. Montanari, G. Pasini, and F. Puletti, "Digital detection and fuzzy classification of partial discharge signals," *Dielectrics and Electrical Insulation, IEEE Transactions on,* vol. 9, pp. 335-348, 2002.

[17] A. Kyprianou, P. L. Lewin, V. Efthimiou, A. Stavrou, and G. E. Georghiou, "Wavelet packet denoising for online partial discharge detection in cables and its application to experimental field results " *Measurement Science and Technology,* vol. 17, pp. 2367-2379 2006.

[18] H. Zhang, T. R. Blackburn, B. T. Phung, and D. Sen, "A novel wavelet transform technique for on-line partial discharge measurements part 1: WT de-noising algorithm," *Dielectrics and Electrical Insulation, IEEE Transactions on,* vol. 14, pp. 3-14, 2007.

[19] S. Boggs, A. Pathak, and P. Walker, "Partial discharge. XXII. High frequency attenuation in shielded solid dielectric power cable and implications thereof for PD location," *Electrical Insulation Magazine, IEEE,* vol. 12, pp. 9-16, 1996.

[20] K. Steinbrich, "Influence of semiconducting layers on the attenuation behaviour of single-core power cables," *Generation, Transmission and Distribution, IEE Proceedings of,* vol. 152, pp. 271-276, 2005.

[21] A. Ametani, Y. Miyamoto, and N. Nagaoka, "Semiconducting Layer impedance and its effect on cable wave-propagation and transient Characteristics," *Power Delivery, IEEE Transactions on,* vol. 19, pp. 1523-1531, 2004.

[22] X. Chunchuan and S. A. Boggs, "High frequency properties of shielded power cable. Part 2: sources of error in measuring shield dielectric properties," *Electrical Insulation Magazine, IEEE,* vol. 22, pp. 7-13, 2006.

[23] W. R. Kegerise, "Feature article - Manufacturing and Performance Criteria for Medium Voltage Power Cable Semiconducting Shields," *Electrical Insulation Magazine, IEEE,* vol. 24, pp. 15-21, 2008.

[24] A. Van Roggen, "An overview of dielectric measurements," *Electrical Insulation, IEEE Transactions on,* vol. 25, pp. 95-106, 1990.

[25] A. Ocera, M. Dionigi, E. Fratticcioli, and R. Sorrentino, "A novel technique for complex permittivity measurement based on a planar four-port device," *Microwave Theory and Techniques, IEEE Transactions on,* vol. 54, pp. 2568-2575, 2006.

[26] D. L. Faircloth, M. E. Baginski, and S. M. Wentworth, "Complex permittivity and permeability extraction for multilayered samples using S-parameter waveguide measurements," *Microwave Theory and Techniques, IEEE Transactions on,* vol. 54, pp. 1201-1209, 2006.

[27] G. Mugala, R. Eriksson, U. Gafvert, and P. Petterson, "Measurement technique for high frequency characterization of semiconducting materials in extruded cables," *Dielectrics and Electrical Insulation, IEEE Transactions on,* vol. 11, pp. 471-480, 2004.

[28] R. Heinrich, S. Bonisch, D. Pommerenke, R. Jobava, and W. Kalkner, "Broadband measurement of the conductivity and the permittivity of semiconducting materials in high voltage XLPE cables," *Dielectric Materials, Measurements and Applications, 2000. Eighth International Conference on (IEE Conf. Publ. No. 473),* pp. 212-217, 2000.

[29] G. Antonini and S. Cristina, "A genetic optimization technique for intrinsic material properties extraction," *Electromagnetic Compatibility, 2002 IEEE International Symposium on,* vol. 1, pp. 144-149, 2002.

[30] D. M. Zhang and C. F. Foo, "A practical method to determine intrinsic complex permeabilities and permittivities for Mn-Zn ferrites," *Magnetics, IEEE Transactions on,* vol. 41, pp. 1226-1232, 2005.

[31] R. F. Harrington, *Time-Harmonic Electromagnetic Fields*. New York: Mc-Graw Hill, 1961.

[32] H. Nishiyama and M. Nakamura, "Capacitance of a Strip Capacitor," *Components, Hybrids, and Manufacturing Technology, IEEE Transactions on,* vol. 13, pp. 417-423, 1990.

[33] H. Nishiyama and M. Nakamura, "Form and Capacitance of Parallel-Plate Capacitors," *Components, Packaging, and Manufacturing Technology, Part A, IEEE Transactions on,* vol. 17, pp. 477-484, 1994.

[34] V. Vahedy, "Polymer insulated high voltage cables," *Electrical Insulation Magazine, IEEE,* vol. 22, pp. 13-18, 2006.

[35] A. Ishibashi, T. Kawai, S. Nakagawa, H. Muto, and S. Katakai, "A study of treeing phenomena in the development of insulation for 500 kV XLPE cables," *Dielectrics and Electrical Insulation, IEEE Transactions on,* vol. 5, pp. 695-706, 1998.

[36] E. Riande, *Electrical properties of polymers*: Marcel Dekker,, 2005.

[37] S. A. Boggs and M. S. Mashikian, "Role of semiconducting compounds in water treeing of XLPE cable insulation," *Electrical Insulation Magazine, IEEE,* vol. 10, pp. 23-27, 1994.

[38] R. Patsch, "Electrical and water treeing: a chairman's view," *Electrical Insulation, IEEE Transactions on,* vol. 27, pp. 532-542, 1992.

[39] G. Katsuta, A. Toya, Y. LI, M. Okashita, F. Aida, and Y. Ebinuma, "Experimental investigation on the cause of harmfulness of the blue water tree to XLPE cable insulation," *Dielectrics and Electrical Insulation, IEEE Transactions on,* vol. 6, pp. 887-891, 1999.

[40] S. V. Nikolajevic, "The influence of water on water absorption and density of XLPE cable insulation," *IEEE Power Engineering Review,* vol. 17, p. 30, 1997.

[41] E. David, J. L. Parpal, and J. P. Crine, "Influence of internal mechanical stress and strain on electrical performance of polyethylene electrical treeing resistance," *Dielectrics and Electrical Insulation, IEEE Transactions on,* vol. 3, pp. 248-257, 1996.

[42] C. Kim, Z. Jin, X. Huang, P. Jiang, and Q. Ke, "Investigation on water treeing behaviors of thermally aged XLPE cable insulation," *Polymer Degradation and Stability,* vol. 92, pp. 537-544, 2007.

[43] H. Faremo and E. Ildstad, "Dissipation factor and water treeing of WTR-XLPE cable insulation," *Dielectric Materials, Measurements and Applications, 1992., Sixth International Conference on,* pp. 306-309, 1992.

[44] S. Boggs, "Mechanisms for Reduction of Impulse Strength Resulting from Small Water Trees," *Electrical Insulation and Dielectric Phenomena, 2000 Annual Report Conference on,* vol. 2, pp. 547-551, 2000.

[45] T. Kaneko, H. Ohno, A. Toya, T. Gotoh, I. Kajiki, F. Aida, K. Kato, and Y. Sakaguchi, "Aging phenomenon by water treeing and its mechanism in high voltage transmission XLPE cables," *Electrical Insulation, 1994., Conference Record of the 1994 IEEE International Symposium on,* pp. 193-196, 1994.

[46] S. Hvidsten, P. Werelius, and J. Christensen, "Evaluation of on-site dielectric response methods for nondestructive testing of water treed MV XLPE cables,"

Electricity Distribution, 2001. Part 1: Contributions. CIRED. 16th International Conference and Exhibition on (IEE Conf. Publ No. 482), vol. 1, p. 5 pp. vol.1, 2001.

[47] E. IIdstad and S. T. hagen, "Electrical treeing and breakdown of mechanically strained XLPE cable insulation," *Electrical Insulation, Conference Record of the 1992 IEEE International Symposium on,* pp. 135-139, 1992.

[48] Suwarno, Y. Suzuoki, and T. Mizutani, "Pulse-sequence analysis of partial discharges in a void and electrical treeing," *Electrical Insulation, Conference Record of the 1996 IEEE International Symposium on,* vol. 1, pp. 130-133, 1996.

[49] R. Sarathi, S. Das, C. Venkataseshaiah, and N. Yoshimura, "Investigations of growth of electrical trees in XLPE cable insulation under different voltage profiles," *Electrical Insulation and Dielectric Phenomena, 2003. Annual Report. Conference on,* pp. 666-669, 2003.

[50] J. V. Champion, S. J. Dodd, Y. Zhao, A. S. Vaughan, M. Brown, A. E. Davies, S. J. Sutton, and S. G. Swingler, "Morphology and the growth of electrical trees in a propylene/ethylene copolymer," *Dielectrics and Electrical Insulation, IEEE Transactions on,* vol. 8, pp. 284-292, 2001.

[51] S. H. Kang, K. J. Lim, H. W. Park, and M. N. Kim, "Correlation between partial discharges and electrical treeing in low density polyethylene blended with organic additives," *Properties and Applications of Dielectric Materials, 1994., Proceedings of the 4th International Conference on,* pp. 409-411, 1994.

[52] S. A. Boggs, "Partial discharge: overview and signal generation," *Electrical Insulation Magazine, IEEE,* vol. 6, pp. 33-39, 1990.

[53] E. Gulski, "Computer-aided measurement of partial discharges in HV equipment," *Electrical Insulation, IEEE Transactions on,* vol. 28, pp. 969-983, 1993.

[54] J. Lopez-Roldan, J. M. Braun, J. Densley, and N. Fujimoto, "The development of electrical trees in epoxy insulation-partial discharge pulse characterization by ultra wideband techniques," *Electrical Insulation and Dielectric Phenomena, 1996. IEEE 1996 Annual Report of the Conference on,* vol. 2, pp. 754-757, 1996.

[55] S. A. Boggs, "Partial discharge. II. Detection sensitivity," *Electrical Insulation Magazine, IEEE,* vol. 6, pp. 35-42, 1990.

[56] F. H. Kreuger, *Partial Discharge Detection in High-Voltage Equipment*. Butterworths: Butterworths & Co. (Publisher) Ltd, 1989.

[57] "Partial Discharge Measurements," *IEC std.60270, 3rd edition,* 2001.

[58] Y. Cheng, X. Hu, X. Chen, and P. Li, "Partial discharge on-line monitoring system based on FPGA," *Electrical Insulating Materials, 2005. (ISEIM 2005). Proceedings of 2005 International Symposium on,* vol. 2, pp. 486-489, 2005.

[59] F. Guastavino and B. Cerutti, "Tree growth monitoring by means of digital partial discharge measurements," *Dielectrics and Electrical Insulation, IEEE Transactions on,* vol. 10, pp. 65-72, 2003.

[60] B. J. Beggs, I. J. Kemp, and A. Wilson, "On the correlation between partial discharge parameters and the degradation characteristics of polyester resin insulating systems," *Dielectric Materials, Measurements and Applications, 1992., Sixth International Conference on,* pp. 213-216, 1992.

[61] D. Pommerenke, R. Jobava, and R. Heinrich, "Numerical simulation of partial discharge propagation in cable joints using the finite difference time domain method," *Electrical Insulation Magazine, IEEE,* vol. 18, pp. 6-11, 2002.

[62] Y. Cheng, X. Chen, S. Zhang, and Y. Lv, "On-line partial discharge monitor system of XLPE power cable based on virtual instrument," *Properties and Applications of Dielectric Materials, 2003. Proceedings of the 7th International Conference on,* pp. 207-210, 2003.

[63] L. Hao, P. L. Lewin, Y. Tian, and S. J. Dodd, "Partial discharge identification using a support vector machine," *Electrical Insulation and Dielectric Phenomena, 2005. CEIDP '05. 2005 Annual Report Conference on,* vol. 2005, pp. 414-417, 2005.

[64] E. Gulski, "Digital analysis of partial discharges," *Dielectrics and Electrical Insulation, IEEE Transactions on,* vol. 2, pp. 822-837, 1995.

[65] Y. H. Cheng, X. L. Chen, M. Z. Rong, and B. Yue, "Study on the partial discharge characteristics of the XLPE insulation samples during electrical treeing ageing," *Properties and Applications of Dielectric Materials, 2003. Proceedings of the 7th International Conference on,* vol. 1, pp. 211-214, 2003.

[66] K. H. Week and F. Weinel, "Noise reduction in on-site partial discharge measurement by the use of the transfer function," *Electrical Power, European Transactions on,* vol. 8, pp. 299-303, 1998.

[67] J. He, J. M. Braun, J. Densley, N. Fujimoto, and H. G. Sedding, "Partial discharge characteristics of electrical trees in polymeric cable insulation," *Electrical Insulation and Dielectric Phenomena, 1994. IEEE 1994 Annual Report., Conference on,* pp. 91 - 96, 1994.

[68] J. E. McBride, V. S. Harper, L. T. Coffeen, F. T. Stanley, and H. W. Ng, "Examination and location of partial discharge sites in severely aged underground distribution cables," *Power Delivery, IEEE Transactions on,* vol. 9, pp. 629-638, 1994.

[69] F. H. Kreuger, M. G. Wezelenburg, A. G. Wiemer, and W. A. Sonneveld, "Partial discharge. XVIII. Errors in the location of partial discharges in high voltage solid dielectric cables," *Electrical Insulation Magazine, IEEE,* vol. 9, pp. 15-22, 1993.

[70] H. Ueno, P. Walter, C. Cornelissen, and A. Schnettler, "Resolution evaluation of ultrasonic diagnosis tools for electrical insulation devices and the detection of electrical trees," *Dielectrics and Electrical Insulation, IEEE Transactions on,* vol. 14, pp. 249-255, 2007.

[71] R. Sarathi and P. G. Raju, "Study of electrical treeing phenomena in XLPE cable samples using acoustic techniques," *Electric Power Systems Research,* vol. 73, pp. 159-168, 2005.

[72] R. Sarathi and P. G. Raju, "Diagnostic study of electrical treeing in underground XLPE cables using acoustic emission technique," *Polymer Testing,* vol. 23, pp. 863-869, 2004.

[73] J. Jonsson, B. Ranby, D. Mary, C. Laurent, and C. Mayoux, "Electroluminescence from polyolefins subjected to a homogeneous ac field," *Dielectrics and Electrical Insulation, IEEE Transactions on,* vol. 2, pp. 107-113, 1995.

[74] S. S. Bamji, A. T. Bulinski, H. Suzuki, M. Matsuki, and Z. Iwata, "Light and tree inception characteristics of XLPE at elevated temperatures," *Electrical Insulation and Dielectric Phenomena, 1993. Annual Report., Conference on,* pp. 688-694, 1993.

[75] N. Shimizu, H. Katsukawa, M. Miyauchi, M. Kosaki, and K. Horii, "The Space Charge Behavior and Luminescence Phenomena in Polymers at 77 K," *Electrical Insulation, IEEE Transactions on,* vol. EI-14, pp. 256-263, 1979.

[76] R. Ishii, S. Lemura, M. Kubo, N. Nagura, and N. Shimizu, "Electroluminescence for XLPE cable diagnosis," *Properties and Applications of Dielectric Materials, 2003. Proceedings of the 7th International Conference on,* vol. 1, pp. 199-202, 2003.

[77] S. S. Bamji, A. T. Bulinski, and R. J. Densley, "Degradation of polymeric insulation due to photoemission caused by high electric fields," *Electrical Insulation, IEEE Transactions on,* vol. 24, pp. 91-98, 1989.

[78] H. Kaneiwa, Y. Suzuoki, and T. Mizutani, "Partial discharge characteristics and tree inception in artificial simulated tree channels," *Dielectrics and Electrical Insulation, IEEE Transactions on,* vol. 7, pp. 843-848, 2000.

[79] J. Bryden, L. J. Kemp, A. Nesbitt, J. V. Champion, and Z. Richardson, "Correlations among tree growth and the measurable parameters of partial discharge activity," *High Voltage Engineering Symposium,* pp. 79-83, 1999.

[80] M. D. Noskov, M. Sack, A. S. Malinovski, and A. J. Schwab, "Measurement and simulation of electrical tree growth and partial discharge activity in epoxy resin," *J.Phys.D: Appl.Phys,* vol. 34, pp. 1389-1398, 2001.

[81] J. V. Champion, S. J. Dodd, and G. C. Stevens, "The application of light emission techniques to study the spatial and temporal development of partial discharge activity during initiation and growth of electrical trees," *Partial Discharge, 1993., International Conference on,* pp. 58-59, 1993.

[82] Y. Ehara, M. Tsuno, H. Kishida, and T. Ito, "Optical and electrical detection of single pulse of partial discharge on electrical treeing," *Electrical Insulating Materials, 1998. Proceedings of 1998 International Symposium on,* pp. 639-642, 1998.

[83] H. Kaneiwa, Y. Suzuoki, and T. Mizutani, "Partial discharge characteristics and tree propagation in artificially-simulated tree channel," *Conduction and Breakdown in Solid Dielectrics, 1998. ICSD '98. Proceedings of the 1998 IEEE 6th International Conference on,* pp. 123-126, 1998.

[84] H. Uehara, K. Shibuyer, and T. K. Arai, K., "Chaotic character of luminous and partial discharge phenomena during ac electrical tree propagation," *Electrical Insulating Materials, 1998. Proceedings of 1998 International Symposium on,* pp. 417-420, 1998.

[85] J. M. Bryden, I. J. Kemp, A. Nesbitt, J. V. Champion, S. J. Dodd, and Z. Richardson, "Correlations among light emission and partial discharge measurements made during electrical tree growth," *Dielectric Materials, Measurements and Applications Conference Publication No.473,* pp. 513-518, 2000.

[86] S. J. Dodd, J. V. Champion, and G. C. Stevens, "Quantitative light emission as a probe of electrical treeing processes," *Conduction and Breakdown in Solid Dielectrics, 1992., Proceedings of the 4th International Conference on,* pp. 308-312, 1992.

[87] M. Nishizaka, H. Kawabata, C.-S. Kim, and T. Mizutani, "Change in partial discharge characteristics by tree propagation from an artificial-simulated tree channel," *Properties and Applications of Dielectric Materials, 2003. Proceedings of the 7th International Conference on,* pp. 887-890, 2003.

[88] M. Conti, A. Cavallini, G. C. Montanari, and F. Guastavino, "Identification of electrical tree growth in insulation systems by fuzzy logic techniques based on

partial discharge acquisition," *Solid Dielectrics, 2004. ICSD 2004. Proceedings of the 2004 IEEE International Conference on,* vol. 2, pp. 661-664, 2004.

[89] H. Kaneiwa, Y. Suzuoki, and T. Mizutani, "Characteristics of partial discharges in artificial simulated tree channels during tree propagation," *Dielectrics and Electrical Insulation, IEEE Transactions on,* vol. 8, pp. 72-77, 2001.

[90] M. Morita, K. Wu, F. Komori, and Y. Suzuoki, "Investigation of electrical tree propagation from water tree by utilizing partial discharge and optical observation," *Properties and Applications of Dielectric Materials, 2003. Proceedings of the 7th International Conference on,* pp. 891-894, 2003.

[91] M. A. Brown, J. V. Champion, S. J. Dodd, and P. Mudge, "An investigation of partial discharge energy dissipation and electrical tree growth in an epoxy resin," *Solid Dielectrics, 2004. ICSD 2004. Proceedings of the 2004 IEEE International Conference on,* vol. 1, pp. 288-291, 2004.

[92] Y. S. Cho, M. J. Shim, and S. W. Kim, "Fractal characteristics of electrical treeing phenomena in electric power distributing cable insulation," *Properties and Applications of Dielectric Materials, 1997., Proceedings of the 5th International Conference on,* pp. 443-446, 1997.

[93] B. Oyegoke, P. Hyvonen, M. Aro, and N. Gao, "Application of dielectric response measurement on power cable systems," *Dielectrics and Electrical Insulation, IEEE Transactions on,* vol. 10, pp. 862-873, 2003.

[94] H. Faremo and E. Ildstad, "Diagnosis and restoration of water tree aged XLPE cable materials," *Electrical Insulation, 1996., Conference Record of the 1996 IEEE International Symposium on,* pp. 596-599, 1996.

[95] H. Faremo and E. Ildstad, "Water treeing and dielectric loss of WTR-XLPE cable insulation," *Science, Measurement and Technology, IEE Proceedings A,* vol. 140, pp. 393-396, 1993.

[96] T. K. Abdel Galil and I. O. Habiballah, "Challenges of Using Partial Discharge Measurements for Predictive Maintenance," *Transmission and Distribution Conference and Exhibition: Asia and Pacific, 2005 IEEE/PES,* pp. 1-6, 2005.

[97] G. Wu, X. Jiang, h. Xie, and D. H. Park, "The experimental study on tree growth in XLPE using 3D PD patterns," *Properties and Applications of Dielectric Materials, 2000. Proceedings of the 6th International Conference on,* vol. 1, pp. 558-561, 2000.

[98] E. Gulski, P. H. F. Morshuis, and F. H. Kreuger, "Conventional and time-resolved measurements of partial discharges as a tool for diagnosis of insulating materials," *Properties and Applications of Dielectric Materials, 1994., Proceedings of the 4th International Conference on,* vol. 2, pp. 666-669, 1994.

[99] N. Hozumi, T. Okamoto, and T. Imajo, "Discrimination of partial discharge patterns using a neural network," *Electrical Insulation, IEEE Transactions on,* vol. 27, pp. 550-556, 1992.

[100] H. Kamikubo, K. Shizu, Y. Suzuoki, and T. Mizutani, "Study on tree propagation from an artificially-simulated tree channel by partial discharges," *Electrical Insulating Materials, 1998. Proceedings of 1998 International Symposium on,* pp. 709-712, 1998.

[101] M. Hoof and R. Patsch, "Analyzing partial discharge pulse sequences-a new approach to investigate degradation phenomena," *Electrical Insulation, 1994., Conference Record of the 1994 IEEE International Symposium on,* pp. 327-331, 1994.

[102] Suwarno, Y. Suzuoki, and T. Mizutani, "Phase-resolved measurement of partial discharge in artificially-simulated tree channel," *Properties and Applications of Dielectric Materials, Proceedings of the 5th International Conference on,* pp. 267-270, 1997.

[103] F. H. Kreuger, E. Gulski, and A. Krivda, "Classification of partial discharges," *Electrical Insulation, IEEE Transactions on,* vol. 28, pp. 917-931, 1993.

[104] P. Basappa and V. Lakdawala, "Application of digital signal processing techniques to analyze partial discharge data," *Electrical Insulation and Dielectric Phenomena, 2000 Annual Report Conference on,* vol. 1, pp. 341-346, 2000.

[105] P. Basappa, V. Lakdawala, and V. K. Agarwal, "An investigation into the effect of thermally stimulated discharges on the partial discharges obtained during electrical treeing," *Electrical Insulation and Dielectric Phenomena, 2002 Annual Report of Conference on,* pp. 971-974, 2002.

[106] P. H. F. Morshuis, A. Cavallini, G. C. Montanari, F. Puletti, and A. Contin, "Theoretical and experimental derivation of partial discharge height distribution models," *Electrical Insulation and Dielectric Phenomena, 1999 Annual Report Conference on,* vol. 1, pp. 222-226, 1999.

[107] A. Contin, E. Gulski, M. Cacciari, and G. C. Montanari, "Applications of the Weibull function to partial discharge data coming from different sources typologies," *Electrical Insulation and Dielectric Phenomena, 1995. Annual Report., Conference on,* pp. 335-338, 1995.

[108] R. Patsch and M. Hoof, "Physical modeling of partial discharge patterns," *Conduction and Breakdown in Solid Dielectrics, 1998. ICSD '98. Proceedings of the 1998 IEEE 6th International Conference on,* pp. 114-118, 1998.

[109] F. Berton and R. Patsch, "The use of time intervals between consecutive discharges to characterize PD-sources," *Electrical Insulation, Conference Record of 1998 IEEE International Symposium on,* pp. 527-530, 2002.

[110] A. Cavallini, R. Ciani, M. Conti, P. F. H. Morshuis, and G. C. Montanari, "Modeling memory phenomena for partial discharge processes in insulation cavities," *Electrical Insulation and Dielectric Phenomena, 2003. Annual Report. Conference on,* pp. 723-727, 2003.

[111] W. Shu, J. Guo, and G. Wu, "Study on characteristic of partial discharge under DC condition," *Electrical Insulation and Dielectric Phenomena, 2005. CEIDP '05. 2005 Annual Report Conference on,* vol. 2005, pp. 83-86, 2005.

[112] T. Kalicki, J. M. Braun, J. Densley, and H. G. Sedding, "Pulse-shape characteristics of partial discharge within electrical trees in polymeric materials," *Electrical Insulation and Dielectric Phenomena, 1995. Annual Report., Conference on,* pp. 380 - 383, 1995.

[113] L. Franks, *Signal Theory*. Englewood Cliffs, N.J.: Prentice-Hall, Inc., 1969.

[114] G. C. Montanari, A. Cavallini, and F. Puletti, "A new approach to partial discharge testing of HV cable systems," *Electrical Insulation Magazine, IEEE,* vol. 22, pp. 14-23, 2006.

[115] A. Contin, G. C. Montanari, and A. Cavallini, "Power spectral density estimation of randomly sampled partial discharge signals," *Conduction and Breakdown in Solid Dielectrics, 1998. ICSD '98. Proceedings of the 1998 IEEE 6th International Conference on,* pp. 135-138, 1998.

[116] D. Suresh, "Feature extraction for multi source partial discharge pattern recognition," *Proceedings of INDICON 2005: An International Conference of IEEE India Council,* pp. 309-312, 2005.

[117] C. G. Karagiannopoulos, "A model for dielectrics experiencing partial discharges under high electric fields," *Journal of Electrostatics,* vol. In Press, Uncorrected Proof.

[118] S. A. Boggs, "Semi-empirical high-field conduction model for polyethylene and implications thereof," *Dielectrics and Electrical Insulation, IEEE Transactions on,* vol. 2, pp. 97-106, 1995.

[119] M. Feliziani, F. Maradei, E. Santani, and C. Santucci, "Simplified model of the discharge path in electrical devices by an iterative FEM procedure," *Magnetics, IEEE Transactions on,* vol. 34, pp. 2513-2516, 1998.

[120] M. D. Noskov, A. S. Malinovski, M. Sack, and A. J. Schwab, "Modeling of partial discharge development in electrical tree channels," *Dielectrics and Electrical Insulation, IEEE Transactions on,* vol. 10, pp. 425-434, 2003.

[121] D. A. L. Piriyakumar, P. Levi, R.Jayaganthan, and R.Sarathi, "A parallel processing technique for electrical tree growth in solid insulating materials using cellular automata," *Parallel Computing in Electrical Engineering, 2000. PARELEC 2000. Proceedings. International Conference on,* pp. 228-231, 2000.

[122] M. G. Danikas, I. Karafyllidis, A. Thanailakis, and A. M. Bruning, "A model for electrical tree growth in solid insulating materials using cellular automata," *Electrical Insulation, 1996., Conference Record of the 1996 IEEE International Symposium on,* vol. 2, pp. 887-890, 1996.

[123] G. Blaise and W. J. Sarjeant, "Space charge in dielectrics. Energy storage and transfer dynamics from atomistic to macroscopic scale," *Dielectrics and Electrical Insulation, IEEE Transactions on,* vol. 5, pp. 779-808, 1998.

[124] H. Fröhlich, "On the theory of dielectric breakdown of solids," *Proc. Roy. Soc. A,* vol. 188, pp. 368-370, 1947.

[125] A. v. Hippel, "Electrical breakdown of solid and liquid insulators," *J. Appl. Phys.,* vol. 8, pp. 815-832, 1937.

[126] A. v. Roggen, "Electrical conduction of polymer single crystals," *Phys. Rev. Lett.,* vol. 9, pp. 368-370, 1962.

[127] T. J. Lewis, "Polyethylene under electrical stress," *Dielectrics and Electrical Insulation, IEEE Transactions on,* vol. 9, pp. 717-729, 2002.

[128] F. Boufayed, G. Teyssedre, C. Laurent, S. L. Roy, L. A. Dissado, P. Segur, and G. C. Montanari, "Models of bipolar charge transport in polyethylene," *Journal of Applied Physics* vol. 100, p. 104105, 2006.

[129] G. Teyssedre and C. Laurent, "Charge transport modeling in insulating polymers: from molecular to macroscopic scale," *Dielectrics and Electrical Insulation, IEEE Transactions on,* vol. 12, pp. 857-875, 2005.

[130] H. J. Wintle, "Basic physics of insulators," *Electrical Insulation, IEEE Transactions on,* vol. 25, pp. 27-44, 1990.

[131] H. J. Wintle, "Charge motion and trapping in insulators: surface and bulk effects," *Dielectrics and Electrical Insulation, IEEE Transactions on,* vol. 6, pp. 1-10, 1999.

[132] S. Boggs, "Very high field phenomena in dielectrics," *Dielectrics and Electrical Insulation, IEEE Transactions on,* vol. 12, pp. 929-938, 2005.

[133] H. R. Zeller and W. R. Schneider, "Electrofracture mechanics of dielectric aging," *J. Appl. Phys.,* vol. 56, pp. 455-459, 1984.

[134] T. Hibma and H. R. Zeller., "Direct measurement of space-charge injection from a needle electrode into dielectrics," *J. Appl. Phys. ,* vol. 59, pp. 1614-1620, 1986.

[135] T. Hibma, H. R. Zeller, P. Plfuger, and T. Baumann., "A Model for space charge injection in dielectrics," *Annual Report of the CEIDP, pp.259-265. IEEE Publication 85CH2165-9.,* 1985.

[136] T. Baumann, T. Hibma, J. B. Pethica, P. Huger, and H. R. Zeller., "Space charge injection in polymers: new experimental results," *1985 Annual Report of the Conference on Electrical Insulation and Dielectric Phenomena, p. 266-273. IEEE Publication 85CH2165-9.,* 1985.

[137] T. Hibma and H. R. Zeller, "Direct measurements of space-charge injection from a needle electrode into dielectrics," *J. Appl. Phys.,* vol. 59, pp. 1614-1620, 1986.

[138] J. Kuang and S. A. Boggs, "Thermal-electric field distribution around a defect in polyethylene," *Power Delivery, IEEE Transactions on,* vol. 13, pp. 23-27, 1998.

[139] S. A. Boggs, "Theory of a field-limiting dielectric," *Power Delivery, IEEE Transactions on,* vol. 9, pp. 1391-1397, 1994.

[140] S. A. Boggs, "Thernal stability of a defect-tolerance dielectric," *Power Delivery, IEEE Transactions on,* vol. 9, pp. 1459-1465, 1994.

[141] G. Jiang and S. A. Boggs., "Mechanism for transition from branch to bush electrical tree," *Annual Report of the 1995 Conference on Electrical Insulation and Dielectric Phenomena. IEEE Publication 95CH35842,* pp. 57-60, 1995.

[142] G. C. Stone and S. A. Boggs, "Propagation of partial discharge pulses in shielded power cable," *Electrical Insulation and Dielectreic Phenomena, Annual Report of Conference* pp. 275-280, 1982.

[143] W. L. Weeks and Y. M. Diao, "Wave propagation characteristics in underground power cable," *Power Apparatus and System, IEEE Transactions on,* vol. PAS-103, pp. 2816-2825, 1984.

[144] X. Chunchuan, Z. Liming, J. Y. Zhou, and S. A. Boggs, "High frequency properties of shielded power cable - part 1: overview of mechanisms," *Electrical Insulation Magazine, IEEE,* vol. 21, pp. 24-28, 2005.

[145] S. A. Boggs, J. M. Braun, and G. C. Stone, "Attenuating voltage surges in power cable by modifying the semiconductive shields," *Electrical Insulation, Conference Record of the 1992 IEEE International Symposium on,* pp. 491 - 494 1992.

[146] R. H. Flake, "Part I. Theory. Signal propagation without distortion on lossy transmission lines having frequency dependent parameters," *Signal Propagation on Interconnects, 2005. Proceedings. 9th IEEE Workshop on,* pp. 43-45, 2005.

[147] N. Amekawa, N. Nagaoka, Y. Baba, and A. Ametani, "Derivation of a semiconducting layer impedance and its effect on wave propagation characteristics on a cable," *Generation, Transmission and Distribution, IEE Proceedings of,* vol. 150, pp. 434-440, 2003.

[148] H. N. O. T. R. Blackburn, B. T. Phung, M. Vakilian, M. S. A. Naderi, and H. A. Zhang, "Investigation of high frequency signal propagation characteristics on HV XLPE cables," in *Power Engineering Conference, 2005. IPEC 2005. The 7th International*, 2005, pp. 776-781

[149] G. Mugala, R. Eriksson, and P. Pettersson, "Dependence of XLPE insulated power cable wave propagation characteristics on design parameters," *Dielectrics and Electrical Insulation, IEEE Transactions on,* vol. 14, pp. 393-399, 2007.

[150] N. Oussalah, Y. Zebboudj, and S. Boggs, "PD Pulse Propagation in Shielded Power Cable for Symmetric and Asymmetric PD Pulses," in *Electrical Insulation, 2006. Conference Record of the 2006 IEEE International Symposium on*, 2006, pp. 30-33.

[151] G. Antonini and S. Cristina, "A genetic optimization technique for intrinsic material properties extraction " *Electromagnetic Compatibility, 2002 IEEE International Symposium on,* vol. 1, pp. 144-149, 2002.

[152] *User's Guide for Insulation Diagnostic System IDA 200*: Programma electric AB, 2002.

[153] *Operating and Maintenance Manual: kV Series High Voltage AC/DC Test System*: T & R Test Equipment Limited: Guildford, Surrey, England.

[154] *TDS7000 Series Digital Phosphor Oscilloscopes Instruction Manual*: Tektronix, Inc. USA, 2002.

[155] *User's Guide: Signal Processing Toolbox for Use with MATLAB*: The MATH WORKS Inc.

[156] *Operation Instructions: Calibrator for Partial Discharge Measurement KAL 451*: HAEFELY TRENCH HIGH VOLTAGE TECHNOLOGY.

[157] A. Cavallini, M. Conti, G. C. Montanari, C. Arlotti, and A. Contin, "PD inference for the early detection of electrical treeing in insulation systems," *Dielectrics and Electrical Insulation, IEEE Transactions on,* vol. 11, pp. 724-735, 2004.

[158] A. Cavallini, G. C. Montanari, M. Olivieri, and F. Puletti, "Diagnostic evaluations of electrical apparatus by a novel partial discharge measurement system," *Power System Technology, Proceedings of 2004 International Conference on, (PowerCon 2004),* vol. 2, pp. 1689-1693, 2004.

[159] L. A. Dissado and R. M. Hill, "The statistics of electrical tree inception," *Electrical Insulation, IEEE Transactions on,* vol. 25, pp. 660-666, 1990.

[160] J. H. Mason, "Breakdown of Insulation by Discharges," *Proc. IEE(IIA),* vol. 100, pp. 149-158, 1953.

[161] R. J. Densley and B. Salvage, "Partial Discharges in Gaseous Cavities in Solid Dielectrics under Impulse Voltage Conditions," *Electrical Insulation, IEEE Transactions on,* vol. EI-6, pp. 54-62, 1971.

[162] M. Gamez-Garcia, R. Bartnikas, and M. R. Wertheimer, "Synthesis Reactions Involving XLPE Subjected to Partial Discharges," *Electrical Insulation, IEEE Transactions on,* vol. EI-22, pp. 199-205, 1987.

[163] S. Wojtas, "Influence of aging by partial discharges on resistivity of polyethylene," in *Dielectric Materials, Measurements and Applications, 1988., Fifth International Conference on*, 1988, pp. 191-193.

[164] T. Tanaka, "Charge transfer and tree initiation in polyethylene subjected to AC voltage stress," *Electrical Insulation, IEEE Transactions on,* vol. 27, pp. 424-430, 1992.

[165] K. Imai, K. Ito, N. Shimizu, and M. Nawata, "Mechanism of tree propagation from a simulated tree channel," *Properties and Applications of Dielectric Materials, 2000. Proceedings of the 6th International Conference on,* pp. 239-242, 2000.

[166] E. Wasilenko, "Electrical ageing of polyethylene at impulse and AC test voltages," *Dielectric Materials, Measurements and Applications, 1988., Fifth International Conference on* pp. 387-390, 1988.

[167] F. Noto and N. Yoshimura, *Annu. Rep. Conf. Electrical Insulation and Dielectric Phenomena* pp. 207-217, 1974.

[168] R. Jocteur, E. Favrie, and H. Auclair, "Influence of surface and internal defects on polyethylene electrical routine test on VHV cables," *Power Apparatus and Systems, IEEE Transactions on,* vol. 96, pp. 513-523, 1977.

[169] K. Suzuki, Y. Tanaka, T. Takada, Y. Ohki, and C. Takeya, "Space charge distribution measurement in XLPE cable for detection of the water tree location," *Electrical Insulation and Dielectric Phenomena, 1999 Annual Report Conference on,* vol. 2, pp. 630-633, 17-20 Oct. 1999 1999.

[170] Y. F. F. Ho, G. Chen, A. E. Davies, S. G. Swingler, S. J. Sutton, R. N. Hampton, and S. Hobdell, "Measurement of space charge in XLPE insulation under 50 Hz ac electric stresses using the LIPP method," *Dielectrics and Electrical Insulation, IEEE Transactions on,* vol. 9, pp. 362-370, 2002.

[171] M. D. Noskov, A. S. Malinovski, M. Sack, and A. J. Schwab, "Self-consistent modeling of electrical tree propagation and PD activity," *Dielectrics and Electrical Insulation, IEEE Transactions on,* vol. 7, pp. 725-733, 2000.

[172] H. Z. Ding and B. R. Varlow, "Thermodynamic model for electrical tree propagation kinetics in combined electrical and mechanical stresses," *Dielectrics and Electrical Insulation, IEEE Transactions on,* vol. 12, pp. 81-89, 2005.

[173] J. M. Alison, J. V. Champion, and S. J. Dodd, "Dynamic model for bipolar charge injection during electrical tree initiation," *Conduction and Breakdown in Solid Dielectrics, 1995. ICSD'95., Proceedings of the 1995 IEEE 5th International Conference on,* pp. 314-318, 1995.

[174] T. Farr, R. Vogelsang, and K. Frohlich, "A new deterministic model for tree growth in polymers with barriers," *Electrical Insulation and Dielectric Phenomena, 2001 Annual Report. Conference on,* pp. 673-676, 2001.

[175] D. SJ, "A deterministic model for the growth of non-conducting electrical tree structures," *J. Phys. D: Appl. Phys. ,* vol. 36, pp. 129-141, 2003.

[176] L. A. Dissado, N. Wise, and J. C. Fothergill, "Electrical tree structures generated by the ab-initio discharge-avalanche model," *Electrical Insulation and Dielectric Phenomena, 1999 Annual Report Conference on,* pp. 605-608, 1999.

[177] J. V. Champion and S. J. Dodd, "An approach to the modeling of partial discharges in electrical trees," *J.Phys.D: Appl.Phys,* vol. 31, pp. 2305-2314, 1998.

[178] Suwarno, Y.Suzuoki, and T. Mizutani, "Model for electrical treeing discharges and computer simulation," *Properties and Applications of Dielectric Materials, 2000. Proceedings of the 6th International Conference on,* vol. 1, pp. 260-263, 2000.

[179] K. Wu, Y. Suzuok, T. Mizutani, and H. Xie, "Model for partial discharges associated with treeing breakdown: I. PDs in tree channels," *J.Phys.D: Appl.Phys,* vol. 33, pp. 1197-1201, 2000.

[180] G. Chen and A. E. Davies, "Electric stress computation- a needel-plane electrode system with space charge effects," *COMPEL,* vol. 15, pp. 40-56, 1996.

[181] X. Wang, D. Tu, Y. Tanaka, T. Muronaka, T. Takada, C. Shinoda, and T. Hashizumi, "Space charge in XLPE power cable under dc electrical stress and

heat treatment," *Dielectrics and Electrical Insulation, IEEE Transactions on,* vol. 2, pp. 467-474, 1995.

[182] T. Hibma and H. R. Zeller, "Direct measurement of space-charge injection from a needle electrode into dielectrics," *Journal of Applied Physics,* vol. 59, pp. 1614-1620, 1986.

[183] R. W. Hare and R. M. Hill, "Space charge in insulators with needle-plane geometry," *J. Phys. D: Appl. Phys.,* vol. 24, pp. 398-406, 1991.

[184] M. Mammeri and C. Laurent, "Influence of space charge buildup on the transition to electrical treeing in PE under ac voltage," *Dielectrics and Electrical Insulation, IEEE Transactions on,* vol. 2, pp. 27-35, 1995.

[185] G. Jiang, J. Kuang, and S. A. Boggs, "Evaluation of High Field Conduction Models of Polymeric Dielectrics," *Electric Insulation & Dielectric Phenomena (CEIDP), IEEE Conference on,* pp. 187-190, 2000.

[186] T. Mizutani, E. Nakane, K. Kaneko, M. Ishioka, and H. Takino, "Space charge and charge transport in polypropylene," *Electrets, 2005. ISE-12. 2005 12th International Symposium on,* pp. 475 - 478 2005.

[187] N. Shimizu and C. Laurent, "Electrical tree initiation," *Dielectrics and Electrical Insulation, IEEE Transactions on,* vol. 5, pp. 651-659, 1998.

[188] J. M. Alison and R. M. Hill, "A model for bipolar charge transport, trapping and recombination in degassed crosslinked polyethene," *Journal of Physics D: Applied Physics,* vol. 27, pp. 1291-1299, 1994.

[189] S. L. Roy, P. Segur, G. Teyssedre, and C. Laurent1, "Description of bipolar charge transport in polyethylene using a fluid model with a constant mobility: model prediction," *J. Phys. D: Appl. Phys. ,* vol. 37, pp. 298-305, 2004.

[190] K. Kaneko, T. Odaka, Y. Suzuoki, and T. Mizutani, "Study on space charge dynamics by computer simulation: Formation and transport of space charge packet," *Properties and Applications of Dielectric Materials, 1997., Proceedings of the 5th International Conference on,* vol. 2, pp. 821 - 824, 1997.

[191] M. Fukuma, M. Nagao, and M. Kosaki, "Computer analysis on transient space charge distribution in polymer," in *Properties and Applications of Dielectric Materials, 1994., Proceedings of the 4th International Conference on*, 1994, pp. 24-27 vol.1.

[192] F. Boufayed, S. Leroy, G. Teyssedre, C. Laurent, P. Segur, E. Cooper, L. A. Dissado, and G. C. Montanari, "Numerical resolution of charge transport in cross-linked polyethylene by means of a bipolar model with a distribution of traps," *Proceedings of 2004 International Conference on Solid Dielecfrics,* pp. 562-566, 2004.

[193] S. L. Roy, F. Boufayed, G. Teyssedre, C. Laurent, P. Segur, R. Bodega, P. H. F. Morshuis, G. C. Montanari4, and L. A. Dissado, "Computer simulation of space charge distribution in an XLPE-EPR sandwich," *Electrical Insulation and Dielectric Phenomena, 2005 Annual Report Conference on* pp. 661-664, 2005.

[194] L. V. Aźaroff, *Electronic processes in materials*: McGraw-Hill, 1963.

[195] B. Benamar, E. Favre, A. Donnot, and M. O. Rigo, "Finite Element Solution for Ionized Fields in DC Electrostatic Precipitator," *Proceedings of the COMSOL Users Conference 2007 Grenoble,* pp. 1-4, 2007.

[196] F. O'Sullivan, J. G. Hwang, M. Zahn, O. Hjortstam, L. Pettersson, R. Liu, and P. Biller, "A Model for the Initiation and Propagation of Positive Streamers in

Transformer Oil," *Electrical Insulation, 2008. ISEI 2008. Conference Record of the 2008 IEEE International Symposium on,* pp. 210 - 214, 2008.

[197] S. Le Roy, "Numerical methods in the simulation of charge transport in solid dielectrics," *Dielectrics and Electrical Insulation, IEEE Transactions on,* vol. 13, pp. 239-246, 2006.

[198] N. F. Mott and E. A. Davis, *Electronic Processes in Non-Crystalline Materials*, 2nd ed.: Clarendon, Oxford, 1979.

[199] O. A. M. Aly and A. S. Omar, "Reconstructing stratified permittivity profiles using super-resolution techniques," *Microwave Theory and Techniques, IEEE Transactions on,* vol. 54, pp. 492-498, 2006.

[200] R. F. Huang and D. M. Zhang, "Application of mode matching method to analysis of axisymmetric coaxial discontinuity structures used in permittivity and/or permeability measurement," *Progress In Electromagnetics Research, PIER* vol. 67, pp. 205-230, 2007.

[201] R. F. Huang, D. M. Zhang, and K. J. Tseng, "An efficient finite-difference-based Newton-Raphson method to determine intrinsic complex permeabilities and permittivities for Mn-Zn ferrites," *Magnetics, IEEE Transactions on,* vol. 42, pp. 1655-1660, 2006.

[202] R. Heinrich, R. Jobava, W. Kalkner, and A. Gheonjian, "Investigation and optimization of a sensor for partial discharge detection on high voltage XLPE cables," *Direct and Inverse Problems of Electromagnetic and Acoustic Wave Theory, 1998. DIPED-98. Proceedings of III International Seminar/Workshop on,* pp. 134-137, 2-5 Nov. 1998 1998.

[203] A. Almaghrawi, Y. K. Wong, G. Saxena, and D. A. Lowther, "Dimensional analysis and constraint propagation systems applied to the design of electromagnetic devices," *Magnetics, IEEE Transactions on,* vol. 36, pp. 1669-1672, 2000.

APPENDIX A: SPECIFICATIONS

Device Name	HV power supply	
Company	T&R Test Equipment Limited, Guildford, Surrey, ENGLAND	
Model	KV100-100 MKII fitted with capacitive voltage divider and DC extension unit	
Output Voltage	100 kV AC	100 kV DC
Output Current	100 mA	25 mA
Duty Cycle	5 min ON; 15 min OFF	
HV Transformer		
Voltage	Primary: 220 V	Secondary: 100,000V
Current	46A	100 mA
Frequency	50/60 Hz	

Device Name	Capacitor
Company	Appareils VETTINER SA LYON FRANCE
Model	CONDENSATEUR A GAZ SF6 6 bar abs CG10 N*6244
U eff. max	100 kV 50 Hz
Capacitance	105.2 pF

Device Name	Cables		
RG58C/U Coaxial Cable	RS Stock No.: 426-1990		
Outer Sheath Material	PVC		
Cable OD	4.95mm		
Sheath Color	Black		
Characteristic Impedance	50 Ω		
Capacitance	100 pF/m		
Max. dc Voltage	4 kVdc		
Max. Peak Voltage	2.6 kV		
Attenuation (per 10 m)	100 MHz 2.1 dB	200 MHz 3.1 dB	1000 MHz 7.6 dB
Overall Diameter	5 mm		
Length	1.2 m		
Connector Type	BNC		
Gender	Plug to plug		
Mounting	Cable mount		
Orientation	Straight		
Terminate To	RG58		

Device Name	Non-inductive resistor
Model	Arcol 82-16 HS50/1k±5%
Resistance	1 kΩ
Model	WH50 50R 5%
Resistance	50 Ω

Device Name	PD calibrator
Company	HAEFELY
Model	Calibrator for Partial Discharge measurement KAL 451
Dimensions	160 × 90 × 70 mm
Weight	500 g
Power Supply	Battery operation (4×1.5V alkaline batteries) Battery life >100 hours - A beep sounds in 20 second intervals if the unit is properly functioning. - A continuous tone sounds if the voltage is too low.
Temperature	+5 °C to +50 °C
Rel. Humidity	Max. 95 %; non-condensing
CAL IMPULSES	2/5/10/20/50/100/200 pC with 100 pF/1% capacitor 20/50/100/200/500/1000/2000 pC with 1 nF/1% capacitor
Tolerance	± 3 %
STEP/75 Ohm	Voltage step for corresponding CAL impulses with 100 pF or 1 nF Rise time 10%-90%: 20 ns typ., max. 50 ns
Triggering	Light triggering 50 Hz/60 Hz or if no light source is available, internal oscillator with frequency of approx. 50 Hz is used. 1 pulse per period.

Device Name	HFCT
Model	IPEC OSM HFCT 140/100
Transfer Impedance, Tr	4.2 - 4.6 mV/mA (5%)
Frequency Response	100kHz - 20MHz
Droop Time	4.5 m Sec (5%)
Typical Risetime Response	Better than 20nSec
Internal Clearance (diameter)	100mm
External Diameter	140mm
Recommended Load Impedance	50 W
Material/Finish	HDPE/Leather Finish
Output Connector	BNC Male
Max 50Hz Current	300Amps (with PVC spacers)
Weight	1.8 kg

Device Name	Oscilloscope
Model	TDS7104 Digital Phosphor Oscilloscope
Input Channels	4
Hardware Analog Bandwidth (-3dB)	1 GHz
Rise Time 10% to 90 % (typical)	400 ps
DC Gain Accuracy	1%
Hardware Bandwidth Limits	250 MHz
Input Coupling	AC, DC, GND
Input Impedance	1 MΩ ± 0.5% or 50 Ω±1%

Input Sensitivity, 1 MΩ	1 mV/div to 10 V/div
Input Sensitivity, 50 Ω	1 mV/div to 1 V/div
Vertical Resolution	8-Bit (>11-Bit with averaging)
Max. Input Voltage, 1 MΩ	±150 V CAT I derate at 20 dB/decade to 9 Vrms above 200 kHz
Max. Input Voltage, 50 Ω	5 Vrms with peaks less than ± 30 Volts
Offset Range	1 mV/div to 100 mV/div: ± 1V 101 mV/div to 1V/div: ± 10V 1.01 V/div to 10V/div: ± 100V
Channel-Channel Isolation Any Two Channels at Equal Vertical Scale Settings	≥ 100: 1 at 100 MHz and ≥ 30: 1 at the rated bandwidth

Device Name	Phase shifter
Model	RF-2 Single-phase phase shifter
Manufacture	Musashi Electrical Instruments Works Ltd., Japan

Device Name	Silicon oil
Model	GE SF97-50 Silicon Transformer Fluid
Dielectric Breakdown, Voltage KV @ 25 °C	35 minimum
Volume Resistivity ohm-cm @ 25 °C	1×10^{14} minimum
Power Factor @ 60 Hz @ 25°C @ 100 °C	0.0001 0.0005
Dielectric Constant, 60 Hz @ 25°C	2.7

Device Name	IDA200™ Insulation Diagnostic System
Manufacture	GE energy
Frequency Range	0.001 Hz to 1 kHz

Device Name	Digital camera
Model	SONY Cyber-shot DSC-F828
Optical Zoom	×7
Pixel	8.0 megapixel

Device Name	Optical microscope
Manufacture	Nikon
Magnification	×80

Device Name	Impedance analyzer
Model	HP 4294A (with 16451B dielectric test fixture)
Frequency Range	40 Hz to 110M Hz
Basic Z Accuracy	0.08 %
Measurement Display Range	25 mΩ to 40 MΩ
Main Application	LCR component,, material, semiconductor

APPENDIX B: SIMULATION SETTINGS IN COMSOL

Table 1 – Settings for nonlinear conductivity modeling

<table>
<tr><td>Model Navigator</td><td>Select Axial symmetry (2D) dimension;
AC/DC Module | Quasi-Statics, Electric | Meridional Electric Currents (V);
COMSOL Multiphysics | Heat Transfer | Conduction (T)</td></tr>
<tr><td>Draw Menu</td><td>Axial cross-section of needle-plane electrode geometry</td></tr>
<tr><td>Constants</td><td>Vp=1e4; er=2.3; e0=8.85e-12; T0=300; RHO=920;
HC=2170;</td></tr>
<tr><td>Scalar Expressions</td><td>E=sqrt(Vr^2+Vz^2);
sig1=62.64/E*exp(-6946/T)*exp(1.1408e-7*E);
sig2=2.025e-6/E*exp(-4066/T)*exp(2.103e-3*sqrt(E));
sig3=1.12e-5/E*exp(-6946/T)*exp(6.307e-2*E^(1/3));
sig=sig1;
V10ns=Vp/2*(1+tanh(1e9*t/0.45e9/tr1-3));
V100ns=Vp/2*(1+tanh(1e9*t/0.45e9/tr2-3));
V1200ns=Vp/2*(1+tanh(1e9*t/0.45e9/tr3-3));
Vtr=k*t.*(0<=t).*(t<=t0)-k*(t-2*t0).*(t0<t).*(t<=2*t0);
Vac=sin(2*pi*50*t)*Vp;
V0=V10ns;
TC=0.335-8.75e-4*(T-293);
Qe=sig*E^2;
rho=-er*e0*(1/r*diff((r*Vr),r)+Vzz);</td></tr>
<tr><td>Subdomain Settings</td><td><table>
<tr><td>Mode V</td><td>σ</td><td>sig</td></tr>
<tr><td></td><td>ε_r</td><td>er</td></tr>
<tr><td>Mode T</td><td>k</td><td>TC</td></tr>
<tr><td></td><td>ρ</td><td>RHO</td></tr>
<tr><td></td><td>C_p</td><td>HC</td></tr>
<tr><td></td><td>Q</td><td>Q_e</td></tr>
<tr><td></td><td>$T(t_0)$</td><td>T0</td></tr>
</table></td></tr>
<tr><td>Boundary Settings</td><td><table>
<tr><td>Mode V</td><td>$r = 0$</td><td>Axial symmetry</td></tr>
<tr><td></td><td>$z = 0$</td><td>Ground</td></tr>
<tr><td></td><td>Needle</td><td>$V_0 = Vac$</td></tr>
<tr><td></td><td>Insulation</td><td>Electric insulation</td></tr>
<tr><td>Mode T</td><td>All boundaries</td><td>Thermal insulation</td></tr>
</table></td></tr>
<tr><td>Mesh</td><td>Number of mesh points=2275; number of element=4376;
Finer mesh near needle tip</td></tr>
<tr><td>Solve Menu</td><td>Transient, electric currents; Time-dependent</td></tr>
</table>

Table 2 – Settings for Model 1.A

<table>
<tr><td>Model Navigator</td><td>Select 1D dimension;
Possion’s Equation (phi);
Convection and Diffusion (neu);
Convection and Diffusion (nhu);
Convection and Diffusion (net);
Convection and Diffusion (nht)</td></tr>
<tr><td>Draw Menu</td><td>Line through Point 1 (x=0) to Point 2 (x=1e-4)</td></tr>
<tr><td>Constants</td><td>A=1.2e6; Be=0.1; Bh=0.2; S0=S1=S2=4e-3; S3=0;
Ue=1e-14; Uh=2e-13; We=1.27; Wh=1.16; T=300; L=1e-4; e=1.6e-19; er=2.3; e0=8.85e-12; kB=1.38e-23; Va=6e3; hp=6.626e-34;
wed=0.96; whd=0.99; v=kB*T/hp; De=v*exp(-wed/kB*T);
Dh=v*exp(-whd/kB*T);
N0et=100; N0ht=100</td></tr>
<tr><td>Scalar Expressions</td><td>E: -phix;
rho: nhu+nht-neu-net;
dtneu: -S1*nht*neu-S3*nhu*neu-Be*neu*(1-net/N0et)+De*net;
dtnhu: -S2*nhu*net-S3*nhu*neu-Bh*nhu*(1-nht/N0ht)+Dh*nht;
dtnet: -S2*nhu*net-S0*nht*net+Be*neu*(1-net/N0et);
dtnht: -S1*nht*neu-S0*nht*net+Bh*nhu*(1-nht/N0ht);
JE2: A*T^2*exp(-e*We/(kB*T))
*exp(e*sqrt(0.25*e*abs(E)/(pi*er*e0))/(kB*T));
JH1: A*T^2*exp(-e*Wh/(kB*T))
*exp(e*sqrt(0.25*e*abs(E)/(pi*er*e0))/(kB*T));
JE1: Ue*E*neu;
JH2: Uh*E*nhu</td></tr>
<tr><td>Subdomain Settings</td><td><table>
<tr><td>Mode phi</td><td>c</td><td>er*e0</td></tr>
<tr><td></td><td>f</td><td>rho</td></tr>
<tr><td>Model neu</td><td>R</td><td>dtneu</td></tr>
<tr><td></td><td>u</td><td>-Ue*E</td></tr>
<tr><td>Model nhu</td><td>R</td><td>dtnhu</td></tr>
<tr><td></td><td>u</td><td>Uh*E</td></tr>
<tr><td>Model net</td><td>R</td><td>dtnet</td></tr>
<tr><td>Model nht</td><td>R</td><td>dtnht</td></tr>
</table></td></tr>
<tr><td>Boundary Settings</td><td><table>
<tr><td>Mode phi</td><td>Point 1</td><td>phi = Va</td></tr>
<tr><td></td><td>Point 2</td><td>Phi=0</td></tr>
<tr><td>Mode neu</td><td>Point 1</td><td>N=-JE1</td></tr>
<tr><td></td><td>Point 2</td><td>N=JE2</td></tr>
<tr><td>Mode nhu</td><td>Point 1</td><td>N=JH1</td></tr>
<tr><td></td><td>Point 2</td><td>N=-JH2</td></tr>
</table></td></tr>
<tr><td>Mesh</td><td>Number of mesh points=1813; number of element=1812;
Finer near Points 1 and 2</td></tr>
<tr><td>Solve Menu</td><td>Time-dependent; Times: 0:1e-3:100</td></tr>
</table>

Table 3 – Settings for Model II.A

<table>
<tr><td>Model Navigator</td><td>Select 1D dimension;
Possion's Equation (phi);
Convection and Diffusion (nhf);
Convection and Diffusion (nef)</td></tr>
<tr><td>Draw Menu</td><td>Line through Point 1 (x=0) to Point 2 (x=1e-4)</td></tr>
<tr><td>Constants</td><td>A=1.2e6; We=1.27; Wh=1.16; T=300; e=1.6e-19; er=2.3;
e0=8.85e-12; kB=1.38e-23; Va=6e3; hp=6.626e-34; v=kB*T/hp;
N1e=N1h=1e46; dem=0.608; dhm=0.534; T0e=T0h=2e4; ae
=T0e/T; ah=T0h/T; de= (N1e*kB*T0e)^(-1/3)*(1-exp(-
dem/kB/T0e))^(-1/3); dh= (N1h*kB*T0h)^(-1/3)*(1-exp(-
dhm/kB/T0h))^(-1/3)</td></tr>
<tr><td>Scalar Expressions</td><td>E: -phix;
rho: nhf+nht-nef-net;
ue: 2*v*de/E*(ne/e/N1e/kB/T0e+exp(-dem*e/kB/T0e))^ae
*sinh(e*E*de/2/kB/T);
uh: 2*v*dh/E*(nh/e/N1h/kB/T0h+exp(-dhm*e/kB/T0h))^ah
*sinh(e*E*dh/2/kB/T);
JE2: A*T^2*exp(-e*We/(kB*T))
*exp(e*sqrt(0.25*e*abs(E)/(pi*er*e0))/(kB*T));
JH1: A*T^2*exp(-e*Wh/(kB*T))
*exp(e*sqrt(0.25*e*abs(E)/(pi*er*e0))/(kB*T));
JE1: Ue*E*neu;
JH2: Uh*E*nhu;
net: ae*nef;
nht: ah*nhf;
ne: (1+ae)*nef;
nh: (1+ah)*nhf</td></tr>
<tr><td>Subdomain Settings</td><td>
<table>
<tr><td>Mode phi</td><td>c</td><td>er*e0</td></tr>
<tr><td></td><td>f</td><td>rho</td></tr>
<tr><td>Model nef</td><td>R</td><td>0</td></tr>
<tr><td></td><td>u</td><td>-ue*E</td></tr>
<tr><td>Model nhf</td><td>R</td><td>0</td></tr>
<tr><td></td><td>u</td><td>uh*E</td></tr>
</table>
</td></tr>
<tr><td>Boundary Settings</td><td>
<table>
<tr><td>Mode phi</td><td>Point 1</td><td>phi = Va</td></tr>
<tr><td></td><td>Point 2</td><td>Phi=0</td></tr>
<tr><td>Mode nef</td><td>Point 1</td><td>N=-JE1</td></tr>
<tr><td></td><td>Point 2</td><td>N=JE2</td></tr>
<tr><td>Mode nhf</td><td>Point 1</td><td>N=JH1</td></tr>
<tr><td></td><td>Point 2</td><td>N=-JH2</td></tr>
</table>
</td></tr>
<tr><td>Mesh</td><td>Number of mesh points=1348; number of element=1347;
Finer near Points 1 and 2</td></tr>
<tr><td>Solve Menu</td><td>Time-dependent; Times: 0:1e-3:100</td></tr>
</table>

APPENDIX C: NEWTON-RAPHSON METHOD

In numerical analysis, Newton's method (also known as the Newton–Raphson method or the Newton–Fourier method) is an efficient algorithm for finding approximations to the zeros (or roots) of a real-valued function. As such, it is an example of a root-finding algorithm. It produces iteratively a sequence of approximations to the root that has a quadratic rate of convergence. The method generalizes to complex and multidimensional versions.

It can also be used to find a minimum or maximum of such a function, by finding a zero in the function's first derivative.
The algorithm is first in the class of Householder's methods, succeeded by Halley's method.

A. Description of the method

The idea of the method is as follows: one starts with an initial guess which is reasonably close to the true root, then the function is approximated by its tangent line (which can be computed using the tools of calculus), and one computes the x-intercept of this tangent line (which is easily done with elementary algebra). This x-intercept will typically be a better approximation to the function's root than the original guess, and the method can be iterated.

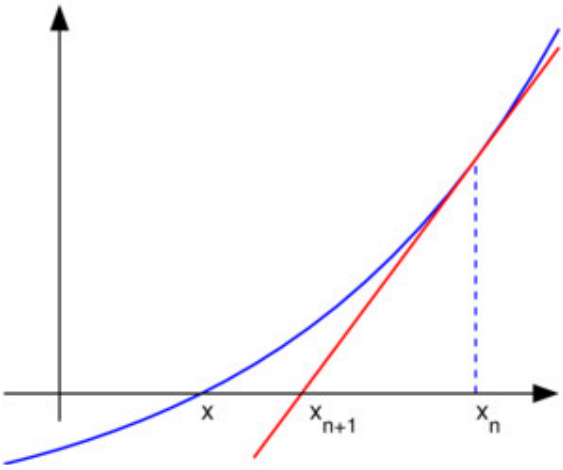

Figure A An illustration of one iteration of Newton's method (the function f is shown in blue and the tangent line is in red). We see that x_{n+1} is a better approximation than x_n for the root x of the function f.

Suppose $f : [a,b] \to \mathbf{R}$ is a differentiable function defined on the interval $[a,b]$ with values in the real numbers **R**. The formula for converging on the root can be easily derived. Suppose we have some current approximation x_n. Then we can derive the formula for a better approximation, x_{n+1} by referring to the diagram on the right. We

know from the definition of the derivative at a given point that it is the slope of a tangent at that point.
That is

$$f'(x_n) = \frac{\text{rise}}{\text{run}} = \frac{\Delta y}{\Delta x} = \frac{f(x_n) - 0}{x_n - x_{n+1}} = \frac{0 - f(x_n)}{(x_{n+1} - x_n)}.$$

Here, f' denotes the derivative of the function f. Then by simple algebra we can derive

$$x_{n+1} = x_n - \frac{f(x_n)}{f'(x_n)}$$

We start the process off with some arbitrary initial value x_0. (The closer to the zero, the better.) But, in the absence of any intuition about where the zero might lie, a "guess and check" method might narrow the possibilities to a reasonably small interval by appealing to the intermediate value theorem.) The method will usually converge, provided this initial guess is close enough to the unknown zero, and that $f'(x_0) \neq 0$. Furthermore, for a zero of multiplicity 1, the convergence is at least quadratic (see rate of convergence) in a neighborhood of the zero, which intuitively means that the number of correct digits roughly at least doubles in every step. More details can be found in the analysis section below.

B. Example

Consider the problem of finding the positive number x with $\cos(x) = x^3$. We can rephrase that as finding the zero of $f(x) = \cos(x) - x^3$. We have $f'(x) = -\sin(x) - 3x^2$. Since $\cos(x) \leq 1$ for all x and $x^3 > 1$ for $x > 1$, we know that our zero lies between 0 and 1. We try a starting value of $x_0 = 0.5$.

$$\begin{aligned}
x_1 &= x_0 - \frac{f(x_0)}{f'(x_0)} &&= 0.5 - \frac{\cos(0.5) - 0.5^2}{-\sin(0.5) - 3 \times 0.5^2} &&= 1.1121416370\ 97 \\
x_2 &= x_1 - \frac{f(x_1)}{f'(x_1)} &&\vdots &&= \underline{0.9}0967269373\ 6 \\
x_3 &\quad \vdots &&\vdots &&= \underline{0.86}7263818209 \\
x_4 &\quad \vdots &&\vdots &&= \underline{0.86547}\,7135298 \\
x_5 &\quad \vdots &&\vdots &&= \underline{0.8654740331}\,11 \\
x_6 &\quad \vdots &&\vdots &&= \underline{0.8654740331\ 02}
\end{aligned}$$

The correct digits are underlined in the above example. In particular, x_6 is correct to the number of decimal places given. We see that the number of correct digits after the decimal point increases from 2 (for x_3) to 5 and 10, illustrating the quadratic convergence.

C. History

Newton's method was described by Isaac Newton in *De analysi per aequationes numero terminorum infinitas* (written in 1669, published in 1711 by William Jones) and in *De metodis fluxionum et serierum infinitarum* (written in 1671, translated and published as

Method of Fluxions in 1736 by John Colson). However, his description differs substantially from the modern description given above: Newton applies the method only to polynomials. He does not compute the successive approximations x_n, but computes a sequence of polynomials and only at the end, he arrives at an approximation for the root x. Finally, Newton views the method as purely algebraic and fails to notice the connection with calculus. Isaac Newton probably derived his method from a similar but less precise method by François Viète. The essence of Viète's method can be found in the work of the Persian mathematician Sharaf al-Din al-Tusi.

Newton's method was first published in 1685 in *A Treatise of Algebra both Historical and Practical* by John Wallis. In 1690, Joseph Raphson published a simplified description in *Analysis aequationum universalis*. Raphson again viewed Newton's method purely as an algebraic method and restricted its use to polynomials, but he describes the method in terms of the successive approximations x_n instead of the more complicated sequence of polynomials used by Newton. Finally, in 1740, Thomas Simpson described Newton's method as an iterative method for solving general nonlinear equations using fluxional calculus, essentially giving the description above. In the same publication, Simpson also gives the generalization to systems of two equations and notes that Newton's method can be used for solving optimization problems by setting the gradient to zero.

Arthur Cayley in 1879 in *The Newton-Fourier imaginary problem* was the first who noticed the difficulties in generalizing the Newton's method to complex roots of polynomials with degree greater than 2 and complex initial values. This opened the way to the study of the theory of iterations of rational functions.

D. Practical considerations

In general the convergence is quadratic: the error is essentially squared at each step (that is, the number of accurate digits doubles in each step). There are some caveats, however. First, Newton's method requires that the derivative be calculated directly. (If the derivative is approximated by the slope of a line through two points on the function, the secant method results; this can be more efficient depending on how one measures computational effort.) Second, if the initial value is too far from the true zero, Newton's method can fail to converge. Because of this, most practical implementations of Newton's method put an upper limit on the number of iterations and perhaps on the size of the iterates. Third, if the root being sought has multiplicity greater than one, the convergence rate is merely linear (errors reduced by a constant factor at each step) unless special steps are taken.

E. Generalizations

1) Nonlinear systems of equations

One may use Newton's method also to solve systems of k (non-linear) equations, which amounts to finding the zeros of continuously differentiable functions $F : R_k \to R_k$. In the formulation given above, one then has to left multiply with the inverse of the k-by-k

Jacobin matrix $J_F(x_n)$ instead of dividing by $f'(x_n)$. Rather than actually computing the inverse of this matrix, one can save time by solving the system of linear equations

$$J_F(x_n)(x_{n+1} - x_n) = -F(x_n)$$

for the unknown $x_{n+1} - x_n$. Again, this method only works if the initial value x_0 is close enough to the true zero. Typically, a region which is well-behaved is located first with some other method and Newton's method is then used to "polish" a root which is already known approximately.

2) Nonlinear equations in a Banach space

Another generalization is the Newton's method to find a zero of a function F defined in a Banach space. In this case the formulation is

$$X_{n+1} = X_n - (F'_{X_n})^{-1}[F(X_n)],$$

where F'_{X_n} is the Fréchet derivative applied at the point X_n. One needs the Fréchet derivative to be invertible at each X_n in order for the method to be applicable.

3) Complex functions

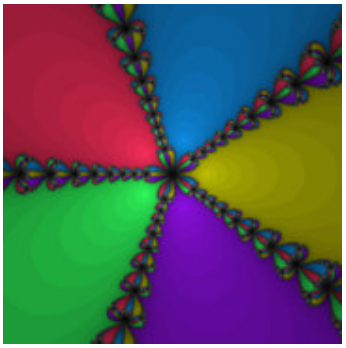

Figure B Basins of attraction for $x^5 - 1 = 0$; darker means more iterations to converge.

When dealing with complex functions, however, Newton's method can be directly applied to find their zeros. For many complex functions, the boundary of the set (also known as the basin of attraction) of all starting values that cause the method to converge to a particular zero is a fractal.